Analysis and Simulation of Molecular Systems: Memory Function Approach and Uncertainty Quantification

by

Changho Kim

B.Sc., KAIST; Daejeon, South Korea, 2001

M.Sc., KAIST; Daejeon, South Korea, 2003

Ph.D., KAIST; Daejeon, South Korea, 2007

M.Sc., Brown University; Providence, RI, 2011

A dissertation submitted in partial fulfillment of the

requirements for the degree of Doctor of Philosophy

in The Division of Applied Mathematics at Brown University

PROVIDENCE, RHODE ISLAND

May 2015

This dissertation by Changho Kim is accepted in its present form
by The Division of Applied Mathematics as satisfying the
dissertation requirement for the degree of Doctor of Philosophy.

Date_____ _____

George Em Karniadakis, Ph.D., Advisor

Recommended to the Graduate Council

Date_____ _____

Anastasios Matzavinos, Ph.D., Reader

Date_____ _____

Richard Stratt, Ph.D., Reader

Date_____ _____

Oleg Borodin, Ph.D., Reader

Approved by the Graduate Council

Date_____ _____

Peter M. Weber, Dean of the Graduate School

Vita

Changho Kim

(김창호)

Date of Birth: September 24, 1979

Place of Birth: Busan, South Korea

EDUCATION

Brown University	*Providence, Rhode Island*
Ph.D. in Applied Mathematics	September 2010 – May 2015
M.Sc. in Applied Mathematics	September 2010 – May 2011
KAIST	*Daejeon, South Korea*
Ph.D. in Chemistry	September 2003 – August 2007
M.Sc. in Chemistry	September 2001 – February 2003
B.Sc. in Chemistry and in Mathematics	March 1997 – August 2001
(double major, summa cum laude)	

EMPLOYMENT

KAIST	*Seoul/Daejeon, South Korea*
Postdoctoral researcher in College of Business	September 2008 – August 2009
Postdoctoral researcher in Department of Mathematics	September 2007 – August 2008

PUBLICATIONS

1. C. Kim and G.E. Karniadakis, "Brownian motion of a Rayleigh particle confined in a channel: A generalized Langevin equation approach", J. Stat. Phys. **158**, 1100–1125 (2015)

[DOI: 10.1007/s10955-014-1160-2]

2. C. Kim and G.E. Karniadakis, "Time correlation functions of Brownian motion and evaluation of friction coefficient in the near-Brownian-limit regime", Multiscale Model. Simul. **12**, 225–248 (2014) [DOI: 10.1137/130929916]

3. C. Kim and G.E. Karniadakis, "Microscopic theory of Brownian motion revisited: The Rayleigh model", Phys. Rev. E **87**, 032129 (2013) [DOI: 10.1103/PhysRevE.87.032129]

4. H. Kim, W.A. Goddard III, K.H. Han, C. Kim, E.K. Lee, P. Talkner and P. Hänggi, "Thermodynamics of d-dimensional hard sphere fluids confined to micropores", J. Chem. Phys. **134**, 114502 (2011) [DOI: 10.1063/1.3564917]

5. H.K. Shin, C. Kim, P. Talkner, and E.K. Lee, "Brownian motion from molecular dynamics", Chem. Phys. **375**, 316–326 (2010) [DOI: 10.1016/j.chemphys.2010.05.019]

6. C. Kim, P. Talkner, E.K. Lee, and P. Hänggi, "Rate description of Fokker–Planck processes with time-periodic parameters", Chem. Phys. **370**, 277–289 (2010) [DOI: 10.1016/j.chemphys.2009.10.027]

7. H. Kim, C. Kim, E.K. Lee, P. Talkner, and P. Hänggi, "Wall-mediated self-diffusion in slit and cylindrical pores", Phys. Rev. E **77**, 031202 (2008) [DOI: 10.1103/PhysRevE.77.031202]

8. C. Kim, E.K. Lee, P. Hänggi, and P. Talkner, "Numerical method for solving stochastic differential equations with Poissonian white shot noise", Phys. Rev. E **76**, 011109 (2007) [DOI: 10.1103/PhysRevE.76.011109]

9. C. Kim, E.K. Lee, and P. Talkner, "Numerical method for solving stochastic differential equations with dichotomous noise", Phys. Rev. E **73**, 026101 (2006) [DOI: 10.1103/Phys-

RevE.73.026101]

10. H.J. Lee, C. Kim, J.G. Kim, and E.K. Lee, "A general scheme for studying the stochastic dynamics of a parametric oscillator driven by coloured noise", J. Phys. A: Math. Gen. **37**, 647–656 (2004) [DOI: 10.1088/0305-4470/37/3/009]

11. J.-W. Lee, C. Kim, E.K. Lee, J. Kim, and S. Lee, "Qubit geometry and conformal mapping", Quantum Information Processing **1**, 129–134 (2002) [DOI: 10.1023/A:1019645000745]

Submitted Manuscript

1. C. Kim, O. Borodin, and G.E. Karniadakis, "Uncertainty quantification for molecular dynamics simulation: Time-dependent diffusion coefficient in simple fluids", submitted to J. Comput. Phys.

Book and Book Chapter (submitted or in preparation)

1. C. Kim and G.E. Karniadakis, "Brownian Motion from a Microscopic Perspective", in preparation for SpringerBriefs in Applied Sciences and Technology.

2. X. Li, Z. Li, X. Bian, M. Deng, C. Kim, Y.-H. Tang, A. Yazdani, and G.E. Karniadakis, "Dissipative particle dynamics: An overview", submitted to Encyclopedia of Nanotechnology.

TEACHING EXPERIENCE

Brown University — *Providence, Rhode Island*

Teaching assistant, Monte Carlo Simulation with Applications to Finance — Spring 2013

Teaching assistant, Methods of Applied Mathematics (honors level) — Fall 2012

KAIST — *Daejeon, South Korea*

Instructor, Introduction to Linear Algebra — Fall 2007

Teaching assistant, Computational Chemistry — Fall 2004

Teaching assistant, Quantum Chemistry I — Spring 2004

Teaching assistant, Statistical Thermodynamics — Fall 2003

SCHOLARSHIPS AND SUPPORT

Research Assistantship, Brown University (June 2013 – May 2015)

Teaching Assistantship, Brown University (September 2012 – May 2013)

Korean Government Scholarship: Study Abroad Program (September 2010 – August 2012)

NRF (Korea) – DAAD (Germany) Summer Institute Program (July 2005 – August 2005)

Preface and Acknowledgments

This dissertation is submitted for the degree of Doctor of Philosophy at Brown University. The research described herein was conducted under the supervision of Professor G.E. Karniadakis in the Division of Applied Mathematics, Brown University, between September 2010 and April 2015. It was partially supported by the Department of Energy (DOE) through the Collaboratory on Mathematics for Mesoscopic Modeling of Materials (CM4) and by the Army Research Laboratory (ARL) through the Alliance for Computationally-guided Design of Energy Efficient Electronic Materials (CDE3M). Computations were performed at IBM BG/Q machines with computer time provided by an INCITE grant. The molecular dynamics (MD) simulation results for the ethylene carbonate liquid, which is presented in Section 6.7, were obtained from a computational code provided by Dr. Oleg Borodin of the Army Research Laboratory (ARL). The simulation results presented in Chapter 5 and Section 6.3 were obtained from computational codes developed by myself. The other MD simulation results presented in the dissertation were obtained from the LAMMPS Molecular Dynamics Simulator. The code was modified so that it launches an ensemble of MD simulators and analyzes results obtained from this ensemble.

Parts of this work has led to the following publications and submission:

- Kim, C., Karniadakis, G.: Microscopic theory of Brownian motion revisited: The Rayleigh model. Phys. Rev. E **87**, 032129 (2013)

- Kim, C., Karniadakis, G.: Time correlation functions of Brownian motion and evaluation of friction coefficient in the near-Brownian-limit regime. Multiscale Model. Simul. **12**, 225–248 (2014)
- Kim, C., Karniadakis, G.: Brownian motion of a Rayleigh particle confined in a channel: A generalized Langevin equation approach. J. Stat. Phys. **158**, 1100–1125 (2015)
- Kim, C., Borodin, O., Karniadakis, G.: Uncertainty quantification for molecular dynamics simulation: Time-dependent diffusion coefficient in simple fluids. Submitted to J. Comput. Phys.

I would like to express my gratitude to all those who gave me the possibility to complete this thesis. Foremost, I would like to express my deepest and sincere gratitude to my advisor Professor George Karniadakis for his enlightening guidance, unreserved support, and wholehearted encouragement. I am indebted to Professor Richard Stratt, Professor Anastasios Matzavinos, and Dr. Oleg Borodin for their careful reading of the thesis manuscript as well as their valuable comments. I would also like to thank Dr. Oleg Borodin for introducing me interesting uncertainty quantification problems and realistic molecular dynamics simulations. I gratefully acknowledge Dr. Jonathan Shiff for his attentive proofreading of the first chapter of the thesis manuscript. I would like to thank all members of the CRUNCH group. Special thanks are extended to the DPD club members, including Xuejin Li, Xin Bian, Zhen Li, and Mingge Deng; Korean lab mates, Minseok Choi, Heyrim Cho, and Seungjoon Lee; and long-time office mates, Mohsen Zayernouri and Mengdi (Summer) Zheng. I would also like to thank my department staffs, Madeline Brewster and Jean Radican, for their assistance.

Finally, I would like to take this chance to extend my heartfelt gratitude to people

who have always supported me in whatever endeavor I choose. I would like to thank Professor Eok Kyun Lee and Professor Peter Talkner, who are my academic parents. My last words should be given in Korean: 멀리 한국에서 응원과 격려를 아끼지 않는 우리 가족 모두 사랑합니다. 미국에서 박사과정을 시작하고 또 마칠 때까지 힘이 되어준 김민호 형에게 감사를 드립니다.

Changho Kim

Providence, Rhode Island

April, 2015

Contents

List of Tables

List of Figures

Chapter One

Overview

In biological and material systems, understanding a phenomenon at the molecular level is of great importance, and the molecular dynamics (MD) simulation technique has played a crucial role in this understanding [161]. In the classical description of any such system, where quantum effects are assumed not to be significant, the time evolution of the system is described by Newton's equations of motion for all atoms and can be calculated by numerically solving a large set of ordinary differential equations. Although in principle any molecular phenomenon can be investigated with this approach, the computation quickly becomes prohibitively expensive as the number of atoms in the system and/or the time scale of the phenomenon increase. Hence, higher-level descriptions, which require a smaller number of degrees of freedom with larger temporal and spatial scales, are necessary, and it is therefore desirable to make use of both microscopic and higher-level descriptions in a complementary fashion.

At the macroscopic scale, the description of a system is based on the continuum hypothesis [111]. The dynamics of the system is described by field variables such as pressure, temperature, density, velocity, etc., which satisfy a set of partial differential equations (e.g., the Navier–Stokes equations). Transport coefficients (e.g., viscosity and diffusion coefficient), which appear in the partial differential equations, represent material properties which are inherent in the microscopic structure of the system. Statistical mechanics connects the microscopic and macroscopic descriptions by providing formulas for the transport coefficients that can be calculated by MD simulations. Conceptually, since an infinitesimal volume element in the continuum description is considered as a molecular subsystem, transport coefficients can be obtained by averaging certain quantities over the microscopic configurations which the molecular subsystem undergoes over time. As a result, while in the microscopic description the system is subject to thermal fluctuations due to molecular motions, such fluctuations do not appear in the macroscopic description and only smooth

changes in the state of the system are depicted.

For a complex system, where the macroscopic continuum description is not possible, the mesoscopic description can be a more promising approach. At the mesoscopic scale, the interaction is broken down into random thermal fluctuation and smoothed interaction, the magnitudes of which are comparable. For example, proteins suspended in water are subject not only to random bombardment of water molecules but also to hydrodynamic interaction with water. As a result, in the mesoscopic description, the time evolution equations contain both stochastic and deterministic terms. The mesoscopic description can be obtained from both microscopic and macroscopic descriptions. In the bottom-up approach, the concepts of coarse-graining and implicit solvation are employed to obtain the dissipative particle dynamics [72] and the Langevin/Brownian dynamics [168]. In the top-down approach, following Landau and Lifshitz [109], stochastic fluxes are incorporated to the continuum description to obtain fluctuating hydrodynamics methods [8, 137].

This study as a whole addresses issues related to the connection between the microscopic and higher-level descriptions for molecular systems and presents relevant analysis of these descriptions and the MD simulation technique. In Part A, I explain how the mesoscopic description is obtained from the microscopic description. Although this has been extensively investigated in the literature, in most cases, results have been obtained under the Markovian assumption that the mesoscopic time scale is fully separated from the microscopic time scale. By using the memory function approach, I present a clear picture for a *continuous* transition to the mesoscopic stochastic description as the time-scale separation is realized. I consider a colloidal particle suspended in a molecular fluid and investigate its Brownian motion. In Part B, I demonstrate a theoretical and computational framework for the uncertainty quantification in MD simulation results. Two types of intrinsic uncertainty

present in MD simulation results—statistical errors and finite-system-size effects—are analyzed. Although the MD procedure and underlying theory for the calculation of transport coefficients have been well established and computational power has been drastically increased, due to severe limitations of the MD simulation technique on time and spatial scales, systematic qualitative analysis on these uncertainties is still required for the accurate estimation of material properties. As an example of a transport coefficient, I consider the diffusion coefficient and analyze the statistical errors and the finite-system-size effects in its evaluation.

In the rest of this chapter, I provide background for Part A (in Section 1.1) and Part B (in Section 1.2) and synopses for each chapter within them (in Section 1.3). Note that, for the completeness of each chapter, some equations in this chapter reappear, sometimes with appropriate modifications.

1.1 Background for Part A

Brownian motion When a colloidal particle is suspended in a fluid, it undergoes a random motion—Brownian motion. Since Einstein explained that this erratic motion is caused by the random bombardment of surrounding fluid particles [43], it has been extensively investigated and well understood both experimentally and theoretically. Due to its broad applications in many areas of science and engineering, there has been a recent increase of interest in this phenomenon. For the history of Brownian motion, the reader is referred to the web page of Professor Peter Hänggi of Universität Augsburg [75], where all important historic sources are accessible, and to Ref. [142], where the history of mathematical formulation of Brownian motion is presented in parallel. The reader is also referred to Ref. [160] for a review of the

phenomenon from the hydrodynamic point of view, to Ref. [121] for recent progress on experimental observation of Brownian motion at short time scales, and to Ref. [60] for applications of Brownian motion to soft matter and biological systems.

Langevin equation The Langevin equation is a phenomenological equation for the velocity $\mathbf{V}$ of a colloidal particle suspended in a fluid,

$$M\dot{\mathbf{V}}(t) = -\gamma\mathbf{V}(t) + \sqrt{\Delta}\dot{\mathbf{W}}_t, \tag{1.1.1}$$

where M and γ are the mass and friction coefficient of the particle, respectively, and $\dot{\mathbf{W}}_t$ is the standard Gaussian white noise. Here, the noise intensity Δ satisfies the fluctuation-dissipation relation with γ,

$$\Delta = 2\gamma k_{\mathrm{B}}T, \tag{1.1.2}$$

where T is the temperature of the system. Compared with the seminal work on Brownian motion by Einstein [43] and Smoluchowski [167], Langevin's description of Brownian motion [110, 116] was the first dynamical theory in Newton's sense. Experimentally, Brownian motion in a gas is well described by the Langevin equation, whereas for the description of Brownian motion in a liquid the hydrodynamic effects of the surrounding fluid is also required to be considered [121].

Microscopic theory of Brownian motion Investigation on the connection of the Langevin description to the microscopic description has been initiated by the pioneering work of Kirkwood [98]. He showed that γ is expressed as the time integral

of the autocorrelation function of the total force $\mathbf{F}$ on the colloidal particle,

$$\gamma = \frac{1}{dk_{\mathrm{B}}T}\int_0^\infty \lim_{M\to\infty} \langle \mathbf{F}(0)\cdot\mathbf{F}(t)\rangle \, dt, \tag{1.1.3}$$

where d is the dimensionality of the system and the brackets $\langle\ \rangle$ denote the equilibrium average. Subsequently, it has been shown that, for a microscopic system consisting of a colloidal particle and surrounding solvent particles, the Langevin equation is obtained in the Brownian limit [112, 113, 158].

The derivations essentially rely on the time-scale separation between the colloidal particle and solvent particles. As the ratio of the mass M of the colloidal particle to the mass m of a solvent particle becomes larger, the colloidal particle is expected to move slower due to the equipartition theorem

$$\frac{1}{2}m\left\langle \mathbf{v}^2\right\rangle = \frac{1}{2}M\left\langle \mathbf{V}^2\right\rangle = \frac{d}{2}k_{\mathrm{B}}T, \tag{1.1.4}$$

where $\mathbf{v}$ is the velocity of a solvent particle. In other words, the colloidal particle moves in a different time scale of the order of $\sqrt{M/m}$, which is called the Brownian time scale τ_{Br}. Assuming this time-scale separation, for the time evolution equation of the probability distribution for the colloidal particle, the leading-order terms with respect to $\sqrt{m/M}$ are collected to obtain the Fokker–Planck equation, which is equivalent to the Langevin equation. Although the Kirkwood formula, Eq. (1.1.3), is also obtained from this approach, it is difficult to investigate finite-mass Brownian motion by further analyzing higher-order terms. This is because the approach employs complicated formal operator manipulation. In addition, the Kirkwood formula has some delicate issues when it is employed in MD simulations [51]. The Brownian limit $M\to\infty$ and the time integral operator are not interchangeable in the formula and the time integral of the total force autocorrelation function $\langle \mathbf{F}(0)\cdot\mathbf{F}(t)\rangle$

eventually becomes zero for a system containing a finite number of solvent particles.

Generalized Langevin equation (GLE) Compared with the Langevin equation, Eq. (1.1.1), in the generalized Langevin equation,

$$M\dot{\mathbf{V}}(t) = -\int_0^t K(t-t')\mathbf{V}(t')dt' + \mathbf{F}^+(t), \tag{1.1.5}$$

the friction term $-\gamma\mathbf{V}(t)$ is replaced by a time convolution term with the memory function $K(t)$ and the Gaussian white noise term $\sqrt{\Delta}\dot{\mathbf{W}}_t$ is replaced by the fluctuating force $\mathbf{F}^+(t)$. Correspondingly, the fluctuation-dissipation relation becomes

$$\left\langle \mathbf{F}^+(0)\cdot\mathbf{F}^+(t)\right\rangle = dk_{\mathrm{B}}TK(t). \tag{1.1.6}$$

In addition, the assumption that the noise is an independent process is weakened as the following uncorrelatedness condition

$$\left\langle \mathbf{V}(0)\cdot\mathbf{F}^+(t)\right\rangle = 0. \tag{1.1.7}$$

From the microscopic time evolution equations, Mori obtained the GLE [140] by using the projection operator technique, which is also known as the Mori–Zwanzig formalism. Contrary to the Langevin equation, which becomes valid only on the Brownian time scale τ_{Br} in the Brownian limit $M \to \infty$, the GLE is equivalent to the microscopic description and is valid at all time scale and for any value of M.

It is noted that this form of the time-convolution memory term in the GLE leads to a time homogeneous process. Although its use (instead of a more general kernel [133, 173] for nonequilibrium systems) may restrict the physics of the model, it allows a system to attain ergodicity. It is also noted that the GLE has been also

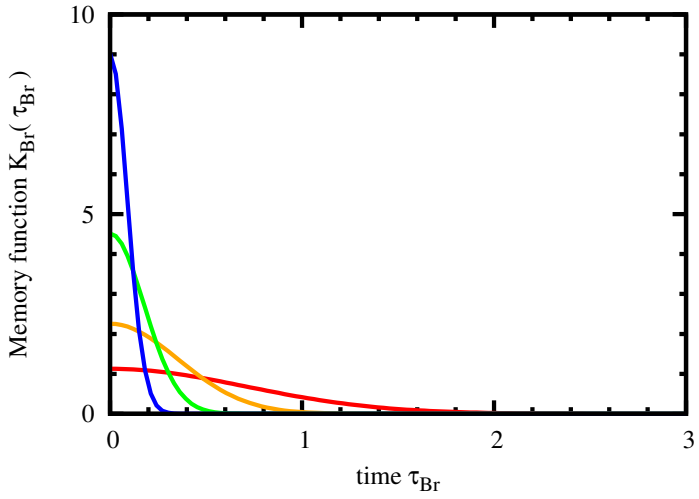

Figure 1.1: Schematic plot for the scaling behavior of the memory function $K_{\rm Br}(\tau_{\rm Br})$ on the Brownian time scale $\tau_{\rm Br}$. As the mass M of the colloidal particle increases, the width of the memory function decreases, whereas its height increases. Compared with the red curve, the orange, green, and blue curves correspond to the cases of larger mass M by factor of 4, 16, and 64, respectively.

used to describe other types of motion such as rotation [32] and vibration [67, 183] as well as chemical kinetics [182].

Heuristic explanation on the transition to the Langevin description By using the GLE, it can be heuristically explained how the microscopic description becomes the Langevin description as the mass M of the colloidal particle increases. First, it is observed that, if $K(t) = 2\gamma\delta(t)$, the GLE is reduced to the Langevin equation. The time convolution term is reduced to $-\gamma V(t)$, whereas by Eq. (1.1.6) the fluctuating force becomes δ-correlated and its noise intensity satisfies Eq. (1.1.2). Second, it can be argued that, on the Brownian time scale, the memory function actually becomes a delta function as the mass M increases. From $\tau_{\rm Br} = \sqrt{\frac{m}{M}}t$, the memory function $K_{\rm Br}(\tau_{\rm Br})$ on the Brownian time scale $\tau_{\rm Br}$ is written as

$$K_{\rm Br}(\tau_{\rm Br}) = \sqrt{\frac{M}{m}} K\left(\sqrt{\frac{M}{m}}\tau_{\rm Br}\right). \tag{1.1.8}$$

As shown in Fig. 1.1, the shape of $K_{\mathrm{Br}}(\tau_{\mathrm{Br}})$ becomes a delta function in the Brownian limit $M \to \infty$. Hence, by combining these two observations, it can be described how the transition from the microscopic description to the Langevin description occurs under the Brownian limit. In addition, the following expression is obtained:

$$\gamma = \lim_{M\to\infty} \int_0^\infty K(t)dt. \tag{1.1.9}$$

However, this heuristic argument assumes that (1) the shape of $K(t)$ does not change significantly as M increases, and (2) the effects of the long-time tail of $K(t)$ are negligible.

Volterra equation Although the memory function $K(t)$ is defined as the auto-correlation function of the fluctuating force $\mathbf{F}^+$, see Eq. (1.1.6), in Mori's derivation, calculating $K(t)$ from this definition is not practical, because the time evolution of $\mathbf{F}^+$ is formally defined by certain operators. Instead, $K(t)$ can be calculated by the following Volterra equation:

$$M\dot{C}(t) = -\int_0^t K(t-t')C(t')dt', \tag{1.1.10}$$

where $C(t)$ is the velocity autocorrelation function $\langle \mathbf{V}(0)\cdot\mathbf{V}(t)\rangle$. In other words, by obtaining $C(t)$ from MD simulation, Eq. (1.1.10) is numerically solved for $K(t)$. This equation is obtained by multiplying $\mathbf{V}(0)$ to Eq. (1.1.5), taking the equilibrium average, and using Eq. (1.1.7).

The following observations are made on the Volterra equation and the memory function. First, as is true for the GLE, the Volterra equation is valid at all time scales and for any value of M. Second, once either $K(t)$ or $C(t)$ is known, the other can be calculated by solving the equation for the latter. Since the mean-squared

displacement can be calculated from $C(t)$ through the relation

$$\left\langle [\mathbf{X}(t) - \mathbf{X}(0)]^2 \right\rangle = 2 \int_0^t dt' \int_0^{t'} dt'' \, C(t'') \tag{1.1.11}$$

and vice versa, $K(t)$ actually contains information on Brownian motion that is equivalent to the velocity autocorrelation function and the mean-squared displacement.

Memory function approach In the memory function approach, the memory function $K(t)$ is assumed to be a more fundamental quantity and its behaviors are investigated to understand the behaviors of the original correlation function (i.e., $C(t)$). Once a certain behavior of $K(t)$ is found, a corresponding behavior of $C(t)$ is investigated through the Volterra equation.

For example, the heuristic scenario of the Brownian motion given above can be examined by the following asymptotic behavior of the memory function for large M [89],

$$K(t) \approx K_0(t) + \frac{1}{M} K_1(t). \tag{1.1.12}$$

This asymptotic form can be verified by numerically calculating $K(t)$ from MD result of $C(t)$, whereas a corresponding asymptotic expansion of $C(t)$ can be derived by analytically solving the Volterra equation for $C(t)$ in terms of $K_0(t)$ and $K_1(t)$.

The *limit memory function* $K_0(t) = \lim_{M\to\infty} K(t)$ satisfies the fluctuation-dissipation relation

$$\langle \mathbf{F}_0(0) \cdot \mathbf{F}_0(t) \rangle = d k_{\mathrm{B}} T K_0(t) \tag{1.1.13}$$

with the force $\mathbf{F}_0$ on the Brownian particle in the *frozen dynamics*. In this dynamics, the colloidal particle is assumed to be fixed due to its infinite mass and only the solvent particles move under the external potential due to the presence of the fixed

colloidal particle. It is noted that, contrary to the velocity autocorrelation function and the mean-square displacement, which become singular in the Brownian limit, the memory function possesses a proper limit, which is defined through the frozen dynamics.

Rayleigh gas model A Rayleigh gas is an ideal gas containing a colloidal particle. In other words, each gas particle does not interact with other gas particles and only interacts with the colloidal particle. As a result, any hydrodynamic effects of the surrounding particles is neglected and only direct interaction between the colloidal particle and gas particles is considered. Although this model loses many interesting physics due to the non-interacting bath assumption, this assumption allows analytic tractability. Mathematical proofs for the Brownian limit are available [39, 108] and analytic results for the friction coefficient are also available [44, 70, 96, 128, 138]. Roughly speaking, this analytic tractability is attributed to the fact that the dynamics of each gas particle becomes decoupled from those of other gas particles in the frozen dynamics.

1.2 Background for Part B

Model and parametric uncertainties in MD simulation The force field is a mathematical model which estimates the potential energy of a molecular system using a certain functional form with a set of parameter values. Since the force exerted on each atom is determined by the force field, the accuracy of MD simulation is critically dependent on it. However, for the sake of computational efficiency, a simple form is usually assumed (e.g., excluding many-body interactions) and the

corresponding parameter set is calibrated by matching some material properties with experimental values. Hence it is important to understand how the uncertainties in the force field affect the resulting values for material properties.

Two types of intrinsic uncertainty in MD simulation Severe limitations on the time-step size and the number of particles in MD simulation impose the following uncertainties in MD simulation results. First, statistical errors arise from insufficient MD runs, which in turn may result from the constraint on the time-step size. While a very small time step ($\lesssim 1$ fs) must be used in order to resolve atomic interactions, only a sufficiently long run will allow a system to explore the entire accessible region of phase space. As a result, an average calculated from an insufficient MD run is different from the true value. The error is random in nature because of the ergodic hypothesis of molecular systems; this is why it is called the statistical error. Second, the finite-system-size effects are due to the relatively small number of atoms in MD simulation. Despite modern computing power, the possible number of atoms that can be calculated in MD simulation is much less than Avogadro's number. To approximate the behavior of a macro-scale system, periodic boundary conditions are usually imposed at the boundaries of the MD simulation box. However, because of the unphysical interaction of a system with its own periodic image, MD results may be affected by the system size, which is called the finite-system-size effect.

It is important to note that, before quantifying the model and parametric uncertainties in MD simulation, one must suppress these intrinsic uncertainties. In fact, in order to analyze any systematic error, the level of statistical error must be smaller than the systematic error. Also, MD results should be corrected through finite-system-size correction before parametric uncertainty quantification. Therefore, accurate prediction of the level of the statistical error and accurate finite-system-size

correction are an important first step before any other type of uncertainty quantification in MD simulation.

1.3 Synopses

Synopsis of Chapter 2

For the Rayleigh gas model, analytic expressions for the frozen dynamics force autocorrelation function $\langle \mathbf{F}_0(0) \cdot \mathbf{F}_0(t) \rangle$ and the friction coefficient γ are obtained in terms of single-gas-particle trajectory by the ensemble-average method and the ray representation approach. For the hard-sphere interaction and the square-well potential between the colloidal particle and a gas particle, closed-form expressions are obtained.

Through the ray representation approach, the microscopic picture near the Brownian limit can be clearly understood. For example, how the total force autocorrelation function $\langle \mathbf{F}(0) \cdot \mathbf{F}(t) \rangle$ becomes $\langle \mathbf{F}_0(0) \cdot \mathbf{F}_0(t) \rangle$ in the Brownian limit and how the latter is interpreted as a delta function on the Brownian time scale can be explained within a mathematical probabilistic setting. In this approach, the noise intensity Δ is obtained in the time-average sense.

In the MD simulation part, MD simulation results for the Rayleigh gases under the Lennard-Jones (LJ) and Week–Chandler–Andersen (WCA) potentials are presented. Three force autocorrelation functions, $\langle \mathbf{F}(0) \cdot \mathbf{F}(t) \rangle$, $\langle \mathbf{F}^+(0) \cdot \mathbf{F}^+(t) \rangle$, and $\langle \mathbf{F}_0(0) \cdot \mathbf{F}_0(t) \rangle$ are calculated. $\langle \mathbf{F}_0(0) \cdot \mathbf{F}_0(t) \rangle$ is compared with the analytic results and the convergence behaviors of $\langle \mathbf{F}(0) \cdot \mathbf{F}(t) \rangle$ and $\langle \mathbf{F}^+(0) \cdot \mathbf{F}^+(t) \rangle$ to $\langle \mathbf{F}_0(0) \cdot \mathbf{F}_0(t) \rangle$

are investigated. The time integrals of the three force autocorrelation functions are also calculated and the issues that the Kirkwood formula poses are discussed.

Synopsis of Chapter 3

From the asymptotic behavior of the memory function $K(t)$ given in Eq. (1.1.12), the asymptotic behaviors of the time correlation functions $\langle \mathbf{V}(0) \cdot \mathbf{V}(t) \rangle$, $\langle \mathbf{V}(0) \cdot \mathbf{F}(t) \rangle$, and $\langle \mathbf{F}(0) \cdot \mathbf{F}(t) \rangle$ are investigated and the numerical procedures to estimate the friction coefficient γ from these time correlation functions are analyzed. For large M, the asymptotic expansions for the time correlation functions are obtained in terms of $K_0(t)$ and $K_1(t)$. It is shown that the numerical methods of estimating γ from the exponential decay of the time correlation functions produce $\gamma + O(M^{-1})$, where the first-order correction depends on the microscopic nature of $K_0(t)$ [i.e., deviation of $K_0(t)$ from the delta function $2\gamma\delta(t)$] as well as the contribution of $K_1(t)$ [i.e., deviation of $K(t)$ from $K_0(t)$].

In the MD simulation part, the asymptotic behavior of $K(t)$ is numerically confirmed, and the analytic results for the asymptotic behaviors of the time correlation functions and the $\gamma + O(M^{-1})$ behaviors of the γ estimates are numerically verified. Although all theoretical results are valid for a general case (i.e., without the non-interacting bath assumption), MD simulations are performed for the Rayleigh gases under the LJ and WCA potentials. This is because the analytic result for $K_0(t)$ is available for the Rayleigh gas model so $K_1(t)$ can be numerically calculated with accuracy. By comparing the LJ and WCA cases, the effects of the tail in the memory function on the evaluation of γ are discussed.

Synopsis of Chapter 4

Despite the importance of Brownian motion in many fields of science, it seems that the microscopic picture available to general scientists has not been improved compared to Einstein's original explanation. One of the reasons may be that most of the microscopic theories of Brownian motion rely on formal operator manipulation, which is exact but usually turns out to be intractable for practical purposes. Using the concepts of the conditional expectation and the infinitesimal deviation of trajectories, a tangible quantitative interpretation of the phenomenon at the microscopic level is presented.

I present a new microscopic interpretation of the friction force on a Brownian particle of finite mass suspended in a fluid: it originates from the deviation of the system trajectory due to the movement of the particle. I perform a systematic theoretical investigation on the observation that, compared with the frozen dynamics of the fluid, the movement of the Brownian particle perturbs the trajectory of the fluid particles and correspondingly the force on the Brownian particle. I show that as the mass M of the Brownian particle increases, the drag force becomes the ensemble average of the force deviation over the fluid configurations, whereas the thermal noise due to the fluctuation of the fluid becomes the force in the frozen dynamics. In addition, I obtain asymptotic expansions (with respect to M) of the friction force and thermal noise defined by the memory function and derive several expressions for single-particle Brownian motion near the Brownian limit. I perform a MD simulation study on the Rayleigh model, which provides a clear validation of the theory. I observe the skewness in the force distributions and the bath-particle density on the simulation, which further explains the microscopic-time-dependent behavior of the drag force.

Synopsis of Chapter 5

When Brownian motion occurs in a confined fluid, many interesting behaviors may be observed. This is attributed to additional interactions of the colloidal particle and solvent particles with the boundaries of the system, which enhance long-time memory of the system. I demonstrate how the effects of confinement are investigated through the memory function approach.

To this end, I study confined Brownian motion by investigating the memory function of a d-dimensional hypercube ($d \geq 2$), which is subject to a harmonic potential and suspended in an ideal gas confined by two parallel walls. For elastic walls and under the infinite-mass limit, I obtain analytic expressions for the force autocorrelation function and the memory function. The transverse-direction memory function possesses a nonnegative tail decaying like $t^{-(d-1)}$, from which anomalous diffusion is expected for $d = 2$. For $d = 3$, the position-dependent friction coefficient becomes larger than the unconfined case and the increment is inversely proportional to the square of the distance from the wall. I also perform MD simulations with thermal walls and/or a finite-mass hypercube. I observe faster decay due to the thermal walls (t^{-3} for $d = 2$ and t^{-5} for $d = 3$ under the fully thermalizing wall) and convergence behaviors of the finite-mass memory function, which are different from the unconfined case.

Synopsis of Chapter 6

I analyze two standard methods to compute the diffusion coefficient of a tracer particle in a medium from MD simulation, the velocity autocorrelation function (VACF) method, and the mean-squared displacement (MSD) method. I show that

they are equivalent in the sense that they provide the same mean values with the same level of statistical errors. I obtain analytic expressions for the level of the statistical errors present in the time-dependent diffusion coefficient as well as the VACF and the MSD. Under the assumption that the velocity of the tracer particle is a Gaussian process, all results are expressed in terms of the VACF. Hence, the standard errors of all relevant quantities are computable once the VACF is obtained from MD simulation. For validation, I perform MD simulations for the self-diffusion of a Lennard-Jones fluid and the diffusion of a large and massive colloid particle suspended in the fluid. In the addendum, I also present a validation case-study for MD simulation of ethylene carbonate liquid.

Synopsis of Chapter 7

I investigate the finite-system-size effects on the evaluation of the diffusion coefficient D. Since D can be calculated from the time integral of the VACF, the finite-system-size effects of D can be understood by those of the VACF. However, due to huge relative statistical errors, it is computationally challenging to observe the long-time behavior of the VACF, which is known to be sensitive to the system size. By performing large-sized-ensemble MD runs, I obtain very accurate results for the long-time tail and time integral of the VACF. For a sufficiently large system, I clearly observe the algebraic decay $t^{-3/2}$ of the VACF at large times.

By using MD simulation results for two states of the WCA fluid, I demonstrate that, in order to observe the $1/L$ dependence of D (where L is the MD simulation box size), D should be estimated from the time-dependent diffusion coefficient $D(t)$ (which is the time integral of the VACF up to time t) at larger time t for a larger system. This is because, in a larger system, the faster decay of the VACF due to

finite system size occurs at larger time. By comparing the $1/L$ dependence obtained from MD simulation with that predicted by the hydrodynamic theory, I examine the validity of the hydrodynamic finite-system-size correction. In addition, by using an asymptotic behavior of the memory function $K(t)$ with respect to L (i.e., the finite-system-size effects of $K(t)$), which is proposed by MD simulation data, I obtain corresponding asymptotic behaviors of the VACF and $D(t)$ for large L.

Part A

Memory Function Approach

Chapter Two

Rayleigh Gas Model:

Unbounded Case

2.1 Introduction

While Brownian motion has inspired researchers from various fields of science [76, 77] as a canonical example of stochastic processes, it has also served as an archetypal model in non-equilibrium statistical mechanics. One of the fundamental questions is how the dynamics of Brownian particles can be described without knowing the dynamics of the entire system. The microscopic theory of Brownian motion addresses how mesoscopic equations for the Brownian particles are derived starting from first principles, i.e., without introducing any *a priori* stochastic features to a microscopic system except the concept of ensemble, and how the parameters of resulting mesoscopic equations are related with the microscopic structure of the system.

In this context, the simplest physical system is arguably a system consisting of a single spherical Brownian particle of mass M surrounded by solvent particles of mass m; this system has been extensively studied [130]. In the Brownian limit $m \ll M$, the momentum $\mathbf{P}$ of the Brownian particle obeys Langevin's phenomenological equation [110, 116],

$$\dot{\mathbf{P}}(t) = -\frac{\gamma}{M}\mathbf{P}(t) + \Gamma(t), \tag{2.1.1}$$

where γ is the friction coefficient, $\Gamma(t)$ is d-dimensional Gaussian white noise with noise intensity Δ, i.e., $\langle \Gamma(t) \cdot \Gamma(t') \rangle = d\Delta\delta(t - t')$, and d is the dimension of the space.

2.1.1 Microscopic expressions of γ

One of the heuristic scenarios toward Eq. (2.1.1) in the Brownian limit can be suggested by the generalized Langevin equation for $\mathbf{P}$, which was derived by Mori [140],

$$\dot{\mathbf{P}}(t) = -\frac{1}{M}\int_0^t K(\tau)\mathbf{P}(t-\tau)d\tau + \mathbf{F}^+(t), \tag{2.1.2}$$

where $K(t)$ is the Mori memory kernel and $\mathbf{F}^+(t)$ is the corresponding fluctuating force. Assuming that the interaction between the Brownian particle and each solvent particle becomes instantaneous on the time scale of the Brownian particle in the Brownian limit, it is expected that the fluctuating force $\mathbf{F}^+(t)$ exerted on the Brownian particle by the solvent becomes delta-correlated. By the fluctuation-dissipation theorem

$$K(t) = \frac{\beta}{d}\left\langle \mathbf{F}^+(0)\cdot\mathbf{F}^+(t)\right\rangle, \tag{2.1.3}$$

the memory kernel $K(t)$ also becomes a delta function. Here, β is the inverse temperature of the system and the brackets denote the equilibrium average. Hence, in the near-Brownian-limit (NBL) regime, a Markovian approximation of Eq. (2.1.2) due to the large time scale separation leads to Eq. (2.1.1) and γ is approximated by the time integral of $K(t)$, which is equal to

$$\gamma^+ = \frac{\beta}{d}\int_0^\infty \left\langle \mathbf{F}^+(0)\cdot\mathbf{F}^+(t)\right\rangle dt. \tag{2.1.4}$$

There have been similar expressions of the Green–Kubo type, which relate the friction coefficient γ with the time integrals of some force autocorrelation functions.

Kirkwood has proposed the following expression [98]

$$\gamma^* = \frac{\beta}{d} \int_0^{\tau^*} \langle \mathbf{F}(0) \cdot \mathbf{F}(t) \rangle \, dt, \tag{2.1.5}$$

where $\mathbf{F}(t)$ is the total force exerted on the Brownian particle. Since the time integral would vanish if the upper time limit is increased to infinity, a cut-off τ^* is introduced under the assumption that the time integral presents a plateau and its value does not depend on the precise value of τ^*. It has been demonstrated that the thermodynamic limit, where the number of the solvent particles tends to infinity, is essential for the existence of τ^* [51, 145].

Another expression which we also consider in this chapter is given from the *frozen dynamics*, where the infinite mass limit $M \to \infty$ is taken so that the Brownian particle is held fixed and the solvent particles move under the external potential due to the presence of the Brownian particle. Under a certain assumption on the time scales of the bath, Mazur and Oppenheim have performed a detailed analysis [131] to show that in the Brownian limit, the friction coefficient γ is given by

$$\gamma_0 = \frac{\beta}{d} \int_0^{\infty} \langle \mathbf{F}_0(0) \cdot \mathbf{F}_0(t) \rangle \, dt, \tag{2.1.6}$$

where $\mathbf{F}_0(t)$ is the force exerted on the *fixed* Brownian particle in the frozen dynamics.

In addition, the value of γ can also be estimated from the momentum autocorrelation function in the NBL regime through the relation

$$\langle \mathbf{P}(0) \cdot \mathbf{P}(t) \rangle = \frac{dM}{\beta} e^{-\gamma t/M}, \tag{2.1.7}$$

which is derived from Eq. (2.1.1).

Molecular dynamics (MD) simulation studies using these relations and corresponding theories have been extensively performed on the system of a single Brownian particle (or a trace particle with different mass and size) in a simple fluid. However, since MD simulations in the NBL regime require high computational cost, it was not until recently that systematic investigations by using long-time and large-size MD simulations were attempted [103, 114, 145]. Specifically, the increase in computational cost of the MD simulation with smaller mass ratio m/M is not only due to the larger time scale separation in the system, but also due to a larger number of solvent particles that are necessary to satisfy the condition $M \ll Nm$, where N is the number of the solvent particles. For this reason, determining a *precise* value of γ from a direct MD simulation approach is not a routine computation of this juncture.

The *primary objective* of this chapter is to systematically explore the limiting behavior of the system in the NBL regime. More specifically, the physical quantities of main interests are the total force autocorrelation function $\langle \mathbf{F}(0) \cdot \mathbf{F}(t) \rangle$ and the fluctuating force autocorrelation function $\langle \mathbf{F}^{+}(0) \cdot \mathbf{F}^{+}(t) \rangle$ in the NBL regime as well as the frozen dynamics force autocorrelation function $\langle \mathbf{F}_0(0) \cdot \mathbf{F}_0(t) \rangle$. We investigate the convergence of the total force and fluctuating force autocorrelation functions in the Brownian limit and compare them with the frozen dynamics force autocorrelation function. Long-time and large-size MD simulations with carefully chosen MD parameters are performed so that the tails of the force autocorrelation functions are clearly compared and the numerical integration of the force autocorrelation functions provides numerically reliable values. Compared to recent related numerical studies [103, 114, 145], we use all methods of obtaining the friction coefficient (i.e., the time integration of the three force autocorrelation functions and the decay rate of the momentum autocorrelation function) and adopt a synergistic approach with analytic methods, which will be described below.

2.1.2 Rayleigh model

We introduce the non-interacting bath assumption to our system, which allows us an alternative analytic approach. Under this assumption, no solvent particle interacts with the other solvent particles, and solvent particles interact only with the Brownian particle. Hence, in the frozen dynamics, the dynamics of each solvent particle is decoupled from those of the other solvent particles. This feature enables us to derive analytic expressions for $\langle \mathbf{F}_0(0) \cdot \mathbf{F}_0(t) \rangle$, which are given in terms of one-particle trajectory. A numerical evaluation of the analytic expression for the frozen dynamics force autocorrelation function allows us to adjust MD simulation parameters. Also, the numerical results with no statistical errors help us to interpret the MD simulation results more clearly. We note that there is a trade-off with the introduction of the non-interacting bath assumption. The system becomes analytically more manageable but it loses some physically interesting features, such as the hydrodynamic effect of the bath [135]. However, the system still legitimately describes a certain physical phenomenon, i.e., Brownian motion in a gaseous medium.

The Rayleigh model (a massive particle in an ideal gas) has been extensively studied with the assumption of elastic collisions. An explicit expression of the friction coefficient γ in the Brownian limit has been derived by various methods [70, 128, 129, 138], and the velocity autocorrelation function and the Mori memory kernel in the NBL regime have been also investigated [88]. Mathematically rigorous results have been available for the one-dimensional model with various limiting procedures toward the Brownian limit [176], and some multi-dimensional extensions [39] and subsequent generalizations to introduce rotational motion to the Brownian particle [40] and to impose a reflecting boundary to the system [19] have followed. Some progress in the generalization of the interaction structure other than elastic collisions and

multiple Brownian particles has been recently made by Kusuoka and Liang [108]. The Rayleigh model has also been studied in the context of the adiabatic piston with nonequilibrium conditions [24, 62, 127, 141, 151, 152, 185] and the reactive Rayleigh gas [143].

An *equally important objective* of this chapter is to comprehensively understand the version of the Rayleigh model where an internal structure of interaction is considered, compared to the version of the Rayleigh model where only elastic collisions are considered. As specific examples, we consider four typical interaction potentials: the hard-sphere (HS) interaction and the square-well (SqW) potential as analytic examples, and the Lennard-Jones (LJ) and Weeks-Chandler-Andersen (WCA) potentials as numerical examples. First, for a general short-ranged interaction potential, we derive two new expressions for the force autocorrelation function $\langle \mathbf{F}_0(0) \cdot \mathbf{F}_0(t) \rangle$ of the frozen dynamics and corresponding new expressions for the friction coefficient γ. The first one is obtained from the ensemble average, whereas the other is from the time average and is given in terms of the ray representation following Kusuoka and Liang's approach [108]. Then, we apply these results to the four potentials. For the HS interaction and the SqW potential, closed-form expressions for γ are obtained, the latter of which is new. For the WCA and LJ potentials, we numerically evaluate the expressions and compare them with the MD simulation results. Based on the results for the four potential cases, theoretical and practical aspects for the evaluation of $\langle \mathbf{F}_0(0) \cdot \mathbf{F}_0(t) \rangle$ and γ are presented.

The rest of the chapter is organized as follows. In Section 2.2, the system is defined and previous theoretical results are summarized. In Section 2.3, the ensemble-averaged expressions for $\langle \mathbf{F}_0(0) \cdot \mathbf{F}_0(t) \rangle$ and γ are derived. In Section 2.4, some relevant portion of Kusuoka and Liang's work is presented with physical explanation followed by the ray representation expressions for $\langle \mathbf{F}_0(0) \cdot \mathbf{F}_0(t) \rangle$ and γ. In Sec-

tion 2.5, analytic results for the HS interaction and the SqW potential are derived. In Section 2.6, numerical results for the WCA and LJ potentials are presented and discussed. In Section 2.7, we provide a summary with some discussion.

2.2 System and known results

2.2.1 System

We consider a system consisting of a single spherical Brownian particle of mass M and a total of N non-interacting solvent particles of mass m. The dimension of the space and the inverse temperature of the system are denoted by d ($d = 2$ or 3) and β, respectively. $\mathbf{X}$ and P denote the position and momentum of the Brownian particle, respectively, and $\mathbf{x}^N = (\mathbf{x}_1, \mathbf{x}_2, \ldots, \mathbf{x}_N)$ and $\mathbf{p}^N = (\mathbf{p}_1, \mathbf{p}_2, \cdots, \mathbf{p}_N)$ denote those of the solvent particles. The interaction potential $U(r)$ between the Brownian particle and a solvent is a function of inter-particle distance. We assume that the potential is short-ranged with a cut-off radius R_0. The Hamiltonian H of the system is written as

$$H = \sum_{n=1}^{N} \left[\frac{\mathbf{p}_n \cdot \mathbf{p}_n}{2m} + U\left(|\mathbf{x}_n - \mathbf{X}|\right) \right] + \frac{\mathbf{P} \cdot \mathbf{P}}{2M}. \tag{2.2.1}$$

Although all particles, including the Brownian particle, have point masses and only their translational motions are considered, the form of $U(r)$ may introduce the size of the Brownian particle. That is, for example, for the LJ and WCA potentials with parameters ϵ and σ, we may think that the radius of the Brownian particle is σ.

In the frozen dynamics, the Brownian particle is held fixed at a certain position

$\mathbf{X}$ and the solvent particles move under the bath Hamiltonian

$$H_0 = \sum_{n=1}^{N} \left[\frac{\mathbf{p}_n \cdot \mathbf{p}_n}{2m} + U\left(|\mathbf{x}_n - \mathbf{X}|\right) \right]. \tag{2.2.2}$$

Since H_0 is the sum of one-particle Hamiltonians, the motion of each solvent particle becomes independent in the frozen dynamics. To distinguish from the frozen dynamics, we call the dynamics under the system Hamiltonian H as the *full* dynamics.

We introduce two statistical averages. The *full-system* equilibrium average of a physical quantity θ is defined as

$$\langle \theta \rangle = \int \theta \, \rho \, d\mathbf{X} \, d\mathbf{P} \, d\mathbf{x}^N \, d\mathbf{p}^N, \tag{2.2.3}$$

where ρ is the equilibrium distribution

$$\rho = e^{-\beta H} \Big/ \int e^{-\beta H} \, d\mathbf{X} \, d\mathbf{P} \, d\mathbf{x}^N \, d\mathbf{p}^N \, . \tag{2.2.4}$$

On the other hand, the *bath* equilibrium average is defined as

$$\langle \theta \rangle_{\mathrm{b}} = \int \theta \, \rho_{\mathrm{b}} \, d\mathbf{x}^N \, d\mathbf{p}^N, \tag{2.2.5}$$

where ρ_{b} is the bath equilibrium distribution

$$\rho_{\mathrm{b}} = e^{-\beta H_0} \Big/ \int e^{-\beta H_0} \, d\mathbf{x}^N \, d\mathbf{p}^N \, . \tag{2.2.6}$$

Note that the bath equilibrium average can be defined for the full dynamics as well as for the frozen dynamics. For the former case, $\langle \theta \rangle_{\mathrm{b}}$ is a function of $\mathbf{X}$ and $\mathbf{P}$. If $\langle \theta \rangle_{\mathrm{b}}$ does not depend on $\mathbf{X}$, $\langle \theta \rangle$ is equal to the average of $\langle \theta \rangle_{\mathrm{b}}$ over the Maxwell distribution of $\mathbf{P}$. For notational simplicity, we drop the subscript for $\langle \mathbf{F}_0(0) \cdot \mathbf{F}_0(t) \rangle_{\mathrm{b}}$

throughout the chapter, i.e., $\langle \mathbf{F}_0(0) \cdot \mathbf{F}_0(t) \rangle \equiv \langle \mathbf{F}_0(0) \cdot \mathbf{F}_0(t) \rangle_{\mathrm{b}}$.

2.2.2 Force autocorrelation functions and their time integrals

As stated in Section 2.1, three force autocorrelation functions, $\langle \mathbf{F}(0) \cdot \mathbf{F}(t) \rangle$, $\langle \mathbf{F}^+(0) \cdot \mathbf{F}^+(t) \rangle$, and $\langle \mathbf{F}_0(0) \cdot \mathbf{F}_0(t) \rangle$ and their time integrals are investigated in this chapter. While $\mathbf{F}(t)$ is the force exerted on the Brownian particle in the full dynamics, $\mathbf{F}_0(t)$ is the force in the frozen dynamics. In other words, for the Liouville operators iL and iL_0 corresponding to H and H_0, respectively, $\mathbf{F}(t) = e^{iLt}\mathbf{F}$ and $\mathbf{F}_0(t) = e^{iL_0 t}\mathbf{F}$. On the other hand, $\mathbf{F}^+(t)$ is defined for the full dynamics through the generalized Langevin equation, Eq. (2.1.2). We note that for the theoretical results summarized in this subsection, the non-interacting bath assumption is not necessary.

Before stating the relations of these force autocorrelation functions in the Brownian limit, we specify the limiting procedure toward the Brownian limit to be considered in this section. The infinite mass limit $M \to \infty$ has been mainly considered in the physics literature. In this limiting procedure, all parameters except the mass M of the Brownian particle are assumed to be fixed. However, as Español and Zúñiga pointed out [51], it has been implicitly assumed that the thermodynamic limit $N \to \infty$ is taken before the infinite mass limit. This is clearly seen through the relation, see Ref. [51],

$$\langle \mathbf{P} \cdot \mathbf{P} \rangle = \frac{d}{\beta} \frac{MNm}{M + Nm} \equiv \frac{d}{\beta} \mu, \tag{2.2.7}$$

which shows that the condition $M \ll Nm$ should be satisfied in order to have

$\langle \mathbf{P} \cdot \mathbf{P} \rangle = \beta^{-1} dM$. Hence, we also assume that the condition is valid along the infinite mass limit so that $\mu \approx M$.

In the infinite mass limit, $\langle \mathbf{F}(0) \cdot \mathbf{F}(t) \rangle$ and $\langle \mathbf{F}^+(0) \cdot \mathbf{F}^+(t) \rangle$ coincide. This can be shown by the relation of the Laplace transforms of these force autocorrelation functions, see Ref. [51],

$$\tilde{C}^+(s) = \tilde{C}(s) \left[1 - \frac{\beta \tilde{C}(s)}{d\mu s} \right]^{-1}, \tag{2.2.8}$$

where $\tilde{C}(s)$ and $\tilde{C}^+(s)$ are the Laplace transforms of $C(t) = \langle \mathbf{F}(0) \cdot \mathbf{F}(t) \rangle$ and $C^+(t) = \langle \mathbf{F}^+(0) \cdot \mathbf{F}^+(t) \rangle$, respectively. By letting $\mu \to \infty$ (i.e., $M \to \infty$ after $N \to \infty$), we see that $\tilde{C}(s)$ and $\tilde{C}^+(s)$ coincide.

Mazur and Oppenheim have investigated the asymptotic form [1] of $\langle \mathbf{F}(0) \cdot \mathbf{F}(t) \rangle$ in the Brownian limit under the assumption that correlation functions which are governed by the frozen dynamics are short-lived [131]. This assumption means that there is a characteristic time τ_{b} of the bath such that, for $t > \tau_{\mathrm{b}}$,

$$\left\langle A_0(t_1) e^{iL_0 t} B_0(t_2) \right\rangle_{\mathrm{b}} = \left\langle A_0(t_1) \right\rangle_{\mathrm{b}} \left\langle B_0(t_2) \right\rangle_{\mathrm{b}}, \tag{2.2.9}$$

where $A_0(t_1) = e^{iL_0 t_1} A$ and $B_0(t_2) = e^{iL_0 t_2} B$. By using projection operator techniques [68] with the projection operator $\langle\ \rangle_{\mathrm{b}}$, they have derived an exact equation for $\mathbf{P}$, which is different from Eq. (2.1.2). For the corresponding fluctuating force $\mathbf{F}^+_{\mathrm{MO}}(t)$, they have shown that $\left\langle \mathbf{F}^+_{\mathrm{MO}}(0) \cdot \mathbf{F}^+_{\mathrm{MO}}(t) \right\rangle_{\mathrm{b}}$ has a well-behaved series expansion in powers of the mass ratio m/M with $\langle \mathbf{F}_0(0) \cdot \mathbf{F}_0(t) \rangle$, the lowest order term. They have also obtained an asymptotic form of $\langle \mathbf{F}(0) \cdot \mathbf{F}(t) \rangle_{\mathrm{b}}$, containing a slowly decaying contribution proportional to $M^{-1} e^{-\gamma_0 t/M}$. By taking the Maxwellian average

[1] In this chapter, we use the term *asymptotic form* (of a force autocorrelation function) only to refer to the Brownian limit $m \ll M$ and not to refer to a long-time limit.

to $\langle \mathbf{F}(0) \cdot \mathbf{F}(t) \rangle_{\mathrm{b}}$, we have the same form for $\langle \mathbf{F}(0) \cdot \mathbf{F}(t) \rangle$,

$$\langle \mathbf{F}(0) \cdot \mathbf{F}(t) \rangle \approx \langle \mathbf{F}_0(0) \cdot \mathbf{F}_0(t) \rangle - \frac{d\gamma_0^2}{\beta M} e^{-\gamma_0 t/M}. \tag{2.2.10}$$

We note that from Eq. (2.2.10) it can be shown that $\int_0^\infty \langle \mathbf{F}(0) \cdot \mathbf{F}(t) \rangle \, dt = 0$.

Under the same assumption for the time scale τ_{b}, Hynes *et al.* have shown that the autocorrelation function of the Mori fluctuating force $\mathbf{F}^+(t)$ has the following form [89]:

$$\left\langle \mathbf{F}^+(0) \cdot \mathbf{F}^+(t) \right\rangle = \frac{dM}{\beta} \left[i\Omega_{11}(t) + \Delta_{11}(t) \right]. \tag{2.2.11}$$

The first term $\beta^{-1} dM i\Omega_{11}(t)$ is equal to the Maxwellian average of Mazur-Oppenheim fluctuating force autocorrelation function $\left\langle \mathbf{F}^+_{\mathrm{MO}}(0) \cdot \mathbf{F}^+_{\mathrm{MO}}(t) \right\rangle_{\mathrm{b}}$ and thus it has a well-behaved series expansion. On the other hand, the second term $\beta^{-1} dM \Delta_{11}(t)$ is proportional to $M^{-3} e^{-3\gamma_0 t/M}$. The exponential decay term, however, does not change the behavior of the time integral significantly in this case, because its contribution to γ^+ in Eq. (2.1.4) is $\mathcal{O}(M^{-2})$. Therefore, in the Brownian limit, $\langle \mathbf{F}^+(0) \cdot \mathbf{F}^+(t) \rangle$ and its time integral γ^+ converge to $\langle \mathbf{F}_0(0) \cdot \mathbf{F}_0(t) \rangle$ and γ_0 (i.e., γ), respectively.

2.3 Ensemble-averaged expressions for $\langle \mathbf{F}_0(0) \cdot \mathbf{F}_0(t) \rangle$ and γ

As discussed in Section 2.2.2, the frozen dynamics force autocorrelation function $\langle \mathbf{F}_0(0) \cdot \mathbf{F}_0(t) \rangle$ provides the asymptotic form [1] of $\langle \mathbf{F}^+(0) \cdot \mathbf{F}^+(t) \rangle$ in the Brownian limit and its time integral is equal to γ. In this section, under the non-interacting

bath assumption, we derive ensemble-averaged expressions for $\langle \mathbf{F}_0(0) \cdot \mathbf{F}_0(t) \rangle$ and γ, which are expressed by one-particle ensemble-averaged quantities.

2.3.1 Expression for $\langle \mathbf{F}_0(0) \cdot \mathbf{F}_0(t) \rangle$

Since $\langle \mathbf{F}_0(0) \cdot \mathbf{F}_0(t) \rangle$ does not depend on the fixed position of the Brownian particle, we assume that the Brownian particle is fixed at the origin. We denote the force exerted on a solvent particle located at $\mathbf{x}$ by $\mathbf{f}(\mathbf{x})$, i.e., $\mathbf{f}(\mathbf{x}) = -U'(|\mathbf{x}|)\frac{\mathbf{x}}{|\mathbf{x}|}$. For the solvent with initial configuration $\left\{\mathbf{x}^N, \mathbf{p}^N\right\}$, the net force $\mathbf{F}_0(0)$ exerted on the Brownian particle by the solvent is given as $-\sum_{i=1}^{N} \mathbf{f}(\mathbf{x}_i)$. Likewise, $\mathbf{F}_0(t) = -\sum_{i=1}^{N} \mathbf{f}(\mathbf{x}_i(t))$, where $\mathbf{x}_i(t) = e^{iL_0 t}\mathbf{x}_i$. Then, we have the following form

$$\langle \mathbf{F}_0(0) \cdot \mathbf{F}_0(t) \rangle = N \left\langle \mathbf{f}(\mathbf{x}_1) \cdot \mathbf{f}(\mathbf{x}_1(t)) \right\rangle_{\mathrm{b}}. \tag{2.3.1}$$

The cross terms $\left\langle \mathbf{f}(\mathbf{x}_i) \cdot \mathbf{f}(\mathbf{x}_j(t)) \right\rangle_{\mathrm{b}}$ with $i \neq j$ disappeared in Eq. (2.3.1), since $\mathbf{x}_i$ and $\mathbf{x}_j(t)$ are independent and $\left\langle \mathbf{f}(\mathbf{x}_i) \right\rangle_{\mathrm{b}} = 0$ by the symmetry of ρ_{b}. The average with respect to ρ_{b} can be reduced to the average with respect to one-particle Boltzmann distribution. With subscript 1 dropped, Eq. (2.3.1) is expressed as follows:

$$\langle \mathbf{F}_0(0) \cdot \mathbf{F}_0(t) \rangle = \frac{N}{V^*} \int d\mathbf{p}\, \phi(\mathbf{p}) I(\mathbf{p}, t), \tag{2.3.2}$$

where V is the volume of the system and

$$I(\mathbf{p}, t) = \int_V d\mathbf{x}\, e^{-\beta U(|\mathbf{x}|)} f(\mathbf{x}) \cdot \mathbf{f}(\mathbf{x}(t)), \tag{2.3.3a}$$

$$\phi(\mathbf{p}) = \left(\frac{\beta}{2\pi m}\right)^{d/2} e^{-\frac{\beta}{2m}\mathbf{p}\cdot\mathbf{p}}, \tag{2.3.3b}$$

$$V^* = \int_V d\mathbf{x}\, e^{-\beta U(|\mathbf{x}|)}. \tag{2.3.3c}$$

As expected, $\langle \mathbf{F}_0(0) \cdot \mathbf{F}_0(t) \rangle$ is proportional to the number density of the solvent. We note that for a sufficiently large value of V and a short-ranged potential $U(r)$, $N/V \approx N/V^*$.

Since the interaction potential U is a function of the inter-particle distance with cut-off R_0, Eq. (2.3.2) can be further simplified. For $d = 2$, by introducing new variables r, θ, u, and ϕ, we parametrize $\mathbf{x} = (r\cos\theta, r\sin\theta)$ and $\mathbf{p} = (u\cos(\theta + \phi), u\sin(\theta + \phi))$. Then, $\mathbf{f}(\mathbf{x}) \cdot \mathbf{f}(\mathbf{x}(t))$ is a function of r, u, and ϕ, but does not depend on θ. Also, for ϕ and $-\phi$, $\mathbf{f}(\mathbf{x}) \cdot \mathbf{f}(\mathbf{x}(\mathbf{t}))$ has the same value. Hence, we obtain

$$\langle \mathbf{F}_0(0) \cdot \mathbf{F}_0(t) \rangle = \frac{2a\beta}{m} \int_0^\infty du \int_0^\pi d\phi \int_0^{R_0} dr\, r\, u\, e^{-\beta\left[\frac{u^2}{2m} + U(r)\right]} \mathbf{f}(\mathbf{x}) \cdot \mathbf{f}(\mathbf{x}(t)), \quad (2.3.4)$$

where a is the number density of the solvent particles and $\mathbf{f}(\mathbf{x}) \cdot \mathbf{f}(\mathbf{x}(t))$ is calculated for $\mathbf{x} = (r, 0)$ and $\mathbf{p} = (u\cos\phi, u\sin\phi)$. Similarly, for $d = 3$, we obtain

$$\begin{aligned} \langle \mathbf{F}_0(0) \cdot \mathbf{F}_0(t) \rangle =& 8\pi^2 a \left(\frac{\beta}{2\pi m}\right)^{3/2} \int_0^\infty du \int_0^\pi d\phi \int_0^{R_0} dr \\ & \times e^{-\beta\left[\frac{u^2}{2m} + U(r)\right]} r^2 u^2 \sin\phi\, \mathbf{f}(\mathbf{x}) \cdot \mathbf{f}(\mathbf{x}(t)). \end{aligned} \quad (2.3.5)$$

Note that since the trajectory under $U(r)$ is on a plane, we can use the same function $\mathbf{f}(\mathbf{x}) \cdot \mathbf{f}(\mathbf{x}(t))$ as $d = 2$.

2.3.2 Expression for γ

From Eqs. (2.1.6) and (2.3.2), we can obtain an expression for γ. Since $\int_0^t \mathbf{f}(\mathbf{x}(s))ds = \mathbf{p}(t) - \mathbf{p}$, we have

$$\gamma = \frac{a\beta}{d} \lim_{t\to\infty} \int d\mathbf{p}\, \phi(\mathbf{p}) \int_V d\mathbf{x}\, e^{-\beta U(|\mathbf{x}|)} \mathbf{f}(\mathbf{x}) \cdot (\mathbf{p}(t) - \mathbf{p}). \quad (2.3.6)$$

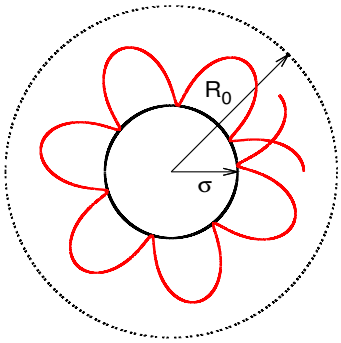

Figure 2.1: A typical trajectory of a solvent particle trapped in the well of the (truncated) LJ potential is depicted by the red line. The solid circle of radius σ indicates the Brownian particle, whereas the dotted circle of radius $R_0 = 2.5\sigma$ indicates the interaction range.

For a purely repulsive potential, $\mathbf{p}_\infty = \lim_{t\to\infty} \mathbf{p}(t)$ is always well-defined, since every trajectory quickly leaves the interaction range and the momentum no longer changes after it leaves the interaction range. Hence, we can take the limit $t \to \infty$ inside by replacing $\mathbf{p}(t)$ with $\mathbf{p}_\infty$. For a potential containing an attractive component, however, some trajectories are trapped in the potential well and the corresponding solvent particles interact with the Brownian particle forever and $\mathbf{p}_\infty$ is not well-defined. For the LJ potential, for example, if

$$\frac{|\mathbf{p}|^2}{2m} + U(|\mathbf{x}|) = \frac{|\mathbf{p}_\perp|^2}{2m}\frac{|\mathbf{x}|^2}{r_*^2} + U(r_*), \tag{2.3.7}$$

where $\mathbf{p}_\perp$ is defined so that $\mathbf{p} = \mathbf{p}_\parallel + \mathbf{p}_\perp$ and $\mathbf{x}\cdot\mathbf{p}_\perp = 0$, has a root r_* in the interval $(|\mathbf{x}|, R_0)$, the particle cannot escape from the potential well, see Fig. 2.1. However, we can show that the net contribution of the trapped particles to γ disappears. The ensemble average of the product of $\mathbf{f}(x)$ and $\mathbf{p}(t)$ over the trapped particles becomes decoupled as t tends to infinity so that it shrinks to zero. Also, the ensemble average of $\mathbf{f}(\mathbf{x})\cdot\mathbf{p}$ over the trapped particles is zero by the time reversal property. Hence,

we obtain

$$\gamma = \frac{a\beta}{d} \int \int_{\text{non-trapped}} d\mathbf{x} d\mathbf{p}\, \phi(\mathbf{p}) e^{-\beta U(|\mathbf{x}|)} \mathbf{f}(\mathbf{x}) \cdot (\mathbf{p}_\infty - \mathbf{p}). \tag{2.3.8}$$

As we did in Section 2.3.1, Eq. (2.3.8) is further simplified; for $d = 2$,

$$\gamma = \frac{a\beta^2}{m} \int_0^\infty du \int_0^\pi d\phi \int_0^{R_0} dr\, r\, u\, e^{-\beta\left[\frac{u^2}{2m} + U(r)\right]} \mathbb{I}(\mathbf{x}, \mathbf{p}) \mathbf{f}(\mathbf{x}) \cdot (\mathbf{p}_\infty - \mathbf{p}) \tag{2.3.9}$$

and, for $d = 3$,

$$\begin{aligned} \gamma =& \frac{8}{3}\pi^2 a\beta \left(\frac{\beta}{2\pi m}\right)^{3/2} \int_0^\infty du \int_0^\pi d\phi \int_0^{R_0} dr \\ & \times e^{-\beta\left[\frac{u^2}{2m} + U(r)\right]} r^2 u^2 \sin\phi\, \mathbb{I}(\mathbf{x}, \mathbf{p}) \mathbf{f}(\mathbf{x}) \cdot (\mathbf{p}_\infty - \mathbf{p}), \end{aligned} \tag{2.3.10}$$

where $\mathbb{I}(\mathbf{x}, \mathbf{p}) = 0$ if the trajectory is trapped and equal to 1, otherwise.

2.4 Ray representation approach

In this section, an alternative method of studying the microscopic theory of Brownian motion is discussed and then applied to obtain a microscopic formula for the frozen dynamics force autocorrelation function. It was devised for the Rayleigh model, and microscopic formulas for the friction coefficient γ and the noise intensity Δ have been derived in terms of the ray representation by Kusuoka and Liang [108]. Instead of considering the ensemble of the solvent and taking the ensemble average (as we did in Section 2.3), they have obtained their results by time-averaging for a given realization of the initial solvent configuration. For mathematical convenience, some restrictive assumptions on the interaction potential and the initial solvent configu-

ration have been made. Under these assumptions, for sufficiently small mass ratio m/M, every incoming solvent particle penetrates the Brownian particle. However, the penetration of solvent particles into the Brownian particle is not valid for our solid Brownian particle case. Specifically, neither the interaction potentials we consider in this chapter nor the Boltzmann distribution satisfy the assumptions. Here we discuss and examine the validity of the ray representation approach beyond the original Kusuoka and Liang's assumptions [108].

Specifically, in this section, we use a different limiting procedure from the infinite mass limit, which has been used in Kusuoka and Liang's work. Roughly speaking, we consider $m \to 0$ rather than $M \to \infty$ to achieve the Brownian limit $m/M \to 0$. Since the momentum of the Brownian particle obeys the Ornstein–Uhlenbeck process *without* scaling under this limit, this limit is more favorable for presenting mathematically rigorous statements and proofs; it has also been used in Refs. [39, 40, 19]. However, we can also use the infinite mass limit with the ray representation approach and the main results under the infinite mass limit are presented below in Section 2.4.6.

We first present some relevant parts of Kusuoka and Liang's work with the emphasis on physical meaning. In Section 2.4.1, a system and a limiting procedure to be considered in this section are introduced. The ray representation and the adiabatic trajectory are explained in Sections 2.4.2 and 2.4.3, respectively. In Section 2.4.4, Kusuoka and Liang's result for the noise intensity Δ is presented in a heuristic way. Then, we derive a new microscopic expression for the frozen dynamics force autocorrelation function in Section 2.4.5. In Section 2.4.6, we present the expressions for $\langle F_0(0) \cdot F_0(t) \rangle$ and γ under the infinite mass limit with further simplified forms.

2.4.1 System description

We consider a Brownian particle of mass M surrounded by an infinite number of solvent particles of mass m in d-dimensional space ($d = 2$ or 3). The position and velocity of the Brownian particle at time t are denoted by $\mathbf{X}(t)$ and $\mathbf{V}(t)$, respectively, while the positions and velocities of the solvent particles are denoted by $\mathbf{x}_i(t)$ and $\mathbf{v}_i(t)$, respectively, with label $i = 1, 2, \ldots$. The Brownian particle interacts with each solvent particle via a short-ranged interaction potential U, but there is no interaction between the solvent particles. We further assume that the interaction potential is a function of the inter-particle distance between the Brownian particle and a solvent particle, i.e., $U = U(r)$, and that the potential has a cut-off R_0, i.e., $U(|\mathbf{X} - \mathbf{x}_i|) = 0$ if $|\mathbf{X} - \mathbf{x}_i| > R_0$. We use the notation $\nabla U(\mathbf{x}) = U'(|\mathbf{x}|)\frac{\mathbf{x}}{|\mathbf{x}|}$ for $\mathbf{x} \in \mathbb{R}^d$.

Since the total energy of the system is given as

$$\frac{1}{2}M\mathbf{V}^2 + \sum_i \left(\frac{1}{2}m\mathbf{v}_i^2 + U\left(|\mathbf{x}_i - \mathbf{X}|\right)\right),$$

the equations of motion for the Brownian particle are given as

$$\dot{\mathbf{X}}(t) = \mathbf{V}(t), \tag{2.4.1a}$$

$$\dot{\mathbf{V}}(t) = -\frac{1}{M}\sum_i \nabla U\left(\mathbf{X}(t) - \mathbf{x}_i(t)\right). \tag{2.4.1b}$$

Note that the sum is over all solvent particles, but it actually contains a finite number of particles at each time since $U(r)$ is a short-ranged potential. On the other hand, the equations of motion for each solvent particle are given as

$$\dot{\mathbf{x}}_i(t) = \mathbf{v}_i(t), \tag{2.4.2a}$$

$$\dot{\mathbf{v}}_i(t) = -\frac{1}{m}\nabla U\left(\mathbf{x}_i(t) - \mathbf{X}(t)\right). \tag{2.4.2b}$$

The only randomness we introduce to the system is the initial conditions of the solvent particles. While the initial conditions for the Brownian particle, i.e., $\mathbf{X}(0) = \mathbf{X}_0$ and $\mathbf{V}(0) = \mathbf{V}_0$, are deterministic, the initial configuration of the solvent particles in the $2d$-dimensional $(\mathbf{x}, \mathbf{v})$ space is given by the Poisson field with intensity

$$\lambda(d\mathbf{x}, d\mathbf{v}) = \frac{a}{\sqrt{m}} e^{-\beta U(|\mathbf{x}-\mathbf{X}_0|)} \left(\frac{m\beta}{2\pi}\right)^{d/2} e^{-\frac{1}{2}\beta m|\mathbf{v}|^2} d\mathbf{x}\, d\mathbf{v}, \tag{2.4.3}$$

where a is introduced as a density parameter and β is the inverse temperature of the solvent. The number of the particles that are found in the volume element $d\mathbf{x}\, d\mathbf{v}$ obeys the Poisson distribution with mean $\lambda(d\mathbf{x}, d\mathbf{v})$ and is independent of those in other non-overlapping volume elements. By integrating λ over $\mathbf{v}$, we see that the number density of the solvent particles beyond the interaction range of the Brownian particle has mean $a/\sqrt{m}$. In turn, by integrating λ over $\mathbf{x}$, we see that the velocity distribution of the solvent particles obeys the Maxwell-Boltzmann distribution. Hence, the initial solvent configuration obtained from the Poisson field is a realization of the solvent configuration in equilibrium.

The Brownian limit we consider in this section is achieved by decreasing m to zero with M fixed. Meanwhile, we fix the parameters a and β and the interaction potential $U(r)$. As we see in Eq. (2.4.3), however, as the Brownian limit is achieved, the system contains a larger number of solvent particles in a unit volume and the solvent particles become lighter and faster. In other words, as m goes to zero, the velocities of the solvent particles increase like $\mathcal{O}(1/\sqrt{m})$ and so does the number density of the solvent.

Comparison of the two settings considered in Sections 2.2.1 and 2.4.1 follows. Two different settings of the systems (i.e., a finite number of solvent particles in a finite volume versus an infinite number of solvent particles in a whole space) do

not make any essential difference, if sufficiently large values of N and V are used in the previous setting and the number densities of the solvent particles are the same. On the other hand, the two limiting procedures are not equivalent and result in the Langevin equations with different values of γ and Δ. In order to derive the Langevin equation from the infinite mass limit considered in the previous section, the momentum $\mathbf{P}$ and time t need to be scaled. For the limiting procedure considered in this section, no scaling is required. However, we note that a system with a non-zero mass ratio $m/M \ll 1$ can be interpreted by either of the two limiting procedures.

In the rest of Section 2.4, we assume that the interaction potential is purely repulsive. In this case, every solvent particle interacts with the Brownian particle for a finite time and then leave the interaction range. On the other had, if the potential contains an attractive component, some solvent particles are trapped in the potential well and it is less likely for them to escape from the well as the mass ratio m/M has a smaller value. Some comments for this case are made in this section if necessary, but the overall discussion takes place in Section 2.6.

2.4.2 Ray representation

The initial conditions of the solvent particles can be equivalently expressed by the ray representation. This is based on the observation that every incoming solvent particle undergoes a free motion until it interacts with the Brownian particle. Hence, its trajectory can be labeled as a corresponding free motion—a ray.

For a solvent particle with initial position $\mathbf{x}$ and initial velocity $\mathbf{v}$ at time $t = 0$, we consider free motion $\mathbf{x} + t\mathbf{v}$. We denote $\bar{t}$ as the time when the position becomes the closest to the origin and $\bar{\mathbf{x}}$ as the position of the particle at this moment, see

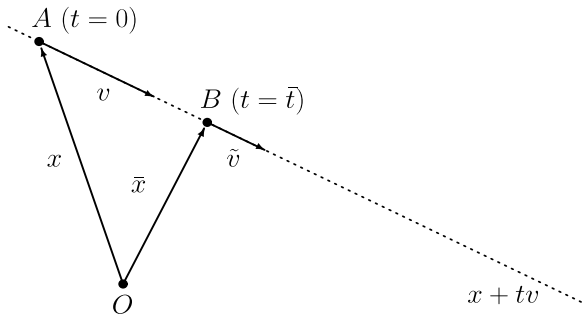

Figure 2.2: Schematic diagram for the ray representation. The dotted line indicates the trajectory of free motion of a particle with initial position $\mathbf{x}$ (point A) and initial velocity v at time $t = 0$, which is parametrized by $\mathbf{x} + t\mathbf{v}$. The ray representation of $(\mathbf{x}, \mathbf{v})$ is given by $(\bar{t}, \bar{\mathbf{x}}, \tilde{\mathbf{v}})$, where $\bar{\mathbf{x}}$ is the closest point (point B) on the line to the origin O (i.e., $\bar{\mathbf{x}} \perp \mathbf{v}$), $\bar{t}$ is the time when the particle arrives at $\bar{\mathbf{x}}$ (i.e., $\mathbf{x} + \bar{t}\mathbf{v} = \bar{\mathbf{x}}$), and $\tilde{\mathbf{v}}$ is the normalized velocity of $\mathbf{v}$ (i.e., $\tilde{\mathbf{v}} = \sqrt{m}\mathbf{v}$).

Fig. 2.2. Hence, the scalar $\bar{t}$ and vector $\bar{\mathbf{x}}$ satisfy

$$\mathbf{v} \cdot (\mathbf{x} + \bar{t}\mathbf{v}) = 0, \tag{2.4.4a}$$

$$\bar{\mathbf{x}} = \mathbf{x} + \bar{t}\mathbf{v}. \tag{2.4.4b}$$

Note that $\bar{t}$ may have a negative value. Also, since v increases like $\mathcal{O}(1/\sqrt{m})$ as $m \to 0$, we introduce the normalized velocity

$$\tilde{\mathbf{v}} = \sqrt{m}\mathbf{v}. \tag{2.4.5}$$

Then, our ray representation of (x, v) is given as $(\bar{t}, \bar{\mathbf{x}}, \tilde{\mathbf{v}})$. We note that bar notation is used for ray representation, whereas tilde notation is used to indicate that a variable is scaled.

There is a one-to-one correspondence between the two representations, i.e., between $(\mathbf{x}, \mathbf{v})$ with $\mathbf{v} \neq 0$ and $(\bar{t}, \bar{\mathbf{x}}, \tilde{\mathbf{v}})$ with $\tilde{\mathbf{v}} \neq 0$ and $\tilde{\mathbf{v}} \cdot \bar{\mathbf{x}} = 0$. For $\tilde{\mathbf{v}} \neq 0$, we define $E_{\tilde{\mathbf{v}}}$ to be the hyperplane perpendicular to $\tilde{\mathbf{v}}$, i.e., $E_{\tilde{\mathbf{v}}} = \{\bar{\mathbf{x}} : \ \tilde{\mathbf{v}} \cdot \bar{\mathbf{x}} = 0\}$. Due to the constraint, the dimension of $E_{\tilde{\mathbf{v}}}$ is $d - 1$. We denote a volume element on $E_{\tilde{\mathbf{v}}}$ by $d\bar{\mathbf{x}}$.

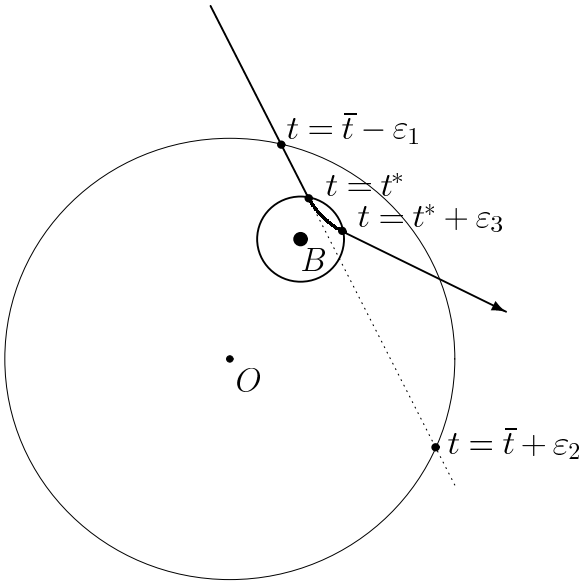

Figure 2.3: A typical trajectory of a solvent particle that interacts with the Brownian particle under a purely repulsive interaction potential. Point O denotes the origin of the space, while the solid circle B denotes the Brownian particle. The smaller circle indicates the interaction range of the Brownian particle while the larger circle indicates some bounded region containing the origin and the Brownian particle. For a solvent particle with its ray representation $(\bar{t}, \bar{\mathbf{x}}, \tilde{\mathbf{v}})$, we denote the times when the free motion $\mathbf{x} + t\tilde{\mathbf{v}}/\sqrt{m}$ (drawn by the dotted line) enters and exits the region by $\bar{t} - \epsilon_1$ and $\bar{t} + \epsilon_2$, respectively, and the times when the particle enters and exits the interaction range by t^* and $t^* + \epsilon_3$, respectively.

We also define a $(2d-1)$-dimensional space

$$E = \{(\bar{\mathbf{x}}, \tilde{\mathbf{v}}) : \ \tilde{\mathbf{v}} \neq 0, \ \bar{\mathbf{x}} \cdot \tilde{\mathbf{v}} = 0\}. \tag{2.4.6}$$

We note that the volume element $d\bar{\mathbf{x}}$ in $E_{\tilde{\mathbf{v}}}$ and the space E appear in the microscopic formulas for the noise intensity Δ and the autocorrelation function of $\mathbf{F}_0$, see Eqs. (2.4.25) and (2.4.32).

From the ray representation of the initial solvent configuration, one can approximate the times when each solvent particle interacts with the Brownian particle, which is advantageous for our problem. If a solvent particle with ray representation

$(\bar{t}, \bar{\mathbf{x}}, \tilde{\mathbf{v}})$ interacts with the Brownian particle, the interaction time is approximated as $\bar{t}$ and this approximation becomes more accurate as m has a smaller value. To see this clearly, we introduce a region centered at the origin, which is assumed to be bounded but sufficiently large so that the Brownian particle moves within the region, see Fig. 2.3. Since the solvent is an ideal gas, the solvent particle undergoes free motion until it enters the interaction range of the Brownian particle. We denote the time interval when the free motion $\mathbf{x} + t\tilde{\mathbf{v}}/\sqrt{m}$ stays in the region by $(\bar{t} - \epsilon_1, \bar{t} + \epsilon_2)$, and the time interval when the solvent particle interacts with the Brownian particle by $(t^*, t^* + \epsilon_3)$. Clearly, t^* is contained in $(\bar{t} - \epsilon_1, \bar{t} + \epsilon_2)$ and ϵ_i $(i = 1, 2, 3)$ are $\mathcal{O}(\sqrt{m})$. Hence, we can approximately consider that the interaction occurs at time $\bar{t}$ with a short duration of order $\sqrt{m}$. Note that this argument is heuristic and it implicitly assumes that the Brownian particle moves much more slowly than the solvent particles and that each solvent particle interacts with the Brownian particle at most once, which is valid for a small value of m.

Now we express the Poisson field for the initial configuration of the solvent in terms of the ray representation. Since we can label the initial configuration of the solvent particles by $\{(\mathbf{x}_i, \mathbf{v}_i)\}$, we can also express it in terms of the ray representation, i.e., $\{(\bar{t}_i, \bar{\mathbf{x}}_i, \tilde{\mathbf{v}}_i)\}$. We define $N(d\bar{t}, d\bar{\mathbf{x}}, d\tilde{\mathbf{v}})$ as the corresponding Poisson field on $(\bar{t}, \bar{\mathbf{x}}, \tilde{\mathbf{v}})$ space and want to find its intensity $\bar{\lambda}(d\bar{t}, d\bar{\mathbf{x}}, d\tilde{\mathbf{v}})$. We assume that the initial position of the Brownian particle is at the origin, i.e., $\mathbf{X}_0 = 0$. For sufficiently small m, if a solvent particle is initially positioned inside the interaction range (i.e., $|\mathbf{x}| \leq R_0$), then it leaves the interaction range in a very short time and then no longer affects the movement of the Brownian particle. Thus, if we are interested in long time average, the initial solvent configuration near the Brownian particle does not need to be imposed precisely. We approximate $\lambda(d\mathbf{x}, d\mathbf{v})$ in Eq. (2.4.3) by the

following intensity $\lambda_0(d\mathbf{x}, d\mathbf{v})$:

$$\lambda_0(d\mathbf{x}, d\mathbf{v}) = \frac{a}{\sqrt{m}} \left(\frac{m\beta}{2\pi} \right)^{d/2} e^{-\frac{1}{2}\beta m|\mathbf{v}|^2} d\mathbf{x} d\mathbf{v}. \tag{2.4.7}$$

Note that λ_0 is the intensity of the Poisson field for a free ideal gas since $U(r) = 0$ everywhere in this case. Since $\tilde{\mathbf{v}} d\bar{t} \perp d\bar{\mathbf{x}}$ and $v = m^{-1/2}\tilde{\mathbf{v}}$, we can express the volume elements

$$d\mathbf{x} = \frac{1}{\sqrt{m}} |\tilde{\mathbf{v}}| \, d\bar{\mathbf{x}} d\bar{t}, \tag{2.4.8a}$$

$$d\mathbf{v} = m^{-d/2} d\tilde{\mathbf{v}}, \tag{2.4.8b}$$

and thus we obtain the intensity of the Poisson field

$$\bar{\lambda}(d\bar{t}, d\bar{\mathbf{x}}, d\tilde{\mathbf{v}}) = \frac{a}{m} \left(\frac{\beta}{2\pi} \right)^{d/2} e^{-\frac{1}{2}\beta|\tilde{\mathbf{v}}|^2} |\tilde{\mathbf{v}}| \, d\bar{t} \, d\bar{\mathbf{x}} \, d\tilde{\mathbf{v}}. \tag{2.4.9}$$

Note that Eq. (2.4.9) is obtained from Eq. (2.4.7) rather than Eq. (2.4.3). For a purely repulsive potential, the difference between the initial configurations near the Brownian particle affects the dynamics of the Brownian particle only for the initial time, the duration of which is of the order of $\sqrt{m}$. On the other hand, if the interaction potential has an attractive component, a particle initially located inside the potential well may be trapped depending on its initial velocity and stay for an infinite time as m tends to zero. Hence, in this case, a different initial configuration may cause different dynamics of the Brownian particle for a long time. Thus, we should treat the contribution of those particles precisely and may not approximate $\lambda(d\mathbf{x}, d\mathbf{v})$ by $\lambda_0(d\mathbf{x}, d\mathbf{v})$.

Since $N(d\bar{t}, d\bar{\mathbf{x}}, d\tilde{\mathbf{v}})$ is a random discrete measure concentrated on $\{(\bar{t}_i, \bar{\mathbf{x}}_i, \tilde{\mathbf{v}}_i)\}$,

an integral with respect to $N(d\bar{t}, d\bar{\mathbf{x}}, d\tilde{\mathbf{v}})$ is interpreted as follows:

$$\int_{(0,t]\times E} N(d\bar{u}, d\bar{\mathbf{x}}, d\tilde{\mathbf{v}}) A(\bar{u}, \bar{\mathbf{x}}, \tilde{\mathbf{v}}) = \sum_{0<\bar{t}_i\leq t} A\left(\bar{t}_i, \bar{\mathbf{x}}_i, \tilde{\mathbf{v}}_i\right). \tag{2.4.10}$$

Its compensated field is denoted by $N_0(d\bar{t}, d\bar{\mathbf{x}}, d\tilde{\mathbf{v}})$, i.e.,

$$N_0(d\bar{t}, d\bar{\mathbf{x}}, d\tilde{\mathbf{v}}) = N(d\bar{t}, d\bar{\mathbf{x}}, d\tilde{\mathbf{v}}) - \bar{\lambda}(d\bar{t}, d\bar{\mathbf{x}}, d\tilde{\mathbf{v}}). \tag{2.4.11}$$

2.4.3 Adiabatic trajectory ψ

As discussed in Section 2.4.2, if the system is near the Brownian limit, a solvent particle interacts with the Brownian particle for a very short time. An adiabatic approximation is considered in order to estimate how this instantaneous collision affects the motion of the Brownian particle. In other words, while the Brownian particle interacts with a certain solvent particle, we assume that its position does not change, and observe the motion of the solvent particle. Then, the equations of motion of the solvent particle are decoupled from those of the other solvent particles.

For a solvent particle with its ray representation $(\bar{t}, \bar{\mathbf{x}}, \tilde{\mathbf{v}})$, the interaction occurs near at time $t = \bar{t}$ and its duration is $\mathcal{O}(\sqrt{m})$. Hence, we introduce a scaled time

$$\tilde{s} = \frac{t - \bar{t}}{\sqrt{m}}. \tag{2.4.12}$$

We also assume that the Brownian particle is held fixed while the interaction occurs, i.e., $\mathbf{X}(\tilde{s}) = \mathbf{X}(\bar{t})$. The adiabatic trajectory $\psi(\tilde{s}) = \psi(\tilde{s}; \bar{\mathbf{x}}, \tilde{\mathbf{v}}, \mathbf{X}(\bar{t}))$ of the solvent particle satisfies

$$\frac{d^2}{d\tilde{s}^2}\psi(\tilde{s}) = -\nabla U\left(\psi(\tilde{s}) - \mathbf{X}(\bar{t})\right). \tag{2.4.13}$$

The initial conditions of Eq. (2.4.13) are given by the fact that before the particle enters the interaction range (i.e., $\tilde{s}$ has a sufficiently large negative value), it satisfies

$$\psi(\tilde{s}) = \bar{\mathbf{x}} + \tilde{s}\tilde{\mathbf{v}}. \tag{2.4.14}$$

Under the adiabatic assumption, the total impulse exerted on the Brownian particle during the interaction is given as

$$\mathbf{A}(\bar{t}, \bar{x}, \tilde{v}) = \sqrt{m} \int_{-\infty}^{\infty} \nabla U \left(\psi\left(\tilde{s}; \bar{\mathbf{x}}, \tilde{\mathbf{v}}, \mathbf{X}(\bar{t})\right) - \mathbf{X}(\bar{t})\right) d\tilde{s}. \tag{2.4.15}$$

We note that the actual integration is over a finite time interval when the particle stays in the interaction range.

2.4.4 Noise intensity Δ

Now we approximate the random force exerted on the Brownian particle. The underlying idea is as follows. In the Brownian limit, a solvent particle with its ray representation $(t, \bar{\mathbf{x}}, \tilde{\mathbf{v}})$ interacts with the Brownian particle instantaneously at time t. The impulse exerted on the Brownian particle by the solvent particle is approximated by $\mathbf{A}(t, \bar{\mathbf{x}}, \tilde{\mathbf{v}})$. We approximate the force exerted on the Brownian particle at time t by the sum of delta impulses (occurring at time t) having intensity $\mathbf{A}(t, \bar{\mathbf{x}}, \tilde{\mathbf{v}})$.

By defining

$$\mathbf{H}(t) = \int_{(0,t]\times E} N(du, d\bar{\mathbf{x}}, d\tilde{\mathbf{v}}) \mathbf{A}(u, \bar{\mathbf{x}}, \tilde{\mathbf{v}}), \tag{2.4.16}$$

we approximate the time integral of the random force exerted on the Brownian particle up to time t. Hence, the random force itself is approximated by the (formal)

time derivative of $\mathbf{H}(t)$, i.e.,

$$\mathbf{F}^{\delta}(t) = \dot{\mathbf{H}}(t), \tag{2.4.17}$$

where we used superscript δ to emphasize that the force consists of the sum of delta peaks by its definition. We can show that in the Brownian limit, the quadratic variation of $\mathbf{H}(t)$ is deterministic (i.e., independent of the realization of the initial solvent configuration) and it grows linearly with time. However, in order to obtain an expression for the slope of the quadratic variation versus time, it suffices to calculate $\mathbb{E}\left[|\mathbf{H}(t)|^2\right]$, where $\mathbb{E}[\ ]$ denotes the expectation over the initial solvent configurations.

We decompose $\mathbf{H}(t)$ into $\mathbf{H}_0(t) + \mathbf{H}_1(t)$, where

$$\mathbf{H}_0(t) = \int_{(0,t]\times E} N_0(du, d\bar{\mathbf{x}}, d\tilde{\mathbf{v}})\mathbf{A}(u, \bar{\mathbf{x}}, \tilde{\mathbf{v}}), \tag{2.4.18a}$$

$$\mathbf{H}_1(t) = \int_{(0,t]\times E} \bar{\lambda}(du, d\bar{\mathbf{x}}, d\tilde{\mathbf{v}})\mathbf{A}(u, \bar{\mathbf{x}}, \tilde{\mathbf{v}}). \tag{2.4.18b}$$

Due to the symmetry properties of the potential U and the intensity $\bar{\lambda}$, we have $\mathbf{H}_1(t) = 0$ and thus $\mathbf{H}(t) = H_0(t)$. By the Itô isometry, we have

$$\mathbb{E}\left[|\mathbf{H}(t)|^2\right] = \int_{(0,t]\times E} \bar{\lambda}(du, d\bar{\mathbf{x}}, d\tilde{\mathbf{v}})\mathbb{E}\left[|\mathbf{A}(u, \bar{\mathbf{x}}, \tilde{\mathbf{v}})|^2\right]. \tag{2.4.19}$$

We note that the dependencies on m of $\mathbf{A}$ (proportional to $\sqrt{m}$) and $\bar{\lambda}$ (proportional to m^{-1}) cancel in Eq. (2.4.19); the latter equation can be further simplified. The time dependence of $\mathbf{A}(u, \bar{x}, \tilde{v})$ is only through the position $\mathbf{X}(u)$ of the Brownian particle, and the integral

$$\int_E \bar{\lambda}(u, d\bar{\mathbf{x}}, d\tilde{\mathbf{v}})|\mathbf{A}(u, \bar{\mathbf{x}}, \tilde{\mathbf{v}})|^2$$

does not depend on $X(u)$ due to the translational invariance of $\bar{\lambda}$. Thus, it is a constant with respect to u. Hence, we may evaluate it with the assumption that the

Brownian particle is at the origin. By introducing

$$\tilde{\mathbf{A}}(\bar{\mathbf{x}},\tilde{\mathbf{v}}) = \int_{-\infty}^{\infty} \nabla U\left(\psi\left(\tilde{s};\bar{\mathbf{x}},\tilde{\mathbf{v}},0\right)\right) d\tilde{s}, \tag{2.4.20}$$

$\mathbb{E}\left[|\mathbf{A}(u,\bar{\mathbf{x}},\tilde{\mathbf{v}})|^2\right]$ is replaced by $m|\tilde{\mathbf{A}}(\bar{\mathbf{x}},\tilde{\mathbf{v}})|^2$ in Eq. (2.4.19), and we obtain from Eq. (2.4.9)

$$\mathbb{E}\left[|\mathbf{H}(t)|^2\right] = dt\Delta, \tag{2.4.21}$$

where

$$\Delta = \frac{a}{d}\left(\frac{\beta}{2\pi}\right)^{d/2} \int_E \left|\tilde{\mathbf{A}}(\bar{\mathbf{x}},\tilde{\mathbf{v}})\right|^2 e^{-\frac{1}{2}\beta|\tilde{\mathbf{v}}|^2}|\tilde{\mathbf{v}}|d\bar{\mathbf{x}}d\tilde{\mathbf{v}}. \tag{2.4.22}$$

By comparing Eq. (2.4.21) with the relation

$$\mathbb{E}\left[|\mathbf{H}(t)|^2\right] = \int_0^t du \int_0^t du' \mathbb{E}\left[\mathbf{F}^\delta(u)\cdot\mathbf{F}^\delta(u')\right], \tag{2.4.23}$$

we have

$$\mathbb{E}\left[\mathbf{F}^\delta(t)\cdot\mathbf{F}^\delta(t')\right] = d\delta(t-t')\Delta, \tag{2.4.24}$$

which means that Δ is actually the noise intensity of $\mathbf{F}^\delta$. Eq. (2.4.22) can be written as follows:

$$\Delta = \frac{a}{d}\int_E \left|\int_{-\infty}^{\infty} \nabla U\left[\psi(\tilde{s};\bar{\mathbf{x}},\tilde{\mathbf{v}},0)\right] d\tilde{s}\right|^2 \bar{\rho}(\bar{\mathbf{x}},\tilde{\mathbf{v}})d\bar{\mathbf{x}}d\tilde{\mathbf{v}}, \tag{2.4.25}$$

where

$$\bar{\rho}(\bar{\mathbf{x}},\tilde{\mathbf{v}}) = \left(\frac{\beta}{2\pi}\right)^{d/2} e^{-\frac{1}{2}\beta|\tilde{\mathbf{v}}|^2}|\tilde{\mathbf{v}}|. \tag{2.4.26}$$

Hence, Δ is expressed as the average of the square of the total momentum change after each collision over the rays with weight $\bar{\rho}$.

As mentioned above, the quadratic variation of $\mathbf{H}(t)$ is $dt\Delta$ in the Brownian limit and Δ is obtained from this relation. Hence, for each initial solvent configuration, *almost surely*, we can obtain Δ from the time average, which means that the use of

the expectation $\mathbb{E}[\ ]$ is not essential.

2.4.5 Time-averaged expression for $\langle \mathbf{F}_0(0) \cdot \mathbf{F}_0(\tilde{\tau}) \rangle$

For a small value of $m \ll M$, the frozen dynamics force autocorrelation function has a time scale of order $\sqrt{m}$. By using the tilde notation $\tilde{\tau}$ for microscopic time, we denote the autocorrelation function by $\langle \mathbf{F}_0(0) \cdot \mathbf{F}_0(\tilde{\tau}) \rangle$. As we did in Section 2.4.4, we derive a microscopic expression for $\langle \mathbf{F}_0(0) \cdot \mathbf{F}_0(\tilde{\tau}) \rangle$ by taking the time average of $\mathbb{E}\left[\mathbf{F}_0(t) \cdot \mathbf{F}_0(t+\tilde{\tau})\right]$, i.e.,

$$\langle \mathbf{F}_0(0) \cdot \mathbf{F}_0(\tilde{\tau}) \rangle = \lim_{T \to \infty} \frac{1}{T} \int_0^T \mathbb{E}\left[\mathbf{F}_0(t) \cdot \mathbf{F}_0(t+\tilde{\tau})\right] dt. \tag{2.4.27}$$

Since $\mathbf{F}_0(t)$ is the sum of the forces exerted by the colliding solvent particles at time t, i.e., $\mathbf{F}_0(t) = \sum_i \mathbf{f}_i(t)$, $\mathbf{F}_0(t) \cdot \mathbf{F}_0(t+\tilde{\tau})$ is decomposed into two parts:

$$\mathbf{F}_0(t) \cdot \mathbf{F}_0(t+\tilde{\tau}) = I_1 + I_2, \tag{2.4.28}$$

where I_1 contains the overlap of the forces of the same particle, i.e., $\sum_i \mathbf{f}_i(t) \cdot \mathbf{f}_i(t+\tilde{\tau})$, and I_2 contains the overlap of the forces of different particles, i.e., $\sum \sum_{i \neq j} \mathbf{f}_i(t) \cdot \mathbf{f}_j(t+\tilde{\tau})$. For a colliding particle with ray representation $(t, \bar{x}, \tilde{v})$, the total overlap between the force and its translation by time $\tilde{\tau}$ is given in terms of the following function:

$$\tilde{B}(\tilde{\tau}, \bar{\mathbf{x}}, \tilde{\mathbf{v}}) = \int_{-\infty}^{\infty} \nabla U[\psi(\tilde{s}; \bar{\mathbf{x}}, \tilde{\mathbf{v}}, 0)] \cdot \nabla U[\psi(\tilde{s}+\tilde{\tau}; \bar{\mathbf{x}}, \tilde{\mathbf{v}}, 0)] d\tilde{s}. \tag{2.4.29}$$

In other words, we have

$$I_1 dt = m \int_E N(dt, d\bar{\mathbf{x}}, d\tilde{\mathbf{v}}) \tilde{B}(\tilde{\tau}, \bar{\mathbf{x}}, \tilde{\mathbf{v}}), \tag{2.4.30}$$

and thus, by Eqs. (2.4.9) and (2.4.26), we obtain

$$\mathbb{E}[I_1] = a \int_E \tilde{B}(\tilde{\tau}, \bar{\mathbf{x}}, \tilde{\mathbf{v}}) \bar{\rho}(\bar{\mathbf{x}}, \tilde{\mathbf{v}}) d\bar{\mathbf{x}} d\tilde{\mathbf{v}}. \tag{2.4.31}$$

On the other hand, by the independence of two colliding particles and the isotropy of $\bar{\lambda}$, we have $\mathbb{E}[I_2] = 0$. Therefore, $\mathbb{E}[\mathbf{F}_0(t) \cdot \mathbf{F}_0(t+\tilde{\tau})] = \mathbb{E}[I_1]$ is *stationary* and we obtain the following expression for $\langle \mathbf{F}_0(0) \cdot \mathbf{F}_0(\tilde{\tau}) \rangle$:

$$\langle \mathbf{F}_0(0) \cdot \mathbf{F}_0(\tilde{\tau}) \rangle = a \int_E \tilde{B}(\tilde{\tau}, \bar{\mathbf{x}}, \tilde{\mathbf{v}}) \bar{\rho}(\bar{\mathbf{x}}, \tilde{\mathbf{v}}) d\bar{\mathbf{x}} d\tilde{\mathbf{v}}. \tag{2.4.32}$$

Now we show that Kusuoka and Liang's microscopic expression [108], Eq. (2.4.25), can be derived from Eq. (2.4.32) by using the Mazur and Oppenheim's result [131]. From Eq. (2.1.6) and the fluctuation-dissipation relation $\beta\Delta = 2\gamma$, we have

$$\Delta = \frac{2}{d} \int_0^\infty \langle \mathbf{F}_0(0) \cdot \mathbf{F}_0(\tilde{\tau}) \rangle \, d\tilde{\tau}. \tag{2.4.33}$$

Since

$$2 \int_0^\infty \tilde{B}(\tilde{\tau}, \bar{\mathbf{x}}, \tilde{\mathbf{v}}) d\tilde{\tau} = \left| \int_{-\infty}^\infty \nabla U \left[\psi(\tilde{s}; \bar{\mathbf{x}}, \tilde{\mathbf{v}}, 0) \right] d\tilde{s} \right|^2, \tag{2.4.34}$$

we retrieve Eq. (2.4.25) from Eqs. (2.4.32) and (2.4.33).

We also discuss the validity of Eq. (2.4.32). Since $\bar{\rho}$ is obtained from $\bar{\lambda}$ and, in turn, $\bar{\lambda}$ is obtained from λ_0 rather than λ, the validity of the expression depends on whether λ is correctly approximated by λ_0. As we discussed in Section 2.4.2, for a purely repulsive potential, the difference of the initial configurations near the Brownian particle does not affect the long time dynamics and thus the approximation is valid. On the other hand, for a potential containing an attractive component, we cannot neglect the initially trapped particles, which will stay in the potential well

forever in the frozen dynamics. Clearly, the contribution of such particles is not considered in Eq. (2.4.32) since their trajectories cannot be expressed by the adiabatic trajectory ψ, which describes a solvent particle entering and then leaving the potential range. Actually, $\langle F(0) \cdot F(\tilde{\tau})\rangle$ in Eq. (2.4.32) contains only the contribution of the incoming solvent particles, and it results from the Poisson field whose intensity is given as follows:

$$\lambda_1(d\mathbf{x}, d\mathbf{v}) = \lambda_0(d\mathbf{x}, d\mathbf{v})\mathbb{I}(\mathbf{x}), \tag{2.4.35}$$

where $\mathbb{I}(\mathbf{x}) = 1$ if $|\mathbf{x}| > R_0$ and $\mathbb{I}(\mathbf{x}) = 0$ otherwise. Note that if $\lambda_1(d\mathbf{x}, d\mathbf{v})$ is assumed for the Poisson field, then there is no trapped particle in the frozen dynamics.

2.4.6 Results under the infinite mass limit

We present the ray representation results under the infinite mass limit, which is considered in Sections 2.2 and 2.3. For ray representation, we use momentum p instead of velocity. For $(\bar{\mathbf{x}}, \mathbf{p}) \in E$, where $E = \left\{(\bar{\mathbf{x}}, \mathbf{p}) \in \mathbb{R}^{2d} : \ \bar{\mathbf{x}} \cdot \mathbf{p} = 0, \ \mathbf{p} \neq 0\right\}$, we define the adiabatic trajectory $\psi(t) = \psi(t; \bar{\mathbf{x}}, \mathbf{p})$ satisfying

$$m\psi''(t) = -\nabla U(\psi(t)) \tag{2.4.36}$$

and $\psi(t) = \bar{x} + \frac{t}{m}p$ for sufficiently negatively large t (i.e., before the particle enters the interaction range). The expression for the frozen dynamics force autocorrelation function is given as

$$\langle \mathbf{F}_0(0) \cdot \mathbf{F}_0(\tau)\rangle = a \int_E B(\tau, \bar{\mathbf{x}}, \mathbf{p})\bar{\rho}(\bar{\mathbf{x}}, \mathbf{p})\bar{d}\bar{\mathbf{x}}d\mathbf{p}, \tag{2.4.37}$$

where a is the number density of the solvent particles,

$$B(\tau, \bar{\mathbf{x}}, \mathbf{p}) = \int_{-\infty}^{\infty} \nabla U(\psi(t)) \cdot \nabla U(\psi(t+\tau)) dt, \tag{2.4.38a}$$

$$\bar{\rho}(\bar{\mathbf{x}}, \mathbf{p}) = \left(\frac{\beta}{2\pi m}\right)^{d/2} \frac{|\mathbf{p}|}{m} e^{-\frac{\beta}{2m}|\mathbf{p}|^2}. \tag{2.4.38b}$$

The expression for the friction coefficient is given as

$$\gamma = \frac{a\beta}{2d} \int_E |\mathbf{p}_\infty - \mathbf{p}|^2 \, \bar{\rho}(\bar{\mathbf{x}}, \mathbf{p}) d\bar{\mathbf{x}} d\mathbf{p}, \tag{2.4.39}$$

where $\mathbf{p}_\infty = m \lim_{t\to\infty} \psi'(t)$.

Since the interaction potential U is a function of inter-particle distance, Eqs. (2.4.37) and (2.4.39) can be further simplified. For $d = 2$, $\bar{\mathbf{x}}$ and p can be parametrized as follows: $\bar{\mathbf{x}} = (-r\sin\phi, r\cos\phi)$ and $\mathbf{p} = (u\cos\phi, u\sin\phi)$ with $u > 0$, $0 \le \phi < 2\pi$, $-R_0 \le r \le R_0$. Since $B(\tau, \bar{\mathbf{x}}, \mathbf{p})$ does not depend on ϕ, we introduce

$$B_0(\tau, r, u) = B(\tau, \bar{\mathbf{x}}_0, \mathbf{p}_0), \tag{2.4.40}$$

where $\bar{\mathbf{x}}_0 = (0, r)$ and $\mathbf{p}_0 = (u, 0)$, and integrate Eq. (2.4.37) over ϕ to obtain in the two-dimensional case:

$$\langle \mathbf{F}_0(0) \cdot \mathbf{F}_0(\tau) \rangle = \frac{2a\beta}{m^2} \int_0^\infty du \int_0^{R_0} dr \; e^{-\frac{\beta}{2m}u^2} u^2 B_0(\tau, r, u). \tag{2.4.41}$$

We also used the fact that $B_0(\tau, -r, u) = B_0(\tau, r, u)$. Likewise, for $d = 3$, we have

$$\begin{aligned} \langle \mathbf{F}_0(0) \cdot \mathbf{F}_0(\tau) \rangle = & \frac{8\pi^2 a}{m} \left(\frac{\beta}{2\pi m}\right)^{3/2} \int_0^\infty du \int_0^{R_0} dr \\ & \times e^{-\frac{\beta}{2m}u^2} r u^3 B_0(\tau, r, u). \end{aligned} \tag{2.4.42}$$

Note that a $(2d-1)$-dimensional integration in Eq. (2.4.37) is reduced to 2-

dimensional integrations in Eqs. (2.4.41) and (2.4.42). Similarly, we obtain simplified expressions for γ; for $d = 2$,

$$\gamma = \frac{a\beta^2}{2m^2} \int_0^\infty du \int_0^{R_0} dr\, e^{-\frac{\beta}{2m}u^2} u^2 |\mathbf{p}_\infty - \mathbf{p}|^2, \tag{2.4.43}$$

and, for $d = 3$,

$$\gamma = \frac{4\pi^2 a\beta}{3m} \left(\frac{\beta}{2\pi m}\right)^{3/2} \int_0^\infty du \int_0^{R_0} dr\, e^{-\frac{\beta}{2m}u^2} r u^3 |\mathbf{p}_\infty - \mathbf{p}|^2. \tag{2.4.44}$$

2.5 Analytic results

In this section, we derive analytic expressions of γ for the HS interaction and the SqW potential and show that the ensemble-averaged expression, Eq. (2.3.8), and the ray representation expression, Eq. (2.4.39), produce identical results for each potential. For the numerical values of γ for these potentials and the comparison with the WCA and LJ potential, see Figs. 2.15 and 2.16. The HS interaction has parameter R as the radius of the Brownian particle; when the inter-particle distance between a solvent particle and the Brownian particle becomes R, an elastic collision occurs. The SqW potential we consider has the following form:

$$U_{\mathrm{SqW}}(r) = \begin{cases} \infty & \text{if } r < R_1, \\ -\epsilon & \text{if } R_1 < r < R_2, \\ 0 & \text{if } r > R_2. \end{cases} \tag{2.5.1}$$

The closed-form expression of γ for the three-dimensional HS system, Eq. (2.5.5), has been derived by the generalized Fokker-Planck equation, the calculation of the

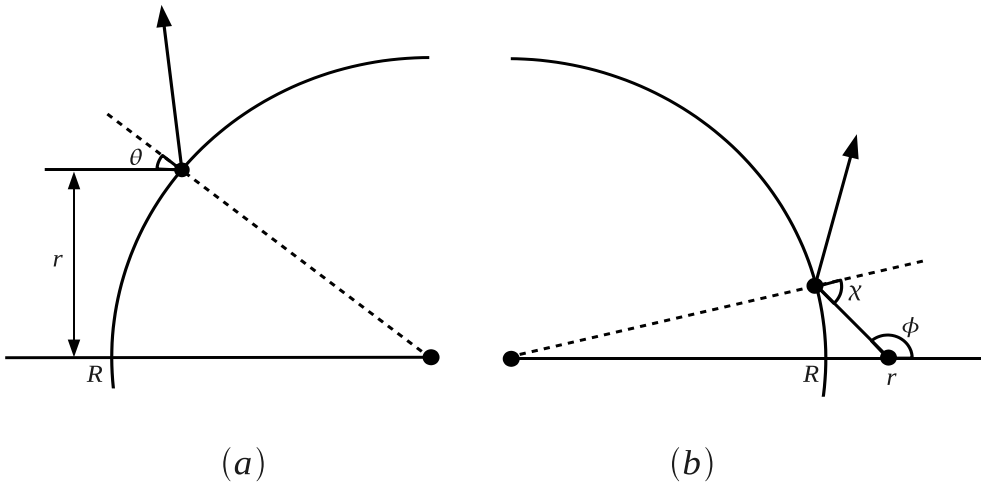

Figure 2.4: Some variables used in the calculation of γ of the HS system for (a) the ray representation approach, and (b) the ensemble average.

distribution of changes of momentum of the Brownian particle, and Kirkwood formula [70], by the density expansion of the momentum autocorrelation function [128], and by the Boltzmann equation [138]. An equivalent expression under the limiting procedure considered in Section 2.4 has been derived by a mathematically rigorous probabilistic method [39].

2.5.1 HS interaction

2.5.1.1 Ray representation

For $d = 2$, we use Eq. (2.4.43) and consider a particle with $\bar{\mathbf{x}} = (0, r)$ and $\mathbf{p} = (u, 0)$. For non-zero $\mathbf{p}_\infty - \mathbf{p}$, it suffices to consider $0 \le r \le R$. By introducing the angle θ, which satisfies $\sin\theta = \frac{r}{R}$, see Fig. 2.4 (a), we express the magnitude of momentum change as follows:

$$|\mathbf{p}_\infty - \mathbf{p}| = 2u\cos\theta. \tag{2.5.2}$$

From Eq. (2.4.43), we have

$$\gamma = \frac{2aR\beta^2}{m^2} \int_0^{\frac{\pi}{2}} d\theta \int_0^{\infty} du\; u^4 \cos^3\theta\, e^{-\frac{\beta}{2m}u^2}, \tag{2.5.3}$$

and thus

$$\gamma = 2aR\sqrt{\frac{2\pi m}{\beta}}. \tag{2.5.4}$$

Similarly, for $d = 3$, from Eqs. (2.4.44) and (2.5.2) we obtain

$$\gamma = \frac{8}{3}aR^2\sqrt{\frac{2\pi m}{\beta}}. \tag{2.5.5}$$

2.5.1.2 Ensemble average

In Eqs. (2.3.9) and (2.3.10), $\mathbf{f}(x)\cdot(\mathbf{p}_\infty - \mathbf{p})$ is non-zero only when $r = R$. To express this as a delta function, we only need to consider $r \geq R$. In order to have a collision with the wall, the angle ϕ should be in the range of $\left[\pi - \arcsin\frac{R}{r}, \pi\right]$. The angle of incidence is denoted by χ, which satisfies $\sin\chi = \frac{r}{R}\sin\phi$, see Fig. 2.4 (b). The time Δt that it takes for the particle to hit the wall is expressed as follows:

$$\Delta t = -\left(\cos\chi + \frac{r}{R}\cos\phi\right)\frac{mR}{u}. \tag{2.5.6}$$

By denoting the momentum change after the collision by Δp, we have

$$\mathbf{f}(\mathbf{x}(t)) = \Delta\mathbf{p}\,\delta(t - \Delta t), \tag{2.5.7}$$

$$\mathbf{p}(t) = \mathbf{p} + \Delta\mathbf{p}\,H(t - \Delta t), \tag{2.5.8}$$

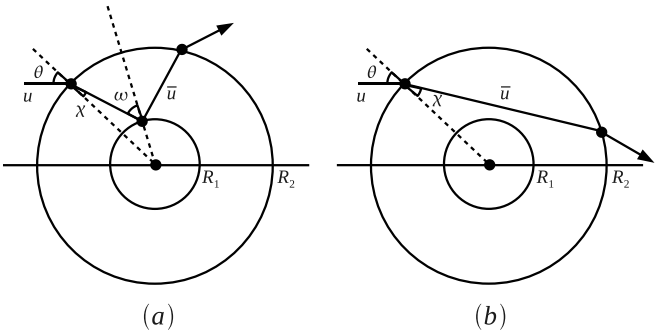

Figure 2.5: Two cases to be considered in the calculation of γ for the SqW system by the ray representation approach. Panel (a) corresponds to the case $(\theta, u) \in \mathcal{D}_1$, whereas panel (b) corresponds to $(\theta, u) \in \mathcal{D}_2$.

where $H(t)$ is the Heaviside step function, and thus

$$\mathbf{f}(\mathbf{x}) \cdot (\mathbf{p}_\infty - \mathbf{p}) = |\Delta\mathbf{p}|^2 \delta(\Delta t) H(\Delta t). \tag{2.5.9}$$

In order to have an instantaneous collision (i.e., $\Delta t = 0$), the limit $r \to R$ with $\frac{\pi}{2} \leq \phi \leq \pi$ is considered, which leads $\chi \to \pi - \phi$. Since $\frac{\partial \Delta t}{\partial r} = -\frac{m}{u \cos\phi}$ and $|\Delta\mathbf{p}| = -2u\cos\phi$ under the limit, we obtain

$$\mathbf{f}(\mathbf{x}) \cdot (\mathbf{p}_\infty - \mathbf{p}) = -\frac{4}{m} u^3 \cos^3\phi \, \delta(r - R) H(r - R). \tag{2.5.10}$$

Hence, for $d = 2$, by introducing $\theta = \pi - \phi$, we obtain the identical integral for γ to Eq. (2.5.3) and thus the identical result to Eq. (2.5.4). Similarly, for $d = 3$, we obtain Eq. (2.5.5) from Eqs. (2.3.10) and (2.5.10).

2.5.2 SqW potential

2.5.2.1 Ray representation

Since we only need to consider $0 \leq r < R_2$, we introduce the angle of incidence to the outer wall, θ, which satisfies $\sin\theta = \frac{r}{R_2}$, see Fig. 2.5. We also denote the angle of refraction and the magnitude of refracted momentum by χ and $\bar{u}$, respectively, which satisfy

$$\frac{1}{2m}\bar{u}^2 - \epsilon = \frac{1}{2m}u^2, \tag{2.5.11a}$$

$$\bar{u}\sin\chi = u\sin\theta. \tag{2.5.11b}$$

The condition $\sin\chi < \frac{R_1}{R_2}$ is equivalent to the condition that the refracted particle collides with the inner wall. Hence, when $\sin\theta < \frac{R_1}{R_2}$, the particle hits the inner wall for all $u > 0$. If $\sin\theta > \frac{R_1}{R_2}$, we define

$$u_* = \frac{R_1\sqrt{2m\epsilon}}{\sqrt{R_2^2\sin^2\theta - R_1^2}}. \tag{2.5.12}$$

If $u < u_*$, the particle hits the inner wall, otherwise, the particle passes through the interaction range without colliding with the inner wall. Hence, we calculate the integral

$$\gamma = \frac{aR_2\beta^2}{2m^2}\int_0^{\frac{\pi}{2}} d\theta \int_0^{\infty} du\; u^2\cos\theta\, e^{-\frac{\beta}{2m}u^2}|p_\infty - p|^2 \tag{2.5.13}$$

by dividing the domain into $\mathcal{D}_1$ and $\mathcal{D}_2$ defined as follows:

$$\begin{aligned}\mathcal{D}_1 = &\left\{0 \le \theta < \arcsin\frac{R_1}{R_2},\ u > 0\right\} \\ &\cup \left\{\arcsin\frac{R_1}{R_2} < \theta < \frac{\pi}{2},\ 0 < u < u_*\right\},\end{aligned} \tag{2.5.14a}$$

$$\mathcal{D}_2 = \left\{\arcsin\frac{R_1}{R_2} < \theta < \frac{\pi}{2},\ u > u_*\right\}. \tag{2.5.14b}$$

For the case of a collision with the inner wall, (i.e., for $(\theta, u) \in \mathcal{D}_1$), we denote the angle of incidence on the inner wall by ω, see Fig. 2.5 (a), which satisfies

$$\sin\omega = \frac{R_2}{R_1}\sin\chi. \tag{2.5.15}$$

We also denote the momentum changes after refraction, reflection, and subsequent refraction by $\Delta\mathbf{p}_1$, $\Delta\mathbf{p}_2$, and $\Delta\mathbf{p}_3$, respectively. Then, the total momentum change is given as $\mathbf{p}_\infty - \mathbf{p} = \Delta\mathbf{p}_1 + \Delta\mathbf{p}_2 + \Delta\mathbf{p}_3$, and we have

$$|\Delta\mathbf{p}_1| = |\Delta\mathbf{p}_3| = \bar{u}\cos\chi - u\cos\theta \equiv A(u,\theta), \tag{2.5.16a}$$

$$|\Delta\mathbf{p}_2| = 2\bar{u}\cos\omega \equiv B(u,\theta), \tag{2.5.16b}$$

$$\Delta\mathbf{p}_1 \cdot \Delta\mathbf{p}_2 = \Delta\mathbf{p}_2 \cdot \Delta\mathbf{p}_3 = -A(u,\theta)B(u,\theta)\cos(\omega - \chi), \tag{2.5.16c}$$

$$\Delta\mathbf{p}_1 \cdot \Delta\mathbf{p}_3 = A^2(u,\theta)\cos 2(\omega - \chi). \tag{2.5.16d}$$

Note that we defined A and B as functions of u and θ since other variables such as $\bar{u}$, χ, and ω are the functions of u and θ. Then, for $(\theta, u) \in \mathcal{D}_1$, we have

$$|\mathbf{p}_\infty - \mathbf{p}|^2 = 2A^2\left[1 + \cos 2(\omega - \chi)\right] - 4AB\cos(\omega - \chi) + B^2. \tag{2.5.17}$$

For the case of no collision with the inner wall, the momentum changes $\Delta\mathbf{p}_1$ and

$\Delta\mathbf{p}_2$ after two sequential refractions satisfy

$$|\Delta\mathbf{p}_1| = |\Delta\mathbf{p}_2| = A(u,\theta), \tag{2.5.18a}$$

$$\Delta\mathbf{p}_1 \cdot \Delta\mathbf{p}_2 = -A^2(u,\theta)\cos 2\chi. \tag{2.5.18b}$$

Hence, for $(\theta, u) \in \mathcal{D}_2$, we have

$$|\mathbf{p}_\infty - \mathbf{p}|^2 = 2A^2\left[1 - \cos 2\chi\right]. \tag{2.5.19}$$

By combining the results for two cases, we obtain a formula for γ as the sum of two integrals defined in Eqs. (2.5.13) and (2.5.14). The expressions for $|\mathbf{p}_\infty - \mathbf{p}|^2$ are given in Eqs. (2.5.17) and (2.5.19). The explicit expressions for the intermediate variables as functions of u and θ are given as follows:

$$A(u,\theta) = \sqrt{u^2\cos^2\theta + 2m\epsilon} - u\cos\theta, \tag{2.5.20a}$$

$$B(u,\theta) = 2\sqrt{\left(1 - \frac{R_2^2}{R_1^2}\sin^2\theta\right)u^2 + 2m\epsilon}, \tag{2.5.20b}$$

$$\cos(\omega - \chi) = \frac{B(u,\theta)\sqrt{u^2\cos^2\theta + 2m\epsilon}}{2(u^2 + 2m\epsilon)} + \frac{R_2 u^2 \sin^2\theta}{R_1(u^2 + 2m\epsilon)}, \tag{2.5.20c}$$

$$1 - \cos 2\chi = \frac{2u^2\sin^2\theta}{u^2 + 2m\epsilon}. \tag{2.5.20d}$$

2.5.2.2 Ensemble average

For instantaneous collisions of non-trapped particles, we consider the following limits:

- (E1) $r \to R_2 - 0$ with $0 \le \phi \le \frac{\pi}{2}$
- (E2) $r \to R_1 + 0$ with $\frac{\pi}{2} \le \phi \le \pi$

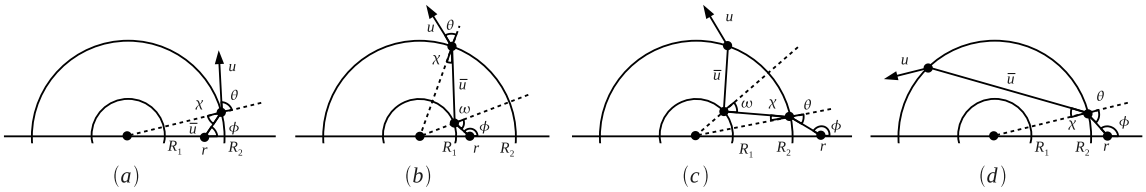

Figure 2.6: Four cases to be considered in the calculation of γ for the SqW system by using the ensemble-averaged expression. Panels (a), (b), (c), and (d) correspond the limits (E1), (E2), (E3), and (E4), respectively, in the text.

- (E3) $r \to R_2 + 0$ with $\frac{\pi}{2} \le \phi \le \pi$ (with collision with the inner wall)
- (E4) $r \to R_2 + 0$ with $\frac{\pi}{2} \le \phi \le \pi$ (without collision with the inner wall)

In order to use the expressions we obtained in the ray representation calculation, we use u as the magnitude of the momentum outside the potential range and $\bar{u}$ as the one inside the potential range. Hence, the magnitude of the initial momentum is denoted by $\bar{u}$ in cases E1 and E2, whereas it is denoted by u in cases E3 and E4. Also, the angles of incidence and refraction when the particle passes through the outer wall from inside are denoted by χ and θ, respectively. If the particle hits the inner wall, the angle of incidence is denoted by ω. For the definition of those variables in each case, see Fig. 2.6.

Since the particle is initially located inside the potential range in cases E1 and E2, there are minima $\bar{u}_*^{(1)}$ and $\bar{u}_*^{(2)}$ for the magnitude of the initial momentum in order for the particle to escape from the interaction range for the two cases. Under the limits E1 and E2 they are given as

$$\bar{u}_*^{(1)} = \frac{\sqrt{2m\epsilon}}{\cos\phi}, \tag{2.5.21a}$$

$$\bar{u}_*^{(2)} = \sqrt{\frac{2m\epsilon}{1 - \frac{R_1^2}{R_2^2}\sin^2\phi}}. \tag{2.5.21b}$$

On the other hand, under the limits E3 and E4, the angle of incidence θ becomes $\pi - \phi$. For $(\theta, u) \in \mathcal{D}_1$ there is a collision with the inner wall (i.e., belonging to case E3), whereas there is no collision (i.e., E4) for $(\theta, u) \in \mathcal{D}_2$.

In case E1, the magnitude of momentum change $\Delta\mathbf{p}_1$ after the refraction is given as

$$|\Delta\mathbf{p}_1| = A(u, \theta), \tag{2.5.22}$$

and thus we have

$$\mathbf{f}(\mathbf{x}) \cdot (\mathbf{p}_\infty - \mathbf{p}) = \frac{1}{m}\bar{u}\cos\phi\,\delta(r - R_2)H(R_2 - r)|\Delta\mathbf{p}_1|^2. \tag{2.5.23}$$

The contribution of case (E1) to the integral for γ is given as

$$\gamma^{(1)} = \frac{aR_2\beta^2}{2m^2}\int_0^{\frac{\pi}{2}} d\chi \int_{\bar{u}_*^{(1)}}^{\infty} d\bar{u}\ \bar{u}^2\cos\chi\, A^2(u, \theta)e^{-\beta\left[\frac{\bar{u}^2}{2m} - \epsilon\right]}, \tag{2.5.24}$$

and by the change of variables from $(\chi, \bar{u})$ to (θ, u) we have

$$\gamma^{(1)} = \frac{aR_2\beta^2}{2m^2}\int_0^{\frac{\pi}{2}} d\theta \int_0^{\infty} du\ u^2\cos\theta\, A^2(u, \theta)e^{-\frac{\beta}{2m}u^2}. \tag{2.5.25}$$

For the other cases, we can similarly express each contribution to γ by an integral for θ and u:

$$\gamma^{(k)} = \frac{aR_2\beta^2}{2m^2}\int\int_{\mathcal{D}^{(k)}} d\theta\, du\ u^2\cos\theta\, e^{-\frac{\beta}{2m}u^2} I^{(k)}, \tag{2.5.26}$$

where $\mathcal{D}^{(1)} = \mathcal{D}_1 \cup \mathcal{D}_2$, $\mathcal{D}^{(2)} = \mathcal{D}^{(3)} = \mathcal{D}_1$, $\mathcal{D}^{(4)} = \mathcal{D}_2$,

$$I^{(1)} = A^2, \tag{2.5.27a}$$

$$I^{(2)} = B^2 - 2AB\cos(\omega - \chi), \tag{2.5.27b}$$

$$I^{(3)} = A^2\left[1 + 2\cos 2(\omega - \chi)\right] - 2AB\cos(\omega - \chi), \tag{2.5.27c}$$

$$I^{(4)} = A^2\left[1 - 2\cos 2\chi\right]. \tag{2.5.27d}$$

Therefore, we obtain the identical expression for $\gamma = \gamma^{(1)} + \gamma^{(2)} + \gamma^{(3)} + \gamma^{(4)}$ to the ray representation approach.

2.6 Numerical results

2.6.1 MD set-up

For the LJ and WCA potentials, we perform two-dimensional NVE molecular dynamics simulations for the full dynamics to observe the convergence of the total force autocorrelation function and the fluctuating force autocorrelation function in the Brownian limit. In other words, we numerically obtain force autocorrelation functions $\langle \mathbf{F}(0)\cdot\mathbf{F}(\tilde{\tau})\rangle_{\mathrm{NBL}}$ and $\langle \mathbf{F}^{+}(0)\cdot\mathbf{F}^{+}(\tilde{\tau})\rangle_{\mathrm{NBL}}$ in the near-Brownian-limit (NBL) regime, which are defined as follows:

$$\langle \mathbf{F}(0)\cdot\mathbf{F}(\tilde{\tau})\rangle = \langle \mathbf{F}(0)\cdot\mathbf{F}(\tilde{\tau})\rangle_{\mathrm{NBL}} + \mathcal{O}\left(\frac{m}{M}\right), \tag{2.6.1a}$$

$$\left\langle \mathbf{F}^{+}(0)\cdot\mathbf{F}^{+}(\tilde{\tau})\right\rangle = \left\langle \mathbf{F}^{+}(0)\cdot\mathbf{F}^{+}(\tilde{\tau})\right\rangle_{\mathrm{NBL}} + \mathcal{O}\left(\frac{m}{M}\right), \tag{2.6.1b}$$

where $\tilde{\tau}$ is the microscopic time defined as $t/\sqrt{m}$. These two functions are introduced for numerical purposes but we do not claim that the rate of convergence in

Eq. (2.6.1) is uniform for all time scales. We also perform the corresponding frozen dynamics simulations to obtain the frozen dynamics force autocorrelation function $\langle \mathbf{F}_0(0) \cdot \mathbf{F}_0(\tilde{\tau}) \rangle$ and then compare the MD simulation results with the results evaluated from the analytic expressions.

The system parameters for the MD simulations are defined as follows. The mass of a solvent particle is set as $m = 0.01$ and the number of the solvent particles is set as $N = 10^4$. The simulation domain is a square with side $L = 100$ and periodic boundary conditions are imposed. For the full dynamics, the mass M of the Brownian particle is increased from $M = 0.01$ to $M = 1$. Note that N is chosen sufficiently large so that $\frac{M}{Nm} \leq 0.01$. The temperature of the system is defined in terms of the average kinetic energy of the system and the inverse temperature is given as $\beta = 1$. For the interaction potential between the Brownian particle and a solvent particle, the WCA potential with parameters $\sigma = 1$ and $\epsilon = 1$ (cut-off $R_0 = 2^{1/6}\sigma$) is chosen for a purely repulsive potential and the LJ potential with parameters $\sigma = 1$ and $\epsilon = 1$ (cut-off $R_0 = 2.5\sigma$) is chosen for a potential with an attractive component. All results are given in reduced units with ϵ the unit of energy, σ the unit of length, and M the unit of mass.

The Brownian particle is initially located at the origin. The initial positions of the solvent particles are chosen randomly so that they are distributed uniformly outside the interaction range of the Brownian particle. The velocities of the solvent particles are chosen from the Maxwell-Boltzmann distribution. The time integration is performed by the velocity Verlet algorithm with time step size $\Delta t = 10^{-4}$. The temperature scaling is performed at time $t = 100n$ $(n = 1, 2, \cdots, 10)$. From $t = 10^3$ to $t = 10^4$, the momentum autocorrelation function $\langle \mathbf{P}(0) \cdot \mathbf{P}(t) \rangle$ $(t = 10^{-3}n$, $n = 0, \ldots, 10^4)$ is calculated and averaged over the samples, which is used to estimate the exponential decay rate. From $t = 10^4$ to $t = 1.5 \times 10^4$, the correlation functions

$\langle \mathbf{P}(0) \cdot \mathbf{P}(t) \rangle$, $\langle \mathbf{P}(0) \cdot \mathbf{F}(t) \rangle$, and $\langle \mathbf{F}(0) \cdot \mathbf{F}(t) \rangle$ ($t = 10^{-4}n$, $n = 0, \ldots, 10^4$) are calculated and averaged over the samples. By using those three correlation functions, the Mori memory kernel $K(t)$ and, thus from Eq. (2.1.3), the fluctuating force autocorrelation function $\langle \mathbf{F}^+(0) \cdot \mathbf{F}^+(t) \rangle$ are calculated following the procedure described in Ref. [164].

For each set of the simulation parameters, a total of 8 samples with different initial solvent configurations are prepared in thermal equilibrium through temperature scaling. For each correlation function $\langle \mathbf{A}(0) \cdot \mathbf{B}(t) \rangle$, we have $\langle A_x(0) B_x(t) \rangle$ and $\langle A_y(0) B_y(t) \rangle$, which are equal to $\frac{1}{2} \langle \mathbf{A}(0) \cdot \mathbf{B}(t) \rangle$. Hence, from $n = 16$ samples, we estimate the value of the correlation function as twice of the sample mean and its standard deviation σ is estimated as

$$\sigma = \frac{2 s_n}{\sqrt{n}}, \tag{2.6.2}$$

where s_n^2 is the sample variance. The statistical errors of the simulation results are suppressed within 1 percent of the maximum magnitude of the correlation functions, see Figs. 2.7, 2.8, 2.12 for the statistical errors of the force autocorrelation functions and Fig. 2.13 for that of the momentum autocorrelation function.

The effect of the boundary conditions, which are introduced due to the finite size of the MD simulation domain, is also investigated. Some artificial effects may be possible due to the possibility that a solvent particle which collided with the Brownian particle can collide again with the Brownian particle after leaving and re-entering the domain. Also, two definitions of the number density of the solvent particles (i.e., N/V or N/V^*) may result in different values, unless the volume of the Brownian particle is negligible compared to the volume of the system. To this end, smaller values of the box size L are used and the results are compared. In addition,

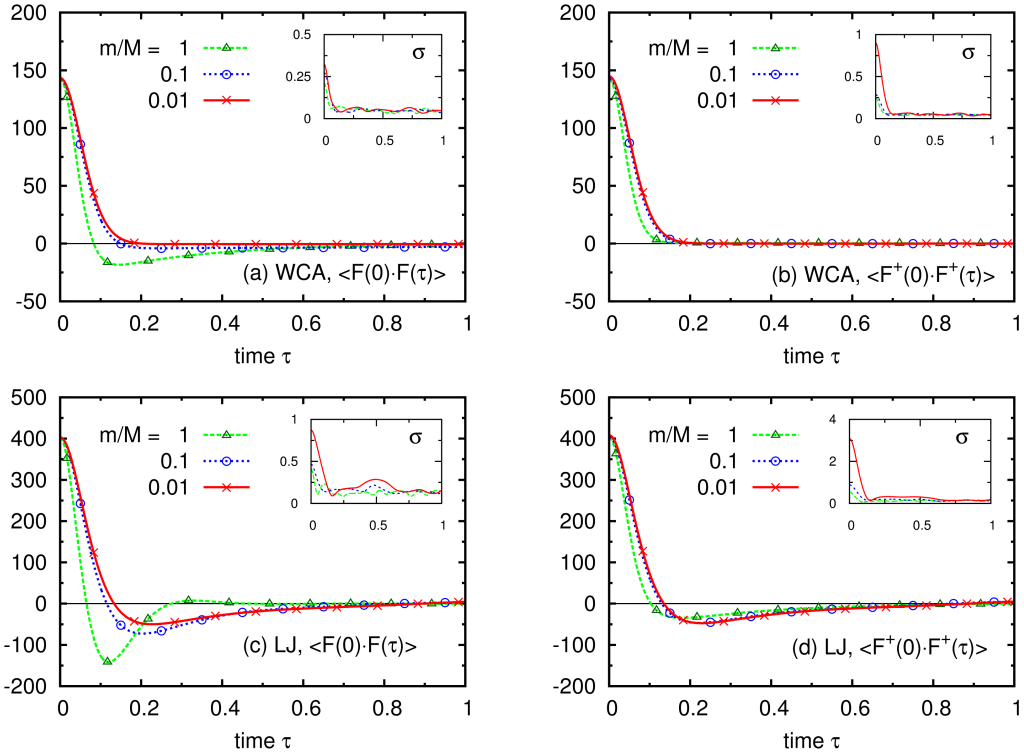

Figure 2.7: Plots of $\langle \mathbf{F}(0) \cdot \mathbf{F}(\tilde{\tau}) \rangle$ (in panels (a) and (c)) and $\langle \mathbf{F}^{+}(0) \cdot \mathbf{F}^{+}(\tilde{\tau}) \rangle$ (in panels (b) and (d)) for various values of the mass ratio m/M from 1 to 0.01. The results are obtained from the MD simulations of the full dynamics under the WCA potential for panels (a) and (b) and under the LJ potential for panels (c) and (d), respectively. The results for $m/M = 0.01$ (depicted by the red solid lines) are chosen as $\langle \mathbf{F}(0) \cdot \mathbf{F}(\tilde{\tau}) \rangle_{\mathrm{NBL}}$ and $\langle \mathbf{F}^{+}(0) \cdot \mathbf{F}^{+}(\tilde{\tau}) \rangle_{\mathrm{NBL}}$ and used in the succeeding figures. Note that the microscopic time $\tilde{\tau} = t/\sqrt{m}$ is used and the force autocorrelations are scaled by the number density a of the solvent particles. In the insets, the standard deviation σ is plotted, see Eq. (2.6.2).

we impose the reflecting boundary conditions for the frozen dynamics simulations and compare the results to the system with the periodic boundary conditions. Hence, we confirm that such effects are negligible in our MD simulation results.

2.6.2 Force autocorrelations

We first observe how the total force autocorrelation function and the fluctuating force autocorrelation function change as the value of m/M is decreasing. In Fig. 2.7,

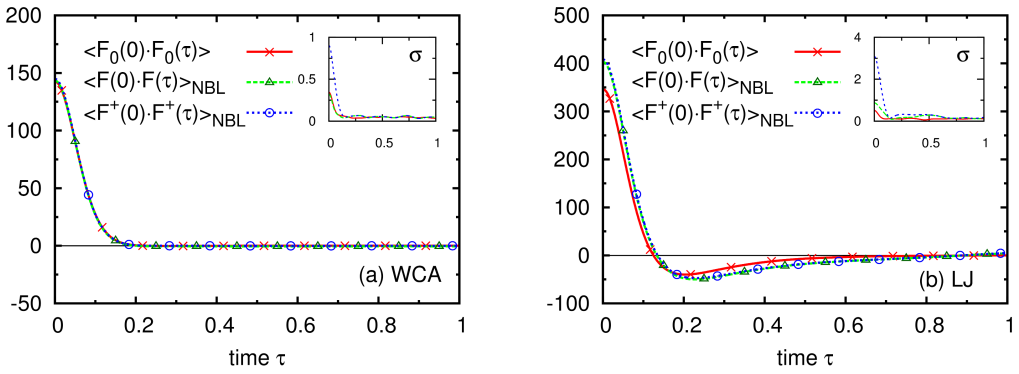

Figure 2.8: Comparison of $\langle \mathbf{F}(0)\cdot\mathbf{F}(\tilde{\tau})\rangle_{\rm NBL}$ and $\langle \mathbf{F}^{+}(0)\cdot\mathbf{F}^{+}(\tilde{\tau})\rangle_{\rm NBL}$ with $\langle \mathbf{F}_0(0)\cdot\mathbf{F}_0(\tilde{\tau})\rangle$ obtained from the frozen dynamics MD simulation. The results for the WCA potential are plotted in panel (a) and those for the LJ potential are in panel (b). For $\langle \mathbf{F}(0)\cdot\mathbf{F}(\tilde{\tau})\rangle_{\rm NBL}$ and $\langle \mathbf{F}^{+}(0)\cdot\mathbf{F}^{+}(\tilde{\tau})\rangle_{\rm NBL}$, the full dynamics MD simulation results for $m/M = 0.01$ are plotted. In the insets, the standard deviation σ is plotted.

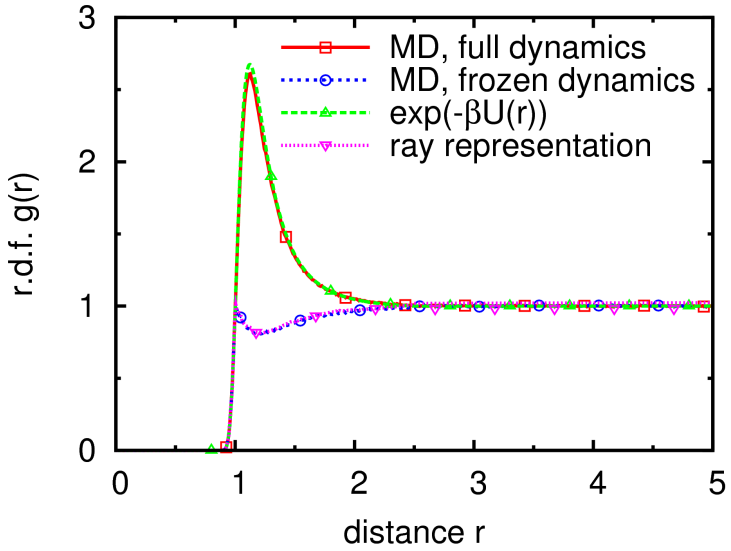

Figure 2.9: For the full dynamics (with $m/M = 0.01$) and the frozen dynamics MD simulations under the LJ potential, the radial distribution functions $g(r)$ are plotted. The distance r is the inter-particle distance between the Brownian particle and a solvent particle. The full dynamics result coincides with $e^{-\beta U(r)}$, while the frozen dynamics result agrees well with the curve calculated from the ray representation approach.

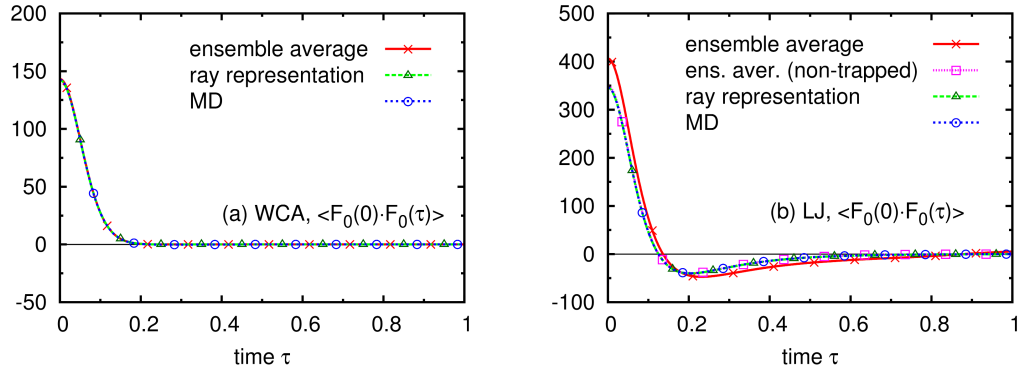

Figure 2.10: Comparison of the curves of $\langle \mathbf{F}_0(0) \cdot \mathbf{F}_0(\tilde{\tau}) \rangle$ obtained by numerical evaluation of the ensemble-averaged expression (i.e., Eq. (2.3.4)), the ray representation expression (i.e., Eq. (2.4.41)), and the frozen dynamics MD simulation. The results are shown in panel (a) for the WCA potential and in panel (b) for the LJ potential, respectively. In panel (b), the ensemble average over the non-trapped particles is also plotted.

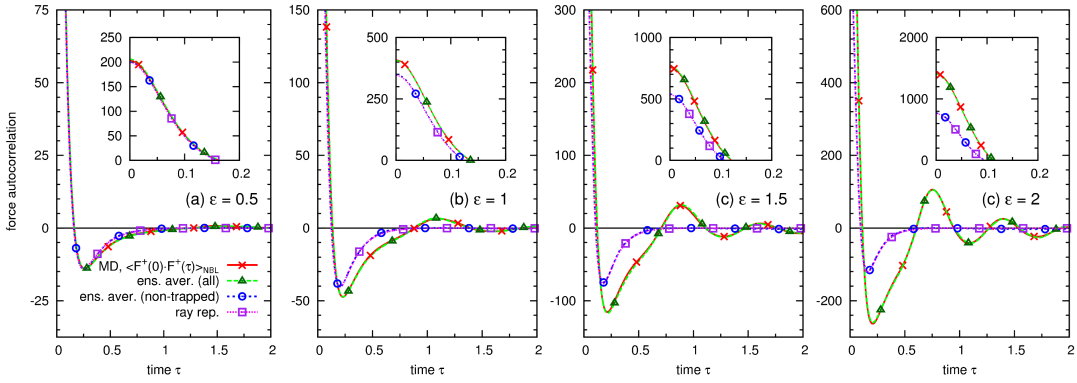

Figure 2.11: For various values of the ϵ parameter of the LJ potential, $\langle \mathbf{F}^+(0) \cdot \mathbf{F}^+(\tilde{\tau}) \rangle_{\mathrm{NBL}}$ obtained from the full dynamics MD simulation and $\langle \mathbf{F}_0(0) \cdot \mathbf{F}_0(\tilde{\tau}) \rangle$ obtained from the ensemble-averaged expression are compared, and $\langle \mathbf{F}_0(0) \cdot \mathbf{F}_0(\tilde{\tau}) \rangle$ obtained from the ensemble average over the non-trapped particles and $\langle \mathbf{F}_0(0) \cdot \mathbf{F}_0(\tilde{\tau}) \rangle$ obtained from the ray representation expression are also compared. The inverse temperature is fixed as $\beta = 1$. In the insets, positive values of the force autocorrelation functions are plotted for short times.

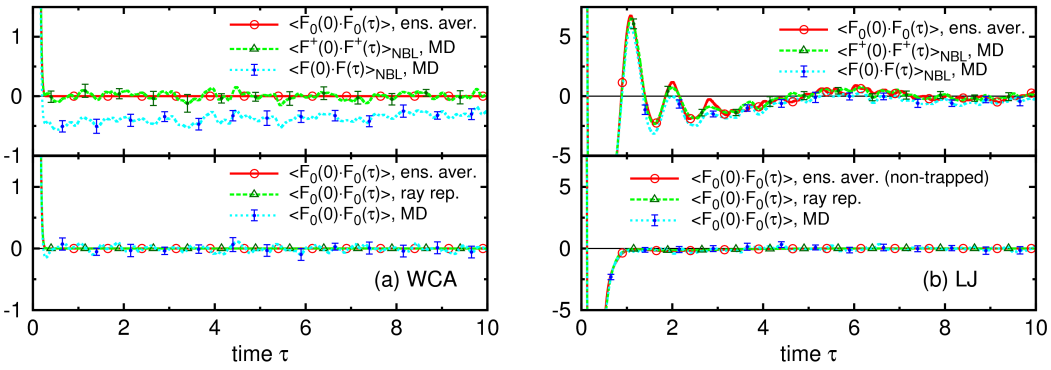

Figure 2.12: Plots of the tails (i.e., long time behavior) of the force autocorrelation functions. The results for the WCA potential are plotted in panel (a), whereas those for the LJ potential are in panel (b). In the upper plot of each panel, plotted are $\langle \mathbf{F}_0(0) \cdot \mathbf{F}_0(\tilde{\tau}) \rangle$ (evaluated from the ensemble-averaged expression, Eq. (2.3.4)), $\langle \mathbf{F}^+(0) \cdot \mathbf{F}^+(\tilde{\tau}) \rangle_{\mathrm{NBL}}$ and $\langle \mathbf{F}(0) \cdot \mathbf{F}(\tilde{\tau}) \rangle_{\mathrm{NBL}}$ (obtained from the full dynamics MD simulation). In the lower plot, three curves of $\langle \mathbf{F}_0(0) \cdot \mathbf{F}_0(\tilde{\tau}) \rangle$ obtained by the following methods are plotted: numerical evaluation of the ensemble average over the non-trapped particles, numerical evaluation of the ray representation expression, and the frozen dynamics MD simulation. For the MD simulation results, error bars with 2σ are also plotted.

these autocorrelation functions obtained from the full dynamics MD simulations are plotted for various values of the mass ratio. The microscopic time $\tilde{\tau} = t/\sqrt{m}$ is used. Since the magnitude of the force autocorrelations is proportional to the number density a of the solvent particles, they are also scaled by a. For both interaction potentials, it is clearly observed that $\langle \mathbf{F}(0) \cdot \mathbf{F}(\tilde{\tau}) \rangle$ and $\langle \mathbf{F}^+(0) \cdot \mathbf{F}^+(\tilde{\tau}) \rangle$ converge. By choosing the results for $m/M = 0.01$ as $\langle \mathbf{F}(0) \cdot \mathbf{F}(\tilde{\tau}) \rangle_{\mathrm{NBL}}$ and $\langle \mathbf{F}^+(0) \cdot \mathbf{F}^+(\tilde{\tau}) \rangle_{\mathrm{NBL}}$, the rate of convergence is investigated. For both potentials, the overall deviation

$$\left(\int_0^\infty \left| \langle \mathbf{F}(0) \cdot \mathbf{F}(\tilde{\tau}) \rangle - \langle \mathbf{F}(0) \cdot \mathbf{F}(\tilde{\tau}) \rangle_{\mathrm{NBL}} \right|^2 d\tilde{\tau} \right)^{1/2} \tag{2.6.3}$$

is decreasing with $\mathcal{O}(m/M)$ and the same rate of convergence is observed for the fluctuating force autocorrelation function. For the WCA potential, pointwise convergence of both force autocorrelation functions is clearly observed to be first order in m/M for all times where the force autocorrelation functions have non-zero val-

ues. For the LJ potential, clear first-order convergence in m/M is observed for short times $\tilde{\tau} < 0.2$ for $\langle \mathbf{F}(0) \cdot \mathbf{F}(\tilde{\tau}) \rangle$ and $\tilde{\tau} < 0.5$ for $\langle \mathbf{F}^+(0) \cdot \mathbf{F}^+(\tilde{\tau}) \rangle$, respectively. We also observe that although two force autocorrelations eventually converge to the same time profile (see Fig. 2.8), for the intermediate values of m/M, the time profiles of $\langle \mathbf{F}^+(0) \cdot \mathbf{F}^+(\tilde{\tau}) \rangle$ are much closer to the limiting time profiles than $\langle \mathbf{F}(0) \cdot \mathbf{F}(\tilde{\tau}) \rangle$ for both potentials.

We compare $\langle \mathbf{F}(0) \cdot \mathbf{F}(\tilde{\tau}) \rangle_{\mathrm{NBL}}$ and $\langle \mathbf{F}^+(0) \cdot \mathbf{F}^+(\tilde{\tau}) \rangle_{\mathrm{NBL}}$ with the frozen dynamics autocorrelation function $\langle \mathbf{F}_0(0) \cdot \mathbf{F}_0(\tilde{\tau}) \rangle$ obtained from the frozen dynamics MD simulations in Fig. 2.8. As expected from Eq. (2.2.8), $\langle \mathbf{F}(0) \cdot \mathbf{F}(\tilde{\tau}) \rangle_{\mathrm{NBL}}$ and $\langle \mathbf{F}^+(0) \cdot \mathbf{F}^+(\tilde{\tau}) \rangle_{\mathrm{NBL}}$ coincide for both potentials. On the other hand, $\langle \mathbf{F}_0(0) \cdot \mathbf{F}_0(\tilde{\tau}) \rangle$ coincides with these two functions for the WCA potential, but for the LJ potential there is a clear discrepancy, which results from the initial configuration of the solvent we imposed in the frozen dynamics MD simulation. Since the initial positions of the solvent particles are uniformly distributed *outside* the interaction range, every solvent particle initially has positive total energy and no particle is trapped in the potential well. However, in order that the frozen dynamics correctly describe the full dynamics in the NBL regime, the trapped particles should also be considered. This can be clearly shown by the radial distribution function $g(r)$ of the inter-particle distance r between the Brownian particle and a solvent. As shown in Fig. 2.9, even though identical initial conditions are used for the full dynamics and the frozen dynamics simulations, the radial distribution function of the frozen dynamics is quite different from that of the full dynamics in the NBL regime. In the full dynamics, $g(r)$ has the form $e^{-\beta U(r)}$, which indicates that the system is in the equilibrium state. In the frozen dynamics, $g(r)$ has smaller values in the potential well region. This is because there is no contribution from the trapped solvent particles. Since the full dynamics is a many-body problem whereas the frozen dynamics is eventually a set of

one-body problems, even if the initial solvent configuration is not in the equilibrium state, the full dynamics attains the equilibrium state by the ergodic postulate but the frozen dynamics may fail to do so. If the initial condition is chosen as described above, the inconsistency between the initial condition and the equilibrium state occurs inside the interaction range. The inconsistency quickly disappears for the WCA potential, but it remains forever for the LJ potential.

Next we compare the time profiles of the frozen dynamics force autocorrelation function $\langle \mathbf{F}_0(0) \cdot \mathbf{F}_0(\tilde{\tau}) \rangle$ obtained by numerical evaluation of the analytic expressions and the frozen dynamics MD simulation. For the numerical evaluation of the ensemble-averaged expression, Eq. (2.3.4) is used. The one-particle trajectory $\mathbf{x}(t)$ is calculated by the fourth-order Runge–Kutta method with $m = 1$ and $\Delta t = 10^{-3}$. For the integrations over r and ϕ variables, the trapezoid rule with 10^3 subintervals is used. The integration interval for r is chosen as $[0.7, 2.5]$. Then, for the integration over u variable, Gaussian quadrature [156] with density e^{-au^2} $(u > 0)$ is employed with 30 quadrature points. Similarly, to numerically evaluate the ray representation expression, Eq. (2.4.41), the fourth-order Runge–Kutta method with $m = 1$ and $\Delta t = 10^{-3}$ is used for the calculation of the trajectory $\psi(t)$. Also, the trapezoid rule with 10^3 subintervals is employed for the integration over r and then Gaussian quadrature with 30 quadrature points is used for the integration over u variable. Fig. 2.10 shows that the three methods produce identical results for the WCA potential, whereas for the LJ potential the ray representation result and the frozen dynamics MD result coincide but they are different from the ensemble average result. The coincidence of the ray representation result and the frozen dynamics MD result is explained by the initial configuration of the solvent that is assumed in the ray representation approach to be identical to the one we imposed in the frozen dynamics MD simulation, see Section 2.4.5. Hence, the discrepancy between the

ray representation result and the ensemble average result is also attributed to no consideration of the trapped particles in the ray representation approach. This can be verified by evaluating the ensemble-averaged equation only over the non-trapped particles. As expected, the resulting time profile coincides with the ray representation result. In addition, we confirm that the radial distribution function obtained from the ray representation approach coincides with that obtained from the frozen dynamics MD simulation, see Fig. 2.9.

Therefore, we have the following relations of the ensemble-averaged expression, Eq. (2.3.2), and the ray representation expression, Eq. (2.4.37), of $\langle \mathbf{F}_0(0) \cdot \mathbf{F}_0(\tilde{\tau}) \rangle$ to the fluctuating force autocorrelation function $\langle \mathbf{F}^+(0) \cdot \mathbf{F}^+(\tilde{\tau}) \rangle_{\mathrm{NBL}}$ in the NBL regime.

- For a purely repulsive potential, both expressions produce $\langle \mathbf{F}^+(0) \cdot \mathbf{F}^+(\tilde{\tau}) \rangle_{\mathrm{NBL}}$.
- For a potential containing an attractive component, the ensemble-averaged expression produces $\langle \mathbf{F}^+(0) \cdot \mathbf{F}^+(\tilde{\tau}) \rangle_{\mathrm{NBL}}$, whereas the ray representation expression produces only the contribution of the non-trapped particles.

We further confirm these by comparing $\langle \mathbf{F}^+(0) \cdot \mathbf{F}^+(\tilde{\tau}) \rangle_{\mathrm{NBL}}$, ensemble average results over all particles and only over the non-trapped particles, and ray representation results for various values of the potential parameters. Fig. 2.11 shows the results under the LJ potential for various values of ϵ. It is observed that for a larger value of ϵ, the discrepancy between the ensemble averages over all particles and over the trapped particles becomes larger. In other words, the contribution of the trapped particles to $\langle \mathbf{F}^+(0) \cdot \mathbf{F}^+(\tilde{\tau}) \rangle_{\mathrm{NBL}}$ increases as the attractive component of the potential is stronger. It is also observed that the contribution of the trapped particles complicates the tail behavior of $\langle \mathbf{F}^+(0) \cdot \mathbf{F}^+(\tilde{\tau}) \rangle_{\mathrm{NBL}}$ with a longer correlation time length.

We also investigate the long-time behavior of the force autocorrelation functions, which is shown in Fig. 2.12. For the WCA potential, $\langle \mathbf{F}_0(0) \cdot \mathbf{F}_0(\tilde{\tau}) \rangle$ quickly decays to zero without attaining negative values. This can be explained by the fact that every one-particle trajectory $\mathbf{x}(t)$ under the WCA potential quickly escapes from the interaction range and the two-time force product $\mathbf{f}(\mathbf{x}) \cdot \mathbf{f}(\mathbf{x}(t))$ has non-negative values for all times. The coincidence of $\langle \mathbf{F}^+(0) \cdot \mathbf{F}^+(\tilde{\tau}) \rangle_{\mathrm{NBL}}$ to $\langle \mathbf{F}_0(0) \cdot \mathbf{F}_0(\tilde{\tau}) \rangle$ is observed for all times. On the other hand, although the overall shape of $\langle \mathbf{F}(0) \cdot \mathbf{F}(\tilde{\tau}) \rangle_{\mathrm{NBL}}$ coincides with $\langle \mathbf{F}_0(0) \cdot \mathbf{F}_0(\tilde{\tau}) \rangle$ for short times (see Fig. 2.8), the total force autocorrelation function has a negative tail, which is expected from Eq. (2.2.10). The magnitude of the negative tail, which is proportional to the mass ratio, is negligible to the magnitude at time $\tilde{\tau} = 0$, but due to its existence the time integral of the total force autocorrelation function eventually decays to zero. Similarly, for the LJ potential, we confirm the coincidence of $\langle \mathbf{F}^+(0) \cdot \mathbf{F}^+(\tilde{\tau}) \rangle_{\mathrm{NBL}}$ to $\langle \mathbf{F}_0(0) \cdot \mathbf{F}_0(\tilde{\tau}) \rangle$ for all times and observe that $\langle \mathbf{F}(0) \cdot \mathbf{F}(\tilde{\tau}) \rangle_{\mathrm{NBL}}$ has slightly smaller values than $\langle \mathbf{F}^+(0) \cdot \mathbf{F}^+(\tilde{\tau}) \rangle_{\mathrm{NBL}}$ and $\langle \mathbf{F}_0(0) \cdot \mathbf{F}_0(\tilde{\tau}) \rangle$. In addition, we also compare the ensemble average $\langle \mathbf{F}_0(0) \cdot \mathbf{F}_0(\tilde{\tau}) \rangle$ over the non-trapped particles, the ray representation result, and the frozen dynamics MD simulation result. For both potentials, the three results agree very well for all times, which confirms that the ray representation approach only considers the contribution of the non-trapped particles.

2.6.3 Friction coefficient γ

We first estimate the friction coefficient γ from the exponential decay rate of the momentum autocorrelation function of the Brownian particle. Fig. 2.13 shows the time profile of $\langle \mathbf{P}(0) \cdot \mathbf{P}(\tilde{\tau}) \rangle$, which is obtained from the full dynamics MD simulation under the LJ potential with $m/M = 0.01$. In a wide time interval, $\langle \mathbf{P}(0) \cdot \mathbf{P}(\tilde{\tau}) \rangle$ ex-

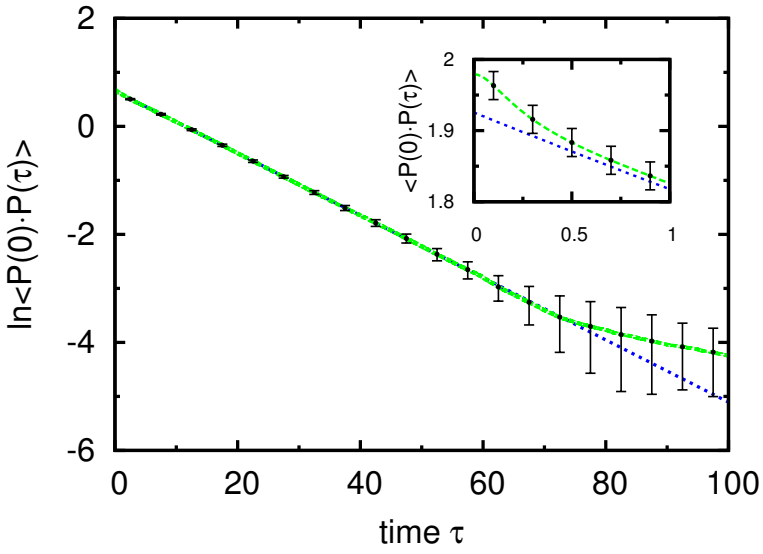

Figure 2.13: The log plot of the momentum autocorrelation function $\langle \mathbf{P}(0) \cdot \mathbf{P}(\tilde{\tau}) \rangle$. The blue dotted line indicates the straight line $\ln c_1 - c_2 \tilde{\tau}$, where c_1 and c_2 are evaluated from the nonlinear least-squares fitting of $\langle \mathbf{P}(0) \cdot \mathbf{P}(\tilde{\tau}) \rangle$ with the form $c_1 e^{-c_2 \tilde{\tau}}$. Error bars with 2σ are also plotted. Since the magnitude of statistical errors is comparable for all times, the error bars become longer for longer times in the log plot. In the inset, the time profile of $\langle \mathbf{P}(0) \cdot \mathbf{P}(\tilde{\tau}) \rangle$ is plotted with $c_1 e^{-c_2 \tilde{\tau}}$ for short times.

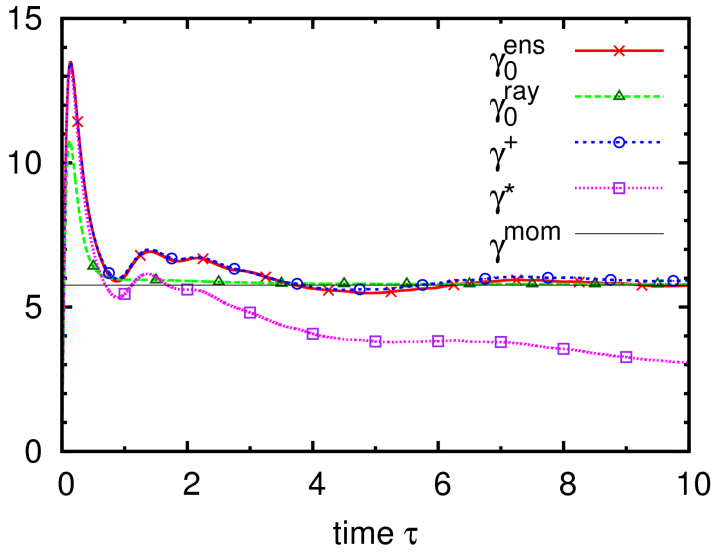

Figure 2.14: Plotted are the time-dependent friction coefficients $\gamma_0^{\rm ens}(\tilde{\tau})$, $\gamma_0^{\rm ray}(\tilde{\tau})$, $\gamma^{+}(\tilde{\tau})$, and $\gamma^{*}(\tilde{\tau})$, defined in Eq. (2.6.4), for the LJ potential. The black horizontal line indicates the value estimated from the exponential decay rate of the momentum autocorrelation function of the Brownian particle for $m/M = 0.01$.

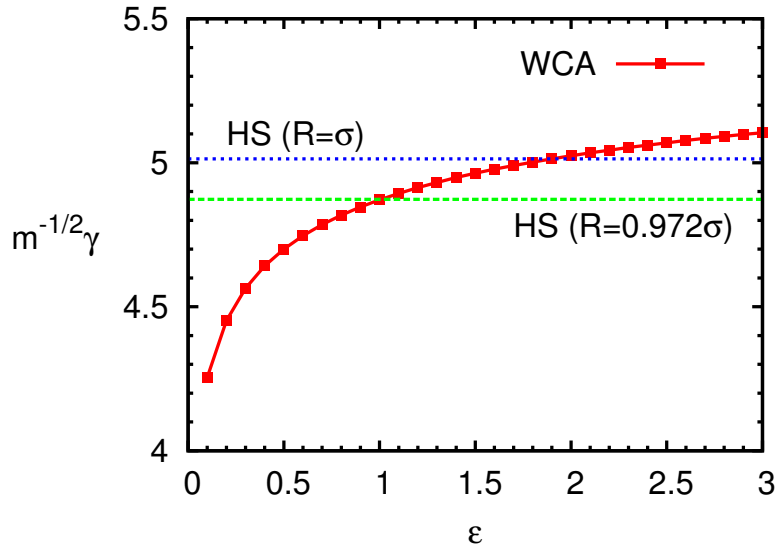

Figure 2.15: Plot of $m^{-1/2}\gamma$ as a function of the ϵ parameter of the WCA potential. The ray representation expression for $d = 2$, Eq. (2.4.43), is used. The other parameters are fixed as $\sigma = 1$, $\beta = 1$, and $a = 1$. The values of γ of the HS system with $R = 0.972\sigma$ and $R = \sigma$ are also plotted by the horizontal lines.

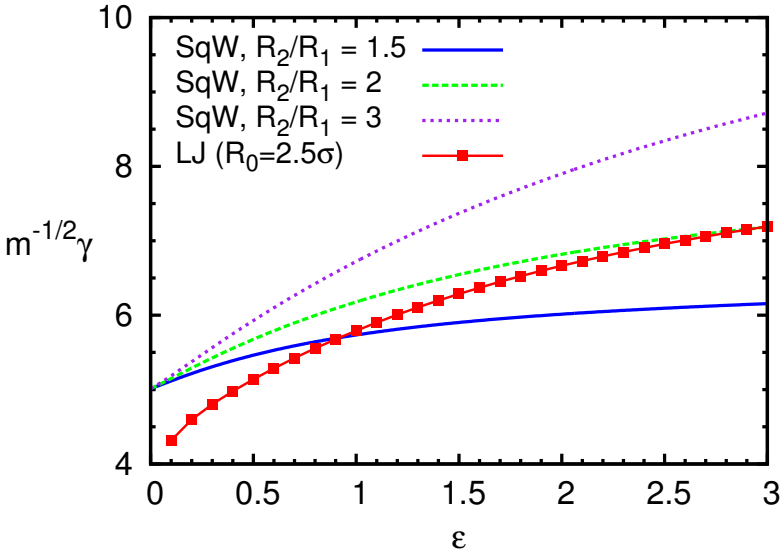

Figure 2.16: Plot of $m^{-1/2}\gamma$ as a function of the ϵ parameter of the LJ potential. The ray representation expression for $d = 2$, Eq. (2.4.43), is used. The other parameters are fixed as $\sigma = 1$, $R_0 = 2.5\sigma$, $\beta = 1$, and $a = 1$. The values of $m^{-1/2}\gamma$ of the SqW system with $\epsilon = 1$, $R_1 = 1$, and different values of R_2 (1.5, 2, and 3) are also plotted by evaluating Eq. (2.5.13). Note that as $\epsilon \to 0$, the value of γ of the SqW system becomes the value for the HS system with $R = R_1$.

hibits exponential decay. By using the nonlinear least-squares Marquardt–Levenberg algorithm [156] with the form $c_1 \exp(-c_2\tilde{\tau})$ for $0 \leq \tilde{\tau} \leq 100$, c_2 is estimated as 5.76×10^{-2} and, from Eq. (2.1.7), $m^{-1/2}\gamma$ is estimated as 5.76. From Eq. (2.6.2) with $n = 16$ samples, the standard deviation of the estimated value is estimated as $\sigma = 0.10$. The deviation from the exponential decay for short times is expected from the fact that the second derivative of the momentum autocorrelation function is equal to the negative of the total force autocorrelation function. Also, the zero slope of $\langle \mathbf{P}(0) \cdot \mathbf{P}(\tilde{\tau}) \rangle$ at $\tilde{\tau} = 0$ is clearly observed. In addition, the initial value of the momentum autocorrelation function is 1.98, which is expected from Eq. (2.2.7) with $N = 10^4$ and $m/M = 0.01$. On the other hand, the decay of the momentum autocorrelation function for long times appears to be algebraic.

Next we investigate the following time integrals of the force autocorrelation functions:

$$\gamma^*(\tilde{\tau}) = \frac{\beta\sqrt{m}}{d} \int_0^{\tilde{\tau}} \langle \mathbf{F}(0) \cdot \mathbf{F}(\tilde{s}) \rangle \, d\tilde{s}, \tag{2.6.4a}$$

$$\gamma_0(\tilde{\tau}) = \frac{\beta\sqrt{m}}{d} \int_0^{\tilde{\tau}} \langle \mathbf{F}_0(0) \cdot \mathbf{F}_0(\tilde{s}) \rangle \, d\tilde{s}, \tag{2.6.4b}$$

$$\gamma^+(\tilde{\tau}) = \frac{\beta\sqrt{m}}{d} \int_0^{\tilde{\tau}} \left\langle \mathbf{F}^+(0) \cdot \mathbf{F}^+(\tilde{s}) \right\rangle d\tilde{s}. \tag{2.6.4c}$$

For $\langle \mathbf{F}_0(0) \cdot \mathbf{F}_0(\tilde{\tau}) \rangle$, both the ensemble-averaged expression and the ray representation expression are used and the corresponding time-dependent friction coefficients are denoted by $\gamma_0^{\mathrm{ens}}(\tilde{\tau})$ and $\gamma_0^{\mathrm{ray}}(\tilde{\tau})$, respectively. In Fig. 2.14, these time-dependent friction coefficients are plotted for the LJ potential. Although $\gamma^*(\tilde{\tau})$ appears similar to $\gamma_0^{\mathrm{ens}}(\tilde{\tau})$ and $\gamma^+(\tilde{\tau})$ for short times, it eventually decays without attaining a stationary value. On the other hand, $\gamma_0^{\mathrm{ens}}(\tilde{\tau})$ and $\gamma^+(\tilde{\tau})$ have very similar time profiles and appear to have the same stationary value. Although the time profile of $\gamma_0^{\mathrm{ray}}(\tilde{\tau})$ is quite different from that of $\gamma_0^{\mathrm{ens}}(\tilde{\tau})$, its stationary value appears to be the

same as that of $\gamma_0^{\rm ens}(\tilde{\tau})$. This confirms that the net contribution of trapped solvent particles to the value of γ is zero. However, to determine the precise value of γ from the time integral $\gamma_0^{\rm ens}(\tilde{\tau})$ or $\gamma^+(\tilde{\tau})$, $\tilde{\tau} = 10$ is rather short, since $\langle \mathbf{F}_0(0) \cdot \mathbf{F}_0(\tilde{\tau}) \rangle$ or $\langle \mathbf{F}^+(0) \cdot \mathbf{F}^+(\tilde{\tau}) \rangle_{\rm NBL}$ still attains non-zero oscillating values and the corresponding time integral has also an oscillation, the magnitude of which is not negligible. The value of $m^{-1/2}\gamma$ is roughly estimated as 5.8 ± 0.2 for $\gamma_0^{\rm ens}$ and γ^+. On the other hand, $\gamma_0^{\rm ray}(\tilde{\tau})$ attains an almost complete plateau for $\tilde{\tau} > 5$ and $m^{-1/2}\gamma$ is estimated as 5.79, which is consistent with the value, 5.76 with $\sigma = 0.10$, estimated from the exponential decay rate of the momentum autocorrelation function. The time integral $\check{\gamma}_0^{\rm ens}(\tilde{\tau})$ of the ensemble average only over the non-trapped particles (cf. $\gamma_0^{\rm ens}(\tilde{\tau})$) has the same time profile as $\gamma_0^{\rm ray}(\tilde{\tau})$ and hence gives the same value of γ. Note that obtaining γ from $\check{\gamma}_0^{\rm ens}(\tilde{\tau})$ and $\gamma_0^{\rm ray}(\tilde{\tau})$ is equivalent to the evaluation of Eq. (2.3.9) and Eq. (2.4.43), respectively.

We evaluate the values of γ of the WCA and LJ potentials as a function of ϵ and compare them with the results of the HS interaction and the SqW potential. For $d = 2$, Eq. (2.3.9) and Eq. (2.4.43) are used for the ensemble average result and the ray representation result, respectively, which produce identical results. In Fig. 2.15, the WCA potential result for $\epsilon \leq 3$ with $\beta = 1$ is presented. As ϵ increases, γ also increases. The friction coefficient $\gamma^{\rm WCA}$ of the WCA potential with $\sigma = 1$ is compared with the friction coefficient $\gamma^{\rm HS}$ of the HS system. For all values of ϵ, $\gamma^{\rm WCA}$ is always smaller than $\gamma^{\rm HS}$ with $R = 2^{1/6}\sigma$. As shown in Fig. 2.15, for $\epsilon = 1$, $\gamma^{\rm WCA}$ is equal to $\gamma^{\rm HS}$ with $R = 0.972\sigma$, and for $\epsilon = 1.9$, $\gamma^{\rm WCA}$ is equal to $\gamma^{\rm HS}$ with $R = \sigma$. Similarly, the LJ potential result is presented and compared with the SqW potential result in Fig. 2.16.

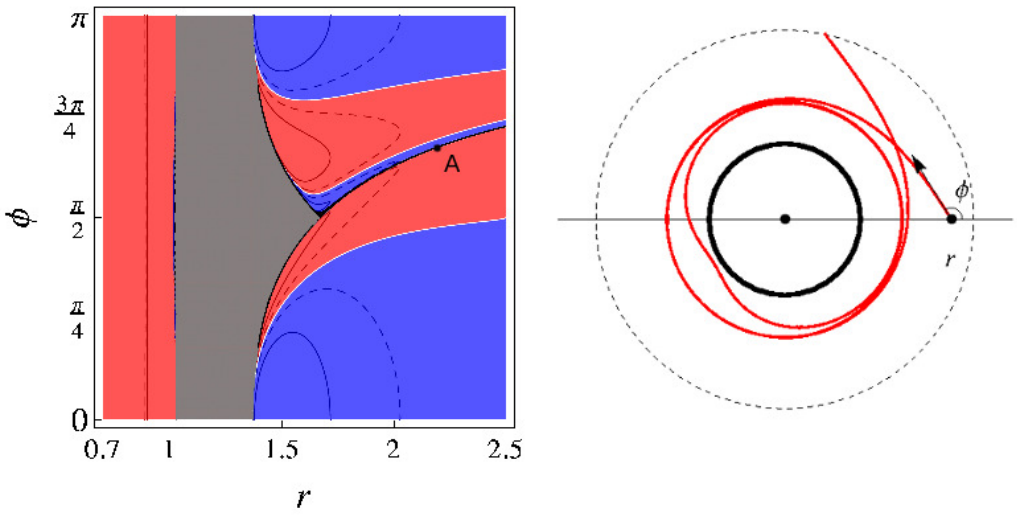

Figure 2.17: In the left plot, the contour plot of $\lim_{t\to\infty} \mathbf{f}(\mathbf{x}) \cdot \mathbf{p}(t)$, which appears in Eq. (2.3.8), is presented. The initial position x and the initial momentum p of the solvent particle are given as $(r, 0)$ and $(u\cos\phi, u\sin\phi)$, respectively, and the value $u = 1$ is used. The gray region indicates the initial values that cause the particle trapped in the potential well forever so that the limit is not defined. The red and blue regions are for positive and negative values of the limit, respectively. The white lines are for the contour with zero value and the red dashed and solid lines are for 0.1 and 0.3, respectively. Similarly, the blue dashed and solid lines are for -0.1 and -0.3. The black points on the boundary of the gray region and the contour line passing through point A indicate that the trajectories with these initial conditions are still inside the interaction range up to $t = 10$ so that the value of the limit is indecisive from the numerical calculation of trajectories up to $t = 10$. In the right diagram, the trajectory $x(t)$ with the initial condition designated by point A is plotted until it leaves the interaction range.

2.7 Summary and Discussion

For the Rayleigh model, the microscopic theory of Brownian motion has been investigated by analytic methods and extensive MD simulations. For a comprehensive understanding of the model in the NBL regime, four typical interaction potentials (the HS interaction, the SqW potential, and the WCA and LJ potentials) have been considered. The physical quantities of main interests are the asymptotic form of the force autocorrelation function of the Brownian particle in the Brownian limit and the friction coefficient γ in the Langevin equation. As pointed out in [1], we always

use the term *asymptotic form* to refer to the Brownian limit rather than to refer to a long time limit. To investigate these quantities, the ensemble-averaged expressions and the ray representation expressions have been derived and numerically evaluated, and MD simulations of the full dynamics with small mass ratio and of the frozen dynamics have been performed.

The theoretical predictions, which have been numerically confirmed, are summarized as follows. As the mass of the Brownian particle increases, the total force autocorrelation function $\langle \mathbf{F}(0) \cdot \mathbf{F}(t) \rangle$ and the fluctuating force autocorrelation function $\langle \mathbf{F}^{+}(0) \cdot \mathbf{F}^{+}(t) \rangle$ have similar time profiles to the frozen dynamics force autocorrelation function $\langle \mathbf{F}_0(0) \cdot \mathbf{F}_0(t) \rangle$ (ensemble average over the bath equilibrium ρ_{b} in Eq. (2.2.6)). However, the time integral of $\langle \mathbf{F}(0) \cdot \mathbf{F}(t) \rangle$ eventually decays, whereas the time integrals of the other autocorrelation functions have the same non-zero stationary value, which is also equal to the friction coefficient estimated from the exponential decay rate of the momentum autocorrelation function of the Brownian particle. Therefore, the asymptotic form of the force autocorrelation function and the friction coefficient can be obtained from $\langle \mathbf{F}_0(0) \cdot \mathbf{F}_0(t) \rangle$.

We have derived two expressions for $\langle \mathbf{F}_0(0) \cdot \mathbf{F}_0(t) \rangle$, Eq. (2.3.2) and Eq. (2.4.37), by using ensemble averaging and the ray representation approach, respectively. From the property that the dynamics of each solvent particle is decoupled from those of the other solvent particles in the frozen dynamics of the Rayleigh model, these expressions are given in terms of one-particle trajectory, which enables one to obtain the desired quantity without performing MD simulations. By time integration, the corresponding expressions for γ have been obtained, see Eq. (2.3.8) and Eq. (2.4.39). For a potential depending only on the inter-particle distance, further simplified expressions have also been derived. The ensemble-averaged expressions are reduced to be three-dimensional integrations, whereas the ray representation expressions are to

be two-dimensional integrations.

We have shown that the ensemble average and the ray representation approach produce identical results for a purely repulsive potential, and that these results also agree very well with the full dynamics and frozen dynamics MD simulation results. Hence, it has been confirmed that the ray representation approach is valid for an unbounded potential containing no attractive component such as the WCA potential, and it is expected that the analysis performed by Kusuoka and Liang [108] under restrictive assumptions can be extended to this case. From the numerical point of view, among the methods we employed to obtain the asymptotic form of the force autocorrelation function and the friction coefficient, the most efficient and numerically reliable one is the ray representation in this case since each one-particle trajectory needs to be calculated for a short time and only a two-dimensional integration needs to be performed. In addition, Gaussian quadrature can be used for both integration variables, which enables one to obtain numerically reliable results with a relatively small number of trajectory calculations.

For a potential containing an attractive component such as the LJ potential, however, it has been observed that there is a clear discrepancy between the ensemble average result and the ray representation result for $\langle \mathbf{F}_0(0) \cdot \mathbf{F}_0(t) \rangle$ and it has been shown that the ray representation only produces the contribution of the non-trapped solvent particles. The initial configuration of the solvent particles which is assumed in the ray representation is that the solvent particles are uniformly distributed outside the interaction range, which is different from the bath equilibrium distribution. Contrary to the purely repulsive potential case where the difference quickly disappears, the difference remains forever in this case since incoming solvent particles to the interaction range cannot be trapped by the potential and thus the contribution of the trapped particles is still missing. The same problem has been observed when

the same initial configuration of the solvent is used for the full dynamics and frozen dynamics MD simulations and the results are compared. These discrepancies are attributed to the fundamental difference between the frozen dynamics and the full dynamics of the Rayleigh model. While the full dynamics always attains the equilibrium distribution by the ergodic postulate, for the frozen dynamics the postulate is no longer valid and thus the equilibrium may fail to be achieved even after a long period of time; also, a time average quantity may be different from the one obtained from the ensemble average depending on the choice of the initial solvent configuration near the Brownian particle. Hence, for the asymptotic form of the force autocorrelation function, if the interaction potential has an attractive component, the only alternative method to the full dynamics MD simulation would be the numerical evaluation of the ensemble-averaged expression. The frozen dynamics MD simulation method with the initial solvent configuration sampled from the bath equilibrium distribution is not efficient since a single sample cannot represent the bath equilibrium and thus a large number of samples should be run. However, if the precise value of the friction coefficient is the only quantity of interest, which is a quite usual case, the ray representation approach and the frozen dynamics MD simulation method can be employed. Actually, it has been shown that they provide a numerically more reliable value of γ than their alternative methods. This is based on the observation that although the contribution of the trapped particles to the time integral of the force autocorrelation function is zero, it complicates the tail behavior of the force autocorrelation function and prevents the time integral from attaining a stationary value.

Another issue that arises for a potential containing an attractive component is the possible existence of the non-trapped trajectories that revolve around the Brownian particle several times, see Fig. 2.17. For some initial conditions, the trajectories

revolve infinitely many times and slight changes in the initial conditions result in large changes in the momentum change $\Delta\mathbf{p} = \mathbf{p}_\infty - \mathbf{p}$. Hence, Δp oscillates very rapidly as the initial condition approaches these points and the analytic expressions we have derived may have some problem with these singular points. Since the set of the singularities has measure zero and we can find a bound for $\Delta\mathbf{p}$ from the conservation of energy, we can show that all expressions are well-defined even in this case. However, the numerical integration of the expressions should be carefully performed and may need more computation time. For example, the use of Gaussian quadrature for all integration variables may not be efficient due to the non-smoothness of the integrand. We note that the SqW potential does not have such complicated trajectories.

Finally, closed-form expressions of γ for the HS interaction and the SqW potential have also been derived. Using these results, it has been analytically confirmed for these potentials that the ray representation approach yields the identical expression of γ to the ensemble average. Although not included in this chapter, expressions for $\langle \mathbf{F}_0(0) \cdot \mathbf{F}_0(t) \rangle$ can also be obtained by following similar procedures performed in Section 2.5. For the HS interaction, it can be easily shown that $\langle \mathbf{F}_0(0) \cdot \mathbf{F}_0(t) \rangle = dD\delta(t)$, where $D = 2\beta^{-1}\gamma$. For the SqW potential, it can be shown that the expression for the contribution of the non-trapped particles obtained by ensemble averaging is equal to the expression obtained by the ray representation approach.

Chapter Three

Time Correlation Functions in the Near-Brownian-Limit Regime

3.1 Introduction

The friction coefficient is one of the essential parameters for simulating transport phenomena in colloidal systems, and estimating it precisely in a systematic manner is important from both theoretical and practical points of view. In addition, as experimental techniques have been improved so that the trajectories of Brownian motion can be observed on shorter time scales than the diffusive time scale of the colloid particles [87, 120], understanding the corresponding phenomena at the molecular level becomes more important.

When a Brownian particle suspended in a fluid has much larger mass than the fluid particles, its velocity satisfies the *phenomenological* Langevin equation [116], where the friction coefficient γ enters as a parameter. The microscopic theory of Brownian motion has addressed the issue of deriving the Langevin equation from first principles (i.e., from the Hamilton's equation or Liouville's equation of the molecular system) and expressing the transport coefficient γ in terms of quantities that can be obtained from the microscopic trajectory of the system, hence computationally from molecular dynamics (MD) simulations.

One such formula proposed by Kirkwood [98] is given by the Green–Kubo expression, where the friction coefficient is related to the time integral of the force autocorrelation function. However, it has a so-called *plateau* problem that the value of the time integral decays to zero as the upper limit of time integration is increased to infinity. Another formula, which has a similar form but does not decay, has been obtained by various techniques [113, 158, 196]; γ is given as the time integral of the force autocorrelation function of the *reference* system. The latter is defined as the frozen dynamics, where the Brownian particle is assumed to be fixed in space and the

fluid particles move under the external potential due to the presence of the Brownian particle. Using the projection operator technique, Mazur and Oppenheim [131] performed a detailed analysis of this formula. They defined a projection operator, which is different from the well-known Mori's projection operator [140], and showed that the corresponding memory function has a well-behaved series expansion in powers of the mass ratio of a fluid particle to the Brownian particle, and that γ is obtained from the zeroth-order term. They also showed that the total force autocorrelation function has a negative and slowly decaying tail, which makes the time integral of the Kirkwood formula vanish. Based on Mazur and Oppenheim's analysis, Hynes *et al.* [89] performed a similar analysis on the generalized Langevin equation derived by Mori [140] to show that the Mori memory function also has a slowly decaying tail but its contribution to the time integral is so negligible in the Brownian limit that the Langevin equation can be derived from the generalized Langevin equation.

Significant progress on understanding the finite-size effect, which is important in MD simulation studies, was made by Español and Zúñiga [51]. They showed that for a Brownian particle suspended in a bath consisting of a *finite* number of particles, the reduced mass μ enters in the generalized Langevin equation rather than the actual mass M of the Brownian particle. Then, they obtained asymptotic expressions for the time correlation functions of the Brownian particles for large μ and t (see also [114, 145]):

$$\langle \mathbf{P}(0) \cdot \mathbf{P}(t) \rangle \approx \frac{d}{\beta}\, \mu\, e^{-\frac{\gamma}{\mu}t}, \tag{3.1.1a}$$

$$\gamma(t) = \frac{\beta}{d} \int_0^t \langle \mathbf{F}(0) \cdot \mathbf{F}(u) \rangle \; du = -\frac{\beta}{d} \langle \mathbf{P}(0) \cdot \mathbf{F}(t) \rangle \approx \gamma\, e^{-\frac{\gamma}{\mu}t}, \tag{3.1.1b}$$

where $\mathbf{P}$ is the momentum of the Brownian particle and $\mathbf{F}$ is the force on the Brownian particle by the fluid (for detailed definitions of other symbols, see Section 3.2.1).

Hence, γ can be estimated from the exponential decay rate of $\langle \mathbf{P}(0) \cdot \mathbf{P}(t) \rangle$ and, alternatively, $\langle \mathbf{P}(0) \cdot \mathbf{F}(t) \rangle$ or the time integral of $\langle \mathbf{F}(0) \cdot \mathbf{F}(t) \rangle$ can be used to determine γ by its extrapolated value at $t = 0$ or by its exponential decay rate. Español and Zúñiga also pointed out that in Mazur and Oppenheim's work [131], the thermodynamic limit $N \to \infty$, where N is the number of the bath particles, was implicitly assumed when the infinite mass limit $M \to \infty$ was taken and, hence, the Brownian limit is achieved as $\mu \to \infty$. From the hydrodynamic point of view, the density ratio of the Brownian particle and the surrounding fluid is also an important parameter [79]. If the ratio is comparable to unity, the motion of the Brownian particle is affected by the long-lived vortices in the fluid, which were developed by its movement in previous times. This hydrodynamic memory explains that the velocity autocorrelation function of the Brownian particle has a long-time tail of the form $t^{-3/2}$ [84]. For an incompressible fluid, the hydrodynamic Brownian motion is described by the generalized Langevin equation with the Boussinesq–Basset force [124]. The effect of compressibility has been investigated to explain the initial rapid change of the velocity autocorrelation function [198]. Since these hydrodynamic effects become negligible as $\mu \to \infty$, we do not further investigate them in this chapter.

Numerous MD studies have been performed on the single Brownian particle system from various points of view and we only mention herein recent work which is relevant to our present work. Through large-size MD simulations, the time-dependent friction coefficient $\gamma(t)$, defined as the time integral of the total force autocorrelation function, see Eq. (3.1.1b), has been investigated to determine the friction coefficient γ [114, 145]. The Mori memory function of Brownian motion has been calculated from MD simulations and investigated for various physical parameters in [102, 164]. The convergence of the Mori memory function under the Brownian limit has also been observed [96, 103]. Using the linear response theory and performing non-equilibrium

MD simulations, it has been shown that the aforementioned finite-size effect is due to the finite *mass* of the bath rather than the finite *volume* of the bath [150] and an alternative method of estimating γ from a finite system has been proposed [149]. An *ad hoc* correction of finite-volume effect has also been attempted [174].

The Rayleigh gas model, which additionally assumes no interaction between bath particles (i.e., a Brownian particle in an ideal gas), has provided plenty of insights on Brownian motion. Owing to the non-interacting bath assumption, the system becomes analytically more manageable so that some exact and explicit results are available. The explicit expression for the friction coefficient has been obtained under the assumption of elastic collisions by various techniques [44, 70, 128, 138] and the convergence of the motion of the Brownian particle to the Ornstein–Uhlenbeck process has been proved [39]. Recently, a corresponding proof for a continuous interaction potential case has been provided [108]. Another favorable feature of the Rayleigh gas model is that an infinite bath is naturally introduced and results without any finite-size effect can be obtained. The force autocorrelation function of the infinite reference system, the time integral of which gives the friction coefficient, has been investigated for various types of interaction potentials [96]. This quantity was accurately calculated from numerical integration of one-particle trajectories of a bath particle and then compared with MD simulation results.

In this chapter, we develop a theory that enables precise and systematic analysis of MD simulation results of the single Brownian system in the near-Brownian-limit regime. More specifically, we obtain asymptotic expansions of the time correlation functions $\langle \mathbf{P}(0) \cdot \mathbf{P}(t) \rangle$, $\langle \mathbf{P}(0) \cdot \mathbf{F}(t) \rangle$, and $\langle \mathbf{F}(0) \cdot \mathbf{F}(t) \rangle$ with respect to μ. Noting that the asymptotic behaviors in Eq. (3.1.1) for large t and μ have been extensively used to determine the value of γ but very little has been theoretically investigated about the criteria for choosing the large values of t and μ and the convergence rate of

the evaluated values to γ, we tackle these issues using asymptotic expansions of the time correlation functions. Although we can retrieve Eq. (3.1.1) from the asymptotic expansions for large t, it is noted that t is not an asymptotic parameter in these asymptotic expansions and hence we can use them for *short* and *intermediate* times as well. Unless explicitly indicated as t-asymptotic or (t, μ)-asymptotic, we use the term *asymptotic* as μ-asymptotic in the rest of the chapter. To derive the asymptotic expansions of the time correlation functions, we use the asymptotic expansion of the Mori memory function $K(t)$. Since the form of the asymptotic expansion of $K(t)$ depends on the limit procedure of achieving the Brownian limit, we consider two important cases. For the first case, where the infinite mass limit $M \to \infty$ is taken under the assumption that the thermodynamic limit $N \to \infty$ has been already achieved (i.e., a finite-mass Brownian particle in an infinite bath), we perform detailed analysis on the numerical methods of determining γ based on Eq. (3.1.1). In addition, we analyze the ratio of $\langle \mathbf{P}(0) \cdot \mathbf{F}(t) \rangle$ to $\langle \mathbf{P}(0) \cdot \mathbf{P}(t) \rangle$, which gives an *instantaneous* exponential decay rate. For the second case, where an infinite mass is assumed for the Brownian particle and the thermodynamic limit is taken (i.e., frozen dynamics in a finite bath), a Rayleigh gas is considered and the finite-volume effect due to the boundary conditions is investigated. To demonstrate the validity of the theory, we perform extensive MD simulations of the Rayleigh gas for the two limit cases.

The rest of the chapter is organized as follows. We derive the asymptotic expansions of the time correlation functions in Section 3.2. We present the analysis on the numerical methods of evaluating the friction coefficient in Section 3.3. The MD simulation results are given in Section 3.4. We provide a summary with some discussion in Section 3.5.

3.2 Asymptotic expansions of time correlation functions

3.2.1 System

We follow the standard setting of the system for microscopic description of a single Brownian particle [89, 131]. A Brownian particle of mass M is suspended in a bath of volume V in a d-dimensional space ($d = 2$ or 3). The bath consists of N bath particles of mass m. The inverse temperature of the system is denoted by $\beta = (k_{\mathrm{B}}T)^{-1}$. Although assuming a specific form of interaction potentials between the Brownian particle and a bath particle and between bath particles is not essential, we introduce a usual assumption that they are functions of inter-particle distance and they are short-ranged. The latter is introduced because the interaction between the Brownian particle and a bath particle is assumed to be instantaneous on the Brownian time scale.

We denote the momentum of the Brownian particle by $\mathbf{P}$ and the force on the Brownian particle by $\mathbf{F}$. We note the following relation, which was derived by Español and Zúñiga [51], see also Ref. [184]:

$$\langle \mathbf{P} \cdot \mathbf{P} \rangle = \frac{d}{\beta}\mu, \tag{3.2.1}$$

where the brackets denote the equilibrium average and the reduced mass μ is defined as

$$\mu = \frac{MNm}{M + Nm}. \tag{3.2.2}$$

In this chapter, the Brownian limit is defined as $\mu \to \infty$, which is equivalent to

achieving *both* the infinite mass limit $M \to \infty$ and the thermodynamic limit $N \to \infty$. When increasing the number of bath particles, we also increase the volume of the system so that the number density N/V stays constant. Other physical conditions such as the temperature and parameters of the interaction potentials, including the size of the Brownian particle, do not change when these limits are achieved.

As mentioned in the introduction, we are interested in the time correlation functions $\langle \mathbf{P}(0) \cdot \mathbf{P}(t) \rangle$, $\langle \mathbf{P}(0) \cdot \mathbf{F}(t) \rangle$, and $\langle \mathbf{F}(0) \cdot \mathbf{F}(t) \rangle$ in the near-Brownian-limit regime $\mu \gg m$ (or, equivalently, $M \gg m$ and $N \gg 1$).

3.2.2 Generalized Langevin equation

The starting point of the theory is the following generalized Langevin equation [51, 140]:

$$\dot{\mathbf{P}}(t) = -\frac{1}{\mu} \int_0^t K(t-u) \mathbf{P}(u) \, du + \mathbf{F}^+(t), \tag{3.2.3}$$

where $K(t)$ is the Mori memory function and $\mathbf{F}^+$ is the fluctuating force satisfying

$$\left\langle \mathbf{F}^+(t) \right\rangle = 0, \quad \left\langle \mathbf{P}(0) \cdot \mathbf{F}^+(t) \right\rangle = 0, \quad \mathbf{F}^+(0) = \mathbf{F}(0). \tag{3.2.4}$$

It is important to realize that this equation is *exact* although the explicit form of $K(t)$ is unknown. The fluctuation-dissipation relation is given as

$$K(t) = \frac{\beta}{d} \left\langle \mathbf{F}^+(0) \cdot \mathbf{F}^+(t) \right\rangle. \tag{3.2.5}$$

As mentioned in the introduction, it is noted that because of Eq. (3.2.1), the factor in Eq. (3.2.3) is μ^{-1} rather than M^{-1}.

We denote the momentum autocorrelation function as

$$C(t) = \langle \mathbf{P}(0) \cdot \mathbf{P}(t) \rangle \,. \tag{3.2.6}$$

Then, the other time correlation functions are given as time derivatives of $C(t)$:

$$\langle \mathbf{P}(0) \cdot \mathbf{F}(t) \rangle = \dot{C}(t), \quad \langle \mathbf{F}(0) \cdot \mathbf{F}(t) \rangle = -\ddot{C}(t). \tag{3.2.7}$$

From Eqs. (3.2.1), (3.2.3), and (3.2.4), we obtain a Volterra integro-differential equation for $C(t)$:

$$\dot{C}(t) = -\frac{1}{\mu} \int_0^t K(t-u) C(u)\, du, \quad C(0) = \frac{d}{\beta}\mu. \tag{3.2.8}$$

3.2.3 Solution of Eq. (3.2.8)

By using the Laplace transform technique, we solve Eq. (3.2.8) for $C(t)$ [i.e., express $C(t)$ in terms of $K(t)$]. We denote the Laplace transform of a function by using tilde notation and we use s as the Laplace variable. For example,

$$\tilde{C}(s) = \int_0^\infty C(t) e^{-st} dt. \tag{3.2.9}$$

From Eq. (3.2.8), we obtain

$$\tilde{C}(s) = \frac{C(0)}{s + \frac{1}{\mu}\tilde{K}(s)} = \frac{C(0)}{s} \sum_{n=0}^{\infty} \left(-\frac{1}{\mu s} \tilde{K}(s) \right)^n, \tag{3.2.10}$$

where we assumed that the series expansion is well-defined. Then, we obtain the following series solution for $C(t)$:

$$C(t) = C(0) \left[1 + \sum_{n=1}^{\infty} \frac{(-1)^n}{\mu^n} \int_0^t G^{*n}(u)\, du \right], \tag{3.2.11}$$

where

$$G(t) = \int_0^t K(u)\, du, \tag{3.2.12}$$

and $G^{*n}(t)$ is the n-fold convolution power of $G(t)$ defined recursively as

$$G^{*1}(t) = G(t), \quad G^{*(n+1)}(t) = (G^{*n} * G)(t) = \int_0^t G^{*n}(t-u)G(u)\, du. \tag{3.2.13}$$

To obtain Eq. (3.2.11), we used properties such as $\tilde{G}(s) = \tilde{K}(s)/s$ and $\tilde{G^{*n}}(s) = \left[\tilde{G}(s)\right]^n$.

3.2.4 $K_0(t)$ and $C_0(t)$

Although we expressed $C(t)$ in terms of $K(t)$ in Eq. (3.2.11), it is noted that the explicit form of $K(t)$ is unknown in practice and, in an MD simulation study, it is obtained by calculating the time correlation functions (i.e., $C(t)$ and its derivatives) and solving Eq. (3.2.8) for $K(t)$ [164] (see also [101]). It is also noted that when the value of N or M varies, both $K(t)$ and $C(t)$ vary. Hence, it appears that there is not much gain from the solution Eq. (3.2.11). However, as observed in several MD simulation studies [96, 102, 164], compared to the change of the overall shape of $C(t)$ and its derivatives for varying μ, that of $K(t)$ is much smoother. In addition, while $C(t)$ does not possess a proper limit under $\mu \to \infty$, $K(t)$ has a well-defined limit, denoted by $K_0(t)$. For the finite value of μ, we express $K(t)$ as follows:

$$K(t) = K_0(t) + \delta K(t). \tag{3.2.14}$$

Using $K_0(t)$ and the lowest-order term $K_1(t)$ of $\delta K(t)$, we shall obtain an asymptotic expansions of $C(t)$ with respect to μ in Section 3.2.5.

The friction coefficient γ is expressed in terms of $K_0(t)$ as follows. Since both $\langle \mathbf{F}(0) \cdot \mathbf{F}(t) \rangle$ and $\langle \mathbf{F}^+(0) \cdot \mathbf{F}^+(t) \rangle$ converge to the frozen dynamics force autocorrelation function of the reference system [51], we have the following relations using Eq. (3.2.5):

$$K_0(t) = \frac{\beta}{d} \lim_{\mu \to \infty} \left\langle \mathbf{F}^+(0) \cdot \mathbf{F}^+(t) \right\rangle = \frac{\beta}{d} \lim_{\mu \to \infty} \langle \mathbf{F}(0) \cdot \mathbf{F}(t) \rangle \,. \tag{3.2.15}$$

Since γ is given as the time integral of $\lim_{\mu \to \infty} \langle \mathbf{F}(0) \cdot \mathbf{F}(t) \rangle$ [131], we have

$$\gamma = \frac{\beta}{d} \int_0^\infty \lim_{\mu \to \infty} \langle \mathbf{F}(0) \cdot \mathbf{F}(t) \rangle \, dt = \int_0^\infty K_0(t) \, dt. \tag{3.2.16}$$

Now, using $K_0(t)$, we define $C_0(t)$ as

$$C_0(t) = C(0) \left[1 + \sum_{n=1}^{\infty} \frac{(-1)^n}{\mu^n} \int_0^t G_0^{*n}(u) \, du \right], \tag{3.2.17}$$

where $G_0(t)$ is correspondingly defined as

$$G_0(t) = \int_0^t K_0(u) \, du. \tag{3.2.18}$$

It is noted that $C_0(t)$ is the solution of Eq. (3.2.8) if $K(t)$ *would* be replaced by $K_0(t)$. Following the procedure demonstrated in [12] with $\tilde{K}_0(0) = \gamma$ from Eq. (3.2.16), it can be shown that, for large μ and t,

$$C_0(t) \approx C(0) \, e^{-\frac{1}{\mu} \tilde{K}_0(0) t} = \frac{d}{\beta} \, \mu \, e^{-\frac{\gamma}{\mu} t}. \tag{3.2.19}$$

Hence, the comparison of Eqs. (3.1.1a) and (3.2.19) shows that $C(t)$ and $C_0(t)$ have the same lowest-order asymptotic expressions. Roughly speaking, as $K(t)$ approaches $K_0(t)$ for large μ, $C(t)$ can be approximated by $C_0(t)$. However, in order to make

this argument rigorous, we need to take the term $\delta K(t)$ into account and obtain an asymptotic expansion of $C(t)$ for large but finite μ. In Section 3.2.5, we obtain such an expansion, which has $C_0(t)$ as the lowest-order term and higher-order terms of which are given as convolutions of $C_0(t)$ and $\delta K(t)$. In addition, we note that although $C_0(t)$ and $C(t)$ have the same lowest-order asymptotic expressions, their higher-order corrections of the (t, μ)-asymptotic exponential decay behaviors are different due to the contribution of $\delta K(t)$, see Sections 3.3.1 and 3.3.2.

3.2.5 Asymptotic expansion of $C(t)$

It is important to realize that the deviation $\delta K(t)$ of $K(t)$ from $K_0(t)$ depends on the limiting procedure of achieving the Brownian limit $\mu \to \infty$ (i.e., how M and N are increased). We shall obtain asymptotic expansions of $C(t)$ and its derivatives for two specific forms of $\delta K(t)$. For each case, we first discuss when the assumed form of $K(t)$ appears and then obtain the asymptotic expansions.

3.2.5.1 Case A ($\mu \approx M$)

Here, we assume that

$$K(t) \approx K_0(t) + \frac{1}{\mu} K_1(t), \tag{3.2.20}$$

where $K_1(t)$ does not depend on μ. This form of $K(t)$ appears when we take the infinite mass limit $M \to \infty$ assuming the thermodynamic limit $N \to \infty$ is already achieved or assuming the condition $M \ll Nm$. Hence, in this case, μ is approximately equal to M. Hynes *et al.* [89] considered this case and showed that the Mori memory function is decomposed into two contributions, which they denoted as

$i\Omega_{11}(t)$ and $\Delta_{11}(t)$. In particular, $i\Omega_{11}(t)$ is given as the Maxwellian average (with respect to $\mathbf{P}$) of the Mazur-Oppenheim memory function [131], which allows a well-behaved expansion in powers of the mass ratio m/M, whereas $\Delta_{11}(t)$ decays on the slow time scale of the Brownian particle, which does not allow such an expansion. However, it was shown that the magnitude of $\Delta_{11}(t)$ is negligible [i.e., $o(m/M)$]. Hence, we have Eq. (3.2.20) with $K_1(t)$ given as the first-order term in the expansion of $i\Omega_{11}(t)$.

By substituting Eq. (3.2.20) into Eq. (3.2.10), we obtain,

$$\tilde{C}(s) \approx \frac{C(0)}{s + \frac{1}{\mu}\tilde{K}_0(s)} \sum_{n=0}^{\infty} \left(-\frac{\frac{1}{\mu^2}\tilde{K}_1(s)}{s + \frac{1}{\mu}\tilde{K}_0(s)} \right)^n, \tag{3.2.21}$$

and, subsequently, by introducing

$$\tilde{C}_0(s) = \frac{C(0)}{s + \frac{1}{\mu}\tilde{K}_0(s)}, \tag{3.2.22}$$

we obtain

$$\tilde{C}(s) \approx \tilde{C}_0(s) \sum_{n=0}^{\infty} \left(-\frac{1}{C(0)\mu^2}\tilde{K}_1(s)\tilde{C}_0(s) \right)^n. \tag{3.2.23}$$

Hence, we obtain the following asymptotic expansion of $C(t)$:

$$C(t) \approx C_0(t) + \sum_{n=1}^{\infty} \left(-\frac{1}{C(0)\mu^2} \right)^n K_1^{*n} * C_0^{*(n+1)}(t). \tag{3.2.24}$$

We note that, contrary to the expansion of $C_0(t)$, see Eq. (3.2.17), keeping a finite number of lower terms does not cause divergence as $t \to \infty$ owing to the exponential decay of $C_0(t)$ (for the decay behavior of the lowest-order term $C_0(t)$ and the higher-order terms, see Eqs. (3.3.8) and (3.3.9), respectively). Hence, in practice, we can

use the following asymptotic expansion:

$$C(t) \approx C_0(t) - \frac{1}{C(0)\mu^2} \left(K_1 * C_0 * C_0\right)(t). \tag{3.2.25}$$

The corresponding asymptotic expansions of the first and second derivatives are given as

$$\dot{C}(t) \approx \dot{C}_0(t) - \frac{1}{\mu^2} K_1 * C_0(t) - \frac{1}{C(0)\mu^2} \left(K_1 * C_0 * \dot{C}_0\right)(t), \tag{3.2.26}$$

$$\ddot{C}(t) \approx \ddot{C}_0(t) - \frac{C(0)}{\mu^2} K_1(t) - \frac{1}{\mu^2} K_1 * \dot{C}_0(t) - \frac{1}{C(0)\mu^2} \left(K_1 * C_0 * \ddot{C}_0\right)(t). \tag{3.2.27}$$

However, as shown in Section 3.3.2, by including all terms in Eq. (3.2.24), we obtain the correction to the exponential decay rate of $C(t)$ due to $K_1(t)$. Roughly speaking, Eq. (3.2.25) approximates Eq. (3.2.24) under the assumption that the approximation

$$e^{-\frac{\tilde{K}_1(0)}{\mu^2}t} \approx 1 - \frac{\tilde{K}_1(0)}{\mu^2}t \tag{3.2.28}$$

is valid.

3.2.5.2 Case B (frozen dynamics of a Rayleigh gas)

Here, we consider a *fixed* Brownian particle immersed in a bath with a *finite* number of bath particles. Hence, we achieve the Brownian limit by increasing the number of bath particles (i.e., by taking the thermodynamic limit). To the best of our knowledge, how the Mori memory function of a finite system converges to that of the infinite reference system has not been known in this case. We investigate this problem under the *non-interacting* bath assumption. In other words, we obtain the form of $\delta K(t)$ for the frozen dynamics of the Rayleigh gas in a finite bath. We first

obtain the form of the tail appearing in the force autocorrelation function in the finite system and then derive the form of $\delta K(t)$.

In order to make the argument clear, we assume that the volume of the bath is given as $V = L^d$, where L is the side of the bath, and periodic boundary conditions are imposed. In addition, we assume that the interaction between the Brownian particle and a bath particle is purely repulsive. Since the number of bath particles, N, is increased with N/V constant, μ is proportional to L^d. Contrary to the force autocorrelation function $\langle \mathbf{F}(0) \cdot \mathbf{F}(t) \rangle$ of the infinite reference system, which is essentially zero at large times, that of the finite system has a small magnitude at large times. This is attributed to the re-collisions of bath particles to the fixed Brownian particle (in the image cells), which is resulted from the introduction of the boundary conditions.

As derived in Appendix, the force autocorrelation function of the Brownian particle interacting with the gas through elastic collisions has a negative tail of a form $L^{-d} f(t/L)$. Roughly speaking, this is because the time scale of the re-collision is proportional to L and the probability of the re-collision decays like $\mathrm{O}(L^{d-1})$. We borrow this result for the purely repulsive potential case. Then, by using Eq. (3.2.15), the force autocorrelation function of the finite system is expressed as

$$\langle \mathbf{F}(0) \cdot \mathbf{F}(t) \rangle = \frac{d}{\beta} K_0(t) + \frac{1}{\mu} f\left(\frac{t}{\mu^{1/d}} \right). \tag{3.2.29}$$

We note that only the contribution of the *first* re-collisions to the *nearest* periodic images (i.e., separated by L) is considered in Eq. (3.2.29). However, the other collisions occur at longer times and Eq. (3.2.29) is a good enough approximation for our purpose.

To derive the form of $\delta K(t)$, we use the following equation, which is obtained by differentiating Eq. (3.2.8) with respect to t:

$$K(t) = -\frac{\beta}{d}\ddot{C}(t) - \frac{\beta}{d\mu}K * \dot{C}(t). \tag{3.2.30}$$

Substituting Eq. (3.2.29) into Eq. (3.2.30), we obtain

$$K(t) = K_0(t) + \frac{\beta}{d\mu}f\left(\frac{t}{\mu^{1/d}}\right) - \frac{\beta}{d\mu}K * \dot{C}(t). \tag{3.2.31}$$

Hence, we obtain $K(t) \approx K_0(t) + \mu^{-1}K_1(t)$, where

$$K_1(t) = -\frac{\beta}{d}K_0 * \dot{C}_0(t) + \frac{\beta}{d}f\left(\frac{t}{\mu^{1/d}}\right). \tag{3.2.32}$$

We note that $K_1(0) = 0$ and the convolution term initially dominates $K_1(t)$ until the effect of re-collisions becomes significant.

By following the same procedure as in Section 3.2.5.1 and using the Laplace transform of $K(t)$,

$$\tilde{K}(s) = \tilde{K}_0(s) + \frac{1}{\mu}\frac{\tilde{K}_0^2(s)}{s + \frac{1}{\mu}\tilde{K}_0(s)} + \frac{\beta}{d}\frac{1}{\mu^{1-1/d}}\tilde{f}(\mu^{1/d}s), \tag{3.2.33}$$

we obtain the same form of the asymptotic expansions, Eqs. (3.2.25), (3.2.26), and (3.2.27) with $K_1(t)$ defined in Eq. (3.2.32).

3.3 Evaluation of γ

In this section, we analyze the numerical methods of evaluating γ that make use of the long-time behavior of $C(t)$ or $\dot{C}(t)$. More specifically, we consider the following values:

- γ_1 obtained from the exponential decay rate of $C(t)$ at large times;
- γ_2 obtained from the extrapolated value at $t = 0$ from $\dot{C}(t)$ at large times;
- γ_3 obtained from the exponential decay rate of $\dot{C}(t)$ at large times;
- γ_4 obtained from the extrapolated value at $t = 0$ from the instantaneous exponential decay rate $-\dot{C}(t)/C(t)$ at large times.

Throughout this section, we consider Case A (i.e., assuming $M \ll Nm$ and finite-volume effect is not significant). In addition, we introduce some time scales τ_0 and τ_1 on $K_0(t)$ and $K_1(t)$, respectively, so that we assume

$$K_0(t) = 0, \quad \text{for } t > \tau_0, \tag{3.3.1a}$$

$$K_1(t) = 0, \quad \text{for } t > \tau_1. \tag{3.3.1b}$$

We note that τ_0 is comparable to or longer than the time duration of a single collision between the Brownian particle and a bath particle. Since $K_0(t)$ and $K_1(t)$ smoothly decay to zero, the assumptions in Eq. (3.3.1) do not hold exactly in practice. For a typical shape of $K_0(t)$ and $K_1(t)$, see Figure 3.3.

By using the following three parameters, we shall obtain the asymptotic behavior of γ_1, γ_2, γ_3 and γ_4:

$$\gamma \equiv \int_0^{\tau_0} K_0(u)\, du, \quad \alpha \equiv \gamma\tau_0 - \int_0^{\tau_0} G_0(u)\, du, \quad \zeta \equiv \int_0^{\tau_1} K_1(u)\, du. \tag{3.3.2}$$

While the total effect of $K_0(t)$ and $K_1(t)$ is considered in γ and ζ, respectively, the effect of microscopic structure of $K_0(t)$ [i.e., deviation of $K_0(t)$ from Dirac delta function $\gamma\delta(t)$] is reflected in α.

We first obtain (t, μ)-asymptotic expressions of $C_0(t)$ and $C(t)$ in Sections 3.3.1 and 3.3.2, respectively, to find estimates for γ_1, γ_2, γ_3, and γ_4. Then, to address the issue of the validity time interval, we analyze lower-order terms with respect to μ, which contribute linear approximations of $C(t)$ and $\dot{C}(t)$ with respect to t in Sections 3.3.3, 3.3.4, and 3.3.5.

3.3.1 (t, μ)-Asymptotic expression of $C_0(t)$

Under the assumption given in Eq. (3.3.1), we have, for $t > \tau_0$,

$$\int_0^t G_0(u)\, du = \gamma t - \alpha. \tag{3.3.3}$$

Similarly, after some transient time $n\tau_0$, the time integral $\int_0^t G^{*n}(u)du$ exhibits t-asymptotic behavior and becomes a polynomial of t having degree n. We obtain the two highest-order terms in the polynomial by using the following identity:

$$\int_0^t G_0^{*n}(u)\, du = \int_0^t dt_1\, G_0(t_1) \int_0^{t-t_1} dt_2\, G_0(t_2) \cdots \int_0^{t-\sum_{k=1}^{n-1} t_k} dt_n\, G_0(t_n), \tag{3.3.4}$$

which can be easily shown by mathematical induction. For large t, by approximating the integrand $G_0(t_1)\dots G_0(t_n)$ as a constant equal to γ^n over the whole region, we obtain the leading term as $\gamma^n t^n/n!$. To obtain the next highest term, we assume $t > n\tau_0$ and consider the following subregions. In the region satisfying $t_k > \tau_0$ for $k = 1, \dots, n$ and $\sum_{k=1}^{n} t_k < t$, the integrand is exactly γ^n and hence the integration over this region is equal to $\gamma^n(t - n\tau_0)^n/n!$. In the region satisfying $0 < t_1 < \tau_0$, $t_k > \tau_0$ for $k = 2, \dots, n$ and $\sum_{k=2}^{n} t_k < t - \tau_0$, the integrand becomes $G_0(t_1)\gamma^{n-1}$ and hence the integration over the region is equal to $\gamma^{n-1}(\gamma\tau_0 - \alpha)(t - n\tau_0)^{n-1}/(n-1)!$. Since there are $n-1$ similar subregions and the volume of the remaining region is $o(t^{n-1})$, we obtain

$$\int_0^t G_0^{*n}(u)\, du = \frac{1}{n!}\gamma^n(t-n\tau_0)^n + \frac{n}{(n-1)!}\gamma^{n-1}(\gamma\tau_0-\alpha)(t-n\tau_0)^{n-1} + o(t^{n-1}), \quad (3.3.5)$$

and equivalently,

$$\int_0^t G_0^{*n}(u)\, du = \frac{1}{n!}\gamma^n t^n - \frac{n}{(n-1)!}\alpha\gamma^{n-1}t^{n-1} + o(t^{n-1}). \quad (3.3.6)$$

By substituting Eq. (3.3.6) to Eq. (3.2.17), we have

$$C_0(t) \approx \frac{d}{\beta}\mu \sum_{n=0}^{\infty} \frac{1}{n!}\left(-\frac{\gamma}{\mu}t\right)^n \left[1 + \frac{(n+1)\alpha}{\mu}\right], \quad (3.3.7)$$

and by using the approximation $(1+\alpha/\mu)^{n+1} \approx 1+(n+1)\alpha/\mu$ for large μ, we finally obtain

$$C_0(t) \approx \frac{d}{\beta}\mu\left(1+\frac{\alpha}{\mu}\right)\exp\left[-\frac{\gamma}{\mu}\left(1+\frac{\alpha}{\mu}\right)t\right]. \quad (3.3.8)$$

We note that although we assumed both t and μ are large in the above derivation, it is not clear what the criteria for t and μ are for Eq. (3.3.8) to be valid. Especially, the validity time interval for Eq. (3.3.6), $t > n\tau_0$, depends on n. We revisit this issue in Sections 3.3.3, 3.3.4, and 3.3.5.

3.3.2 (t, μ)-Asymptotic expression of $C(t)$

Using the asymptotic expansion of $C(t)$, Eq. (3.2.24), and the first-order-corrected asymptotic expression of $C_0(t)$, Eq. (3.3.8), we obtain the (t, μ)-asymptotic expression of $C(t)$. We introduce the following rather crude assumptions to estimate the correction terms in Eq. (3.2.24). We assume that $C_0(t)$ is exactly given by Eq. (3.3.8) for all t and $K_1(t)$ is a Dirac delta function, $\zeta\delta(t)$ (i.e., $G_1(t) = \int_0^t K_1(u)du = \zeta$ for all t). Then, we obtain

$$\frac{1}{[C_0(0)]^n} K_1^{*n} * C_0^{*(n+1)}(t) = \frac{1}{n!}\zeta^n t^n C_0(t), \tag{3.3.9}$$

and by substituting this into Eq. (3.2.24), we finally obtain

$$C(t) \approx \frac{d}{\beta}\mu\left(1 + \frac{\alpha}{\mu}\right)\exp\left[-\frac{\gamma}{\mu}\left(1 + \frac{\alpha + \zeta/\gamma}{\mu}\right)t\right]. \tag{3.3.10}$$

Then, by differentiating Eq. (3.3.10), we obtain

$$\dot{C}(t) \approx -\frac{d}{\beta}\gamma\left(1 + \frac{2\alpha + \zeta/\gamma}{\mu}\right)\exp\left[-\frac{\gamma}{\mu}\left(1 + \frac{\alpha + \zeta/\gamma}{\mu}\right)t\right]. \tag{3.3.11}$$

By using Eqs. (3.3.10) and (3.3.11), we can obtain the following estimates of γ_1, γ_2, γ_3, and γ_4:

$$\gamma_1 \approx \gamma_3 \approx \gamma_4 \approx \gamma\left(1 + \frac{\alpha + \zeta/\gamma}{\mu}\right), \tag{3.3.12a}$$

$$\gamma_2 \approx \gamma\left(1 + \frac{2\alpha + \zeta/\gamma}{\mu}\right). \tag{3.3.12b}$$

3.3.3 Linear approximation of $C(t)$

As mentioned above, the time interval where the exponentially decaying behavior with the first-order-corrected prefactor and decay rate occurs is not clearly defined. We investigate this issue by analyzing the lowest-order terms in $C(t)$ with respect to μ which contribute a linear approximation of $C(t)$ with respect to t.

From Eqs. (3.2.17) and (3.2.25) or alternatively from Eqs. (3.2.11) and (3.2.20), we obtain the following series:

$$C(t) \approx \frac{d}{\beta}\mu \left[1 - \frac{1}{\mu}\int_0^t G_0(u)\, du - \frac{1}{\mu^2}\int_0^t G_1(u)\, du + \frac{1}{\mu^2}\int_0^t G_0 * G_0(u)\, du\right]. \tag{3.3.13}$$

The validity of the above approximation is guaranteed if the higher-order terms are negligible compared with these lowest-order terms. By a rough estimate, the condition is given as $\frac{\gamma}{\mu}t \ll 1$, so by increasing μ, we have a longer time interval.

By using Eq. (3.3.3) and the following t-asymptotic expressions,

$$\int_0^t G_1(u)\, du = \zeta t + \text{const}, \quad \text{for } t > \tau_1, \tag{3.3.14a}$$

$$\int_0^t G_0 * G_0(u)\, du = \frac{1}{2}\gamma^2 t^2 - 2\alpha\gamma t + \text{const}, \quad \text{for } t > 2\tau_0, \tag{3.3.14b}$$

we obtain, for $t > \max\{2\tau_0, \tau_1\}$,

$$C(t) \approx \frac{d}{\beta}\mu \left(1 + \frac{\alpha}{\mu}\right)\left[1 - \frac{\gamma}{\mu}\left(1 + \frac{\alpha + \zeta/\gamma}{\mu}\right)t\right]. \tag{3.3.15}$$

Since the validity of Eq. (3.3.13) is guaranteed under the condition $\frac{\gamma}{\mu}t \ll 1$, we collected only constant terms and linear terms in t and neglected $\gamma^2 t^2/\mu^2$. Then we kept only up to the first-order correction terms for the constant terms. Eq (3.3.15) is

the correction to $C(t) \approx C(0)\exp\left(-\frac{\gamma}{\mu}t\right) \approx C(0)\left[1-\frac{\gamma}{\mu}t\right]$ and the estimate of γ_1 is retrieved from it. It is also noted that we have confirmed that this estimate is valid *at least* in the time interval $\max\{2\tau_0, \tau_1\} < t \ll \frac{\mu}{\gamma}$.

3.3.4 Linear approximation of $\dot{C}(t)$

Similarly, we obtain the following expansion

$$\dot{C}(t) = -\frac{d}{\beta}\left[G_0(t) + \frac{1}{\mu}G_1(t) - \frac{1}{\mu}G_0^{*2}(t) + \frac{1}{\mu^2}G_2(t) - \frac{2}{\mu^2}G_0 * G_1(t) + \frac{1}{\mu^2}G_0^{*3}(t)\right], \tag{3.3.16}$$

where we introduced the second-order correction $G_2(t)$ of $G(t)$ by employing the second-order correction $K_2(t)$ of $K(t)$ and assuming the existence of τ_2. By using the following relations

$$G_0 * G_0(t) = \gamma^2 t - 2\alpha\gamma, \quad \text{for } t > 2\tau_0, \tag{3.3.17a}$$

$$G_0 * G_1(t) = \gamma\zeta t + \text{const}, \quad \text{for } t > \tau_0 + \tau_1, \tag{3.3.17b}$$

$$G_0 * G_0 * G_0(t) = \frac{1}{2}\gamma^3 t^2 - 3\alpha\gamma^2 t + \text{const}, \quad \text{for } t > 3\tau_0, \tag{3.3.17c}$$

we obtain, for $t > \max\{3\tau_0, \tau_0 + \tau_1, \tau_2\}$,

$$\dot{C}(t) = -\frac{d}{\beta}\gamma\left(1 + \frac{2\alpha + \zeta/\gamma}{\mu}\right)\left[1 - \frac{\gamma}{\mu}\left(1 + \frac{\alpha + \zeta/\gamma}{\mu}\right)t\right], \tag{3.3.18}$$

and hence we retrieve the estimates for γ_2 and γ_3 given in Eq. (3.3.12). We note that although we introduced the second-order correction $G_2(t)$, we neglected its contribution, which is a second-order correction to the constant term.

3.3.5 Linear approximation of $-\dot{C}(t)/C(t)$

By using Eqs. (3.3.15) and (3.3.18), we obtain the following linear approximation of the instantaneous exponential decay rate of $C(t)$:

$$-\frac{\dot{C}(t)}{C(t)} = \frac{\gamma}{\mu}\left(1 + \frac{\alpha + \zeta/\gamma}{\mu}\right), \tag{3.3.19}$$

which is valid for $\max\{3\tau_0, \tau_0 + \tau_1, \tau_2\} < t \ll \frac{\mu}{\gamma}$. Hence, we retrieve the estimate for γ_4. We note that the slope (with respect to time t) is zero in this first-order correction with respect to μ [i.e., the slope is $o(\mu^{-2})$].

We also derive the limit of the instantaneous exponential decay rate normalized by μ. From Eqs. (3.3.13) and (3.3.16), we obtain

$$-\mu\frac{\dot{C}(t)}{C(t)} \approx G_0(t) + \frac{1}{\mu}G_1(t) + \frac{1}{\mu}\int_0^t G_0(u)\left[G_0(t) - G_0(t-u)\right]du. \tag{3.3.20}$$

Since $G_1(t)$ and the integral in Eq. (3.3.20) are bounded, we obtain

$$\lim_{\mu\to\infty}\left[-\mu\frac{\dot{C}(t)}{C(t)}\right] = G_0(t). \tag{3.3.21}$$

We note that the time interval where the approximation, Eq. (3.3.20), is valid becomes larger as $\mu \to \infty$ and thus the relation, Eq. (3.3.21), is valid for all t.

3.4 MD simulation results

To confirm the theoretical predictions obtained in Sections 3.2 and 3.3, we perform MD simulations of the Rayleigh gas system. Although the theoretical predictions

obtained for Case A is valid for an interacting bath as well as for an non-interacting bath, we choose this system for the following reasons. First of all, $K_0(t)$ and γ can be accurately obtained from numerical integration of one-particle trajectories of a bath particle for this system [96]. Also, when a purely repulsive interaction potential between the Brownian particle and a bath particle is chosen, $K_0(t)$ and $K_1(t)$ satisfy the assumption on the existence of time scales τ_0 and τ_1 and hence we can verify the results in Section 3.3. On the other hand, when an interaction potential contains an attractive component, these time scales become much longer and may not be clearly defined [96]. By comparing with the results in the purely repulsive potential case, we can observe how the failure of the time scale assumption, which may also occur for Brownian motion in an interacting bath, affects the behavior of the time correlation functions.

Three sets of MD simulations are performed. The first two sets correspond to Case A with a purely repulsive interaction potential and an interaction potential with an attractive component, respectively. The last set is the frozen dynamics simulations corresponding to Case B.

3.4.1 MD setup

We perform two-dimensional NVE MD simulations. The Weeks–Chandler–Andersen (WCA) potential and the truncated Lennard-Jones (LJ) potential with cutoff 2.5σ are chosen as a purely repulsive interaction potential and an interaction potential containing an attractive component, respectively. The truncated LJ potential $V(r)$

with cutoff r_{cut} is defined as

$$V(r) = \begin{cases} V_0(r) - V_0(r_{\text{cut}}) & \text{if } r < r_{\text{cut}}, \\ 0 & \text{otherwise,} \end{cases} \tag{3.4.1}$$

where r is the inter-particle distance between the Brownian particle and a bath particle and $V_0(r)$ is the LJ potential with parameters ϵ and σ, defined as

$$V_0(r) = 4\epsilon \left[\left(\frac{\sigma}{r}\right)^{12} - \left(\frac{\sigma}{r}\right)^{6} \right]. \tag{3.4.2}$$

The WCA potential is defined as the truncated LJ potential with cutoff $2^{1/6}\sigma$, where the minimum of $V_0(r)$ is attained. We choose σ as the radius $R = 1$ of the Brownian particle and $\epsilon = 1$.

The system parameters are chosen as follows. For the first two sets of MD simulations, various values of the mass M of the Brownian particle are used: $M = 2$, 5, 10, 20, 50, 100. The mass m of a bath particle is set as $m = 1$ and the number of bath particles is $N = 10^4$. The simulation box is a square with side $L = 100$ and periodic boundary conditions are imposed. The inverse temperature of the system is set as $\beta = 1$. For the last set of MD simulations, the WCA potential is used. Various values of the side of the simulation box are used: $L = 10$, 15, 20, 30, 50, 70, 100. The number of bath particles is correspondingly increased so that the number density is equal to $N/L^2 = 1$. The other parameters are the same except that the mass of the Brownian particle is not defined (i.e., infinite) in this case. All simulation results are reported in reduced units with ϵ the unit of energy, σ the unit of length, and m the unit of mass.

The MD simulations are performed as follows. For the first two sets of MD

simulations, the initial position of the Brownian particle is randomly chosen with a uniform distribution in the simulation box and then the initial positions of the bath particles are randomly chosen with a uniform distribution outside the interaction range of the Brownian particle. The initial velocity of the Brownian particle is set as zero whereas the velocities of the bath particles are sampled from the Maxwell–Boltzmann distribution. The velocity Verlet algorithm is used for time integration and the time step size is set as $\Delta t = 10^{-3}$. To obtain a sample in equilibrium, temperature scaling is performed ten times at every 10^6 time steps. Then, the trajectory is obtained for 5×10^6 time steps for the WCA potential case and for 10^7 time steps for the LJ potential to calculate $\langle \mathbf{P}(0) \cdot \mathbf{P}(t) \rangle$, $\langle \mathbf{P}(0) \cdot \mathbf{F}(t) \rangle$, and $\langle \mathbf{F}(0) \cdot \mathbf{F}(t) \rangle$. For the last set of MD simulations, all procedures are the same except that the Brownian particle is fixed at the randomly chosen initial position and the momentum of the Brownian particle is defined as the negative of the total bath momentum [51].

A total of 128 samples are obtained for each set of the simulation parameters. When a certain physical quantity, for example $K(t)$, is calculated from the time correlation functions, the statistical error present in the quantity is estimated as follows. The samples are grouped into $n = 8$ bins and the time correlation functions are obtained by averaging over each bin. Using these averaged time correlation functions, 8 samples of the physical quantity are obtained and the sample variance s^2 is calculated. Then, the standard deviation of the quantity obtained from the fully averaged time correlation functions over the whole samples is estimated by $\sigma = s/\sqrt{n}$. Owing to a large number of samples, the limiting behavior of the time correlation functions are clearly observed without any significant interference with statistical errors. However, when the first-order corrections for the limiting behavior is investigated, the statistical errors are no more negligible. In these cases, the error

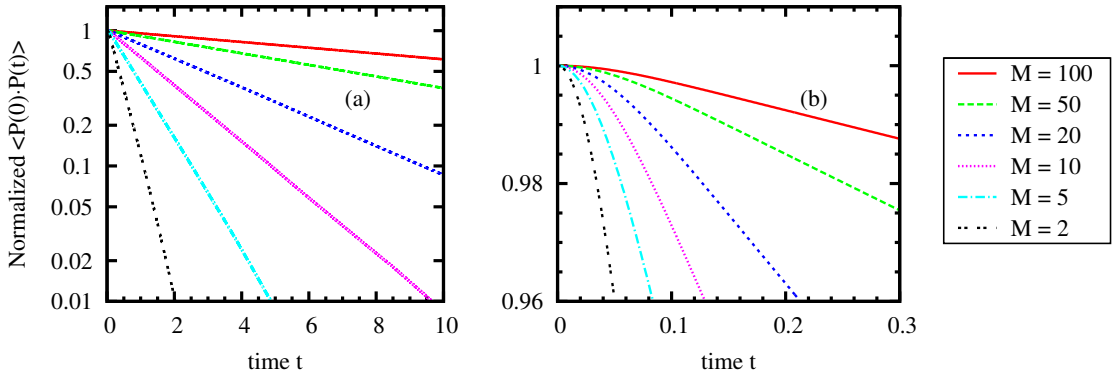

Figure 3.1: For Case A with the WCA potential, the normalized momentum autocorrelation function $C(t)/C(0)$ is plotted for various values of the mass M of the Brownian particle for long times in panel (a) and for short times in panel (b). Note that the vertical axis in panel (a) is logarithmic scale.

bars corresponding to 3σ are also plotted.

3.4.2 Case A with WCA potential

We first observe the behavior of the time correlation functions for various values of the mass M of the Brownian particle. Then, we confirm the estimates, Eq. (3.3.12), of γ_1, γ_2, γ_3, and γ_4 from the time correlation functions after we discuss the behavior of the Mori memory function $K(t)$. Figure 3.1 shows the time profiles of $C(t) = \langle \mathbf{P}(0) \cdot \mathbf{P}(t) \rangle$ for various values of M. As expected from Eq. (3.1.1a), $C(t)$ decays exponentially at large times and the exponential decay rate is inversely proportional to the reduced mass μ. However, from the short-time behavior of $C(t)$ it is observed that the slope at $t = 0$ is zero and it takes some time for $C(t)$ to exhibit a linear decay. The initial zero slope is expected from the fact that $C(t)$ is an even function (i.e., $C(t) = C(-t)$) or from a short-time expansion $C(t) = C(0)\left[1 - \frac{1}{2!}\omega_v^{(2)} t^2 + \frac{1}{4!}\omega_v^{(4)} t^4 \pm \dots\right]$, where $\omega_v^{(n)}$ is the n-th frequency mo-

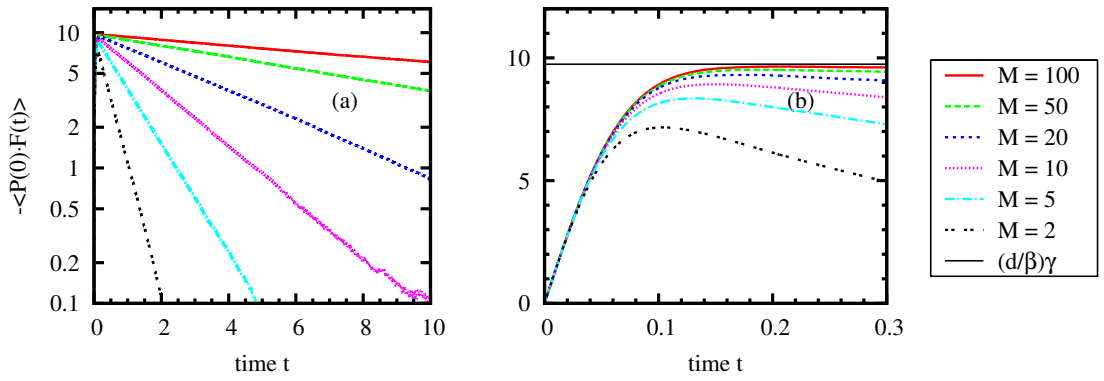

Figure 3.2: For Case A with the WCA potential, the negative of the momentum-force correlation function, $-\langle \mathbf{P}(0)\cdot\mathbf{F}(t)\rangle = -\dot{C}(t)$, is plotted for various values of the mass M of the Brownian particle for long times in panel (a) and for short times in panel (b). The black solid lines indicate the plateau value $\frac{d}{\beta}\gamma$. Note that the vertical axis in panel (a) is logarithmic scale.

ment [13]. The time profiles of $\dot{C}(t) = \langle \mathbf{P}(0)\cdot\mathbf{F}(t)\rangle$ are shown in Figure 3.2. As expected from Eq. (3.1.1b), $\dot{C}(t)$ exhibits an exponential decay, at large times, with the same exponential decay rate as $C(t)$. From the short-time behavior of $\dot{C}(t)$ it is observed that the magnitude of $\dot{C}(t)$ is initially zero and, after attaining the maximum, it exhibits a linear decay. As M becomes larger, the maximum approaches the *theoretical plateau* value $\frac{d}{\beta}\gamma = -\lim_{t\to\infty}\lim_{\mu\to\infty}\dot{C}(t)$.

We observe the Mori memory function $K(t)$ in Figure 3.3. It is calculated from the time correlation functions following the procedure presented in [164]. Its limit under the Brownian limit, $K_0(t) = \lim_{\mu\to\infty} K(t)$, is obtained by numerical integration of one-particle trajectories of a bath particle following the procedure presented in [96]. In the left panel of Figure 3.3, the time profiles of $K(t)$ for various values of M as well as that of $K_0(t)$ are shown. The convergence of $K(t)$ to $K_0(t)$ is clearly observed as M increases. The next-order correction $K_1(t)$, defined in Eq. (3.2.20), is obtained by using $K(t)$ for intermediate values of M and calculating $\mu\,[K(t) - K_0(t)]$. The time profiles of $K_1(t)$, obtained from the results for $M = 5$ and 10, are shown in

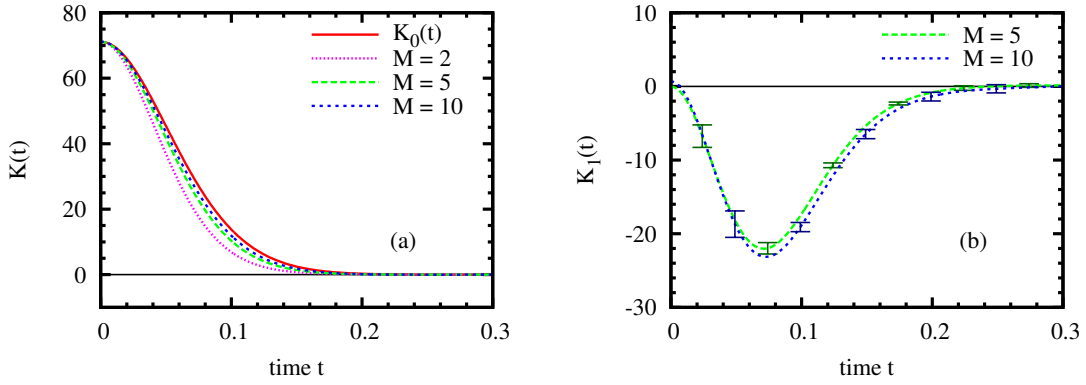

Figure 3.3: For Case A with the WCA potential, the Mori memory function $K(t)$ is plotted for various values of the mass M of the Brownian particle in panel (a). The limit $K_0(t) = \lim_{\mu\to\infty} K(t)$ is also plotted. In panel (b), the time profile of $K_1(t)$, which is obtained by subtracting $K_0(t)$ from $K(t)$ for $M = 5$ or 10 and multiplying by the corresponding value of μ, is plotted with the error bars corresponding to 3σ.

the right panel of Fig 3.3, which show close agreement with each other. As expected from the fact that the initial value $K(0)$ is equal to $\langle \mathbf{F}\cdot\mathbf{F}\rangle$ regardless of the value of M, the initial value of $K_1(t)$ is shown to be zero. The time profile of $K_1(t)$ attains a negative peak and then decays to zero. From the time profiles of $K_0(t)$ and $K_1(t)$, we estimate the time scales of τ_0 and τ_1 of $K_0(t)$ and $K_1(t)$ as 0.2 and 0.3, respectively. The parameters defined in Eq. (3.3.2) are evaluated as $\gamma = 4.87$, $\alpha = 0.22$, and $\zeta = -2.1$.

Using the estimated values of γ, α, and ζ, we confirm the estimates of γ_1, γ_2, γ_3, and γ_4 given in Eq. (3.3.12). For the log plot of the normalized momentum autocorrelation function $C(t)/C(0)$ versus t, linear regression is performed and the slope and intercept are obtained. The time interval for the linear regression is chosen such that the lower endpoint is set as $\tau_0 + \tau_1 = 0.5$ and the upper endpoint is chosen as the time when $C(t)$ decays to one half of the initial value. For $M = 100$, the half-life is longer than $t = 10$ and time interval $[0.5, 10]$ is used instead. The prefactor of the exponential decay of $C(t)/C(0)$ at large times is estimated from the intercept and

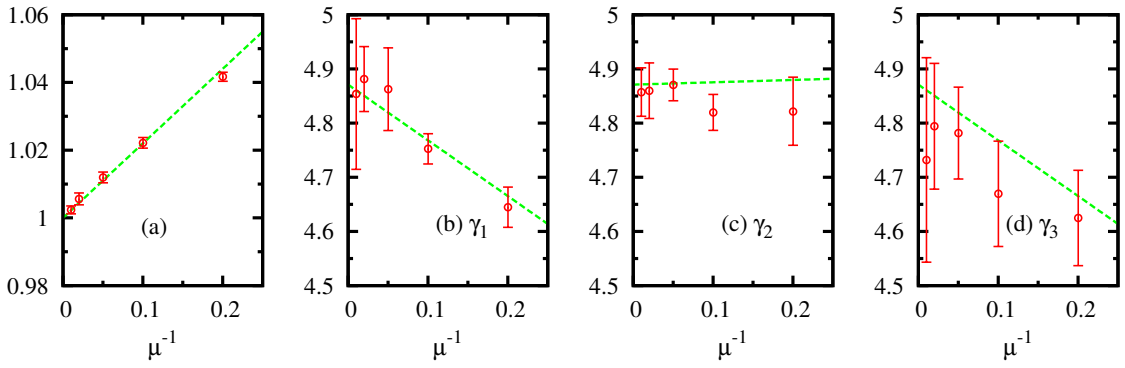

Figure 3.4: For Case A with the WCA potential, the prefactor of the exponential decay of the normalized momentum autocorrelation function at large times is plotted versus the reciprocal of the reduced mass μ in panel (a). The values of γ_1, γ_2, and γ_3 are plotted versus μ^{-1} in panels (b), (c), and (d), respectively. All values are obtained from the linear regression of $\log(C(t)/C(0))$ or $\log\left|\dot{C}(t)\right|$. For details, see the text. The error bars corresponding to 3σ are also plotted. The green dotted line in each panel is the theoretical prediction: for (a), $1+\alpha/\mu$ and for (b), (c), and (d), see Eq. (3.3.12).

plotted versus μ^{-1} in panel (a) of Figure 3.4. The dependence of the prefactor on μ is explained very well by $1+\alpha/\mu$, which is obtained from Eq. (3.3.10). From the slope of the linear regression, the value of γ_1 is estimated by using Eq. (3.3.10) and plotted in panel (b) of Figure 3.4. As predicted by Eq. (3.3.12), it is observed that as M increases, the value of γ_1 converges to the value of γ and the deviation is proportional to μ^{-1}. For the momentum-force correlation function $\dot{C}(t) = \langle \mathbf{P}(0)\cdot\mathbf{F}(t)\rangle$, linear regression is performed to its log plot using the same time interval as the normalized momentum autocorrelation function. Using Eq. (3.3.11), the values of γ_2 and γ_3 are estimated from the intercept and slope of the linear regression and plotted in panels (c) and (d) of Figure 3.4, respectively. Their asymptotic behavior is well explained by Eq. (3.3.12). Although the values 2α and ζ/γ, which appears in the estimate of γ_2, happen to cancel each other so we cannot accurately estimate the value $2\alpha+\zeta/\gamma$, it is clearly seen that the slope of the deviation $(\gamma_2-\gamma)$ with respect to μ^{-1} is different

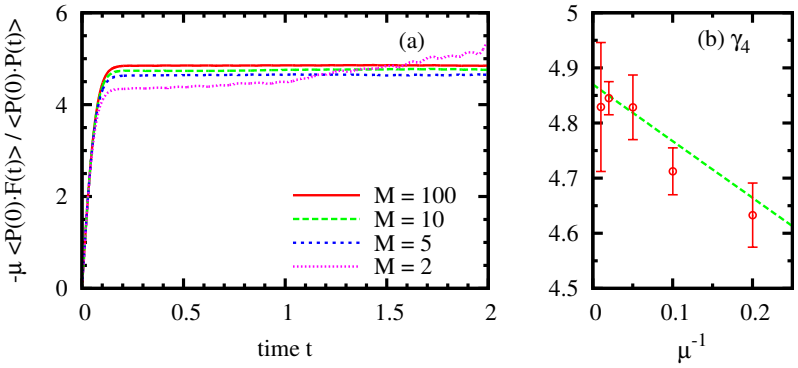

Figure 3.5: For Case A with the WCA potential, the instantaneous exponential decay rate $-\dot{C}(t)/C(t)$ normalized by the reduced mass μ is plotted, in panel (a), for various values of the mass M of the Brownian particle. The plateau values in panel (a), which correspond to γ_4, are plotted, with the error bars corresponding to 3σ, versus the values of μ^{-1} in panel (b). The dotted green line in panel (b) indicates the prediction of Eq. (3.3.12).

from that of γ_1 and γ_3.

Next, we compile the instantaneous exponential decay rate $-\dot{C}(t)/C(t)$. In the left panel of Figure 3.5, its time profiles for various values of M are plotted. The instantaneous exponential decay rate attains a plateau after some time which corresponds to $\tau_0 = 0.2$. As M increases, the plateau value, which is normalized by factor μ, increases and approaches to the value of γ. Using the same time interval as the above cases, an extrapolated value at $t = 0$ is obtained from linear regression for each value of M. It is noted that for linear regression, we use $-\dot{C}(t)/C(t)$ itself rather than its logarithm in this case. In the right panel of Figure 3.5, these extrapolated values, which correspond to γ_4, are plotted versus μ^{-1}. The convergence of γ_4 to γ is well explained by Eq. (3.3.12). It is also clearly seen that the asymptotic behavior of γ_4 is very similar to those of γ_1 and γ_3.

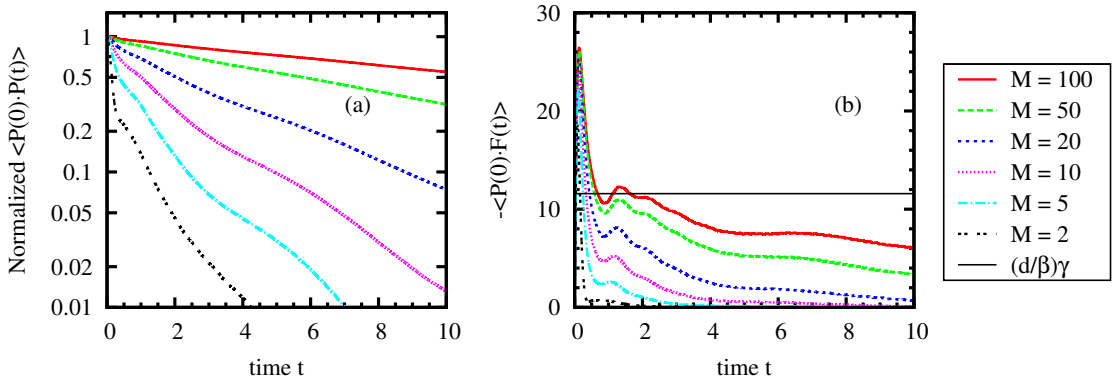

Figure 3.6: For Case A with the LJ potential, the normalized momentum autocorrelation function $C(t)/C(0)$ and the negative of the momentum-force correlation function, $-\dot{C}(t)$, are plotted in panels (a) and (b), respectively, for various values of the mass M of the Brownian particle. The plateau value $\frac{d}{\beta}\gamma$ is also plotted as a black solid line in panel (b). Note that the vertical axis in panel (a) is logarithmic scale.

3.4.3 Case A with LJ potential

We first compare the decay behavior of the time correlation functions in the LJ potential case with that of the WCA potential case. In Figure 3.6, the normalized momentum autocorrelation function and the momentum-force correlation functions are shown for various values of M. Although the decay rate decreases as M increases in both correlation functions, the decay is far from being a pure exponential decay. This implies that $K(t)$ has a tail and the microscopic structure of $K(t)$ affects the time correlation functions even at large times.

In Figure 3.7, the time profiles of $K(t)$ are shown for various of values of M, as well as $K_0(t)$ and $K_1(t)$. Convergence of $K(t)$ to $K_0(t)$ is clearly observed for increasing values of M, and the time profiles of $K_1(t)$ obtained from the results for $M = 5$ and 10 agree very well with each other, which confirms our assumption on the asymptotic form of $K(t)$, Eq. (3.2.20). However, the time scales τ_0 and τ_1 cannot

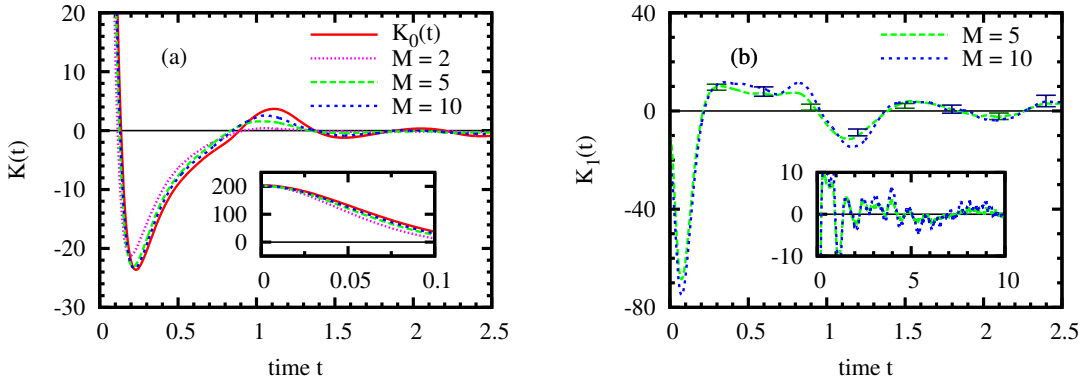

Figure 3.7: For Case A with the LJ potential, the time profiles of the Mori memory function $K(t)$ are plotted for various values of the mass M of the Brownian particle in panel (a). The limit $K_0(t) = \lim_{\mu\to\infty} K(t)$ is also plotted. In the inset, the main peak of $K(t)$ at short times is plotted. In panel (b), the time profiles of $K_1(t)$, which are obtained by using the results of $M = 5$ and $M = 10$, are plotted with the error bars corresponding to 3σ. In the inset, the tails of $K_1(t)$ are plotted.

be clearly defined in this case; $K_0(t)$ has an oscillating tail due to the effect of the trapped bath particles to the potential well of the LJ potential [96] and it is observed that $K_1(t)$ also has an oscillating tail.

Since both the exponential decay and the influence of the microscopic structure affect the time correlation functions over the whole time interval of our observation, we fail to accurately estimate the values of γ_1, γ_2, and γ_3. These values vary for different choices of the time interval for the curve fitting since the time correlation functions do not exhibit a pure exponential decay. However, for γ_4, it is expected that the effect of the exponential decay disappears or is reduced significantly since the exponential decay of $C(t)$ and $\dot{C}(t)$ may cancel in the instantaneous exponential decay rate, $-\dot{C}(t)/C(t)$. In Figure 3.8, the instantaneous exponential decay rate is plotted for various values of M. It does not exhibit an exponential decay and at large times it starts to form a plateau. For $M = 100$, the instantaneous exponential decay rate is calculated up to $t = 20$ and it is confirmed that it attains a plateau. In

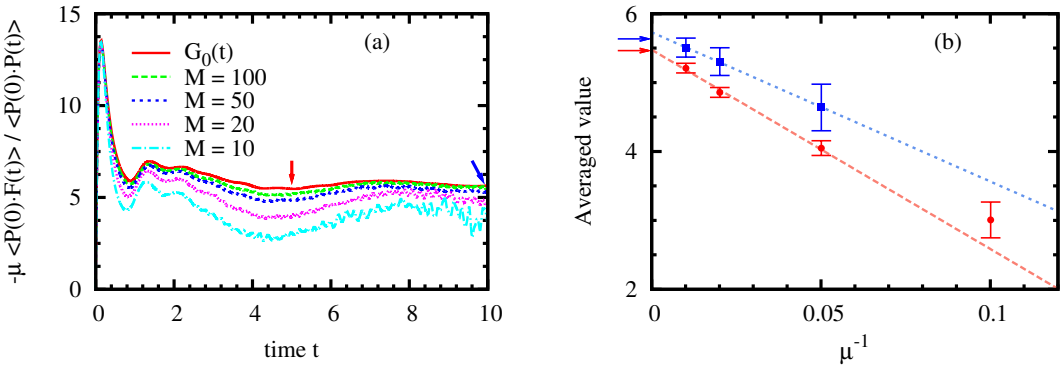

Figure 3.8: For Case A with the LJ potential, the instantaneous exponential decay rate $-\dot{C}(t)/C(t)$ normalized by factor μ is plotted for various values of the mass M of the Brownian particle in panel (a). The time integral of $K_0(t)$, i.e., $G_0(t)$, is also plotted. As M increases, the deviation of $-\mu\dot{C}(t)/C(t)$ from $G_0(t)$ is observed to decrease like $\mathrm{O}(\mu^{-1})$ for all points on the time axis. Two time points $t = 5$ and $t = 10$, representative of the cases $t < \tau_0$ and $t \approx \tau_0$, are chosen and their values $-\mu\dot{C}(t)/C(t)$ versus μ^{-1} are plotted with corresponding linear regressions in panel (b). To reduce statistical errors, the time-averaged values of $-\mu\dot{C}(t)/C(t)$ over short time intervals [5,5.1] and [9.9,10] are used. The error bars correspond to 3σ. The blue square for $t = 10$ and $M = 10$ is omitted since the value is not reliable due to large decay of $C(t)$ and $\dot{C}(t)$. The arrows in panel (a) indicate the location of the time points ($t = 5$ for the red one and $t = 10$ for the blue one) where two sets of data in panel (b) are obtained, whereas the arrows at the vertical axis in panel (b) indicate the corresponding values of $G_0(t)$.

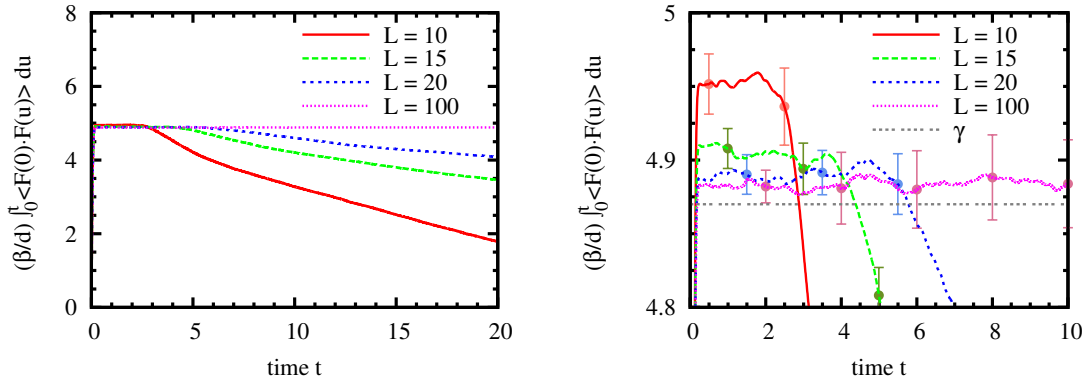

Figure 3.9: For Case B (with the WCA potential), $-\dot{C}(t)$ evaluated from the time integral of the force autocorrelation function is plotted for various values of the box size L in panel (a). In panel (b), the same quantity is plotted near the value of γ, which is plotted as a gray dotted line. It is noted that the error bars corresponding to σ rather than 3σ are plotted for clear presentation.

addition, as predicted from Eqs. (3.3.20) and (3.3.21), it is observed that for each t, $-\dot{C}(t)/C(t)$ approaches $G_0(t)$, which is the time integral of $K_0(t)$, as M increases. The deviation is inversely proportional to the reduced mass μ.

3.4.4 Case B

We first observe a characteristic behavior of $\dot{C}(t)$ in the frozen dynamics of the Rayleigh gas system. Figure 3.9 shows the time profiles of $-\dot{C}(t)$ for various values of the simulation box size L. We use the values of $\dot{C}(t)$ obtained from the time integral of the force autocorrelation function rather than those obtained from the momentum-force correlation function since the latter contain much larger statistical errors than the former. This is because the momentum of the Brownian particle is defined as the negative of the total momentum of the bath particles and thus its variance is very large in this case. Contrary to Case A, we observe that $\dot{C}(t)$ attains a plateau before it starts to decay. For $L = 10$, 15, and 20, the duration of

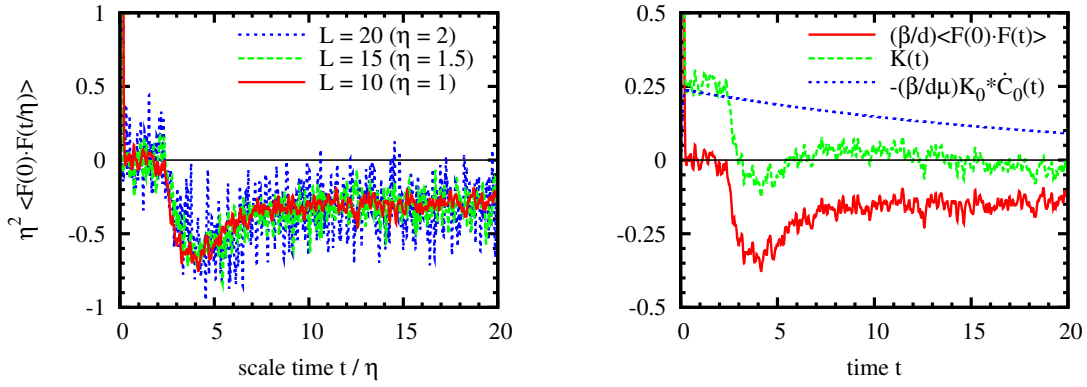

Figure 3.10: For Case B, the time profiles of the force autocorrelation function for various values of the box size L are plotted in panel (a). Following Eq. (3.2.29), scaled time t/η and scaling factor η^2 are used. In panel (b), the tails of the force autocorrelation and the Mori memory function for $L = 10$ are compared. The time profile of $K_0 * \dot{C}_0(t)$ is also plotted.

exhibiting such a plateau is proportional to L and the plateau value becomes closer to the value of γ as the system size increases. The deviation of the plateau value from γ is observed to be inversely proportional to L^2. It is also observed that even after the plateau region, $\dot{C}(t)$ does not exhibit a clear exponential decay.

As mentioned in Section 3.2.5.2, this characteristic behavior of $\dot{C}(t)$ is explained by the tail of the force autocorrelation function which develops in the finite-size Rayleigh gas system. In the left panel of Figure 3.10, the time profiles of the force autocorrelation function for $L = 10$, 15, and 20 are compared by using scaled time t/L and scaling factor L^2. The scaled tails show good agreement with each other, which confirms Eq. (3.2.29). In the right panel of Figure 3.10, the Mori memory function is compared with the force autocorrelation function for $L = 10$. The overall shape of $K(t)$ is similar to $\langle \mathbf{F}(0) \cdot \mathbf{F}(t) \rangle$ and it is lifted by $-\frac{\beta}{d\mu} K_0 * \dot{C}_0(t)$ as predicted from Eq. (3.2.31).

For larger values of L, the decay is not observed and the momentum-force cor-

relation function maintains the plateau up to $t = 10$, which is the maximum time of our observation. In this case, the momentum autocorrelation function exhibits a pure exponential decay.

3.5 Summary and discussion

For a Brownian particle suspended in a bath, corrections to the (t, μ)-asymptotic expressions of $\langle \mathbf{P}(0) \cdot \mathbf{P}(t) \rangle$ and $\langle \mathbf{P}(0) \cdot \mathbf{F}(t) \rangle$, Eqs. (3.1.1a) and (3.1.1b), have been obtained in Eqs. (3.3.10) and (3.3.11). Using these corrections, it has been shown that various numerical methods which estimate the value of the friction coefficient γ using the exponential decay of the time correlation functions at large times, produce $\gamma + O(\mu^{-1})$, see Eq. (3.3.12).

To obtain these results, the asymptotic expansion of $C(t) = \langle \mathbf{P}(0) \cdot \mathbf{P}(t) \rangle$, Eq. (3.2.24), has been derived by solving the Volterra integro-differential equation, Eq. (3.2.8), and by introducing the asymptotic expansion of the Mori memory function $K(t)$. The lowest-order term $C_0(t)$ in the asymptotic expansion of $C(t)$ is defined in terms of the Mori memory function $K_0(t)$ of the infinite reference system. $C_0(t)$ itself is given as a series of convolution powers and higher-order terms in the asymptotic expansion of $C(t)$ are given as multiple convolutions of $C_0(t)$ with higher-order terms in the asymptotic expansion of $K(t)$.

By introducing time scales τ_0 and τ_1 of $K_0(t)$ and $K_1(t)$, (t, μ)-asymptotic expressions of $C_0(t)$ and $C(t)$, Eqs. (3.3.8) and (3.3.10), have been derived. However, owing to a feature of convolution, each term in the asymptotic expansion of $C_0(t)$ and $C(t)$ has different length of transient time before it exhibits a t-asymptotic behavior,

and hence the time intervals, where the asymptotic expressions are valid, become questionable. To address this issue, lower-order terms in the asymptotic expansions of $C(t)$ and $\dot{C}(t)$ have been analyzed and the validity time intervals for the *linear* decay expressions, Eqs. (3.3.15) and (3.3.18), have been found. The lower endpoint of the time intervals is determined by τ_0 and τ_1, whereas the upper endpoint is given by the condition $\frac{\gamma}{\mu}t \ll 1$. However, it is noted that our result does not imply that the *exponential* decay behavior is only valid in these intervals. Our analysis demonstrates one of the essential reasons that the evaluation of the friction coefficient is not straightforward; there are two limits involved (i.e., the Brownian limit and the long time limit) and they are not interchangeable with each other. Since it is virtually impossible to simulate the infinite reference system using MD simulation technique, Eq. (3.2.16) cannot be used as it is from MD simulations. Instead, a finite system corresponding to a large value of μ is simulated and a long-time behavior in a certain time interval is observed. As shown in our analysis, an appropriate choice of the time interval depends on not only the microscopic times t_0 and t_1 but also the condition determined by the value of μ.

For a Rayleigh gas under the WCA potential, which satisfies the time scale assumption, the theoretical predictions have been confirmed by a systematic MD simulation study. In particular, as predicted from Eq. (3.3.12), γ_2 has been shown to have a different first-order correction from those of γ_1, γ_3, and γ_4. Then, to observe a case where the assumption of the time scales fails, a counterpart system under the LJ potential has been investigated. Due to the influence of the oscillating tail, it has been observed that the decay is not clearly exponential even at large times and accurate evaluation of γ_1, γ_2, and γ_3 fail. However, the normalized instantaneous exponential decay rate defined as $-\mu\dot{C}(t)/C(t)$ has been observed to have the following favorable features which makes γ_4 be a practically better measure of γ rather

than γ_1, γ_2, and γ_3: first, the quantity does not exhibit an exponential decay and eventually forms a plateau; second, it is easily calculated from the time correlation functions; third, for each t, it converges to the time integral of the Mori memory function up to time t as $\mu \to \infty$, see Eqs. (3.3.20) and (3.3.21).

Our approach is new in the sense that the Mori memory function is employed and explicit dependence of the time correlation functions in the near-Brownian-limit regime on the memory function is determined. A close connection of the Mori memory function to the Brownian motion theory has been pointed out from several points of view [51, 89, 103]. Compared with Mazur and Oppenheim's memory function, Mori's memory function $K(t)$ can be relatively easily calculated from the time correlation functions. However, since its analytic properties are not so favorable as those of the former [89], determining an asymptotic expansion of $K(t)$ may not be straightforward and some physical arguments or numerical experiments are needed. For the infinite mass limit (i.e., Case A), by previous theoretical analysis [89, 131], a simple form, Eq. (3.2.20), has been found. As a *counter* example, we have considered the frozen dynamics of the Rayleigh gas in a finite bath. We have demonstrated that due to the boundary conditions $\dot{C}(t)$ exhibits a characteristic behavior, which is not explained by the asymptotic expression of $C_0(t)$, and $K(t)$ has a different form from Case A. Considering that several MD simulation studies have performed frozen dynamics simulations and determined the value of γ by using Eq. (3.1.1), a future investigation on asymptotic behavior of the time correlation functions along the thermodynamic limit is called for.

In this chapter, we have analyzed one of the prototypical systems where multiscales are present and play an important role. Our work has provided a method of evaluating the friction coefficient γ in a systematic manner. A precise evaluation of γ is essential for mesoscopic simulation methods such as Langevin/Brownian

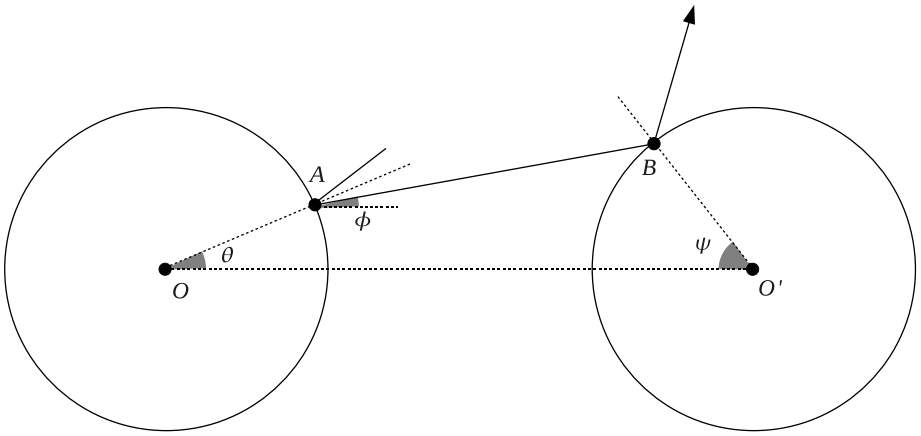

Figure 3.11: A typical trajectory of a bath particle sequentially colliding with the fixed Brownian particle at the origin O and its image at O'. The Brownian particle and its image are represented as disks of radius R and the bath particle elastically collides at points A and B. The angles $\angle AOO'$ and $\angle BO'O$ and the angle between $\overline{AB}$ and the horizontal line are denoted as θ, ψ and ϕ, respectively. While θ and ϕ are anticlockwise angles from the horizontal lines, ψ is a clockwise angle. It is assumed that the separation L between the Brownian particle and its image is much larger than R.

dynamics and dissipative particle dynamics. Since the time scale of the Brownian motion is not completely separated from that of the surrounding fluid particles in the phenomena simulated by these methods, consideration of the asymptotic behavior of the time correlation function of the Brownian particle at microscopic times will help to develop a more realistic model.

3.6 Appendix

The scaling property of the tail present in the force autocorrelation function due to the re-collisions of bath particles to the periodic images of the Brownian particle is derived for a finite-volume Rayleigh gas under periodic boundary conditions, where the fixed Brownian particle interacts with the gas through elastic collisions. By considering a bath particle colliding with the Brownian particle and subsequently

with its periodic image, we calculate the autocorrelation function of the force exerted on the Brownian particle or its image by the bath particle. The scaling parameter is the separation distance L between the Brownian particle and its image, which is assumed to be much larger than the radius R of the Brownian particle. We first consider the two-dimensional case and then discuss the general case.

For simplicity, we assume that there is a single image. We denote the positions of the Brownian particle and its image by $O(0,0)$ and $O'(L,0)$, respectively. By introducing θ and ψ, we denote the points at which the bath particle collides with the Brownian particle and its image as $A(R\cos\theta, R\sin\theta)$ and $B(L - R\cos\psi, R\sin\psi)$, respectively (see Figure 3.11). We also denote the angle formed by the line $\overline{AB}$ and the horizontal line as ϕ and its possible range as $\phi_1 < \phi < \phi_2$. Since $\lim_{L\to\infty} L\phi_1 = -R(1+\sin\theta)$ and $\lim_{L\to\infty} L\phi_2 = R(1-\sin\theta)$, we have $\phi = \mathrm{O}(L^{-1})$. By denoting the magnitude of the bath particle's velocity as v and the time duration that it moves from A to B as t_{AB}, vt_{AB} satisfies $(R\cos\theta + vt_{AB}\cos\phi - L)^2 + (R\sin\theta + vt_{AB}\sin\theta)^2 = R^2$. Since $vt_{AB} = L + \delta x$ with $\delta x = \mathrm{O}(1)$ for large L, we obtain $\delta x = -R\cos\theta - \sqrt{R^2 - (R\sin\theta + L\phi)^2} + \mathrm{O}(L^{-1})$. Hence, we obtain an expression for ψ in terms of θ and ϕ: $\sin\psi = \sin\theta + \frac{L\phi}{R} + \mathrm{O}(L^{-1})$.

The impulses exerted on the bath particle during the collisions at A and B are expressed as $\mathbf{I}_A = 2mv\cos(\theta-\phi)(\cos\theta, \sin\theta)$ and $\mathbf{I}_B = 2mv\cos(\psi+\phi)(-\cos\psi, \sin\psi)$, respectively. By denoting the time when the bath particle collides at A by t_A, the force it exerts on the Brownian particle or its image is expressed as $\mathbf{F}(t) = -\mathbf{I}_A\delta(t - t_A) - \mathbf{I}_B\delta(t - t_A - t_{AB})$. Hence, we have $\langle \mathbf{F}(0)\cdot\mathbf{F}(t)\rangle = \langle |\mathbf{I}_A|^2\delta(-t_A)\delta(t-t_A)\rangle + \langle \mathbf{I}_A\cdot\mathbf{I}_B\delta(-t_A)\delta(t-t_A-t_{AB})\rangle \equiv c_1(t) + c_2(t)$. The first term $c_1(t)$ corresponds to the result for the infinite reference system (i.e., without the image of the Brownian particle), whereas the second term $c_2(t)$ is the contribution of the re-collision to the image. Following a similar procedure demonstrated

in [96], the ensemble averages $c_1(t)$ and $c_2(t)$ are obtained by averaging with respect to the equilibrium distribution of the initial condition of the bath particle. We denote the initial position and velocity as $(r\cos\chi, r\sin\chi)$ and $(v\cos\omega, v\sin\omega)$, respectively, and assume that the equilibrium measure is approximated by that of the infinite reference system [i.e., $(a\mathbb{I}_{\{r\geq R\}}rdrd\chi)(\frac{m\beta}{2\pi}e^{-\frac{1}{2}\beta mv^2}vdvd\omega)$ with a the number density of bath particles], which becomes valid for $r \ll L$ and $R \ll L$. By using that $\delta(t_A) = v|\cos(\chi-\omega)|\delta(r-R)$ for $\frac{1}{2}\pi+\chi < \omega < \frac{3}{2}\pi+\chi$, we perform integration with respect to r and consider $r \to R+$ for the remaining integration with respect to χ, ω, and v. By symmetry, we only need to consider the case $0 < \chi < \frac{\pi}{2}$ and multiply by factors 4 and 2 for $c_1(t)$ and $c_2(t)$, respectively. We have $\theta \to \chi$ and $\phi \to 2\chi-\omega-\pi$ as $r \to R+$. Through the following integration

$$4m^2aR\left(\int_0^\infty \frac{m\beta}{2\pi}v^4e^{-\frac{1}{2}\beta mv^2}dv\right)\left(4\int_0^{\frac{\pi}{2}}d\chi\int_{\chi+\frac{1}{2}\pi}^{\chi+\frac{3}{2}\pi}|\cos(\chi-\omega)|^3d\omega\right)\delta(t), \quad (3.6.1)$$

we obtain $c_1(t) = \frac{8aR}{\beta}\sqrt{\frac{2\pi m}{\beta}}\delta(t)$, which leads to the friction coefficient $\gamma = 2aR\sqrt{\frac{2\pi m}{\beta}}$ for the infinite reference system [96].

In order to estimate $c_2(t)$, we note that the interval of ω for the re-collision is of length $\mathrm{O}(L^{-1})$ from the constraint $\phi_1 < \phi < \phi_2$. Since $\omega \in (2\chi-\pi-\frac{R}{L}(1-\sin\chi), 2\chi-\pi+\frac{R}{L}(1+\sin\chi))$, we approximate the integrand by its value at $\omega_0 = 2\chi-\pi$ and consider the width of the interval $\Delta w = \frac{2R}{L}$. We note that ω_0 corresponds to the case that the trajectory of the bath particle from A to B is parallel to the horizontal line. Then, $\mathbf{I}_A\cdot\mathbf{I}_B$ is approximated by $-4m^2v^2\cos^2\chi\cos 2\chi$, whereas $\delta(t_A)$ is by $v\cos\chi\delta(r-R)$. On the other hand, since $t_A \to 0$ as $r \to R+$, $\delta(t-t_A-t_{AB})$ can be replaced by $\delta(t-t_{AB})$ in the integrand, which is further approximated by

$\delta(t-\frac{L}{v}) = \frac{L}{t^2}\delta(v-\frac{L}{t})$. Hence, through the following integration

$$-4m^2aR\left(\frac{L}{t^2}\int_0^\infty \frac{m\beta}{2\pi}v^4 e^{-\frac{1}{2}\beta m v^2}\delta\left(v-\frac{L}{t}dv\right)\right)\left(2\Delta w\int_0^{\frac{\pi}{2}}\cos^3\chi\cos 2\chi d\chi\right), \tag{3.6.2}$$

we finally obtain

$$c_2(t) \approx -\frac{16aR^2m^3\beta}{5\pi L^2}\left(\frac{L}{t}\right)^6 e^{-\frac{1}{2}m\beta\left(\frac{L}{t}\right)^2}. \tag{3.6.3}$$

Hence, $c_2(t)$ has a form of $L^{-2}f\left(\frac{t}{L}\right)$.

For the three dimensional case, the integration with respect to two spherical angles for the initial velocity gives $\mathrm{O}(L^{-2})$ dependence. This is because in order for the bath particle to collide with the image, both angles should be in narrow intervals of length $\mathrm{O}(L^{-1})$. The integration with respect to the magnitude v of the bath particle's velocity gives the same form of the L-dependence as in the two-dimensional case. That is, integrating $g(v)\delta(t-t_A-t_{AB})$ with respect to v gives $\frac{L}{t^2}g(\frac{L}{t})$. Hence, we obtain $L^{-3}f(\frac{t}{L})$.

Chapter Four

Microscopic Theory of Brownian Motion

4.1 Introduction

Brownian motion, a random movement caused by thermal agitation of the surrounding particles, is a phenomenon pervasively observed in many fields of science [60]. Leaving aside its traditional fields such as physics and chemistry, it has been realized that Brownian motion provides an efficient transport mechanism for many biological functions at the cellular and subcellular level [177] and plays an important role in the movement and chemotaxis of microorganisms [125, 119]. Although in many experimental studies Brownian motion is considered as something to be suppressed or controlled for better observations [25], its use as a probing tool investigating topological and rheological properties of soft materials has been of great interest [181, 165].

Spatial and temporal resolutions of observing Brownian motion have been greatly increased, and the transition from ballistic to diffusive Brownian motion has been observed in gases [11, 120] and in liquids [126, 87]. For Brownian motion in a gas, it has been shown that the standard Langevin description explains very well experimental results. On the other hand, for Brownian motion in a liquid, where the densities of the Brownian particle and the fluid are comparable, the hydrodynamic memory effect by the inertia of the surrounding fluid cannot be neglected [160]. Hence, the thermal noise is no more assumed to be white and its color has been experimentally determined [56, 90]. However, we note that direct observation of Brownian motion on the time scale of molecular collisions is still experimentally infeasible.

Macroscopically, a moving object immersed in a fluid experiences a friction force with the friction coefficient defined as the ratio of the friction force to the moving velocity. In contrast, at the microscopic level, the total force $\mathbf{F}$ on a Brownian

particle can be decomposed as:

$$\mathbf{F} = \mathbf{F}_{\text{ext}} + \mathbf{F}_{\text{fr}} + \mathbf{F}_{\text{th}}, \tag{4.1.1}$$

where $\mathbf{F}_{\text{ext}}$ denotes the force due to any external potential and $\mathbf{F}_{\text{fr}}$ and $\mathbf{F}_{\text{th}}$ denote the friction force and the thermal noise exerted by the surrounding fluid, respectively. Specifically, $\mathbf{F}_{\text{fr}}$ describes the collective motion of the surrounding fluid, whereas $\mathbf{F}_{\text{th}}$ reflects the randomness of each interacting fluid particle. Despite their different characters, they share the same origin, i.e., the interaction between the Brownian particle and the fluid, and hence they are related by the fluctuation-dissipation relation [107]. This form of force decomposition is adopted by mesoscopic simulation methods such as Langevin/Brownian dynamics [161, 168] and dissipative particle dynamics [72] with simplified forms of $\mathbf{F}_{\text{fr}}$ and $\mathbf{F}_{\text{th}}$.

In the Langevin equation (assuming $\mathbf{F}_{\text{ext}} = 0$)

$$\mathbf{F}(t) = -\gamma \mathbf{V}(t) + \sqrt{\Delta}\dot{\mathbf{W}}_t, \tag{4.1.2}$$

$\mathbf{F}_{\text{fr}}$ is assumed to be linearly proportional to the instantaneous velocity $\mathbf{V}$ of the Brownian particle with γ the friction coefficient, while $\mathbf{F}_{\text{th}}$ is given as independent Gaussian white noise with Δ the noise intensity and $\mathbf{W}$ the standard Wiener process. This Markovian approximation is valid only on the time scale of the Brownian particle and only in the Brownian limit, i.e., when the mass ratio of the Brownian particle to a fluid particle tends to infinity. Microscopic justification of the phenomenological Langevin equation has been presented in [30, 51, 112, 113, 131, 158]. In the corresponding generalized Langevin equation derived by Mori [140],

$$\mathbf{F}(t) = -\int_0^t K(t-s)\mathbf{V}(s)ds + \mathbf{F}^+(t), \tag{4.1.3}$$

$\mathbf{F}_{\rm fr}$ is defined as the convolution of $\mathbf{V}$ with the memory function $K(t)$ and $\mathbf{F}_{\rm th}$ is given as the fluctuating force $\mathbf{F}^{+}$. Eq. (4.1.3) is obtained by the projection operator technique [68]; it is formally exact and, hence, it is valid on *all* time scales. However, despite its appealing form, which heuristically suggests Eq. (4.1.2) through the Markovian approximation in the Brownian limit, investigating the microscopic structure of the memory function $K(t)$ is not straightforward [89].

In this chapter, we investigate Eq. (4.1.1) on the microscopic time scale for the system in the near-Brownian-limit regime. More specifically, we propose a force decomposition of the total force on the Brownian particle, which leads to new interpretation of $\mathbf{F}_{\rm fr}$ and $\mathbf{F}_{\rm th}$. Compared with traditional approaches [30, 112, 113, 131, 158] which employ formal operator algebra, we introduce two types of dynamics (the frozen dynamics and the constant-velocity dynamics) and explain the form of $\mathbf{F}_{\rm fr}$ and $\mathbf{F}_{\rm th}$ in the near-Brownian-limit regime. Through this approach, we obtain not only well-known results for the Brownian limit but also higher-order corrections for finite mass ratio. In Section 4.2, we first present our theoretical results. In Section 4.3, we provide our MD simulation results. In Section 4.4, we conclude the chapter with a brief discussion.

4.2 Theoretical Results

We describe the system and introduce a conditional expectation based on assumptions on the equilibrium distribution of the system. Under this setup, we propose a force decomposition and obtain asymptotic expansions of the time correlation functions. Our approach is also applied to the pulling experiment of an object in a fluid and previously known results are derived. Finally, from the comparison with the

memory function approach, we obtain asymptotic expansions for the friction force and the thermal noise.

4.2.1 Microscopic model for Brownian motion of a single particle

We follow the standard setting for a Brownian particle suspended in a bath [131, 51]. In addition, we assume that the bath is unbounded. The mass M of the Brownian particle is finite but much larger than the mass m of a bath particle. We first describe this finite-mass dynamics and then, in order to approximate it, we introduce two types of the *infinite-mass* dynamics.

The position and velocity of the Brownian particle are denoted by $\mathbf{X}$ and $\mathbf{V}$, respectively, whereas the position and velocity of the i-th bath particle are denoted by $\mathbf{x}^{(i)}$ and $\mathbf{v}^{(i)}$, respectively. Collectively, the positions and velocities of bath particles are denoted by $\mathbf{x} = \{\mathbf{x}^{(i)}\}$ and $\mathbf{v} = \{\mathbf{v}^{(i)}\}$, respectively. The Brownian particle interacts with a bath particle through the interaction potential U_1, while the interaction potential between bath particles is denoted by U_2. The time evolution of the system follows the Newtonian dynamics. The initial condition $\{\mathbf{X}(0), \mathbf{V}(0), \mathbf{x}(0), \mathbf{v}(0)\}$ is assumed to be sampled from the equilibrium distribution and the trajectory of the system at time t is denoted by $\{\mathbf{X}(t), \mathbf{V}(t), \mathbf{x}(t), \mathbf{v}(t)\}$. To distinguish this dynamics from the two types of infinite-mass dynamics to be defined below, we call it the *full* dynamics.

If the Brownian particle has an infinite mass, its motion would not be affected by collisions with bath particles and thus its trajectory can be specified irrespective of the motion of the bath particles. In order to approximate the trajectory $\{\mathbf{X}(t), \mathbf{V}(t)\}$

by some infinite-mass dynamics trajectories, we note that for large M, $\mathbf{V}(t)$ is very small and does not change very much. Rough estimates give that $|\mathbf{V}(t)|$ is $\mathrm{O}(M^{-1/2})$ from the equipartition theorem, see Eq. (4.2.4), and that the velocity autocorrelation function $\langle \mathbf{V}(0) \cdot \mathbf{V}(t) \rangle$ decays in time as $\langle \mathbf{V} \cdot \mathbf{V} \rangle \, e^{-\gamma t/M}$ from Eq. (4.1.2). Hence, the crudest approximation is given as $\mathbf{X}_0(t) = \mathbf{X}(0)$ and $\mathbf{V}_0(t) = 0$, which means that the Brownian particle is assumed to be fixed at the initial position $\mathbf{X}(0)$. A more accurate approximation is that the Brownian particle moves at a constant velocity $\mathbf{V}(0)$, i.e., $\mathbf{X}_1(t) = \mathbf{X}(0) + t\mathbf{V}(0)$ and $\mathbf{V}_1(t) = \mathbf{V}(0)$. Under the infinite-mass dynamics provided with the specified trajectory $\{\mathbf{X}_k(t), \mathbf{V}_k(t)\}$ ($k = 0$ or 1), the bath particles move under the external potential due to the presence of the Brownian particle and the bath trajectory is denoted by $\{\mathbf{x}_k(t), \mathbf{v}_k(t)\}$. We call the case with $k = 0$ as the *frozen* dynamics, whereas for $k = 1$ as the *constant-velocity* dynamics. The initial condition $\{\mathbf{x}_k(0), \mathbf{v}_k(0)\}$ of the bath for both infinite-mass dynamics is given as $\{\mathbf{x}(0), \mathbf{v}(0)\}$.

The forces on the Brownian particle in the full, frozen, and constant-velocity dynamics are denoted by $\mathbf{F}(t)$, $\mathbf{F}_0(t)$, $\mathbf{F}_1(t)$, respectively. We note that they are completely determined by the initial condition $\{\mathbf{X}(0), \mathbf{V}(0), \mathbf{x}(0), \mathbf{v}(0)\}$ and $\mathbf{F}(0) = \mathbf{F}_0(0) = \mathbf{F}_1(0)$.

Through their Hamiltonians, the time evolution of these dynamics can be obtained. The Hamiltonians are written as

$$H(\mathbf{x}, \mathbf{p}, \mathbf{X}, \mathbf{P}) = \frac{1}{2m}\mathbf{p}\cdot\mathbf{p} + \frac{1}{2M}\mathbf{P}\cdot\mathbf{P} + \sum_i U_1(\mathbf{x}^{(i)} - \mathbf{X}) + \sum_i \sum_{j>i} U_2(\mathbf{x}^{(i)} - \mathbf{x}^{(j)}) \quad (4.2.1)$$

for the full dynamics, and

$$H_k(\mathbf{x}, \mathbf{p}, t) = \frac{1}{2m}\mathbf{p} \cdot \mathbf{p} + \sum_i U_1(\mathbf{x}^{(i)} - \mathbf{X}_k(t)) + \sum_i \sum_{j>i} U_2(\mathbf{x}^{(i)} - \mathbf{x}^{(j)}) \quad (4.2.2)$$

for the frozen dynamics ($k = 0$) and the constant-velocity dynamics ($k = 1$). Here, $\mathbf{P} = M\mathbf{V}$ and $\mathbf{p} = m\mathbf{v}$. For the two types of the infinite-mass dynamics, the forces on the Brownian particle are expressed as $\mathbf{F}_k(t) = \sum_i \nabla U_1(\mathbf{x}_k^{(i)}(t) - \mathbf{X}_k(t))$ and the equations of motion of the bath particles are given as

$$m\ddot{\mathbf{x}}_k^{(i)}(t) = -\nabla U_1\left(\mathbf{x}_k^{(i)}(t) - \mathbf{X}_k(t)\right) - \sum_{j\neq i} \nabla U_2\left(\mathbf{x}_k^{(i)}(t) - \mathbf{x}_k^{(j)}(t)\right), \tag{4.2.3}$$

For the full dynamics, we have expressions of the same forms for the force $\mathbf{F}(t)$ and the equations of motion of the bath particles, where $\mathbf{x}_k^{(i)}(t)$ and $\mathbf{X}_k(t)$ are replaced with $\mathbf{x}^{(i)}(t)$ and $\mathbf{X}(t)$.

4.2.2 Equilibrium distribution and conditional expectation

We sample the initial condition $\{\mathbf{X}(0), \mathbf{V}(0), \mathbf{x}(0), \mathbf{v}(0)\}$ from the equilibrium distribution of the full dynamics, on which we make the following assumptions. First, the distribution is completely decomposed into that of $\mathbf{V}$ and that of the other variables. By denoting $\Theta = \{\mathbf{X}, \mathbf{x}, \mathbf{v}\}$, the equilibrium density is expressed as $\rho(\mathbf{X}, \mathbf{V}, \mathbf{x}, \mathbf{v}) = \rho_\Theta(\Theta)\rho_\mathbf{V}(\mathbf{V})$. Second, $\rho_\mathbf{V}$ is a normal probability density satisfying

$$\langle \mathbf{V} \cdot \mathbf{V} \rangle = \frac{d}{\beta M}, \tag{4.2.4}$$

where d is the dimensionality of the space and $\beta = (k_\mathrm{B}T)^{-1}$ is the inverse temperature of the system with k_B the Boltzmann constant. Third, ρ_Θ does not depend on the mass M of the Brownian particle. Lastly, we assume that the equilibrium distribution is isotropic. We note that these assumptions are easily shown to be valid for the canonical ensemble. We also note that $\mathbf{V}(0)$ can be roughly estimated as $\mathrm{O}(M^{-1/2})$ from Eq. (4.2.4).

We denote by the brackets $\langle\cdot\rangle$ the ensemble average (i.e., average over ρ) and by $\langle\cdot\rangle_\Theta$ the average over ρ_Θ. We note that $\langle\cdot\rangle_\Theta$ may depend on $\mathbf{V}(0)$, in general, if the quantity to be averaged depends on $\mathbf{V}(0)$; in fact, $\langle\cdot\rangle_\Theta$ is the conditional expectation given $\mathbf{V}(0)$. For notational simplicity, we omit the dependence on $\mathbf{V}(0)$. When we evaluate the ensemble average, we use the following property of the conditional expectation: for arbitrary functions f and g,

$$\langle f(\mathbf{V})g(\mathbf{V},\Theta)\rangle = \langle f(\mathbf{V})\langle g(\mathbf{V},\Theta)\rangle_\Theta\rangle\,. \tag{4.2.5}$$

In other words, we first take the conditional average over ρ_Θ and then take average over $\rho_{\mathbf{V}}$.

4.2.3 Force decomposition

We express the total force $\mathbf{F}(t)$ on the Brownian particle in the full dynamics as follows:

$$\mathbf{F}(t) = \mathbf{F}_0(t) + \delta\mathbf{F}(t) + \tilde{\mathbf{F}}(t), \tag{4.2.6}$$

where $\delta\mathbf{F}(t) = \mathbf{F}_1(t) - \mathbf{F}_0(t)$ and $\tilde{\mathbf{F}}(t) = \mathbf{F}(t) - \mathbf{F}_1(t)$. Using the fact that the force deviation is explained by the system trajectory deviation, which, in turn, is attributed to the deviation between the Brownian particle trajectories, we obtain the following asymptotic expansions (see below Tensor notation and Derivation):

$$\delta\mathbf{F}(t) \approx \mathbf{A}_1(t)\mathbf{V}(0) + \mathbf{A}_2(t)\mathbf{V}^2(0) + \mathbf{A}_3(t)\mathbf{V}^3(0), \tag{4.2.7}$$

$$\tilde{\mathbf{F}}(t) \approx \frac{1}{M}\left[\mathbf{B}_1(t) + \mathbf{B}_2(t)\mathbf{V}(0)\right]. \tag{4.2.8}$$

Here, $\mathbf{A}_n(t)$ and $\mathbf{B}_n(t)$ are $(n+1)$th- and nth-rank tensors, respectively, and $\mathbf{V}^n(0)$ are the nth tensor power of $\mathbf{V}(0)$. Appropriate inner products are implicitly (i.e., without any dot product notation) assumed so that $\mathbf{A}_n(t)\mathbf{V}^n(0)$ and $\mathbf{B}_2(t)\mathbf{V}(0)$ become first-rank tensors. We note that $\mathbf{A}_n(t)$ and $\mathbf{B}_n(t)$ depend not on $\mathbf{V}(0)$ but on $\Theta(0)$ and that terms up to $\mathrm{O}(M^{-3/2})$ are considered in Eqs. (4.2.7) and (4.2.8).

Tensor notation We explain the tensor notation used in this chapter. For $\mathbf{V}(0) = \{V_i\}$, its nth tensor power $\mathbf{V}^n(0)$ is defined as $(\mathbf{V}^n(0))_{i_1 i_2 \cdots i_n} = V_{i_1} V_{i_2} \cdots V_{i_n}$. For a n-th rank tensor $\mathbf{C} = \{C_{i_1 i_2 \cdots i_n}\}$, the products $\mathbf{C}\mathbf{V}^{n-1}(0)$ and $\mathbf{C}\mathbf{V}^n(0)$ are defined as $(\mathbf{C}\mathbf{V}^{n-1}(0))_i = C_{i i_1 \cdots i_{n-1}} V_{i_1} \cdots V_{i_{n-1}}$ and $\mathbf{C}\mathbf{V}^n(0) = C_{i_1 \cdots i_n} V_{i_1} \cdots V_{i_n}$, respectively, where the Einstein summation convention is used. For $\mathbf{F}(0) = \{F_i\}$ and a n-th rank tensor $\mathbf{D} = \{D_{i_1 i_2 \cdots i_n}\}$, the product $\mathbf{F}(0)\mathbf{D}$ is defined as $(\mathbf{F}(0)\mathbf{D})_{i_1 i_2 \cdots i_{n-1}} = F_i D_{i i_1 \cdots i_{n-1}}$.

Derivation of Eqs. (4.2.7) and (4.2.8) By relating the force deviations with the bath trajectory deviations, we derive their asymptotic expansions shown in Eqs. (4.2.7) and (4.2.8). We first investigate the deviations between the two infinite-mass dynamics. The bath trajectory deviation, defined as $\delta\mathbf{x}_1(t) = \mathbf{x}_1(t) - \mathbf{x}_0(t)$, is attributed to the deviation between the two prescribed trajectories of the Brownian particle, i.e., $\mathbf{X}_1(t) - \mathbf{X}_0(t) = t\mathbf{V}(0)$. Hence, for sufficiently small $\mathbf{V}(0)$, $\delta\mathbf{x}_1(t)$ also has a small magnitude. Then, we obtain the leading term of $\delta\mathbf{F}(t)$ in terms of $\delta\mathbf{x}_1(t)$ as follows:

$$\delta\mathbf{F}(t) \approx \sum_i \nabla^2 U_1 \left(\mathbf{x}_0^{(i)}(t) - \mathbf{X}(0)\right) \left[\delta\mathbf{x}_1^{(i)}(t) - t\mathbf{V}(0)\right]. \tag{4.2.9}$$

The error in Eq. (4.2.9) is estimated as $\mathrm{O}(|\mathbf{V}(0)|^2)$. This is because for *infinitesimal* $\mathbf{V}(0)$, the magnitude of $\delta\mathbf{x}_1^{(i)}(t)$ is linearly proportional to that of $\mathbf{V}(0)$, which can be shown as follows. From Eq. (4.2.3), the equations of motion of the infinitesimal

deviation $\delta\mathbf{x}_1(t)$ are given as

$$\begin{aligned} m\delta\ddot{\mathbf{x}}_1^{(i)}(t) = &- \nabla^2 U_1\left(\mathbf{x}_0^{(i)}(t) - \mathbf{X}(0)\right)\left[\delta\mathbf{x}_1^{(i)}(t) - t\mathbf{V}(0)\right] \\ &- \sum_{j\neq i}\nabla^2 U_2\left(\mathbf{x}_0^{(i)}(t) - \mathbf{x}_0^{(j)}(t)\right)\left[\delta\mathbf{x}_1^{(i)}(t) - \delta\mathbf{x}_1^{(j)}(t)\right]. \end{aligned} \tag{4.2.10}$$

We note that the system of differential equations, Eq. (4.2.10), is linear and its initial condition is given as $\delta\mathbf{x}_1(0) = 0$. Since the non-homogeneous terms are proportional to $\mathbf{V}(0)$, it follows that $\delta\mathbf{x}_1(t)$ is also proportional to $\mathbf{V}(0)$. By applying this fact to the expansion of $\delta\mathbf{F}(t)$ with respect to $\delta\mathbf{x}_1^{(i)}(t) - t\mathbf{V}(0)$, we obtain the asymptotic expansion of $\delta\mathbf{F}(t)$ with respect to $\mathbf{V}(0)$ shown in Eq. (4.2.7). We note that the microscopic expression for $\mathbf{A}_1(t)\mathbf{V}(0)$ is given in Eq. (4.2.9).

Similarly, the deviation $\delta\mathbf{x}_2(t) = \mathbf{x}(t) - \mathbf{x}_1(t)$ is attributed to the deviation of the Brownian particle trajectory. However, in this case, the latter deviation $\mathbf{X}(t) - \mathbf{X}_1(t) = \frac{1}{M}\int_0^t ds\int_0^s du\ \mathbf{F}(u)$ is not known *a priori*. In fact, $\mathbf{F}(t)$ is the quantity we want to investigate through approximations. However, since we can approximate $\mathbf{F}(t)$ by $\mathbf{F}_0(t)$, which does not depend neither on $\mathbf{V}(0)$ nor on M, $\mathbf{X}(t) - \mathbf{X}_1(t)$ is expected to be linearly proportional to M^{-1} for sufficiently large M. Hence, by the same argument as in $\delta\mathbf{F}(t)$, the leading term $\tilde{\mathbf{F}}(t)$ is linearly proportional to M^{-1}, which allows us to introduce $\mathbf{B}(t)$ such that $\tilde{F}(t) = \frac{1}{M}\mathbf{B}(t) + \mathrm{O}(M^{-2})$. Since $\mathbf{B}(t)$ is dependent on $\mathbf{x}_1(t)$, it has dependence on $\mathbf{V}(0)$ as well as $\Theta(0)$. By considering up to its linear dependence on $\mathbf{V}(0)$ (i.e., $\mathbf{B}(t) \approx \mathbf{B}_1(t) + \mathbf{B}_2(t)\mathbf{V}(0)$), we obtain the asymptotic expansion of $\tilde{\mathbf{F}}(t)$ shown in Eq. (4.2.8).

4.2.4 Time correlation functions

Using the force decomposition with the asymptotic expansions above, we express the time correlation functions $\langle \mathbf{V}(0) \cdot \mathbf{F}(t) \rangle$ and $\langle \mathbf{F}(0) \cdot \mathbf{F}(t) \rangle$. For the tensors $\mathbf{A}_n(t)$ and $\mathbf{B}_n(t)$, we introduce corresponding scalar functions, which can easily be estimated by the standard time-averaging technique of MD simulation. We use the dot product notation only for inner products between first-rank tensors.

To obtain an expression for $\langle \mathbf{V}(0) \cdot \mathbf{F}(t) \rangle$, we multiply $\mathbf{V}(0)$ with Eq. (4.2.6) and take the ensemble average by using Eq. (4.2.5). Because of the isotropy of the equilibrium distribution, some terms such as $\langle \mathbf{V}(0) \cdot \mathbf{F}_0(t) \rangle$ disappear. Moreover, we can express the nonzero terms in a simpler way. That is, we can introduce scalar functions $a_1(t)$, $a_3(t)$, and $b_2(t)$ such that

$$\langle \mathbf{A}_1(t) \rangle_\Theta = a_1(t)\mathbf{I}, \tag{4.2.11a}$$

$$\langle \mathbf{B}_2(t) \rangle_\Theta = b_2(t)\mathbf{I}, \tag{4.2.11b}$$

$$\langle \mathbf{A}_3(t) \rangle_\Theta \, \mathbf{V}^3(0) = a_3(t) \, |\mathbf{V}(0)|^2 \, \mathbf{V}(0). \tag{4.2.11c}$$

Here, we have used properties of isotropic tensors (see below Derivation). From Eqs. (4.2.7) and (4.2.8), we obtain

$$\langle \mathbf{V}(0) \cdot \delta\mathbf{F}(t) \rangle \approx \langle \mathbf{V} \cdot \mathbf{V} \rangle \, a_1(t) + \left\langle |\mathbf{V}|^4 \right\rangle a_3(t), \tag{4.2.12a}$$

$$\langle \mathbf{V}(0) \cdot \tilde{\mathbf{F}}(t) \rangle \approx \frac{1}{M} \langle \mathbf{V} \cdot \mathbf{V} \rangle \, b_2(t). \tag{4.2.12b}$$

Hence, by using Eq. (4.2.4) and $\left\langle |\mathbf{V}|^4 \right\rangle = \frac{d+2}{d} \langle \mathbf{V} \cdot \mathbf{V} \rangle^2$, we obtain

$$\langle \mathbf{V}(0) \cdot \mathbf{F}(t) \rangle \approx \frac{d}{\beta M} \left[a_1(t) + \frac{d+2}{\beta M} a_3(t) + \frac{1}{M} b_2(t) \right]. \tag{4.2.13}$$

To obtain a similar expression for $\langle \mathbf{F}(0) \cdot \mathbf{F}(t) \rangle$, we follow the same procedure as above. The only difference is that the tensors are averaged after multiplied by $\mathbf{F}(0)$ since $\mathbf{F}(0)$ depends not on $\mathbf{V}(0)$ but on $\Theta(0)$. Hence, by introducing $\bar{a}_2(t)$ and $\bar{b}_1(t)$ (see below Derivation) such that

$$\langle \mathbf{F}(0)\mathbf{A}_2(t) \rangle_\Theta = \bar{a}_2(t)\mathbf{I}, \tag{4.2.14a}$$

$$\langle \mathbf{F}(0) \cdot \mathbf{B}_1(t) \rangle_\Theta = \bar{b}_1(t), \tag{4.2.14b}$$

we have

$$\langle \mathbf{F}(0) \cdot \delta\mathbf{F}(t) \rangle \approx \langle \mathbf{V} \cdot \mathbf{V} \rangle \, \bar{a}_2(t), \tag{4.2.15a}$$

$$\langle \mathbf{F}(0) \cdot \tilde{\mathbf{F}}(t) \rangle \approx \frac{1}{M} \bar{b}_1(t). \tag{4.2.15b}$$

Therefore, we obtain

$$\langle \mathbf{F}(0) \cdot \mathbf{F}(t) \rangle \approx \langle \mathbf{F}_0(0) \cdot \mathbf{F}_0(t) \rangle + \frac{d}{\beta M} \bar{a}_2(t) + \frac{1}{M} \bar{b}_1(t). \tag{4.2.16}$$

Derivation of Eqs. (4.2.11) and (4.2.14) We explain how we use properties of isotropic tensors, when we obtain the asymptotic expansions of $\langle \mathbf{V}(0) \cdot \mathbf{F}(t) \rangle$ and $\langle \mathbf{F}(0) \cdot \mathbf{F}(t) \rangle$ by introducing the scalar functions $a_1(t)$, $\bar{a}_2(t)$, $a_3(t)$, $\bar{b}_1(t)$, and $\bar{b}_2(t)$. By the isotropy of the equilibrium distribution function, the conditional averages of several tensors become isotropic. Since there is no isotropic first-rank tensor, we show that $\langle \mathbf{F}_0(t) \rangle_\Theta$, $\langle \mathbf{B}_1(t) \rangle_\Theta$, $\langle \mathbf{F}(0)\mathbf{A}_1(t) \rangle_\Theta$ and $\langle \mathbf{F}(0)\mathbf{B}_2(t) \rangle_\Theta$ are zero. Since every isotropic second-rank tensor is expressed as $\lambda\mathbf{I}$ for some scalar λ, we can introduce $a_1(t)$, $b_2(t)$, and $\bar{a}_2(t)$ from $\langle \mathbf{A}_1(t) \rangle_\Theta$, $\langle \mathbf{B}_2(t) \rangle_\Theta$, and $\langle \mathbf{F}(0)\mathbf{A}_2(t) \rangle_\Theta$, respectively. For the conditional averages of third-rank tensors, we use that there is no two-dimensional isotropic tensor and every three-dimensional isotropic tensor is a

scalar multiple of the permutation tensor, i.e., $\lambda\epsilon_{ijk}$. For a third-rank isotropic tensor $\mathbf{C} = \{\lambda\epsilon_{ijk}\}$, we can show that $\mathbf{C}\mathbf{V}^2(0)$ and $\mathbf{C}\mathbf{V}^3(0)$ are zero by using $\epsilon_{ijk} = -\epsilon_{ikj}$. Hence, for $d = 2, 3$, we show that $\langle \mathbf{A}_2(t)\rangle_\Theta \mathbf{V}^2(0)$ and $\langle \mathbf{F}(0)\mathbf{A}_3(t)\rangle_\Theta \mathbf{V}^3(0)$ are zero. Finally, by using that every fourth-order isotropic tensor has a form $\lambda_1\delta_{ij}\delta_{kl} + \lambda_2\delta_{ik}\delta_{jl} + \lambda_3\delta_{il}\delta_{jk}$, we can show that $\langle \mathbf{A}_3(t)\rangle_\Theta \mathbf{V}(0)^3 = a_3(t)|\mathbf{V}(0)|^2\mathbf{V}(0)$, where $a_3(t)$ is the sum of the constants λ_1, λ_2, and λ_3 of $\langle \mathbf{A}_3(t)\rangle_\Theta$.

4.2.5 Resulting relations

Now we derive relations for the scalar functions $a_1(t)$, $\bar{a}_2(t)$, $\bar{a}_3(t)$, $\bar{b}_1(t)$, and $b_2(t)$. By substituting Eqs. (4.2.13) and (4.2.16) into the relation $\langle \mathbf{V}(0)\cdot\mathbf{F}(t)\rangle = -\frac{1}{M}\int_0^t \langle \mathbf{F}(0)\cdot\mathbf{F}(s)\rangle\, ds$ and equating terms with the same order of M, we obtain

$$a_1(t) = -\frac{\beta}{d}\int_0^t \langle \mathbf{F}_0(0)\cdot\mathbf{F}_0(s)\rangle\, ds, \tag{4.2.17}$$

$$\frac{d+2}{\beta}a_3(t) + b_2(t) = -\int_0^t \bar{a}_2(s)ds - \frac{\beta}{d}\int_0^t \bar{b}_1(s)ds. \tag{4.2.18}$$

We note that in order to derive relations, which are valid under the Brownian limit (i.e., leading-order relations), Eq. (4.2.17) is used. For the next-order corrections, Eq. (4.2.18) is also needed. For example, by using Eqs. (4.2.12a) and (4.2.17), we obtain

$$-\lim_{M\to\infty}\frac{\langle \mathbf{V}(0)\cdot\mathbf{F}_1(t)\rangle}{\langle \mathbf{V}\cdot\mathbf{V}\rangle} = \frac{\beta}{d}\int_0^t \langle \mathbf{F}_0(0)\cdot\mathbf{F}_0(s)\rangle\, ds. \tag{4.2.19}$$

We note that $\delta\mathbf{F}(t)$ has been replaced by $\mathbf{F}_1(t)$ in Eq. (4.2.19) since $\langle \mathbf{F}_0(t)\rangle_\Theta = 0$ and thus $\langle \delta\mathbf{F}(t)\rangle_\Theta = \langle \mathbf{F}_1(t)\rangle_\Theta$.

4.2.6 Pulling experiment

We demonstrate that the linear response expression of the pulling experiment, which has been derived in [150], can be obtained by our approach. We assume that an object is held fixed in an unbounded equilibrium bath for $t < 0$ and it starts to be pulled at a constant velocity $\mathbf{U}$ at $t = 0$. The force on the object at time $t > 0$ is denoted by $\mathbf{F}_1^{\mathbf{U}}(t)$ and the quantity of interest is the ratio of the average force $\left\langle \mathbf{F}_1^{\mathbf{U}}(t) \right\rangle$ to $\mathbf{U}$. We note that this pulling experiment corresponds to the constant-velocity dynamics, where the constant velocity $\mathbf{V}(0)$ is replaced by $\mathbf{U}$ and that the average in this case is actually the conditional average $\langle \cdot \rangle_\Theta$ given $\mathbf{V}(0) = \mathbf{U}$. Hence, we have $\left\langle \mathbf{F}_1^{\mathbf{U}}(t) \right\rangle \approx a_1(t)\mathbf{U}$ for small $\mathbf{U}$ and obtain

$$-\lim_{\mathbf{U}\to 0} \frac{\left\langle \mathbf{F}_1^{\mathbf{U}}(t) \right\rangle}{\mathbf{U}} = \frac{\beta}{d} \int_0^t \langle \mathbf{F}_0(0) \cdot \mathbf{F}_0(s) \rangle \, ds. \tag{4.2.20}$$

Furthermore, by noting that at large time t the left-hand side of Eq. (4.2.20) tends to γ from the macroscopic definition of the friction coefficient, we obtain the microscopic formula for γ [131, 51]:

$$\gamma = \frac{\beta}{d} \int_0^\infty \langle \mathbf{F}_0(0) \cdot \mathbf{F}_0(t) \rangle \, dt. \tag{4.2.21}$$

4.2.7 Comparison with the memory function approach

We first obtain relations between the memory function $K(t)$ in Eq. (4.1.3) and our scalar functions. For a Brownian particle embedded in an unbounded bath, the memory function $K(t)$ is known to have the following asymptotic expansion for large M [89]: $K(t) \approx K_0(t) + \frac{1}{M} K_1(t)$. Then, the time correlation functions $\langle \mathbf{V}(0) \cdot \mathbf{F}(t) \rangle$ and $\langle \mathbf{F}(0) \cdot \mathbf{F}(t) \rangle$ have the following asymptotic expansions with respect to M, the

first two coefficient functions of which are given in terms of $K_0(t)$ and $K_1(t)$ [97]:

$$\langle \mathbf{V}(0)\cdot\mathbf{F}(t)\rangle \approx -\frac{d}{\beta M}\left[G_0(t)+\frac{G_1(t)-G_0*G_0(t)}{M}\right], \tag{4.2.22}$$

$$\langle \mathbf{F}(0)\cdot\mathbf{F}(t)\rangle \approx \frac{d}{\beta}\left[K_0(t)+\frac{K_1(t)-K_0*G_0(t)}{M}\right], \tag{4.2.23}$$

where $G_i(t)=\int_0^t K_i(s)ds$ for $i=0,1$ and $*$ denotes convolution. We compare these expansions with Eqs. (4.2.13) and (4.2.16). By equating the leading order terms, we retrieve the fluctuation-dissipation relation for the frozen dynamics and express $a_1(t)$ in terms of $K_0(t)$:

$$K_0(t)=\frac{\beta}{d}\langle \mathbf{F}_0(0)\cdot\mathbf{F}_0(t)\rangle, \quad a_1(t)=-\int_0^t K_0(s)ds. \tag{4.2.24}$$

We also obtain expressions for the next order:

$$K_1(t)=\dot{a}_1*a_1+\bar{a}_2+\frac{\beta}{d}\bar{b}_1=\dot{a}_1*a_1-\frac{d+2}{\beta}\dot{a}_3-\dot{b}_2. \tag{4.2.25}$$

Using these results, we obtain asymptotic expansions for the memory term $-\int_0^t K(t-s)\mathbf{V}(s)ds$ and the fluctuating force $\mathbf{F}^+(t)$. Following their physical meaning, we denote them by $\mathbf{F}_{\mathrm{fr}}^{\mathrm{Mori}}(t)$ and $\mathbf{F}_{\mathrm{th}}^{\mathrm{Mori}}(t)$, respectively. Their two lowest order terms are expressed as

$$\mathbf{F}_{\mathrm{fr}}^{\mathrm{Mori}}(t)=a_1(t)\mathbf{V}(0)+\frac{1}{M}a_1*\mathbf{F}_0(t)+\mathrm{O}\left(M^{-3/2}\right), \tag{4.2.26}$$

$$\mathbf{F}_{\mathrm{th}}^{\mathrm{Mori}}(t)=\mathbf{F}_0(t)+\left[\mathbf{A}_1(t)-a_1(t)\mathbf{I}\right]\mathbf{V}(0)+\mathrm{O}\left(M^{-1}\right), \tag{4.2.27}$$

(see below Derivation). Hence, we obtain the following approximations

$$\mathbf{F}_{\rm fr}^{\rm Mori}(t) = \langle \mathbf{F}_1(t) \rangle_\Theta + \mathrm{O}\left(\tfrac{1}{M}\right), \tag{4.2.28}$$

$$\mathbf{F}_{\rm th}^{\rm Mori}(t) = \mathbf{F}_0(t) + \mathrm{O}\left(\tfrac{1}{\sqrt{M}}\right) = \mathbf{F}_1(t) - \langle \mathbf{F}_1(t) \rangle_\Theta + \mathrm{O}\left(\tfrac{1}{M}\right). \tag{4.2.29}$$

We note that $\mathbf{F}_{\rm fr}^{\rm Mori}(t)$ and $\mathbf{F}_{\rm th}^{\rm Mori}(t)$ depend on both $\mathbf{V}(0)$ and $\Theta(0)$, whereas their leading terms $\langle \mathbf{F}_1(t) \rangle_\Theta$ and $\mathbf{F}_0(t)$ are functions of only $\mathbf{V}(0)$ and $\Theta(0)$, respectively. Hence, we show the independence of the friction force and thermal noise in the Brownian limit as follows. As $M \to \infty$, the friction force loses its dependence on $\Theta(0)$, whereas the thermal noise loses its dependence on $\mathbf{V}(0)$.

Derivation of Eqs. (4.2.26) and (4.2.27) We obtain the asymptotic expansions up to the order of $M^{-3/2}$. In order to handle the memory term, we use the following equation:

$$K * \mathbf{V}(t) = G(t)\mathbf{V}(0) + \frac{1}{M} G * \mathbf{F}(t). \tag{4.2.30}$$

The right-hand side of Eq. (4.2.30) is obtained by substituting $\mathbf{V}(s) = \mathbf{V}(0) + \frac{1}{M}\int_0^t \mathbf{F}(u)du$ into the convolution $K * \mathbf{V}(t)$ and using a change of variables. On the other hand, for the total force $\mathbf{F}(t)$, we use its asymptotic expansion defined through Eqs. (4.2.6), (4.2.7), and (4.2.8). By introducing the asymptotic expansions of $G(t)$ and $\mathbf{F}(t)$ to Eq. (4.2.30), we obtain

$$K * \mathbf{V}(t) \approx G_0(t)\mathbf{V}(0) + \frac{G_0 * \mathbf{F}_0(t)}{M} + \frac{G_1(t) - G_0 * G_0(t)}{M}\mathbf{V}(0). \tag{4.2.31}$$

By using $G_0(t) = -a_1(t)$ and Eq. (4.2.25), we obtain

$$\mathbf{F}_{\rm fr}^{\rm Mori}(t) \approx a_1(t)\mathbf{V}(0) + \frac{1}{M} a_1 * \mathbf{F}_0(t) + \frac{1}{M}\left(\frac{d+2}{\beta} a_3(t) + b_2(t)\right)\mathbf{V}(0). \tag{4.2.32}$$

By subtracting this from the asymptotic expansion of $\mathbf{F}(t)$, we also obtain that of $\mathbf{F}^{\rm Mori}_{\rm th}(t) \equiv \mathbf{F}^{+}(t)$, the two lowest order terms of which are shown in Eq. (4.2.27).

4.2.8 Further investigations

By using our asymptotic expansions, we investigate the following interesting properties of the fluctuating force $\mathbf{F}^{+}(t)$.

Dependence of $\langle \mathbf{F}^{+}(t) \rangle_{\Theta}$ on $\mathbf{V}(0)$ Although $\langle \mathbf{F}^{+}(t) \rangle = 0$, the conditional average $\langle \mathbf{F}^{+}(t) \rangle_{\Theta}$ is non-zero. We can show that $\langle \mathbf{F}^{+}(t) \rangle_{\Theta}$ is parallel or antiparallel to $\mathbf{V}(0)$ depending on the magnitude of $\mathbf{V}(0)$ as follows. Since $\mathbf{F}^{+}(t) = \mathbf{F}(t) - \mathbf{F}^{\rm Mori}_{\rm fr}(t)$, we calculate $\langle \mathbf{F}^{+}(t) \rangle_{\Theta}$ from $\langle \mathbf{F}(t) \rangle_{\Theta}$ and $\langle \mathbf{F}^{\rm Mori}_{\rm fr}(t) \rangle_{\Theta}$. From the discussion above about isotropic tensors, we have

$$\langle \mathbf{F}(t) \rangle_{\Theta} \approx a_1(t)\mathbf{V}(0) + a_3(t)|\mathbf{V}(0)|^2\mathbf{V}(0) + \frac{1}{M}b_2(t)\mathbf{V}(0). \tag{4.2.33}$$

Hence, by using Eqs. (4.2.32) and (4.2.33), we obtain

$$\left\langle \mathbf{F}^{+}(t) \right\rangle_{\Theta} \approx a_3(t) \left[|\mathbf{V}(0)|^2 - \frac{d+2}{d} \left\langle \mathbf{V} \cdot \mathbf{V} \right\rangle \right] \mathbf{V}(0). \tag{4.2.34}$$

We note that all the lower-order terms than $\mathrm{O}(M^{-3/2})$ cancel. We also note that the contribution of the leading term shown in Eq. (4.2.34) disappears when $\langle \mathbf{F}^{+}(t) \rangle_{\Theta}$ and $\mathbf{V}(0) \cdot \langle \mathbf{F}^{+}(t) \rangle_{\Theta}$ are averaged over $\rho_{\mathbf{V}}$, as expected from $\langle \mathbf{F}^{+}(t) \rangle = 0$ and $\langle \mathbf{V}(0) \cdot \mathbf{F}^{+}(t) \rangle = 0$. From Eq. (4.2.34), we show that the conditional average of the fluctuating force given initial velocity of the Brownian particle does not vanish.

Linear regression of $\mathbf{F}^+$ with respect to $\mathbf{F}$ We can also explain the following near-Brownian-limit regime simulation result reported in [164]: for linear regression $\mathbf{F}^+ = c\mathbf{F} + \xi$ with ξ the error term, the coefficient c is observed to be $1 - \mathrm{O}(M^{-1})$. In [164], it was discussed that the $\mathrm{O}(M^{-1})$ dependence is faster than expected from the rough estimate $\mathbf{F}^+(t) = [1 + \mathrm{O}(M^{-1/2})]\mathbf{F}(t)$. Theoretical explanation for this observation can be given as follows. Since the error term ξ is uncorrelated with $\mathbf{F}$ by assumption, we obtain $\langle \mathbf{F} \cdot \mathbf{F}^+ \rangle = c \langle \mathbf{F} \cdot \mathbf{F} \rangle$. Since $\langle \mathbf{F} \cdot \mathbf{F} \rangle$ is an equilibrium quantity that does not depend on M, we only need to investigate the M dependence of $\langle \mathbf{F} \cdot \mathbf{F}^+ \rangle$. We first obtain asymptotic expansion of $\langle \mathbf{F}(t) \cdot \mathbf{F}^+(t) \rangle$ and then take the limit $t \to \infty$ to obtain the stationary value. By multiplying $\mathbf{F}(t)$ with the generalized Langevin equation and taking the ensemble average, we obtain

$$\left\langle \mathbf{F}(t) \cdot \mathbf{F}^+(t) \right\rangle = \langle \mathbf{F} \cdot \mathbf{F} \rangle + \int_0^t K(s) \langle \mathbf{V}(0) \cdot \mathbf{F}(s) \rangle \, ds, \tag{4.2.35}$$

where we have used $\langle \mathbf{F}(t) \cdot \mathbf{F}(t) \rangle = \langle \mathbf{F} \cdot \mathbf{F} \rangle$ and $\langle \mathbf{V}(s) \cdot \mathbf{F}(t) \rangle = \langle \mathbf{V}(0) \cdot \mathbf{F}(t-s) \rangle$. By using Eq. (4.2.22), the leading term of the integral in Eq. (4.2.35) is obtained as $-\frac{d}{\beta M} \int_0^t K_0(s) G_0(s) ds$, which is further reduced to $-\frac{d}{2\beta M} G_0^2(t)$. Since $\lim_{t\to\infty} G_0(t) = \gamma$, we obtain

$$\left\langle \mathbf{F} \cdot \mathbf{F}^+ \right\rangle \approx \langle \mathbf{F} \cdot \mathbf{F} \rangle - \frac{d\gamma^2}{2\beta M} \tag{4.2.36}$$

and c is evaluated as $1 - \frac{d\gamma^2}{2\beta M} \langle \mathbf{F} \cdot \mathbf{F} \rangle^{-1}$.

4.3 Verification by MD simulation

To confirm our theoretical results, we perform MD simulations of the two-dimensional Rayleigh model (i.e., a colloidal particle in an ideal gas). While this model possesses essential features of physical Brownian motion in a gas, it can be studied with math-

ematical rigor [39, 40, 19, 108] and allows some analytical results [44, 70, 128, 138]. Formulas for the frozen dynamics force autocorrelation function $\langle \mathbf{F}_0(0) \cdot \mathbf{F}_0(t) \rangle$ and the limit memory function $K_0(t)$ have been obtained in terms of the average over the trajectories of a single bath particle and precisely calculated [96]. For a purely repulsive interaction potential between the Brownian particle and a bath particle, $K_0(t)$ has no oscillating tail and decays to zero after a short time. Along with the availability of the analytic method, this behavior enables us to clearly confirm our theoretical predictions.

In order to calculate various ensemble-averaged quantities, we perform MD simulations for the full dynamics and the two types of the infinite-mass dynamics as well as the pulling experiment. We also observe the skewness in the force distributions and the bath-particle density to further investigate the microscopic origin of the drag force.

4.3.1 MD procedures

The MD simulation setting for the two-dimensional Rayleigh model is as follows. The interaction potential U_1 between the Brownian particle and a bath particle is the Weeks–Chandler–Andersen (WCA) potential with parameters $\epsilon = 1$ and $\sigma = 1$. While the mass of a bath particle is fixed at $m = 1$, the mass of the Brownian particle (in the full dynamics) is varied from $M = 5$ to 100. The simulation box is a square with side $L = 100$ and the number of the bath particles is set as $N = 10^4$. Periodic boundary conditions are imposed in both x and y directions. The inverse temperature of the system is set to $\beta = 1$. All simulation results are reported in reduced units with ϵ the unit of energy, σ the unit of length, and m the unit of mass.

For all MD simulations, the velocity Verlet algorithm is employed with integration time step $\Delta t = 5 \times 10^{-3}$. Subsequently, a total of 400 configurations of the system are collected from the full dynamics simulation of the sample at every 2×10^4 time steps. For each set of the parameters, 128 samples are calculated and thus a total of 51200 configurations are collected as the initial condition $\{\mathbf{X}(0),\ \mathbf{V}(0),\ \mathbf{x}(0),\ \mathbf{v}(0)\}$. For each configuration, three types of simulations—the full dynamics, the frozen dynamics, and the constant-velocity dynamics—are performed for 400 time steps and the forces $\mathbf{F}(t)$, $\mathbf{F}_0(t)$, and $\mathbf{F}_1(t)$ are obtained up to time $T = 2$ from the corresponding simulations, respectively.

For the pulling experiment, the initial equilibrium configurations are obtained from the frozen dynamics. The equilibration process of the frozen dynamics and the other parameters except the mass M of the Brownian particle are the same as above. For each configuration, $\mathbf{F}_0(t)$ and $\mathbf{F}_1(t)$ are obtained from the frozen and the constant-velocity dynamics simulations, respectively. The pulling velocity $\mathbf{U}$ is along the x-axis, i.e., $\mathbf{U} = (U_x, 0)$ and its magnitude is set from $U_x = 0.05$ to 2.

Since the main purpose of our simulation study is to confirm the theoretical results for the microscopic system described by Hamilton's equations, we do not use any thermostat, which can alter the microscopic trajectory of the system, for all three types of dynamics. Hence, the total energy of the system is conserved in the full dynamics and frozen dynamics simulations, whereas it is increasing in the constant-velocity dynamics simulation. However, we confirm that the heat generated in the constant-velocity dynamics does not perturb the system so much that the surrounding fluid is nearly in equilibrium for our choice of large system size L and short simulation time $T_{\mathrm{sim}} = 2$. This can also be shown as follows. Since the drag force is roughly estimated as $-\gamma\mathbf{V}$, the rate of increase of the total energy of the system is $\gamma\mathbf{V} \cdot \mathbf{V}$. Compared to the initial kinetic energy of the bath estimated as

$N\beta^{-1}$, the increased total energy of the system up to time $T_{\rm sim}$, which is estimated as $\gamma T_{\rm sim} M^{-1}\beta^{-1}$, is very small. Moreover, for the Rayleigh model under a purely repulsive potential, a bath particle interacts with the Brownian particle again only after a long time since it needs to cross the periodic boundary at least once. Hence, if $T_{\rm sim}$ is much smaller than this time scale, the Brownian particle is surrounded by the bath particles, which have entered the interaction range for the first time and thus the environment can be assumed to be in the thermal equilibrium.

4.3.2 Full dynamics and the two types of the infinite-mass dynamics

We present simulation results of various ensemble-averaged quantities. First, we compare the mean-squared forces of the full, frozen, and constant-velocity dynamics. Second, we observe the correlation between the forces of these dynamics and investigate the magnitude of the force deviations. Third, we estimate the limit memory function as well as the higher-order contributions.

While the mean-squared forces $\langle \mathbf{F}(t)\cdot\mathbf{F}(t)\rangle$ and $\langle \mathbf{F}_0(t)\cdot\mathbf{F}_0(t)\rangle$ are constant in time, $\langle \mathbf{F}_1(t)\cdot\mathbf{F}_1(t)\rangle$ changes at short times and eventually becomes stationary, see Fig. 4.1(A). Since for the full dynamics the system is in equilibrium, the mean-squared force can be denoted by $\langle \mathbf{F}\cdot\mathbf{F}\rangle$ and it can be calculated from the bath-particle density, which can be deduced from ρ_Θ. For the Rayleigh model, from the Boltzmann distribution law, the bath-particle density for the Brownian particle located at $\mathbf{X}$ is given as $\rho_{\rm fl}^{\rm B}(\mathbf{r}-\mathbf{X})$, where $\rho_{\rm fl}^{\rm B}(\mathbf{r}) = ae^{-\beta U_1(\mathbf{r})}$ with $\mathbf{r}$ a d-dimensional vector and a the number density of the bath particles. From the assumption on ρ_Θ, $\langle \mathbf{F}_0(t)\cdot\mathbf{F}_0(t)\rangle$ is also equal to $\langle \mathbf{F}\cdot\mathbf{F}\rangle$. The simulation results for the mean-

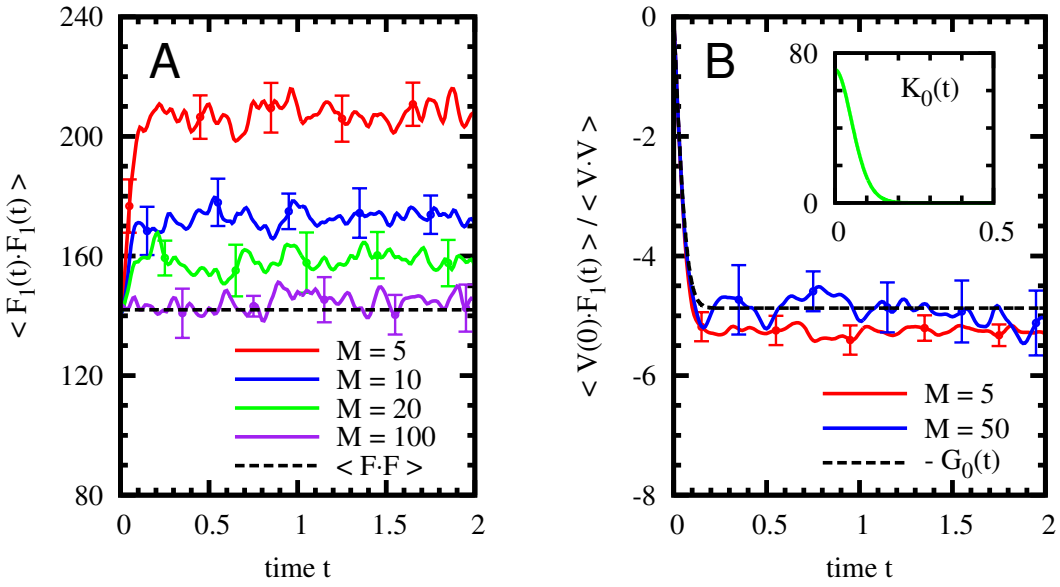

Figure 4.1: Constant-velocity dynamics. (A) The deviation of its mean-squared force $\langle \mathbf{F}_1(t) \cdot \mathbf{F}_1(t) \rangle$ from $\langle \mathbf{F} \cdot \mathbf{F} \rangle$ reveals the development of a different bath environment around the Brownian particle. The deviation is proportional to M^{-1}. (B) The limit memory function $K_0(t)$ can be estimated from the time profile of $\langle \mathbf{V}(0) \cdot \mathbf{F}_1(t) \rangle / \langle \mathbf{V} \cdot \mathbf{V} \rangle$, which converges to $-G_0(t) = -\int_0^t K_0(s)ds$ as M increases. The friction coefficient γ is also estimated from its plateau value. For a smaller value of M, there is clear deviation due to higher-order contributions. The time profile of $K_0(t)$ is shown in the inset, from which the time scale of a collision between the Brownian particle and a bath particle can be estimated. For the simulation results, error bars corresponding to ± 2 standard deviations are shown together.

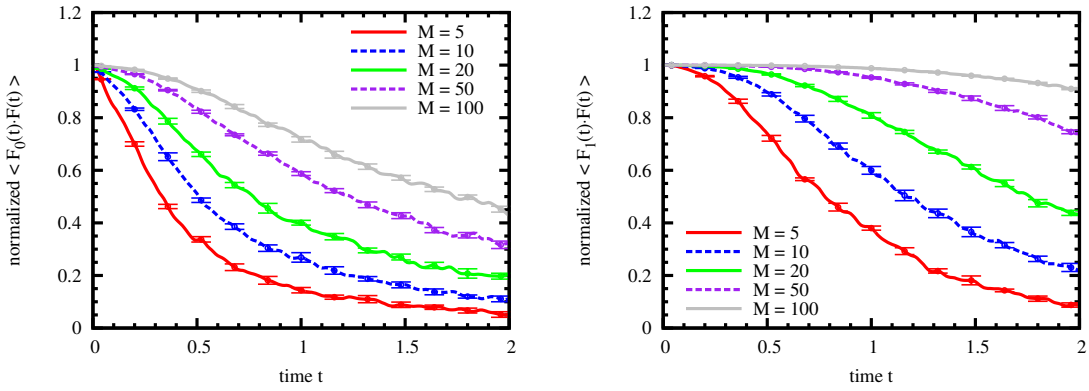

Figure 4.2: Correlations of the forces between the full dynamics and the infinite-mass dynamics. From the normalized correlation functions $\langle \mathbf{F}_0(t) \cdot \mathbf{F}(t) \rangle$ and $\langle \mathbf{F}_1(t) \cdot \mathbf{F}(t) \rangle$, we observe the validity of approximating $\mathbf{F}(t)$ by $\mathbf{F}_0(t)$ and $\mathbf{F}_1(t)$. As the mass M of the Brownian particle increases, the normalized correlation functions maintain their values around the unity for longer times. For the same value of M, the correlation with $\mathbf{F}_1(t)$ is closer to the unity than that with $\mathbf{F}_0(t)$. For $k = 0$ and 1, $\langle \mathbf{F}_k(t) \cdot \mathbf{F}(t) \rangle$ is normalized by the root mean-squared averages of $\mathbf{F}_k(t)$ and $\mathbf{F}(t)$. The error bars correspond to ± 2 standard deviations.

squared forces of the full and frozen dynamics agree very well with the theoretical value of $\langle \mathbf{F} \cdot \mathbf{F} \rangle$, which is obtained from $\rho_{\rm fl}^{\rm B}(\mathbf{r})$. Contrary to these dynamics, the constant-velocity dynamics is near-equilibrium dynamics, which is perturbed by the rectilinear movement of the Brownian particle. Although its mean-squared force is initially equal to $\langle \mathbf{F} \cdot \mathbf{F} \rangle$, $\langle \mathbf{F}_1(t) \cdot \mathbf{F}_1(t) \rangle$ increases in time until it achieves the stationary value. Since $\mathbf{F}_1(t) \approx \mathbf{F}_0(t) + \mathbf{A}_1(t)\mathbf{V}(0)$, the increase is proportional to $\langle \mathbf{V} \cdot \mathbf{V} \rangle$ or M^{-1} as shown in Fig. 4.1(A). In addition, the stationary value shown at larger times indicates that a stationary state for the surrounding bath particles emerges. We shall revisit the distribution of the surrounding bath particles below.

In order to investigate the validity of Eq. (4.2.6), we examine the force-force correlation functions $\langle \mathbf{F}_0(t) \cdot \mathbf{F}(t) \rangle$ and $\langle \mathbf{F}_1(t) \cdot \mathbf{F}(t) \rangle$ (see Fig. 4.2) and the mean-squared values of $\delta\mathbf{F}(t)$ and $\tilde{\mathbf{F}}(t)$ (see Fig. 4.3). As M increases, the normalized force-force correlation functions resist decaying from the unity for larger times. For the same value of M, the decay is faster for $\mathbf{F}_0(t)$ than for $\mathbf{F}_1(t)$. The mean-squared

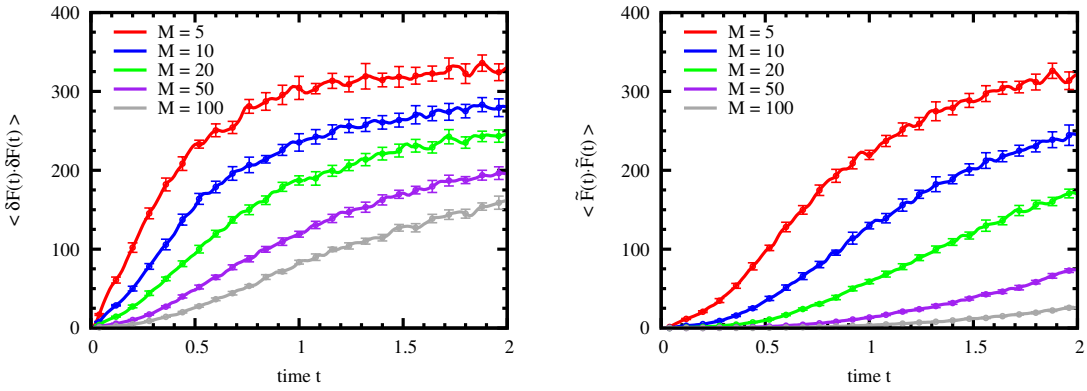

Figure 4.3: Mean-squared values of the force deviations. From these values, we confirm that the magnitude of $\delta\mathbf{F}(t)$ is $\mathrm{O}(M^{-1/2})$, whereas that of $\tilde{\mathbf{F}}(t)$ is $\mathrm{O}(M^{-1})$. At short times, $\langle\delta\mathbf{F}(t)\cdot\delta\mathbf{F}(t)\rangle$ and $\langle\tilde{\mathbf{F}}(t)\cdot\tilde{\mathbf{F}}(t)\rangle$ are proportional to M^{-1} and M^{-2}, respectively. The mean-squared values increase as t increases, which indicate that the approximations $\mathbf{F}(t)\approx\mathbf{F}_0(t)$ and $\mathbf{F}(t)\approx\mathbf{F}_1(t)$ become gradually less accurate. The error bars correspond to ± 2 standard deviations.

values of $\delta\mathbf{F}(t)$ and $\tilde{\mathbf{F}}(t)$ increase in time at short times. The former is proportional to M^{-1}, whereas the latter to M^{-2}. Although these mean-squared values eventually become stationary, the times when they become saturated increase as M increases. All these observations are consistent with our theoretical predictions: $\mathbf{F}_0(t)$ is the zero-order approximation of $\mathbf{F}(t)$, whereas $\mathbf{F}_1(t)$ is the $\mathrm{O}(M^{-1/2})$ approximation; the corresponding time intervals where these approximations are valid increase as M becomes larger.

We compare the time profile of $\langle\mathbf{V}(0)\cdot\mathbf{F}_1(t)\rangle\,/\,\langle\mathbf{V}\cdot\mathbf{V}\rangle$ with the time integral of the limit memory function $K_0(t)$, which is calculated by the method in [96]. As shown in Fig. 4.1(B), close agreement is observed for larger M, whereas there is clear deviation for smaller M. The deviation is expected from Eq. (4.2.12a) and the time profile of $a_3(t)$ is obtained. Similarly, the other higher-order correction coefficients $\bar{a}_2(t)$, $\bar{b}_1(t)$ and $b_2(t)$ are calculated from Eqs. (4.2.12b) and (4.2.15), see Fig. 4.4. The estimation of these coefficients for several values of M produces very similar results, which further confirm the validity of our approach.

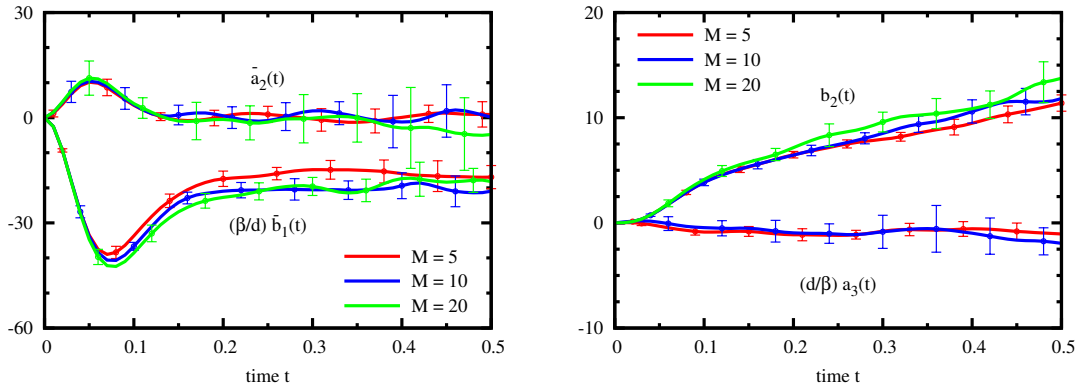

Figure 4.4: Time profiles of the higher-order correction coefficients $\bar{a}_2(t)$, $a_3(t)$, $\bar{b}_1(t)$, and $b_2(t)$. These scalar functions are evaluated from the time correlation functions obtained from MD simulations by using Eqs. (4.2.12) and (4.2.15). The coincidence of the results for various values of M shows the validity of our force decomposition. The error bars correspond to ± 2 standard deviations.

4.3.3 Pulling experiment

To clearly observe the dependence of $\mathbf{F}_1(t)$ on a given moving velocity $\mathbf{U}$, we simulate the pulling experiment. We denote by $\mathbf{F}_0(t)$ the force in the corresponding frozen dynamics (i.e., $\mathbf{U} = 0$) and by $\delta\mathbf{F}^{\mathbf{U}}(t)$ the force difference $\mathbf{F}_1^{\mathbf{U}}(t) - \mathbf{F}_0(t)$. We impose the moving velocity along the x-axis, i.e., $\mathbf{U} = (U_x, 0)$.

The drag force at time t is obtained from the average force $\left\langle \mathbf{F}_1^{\mathbf{U}}(t) \right\rangle$. Alternatively, $\left\langle \delta\mathbf{F}^{\mathbf{U}}(t) \right\rangle$ can be used since $\langle \mathbf{F}_0(t) \rangle = 0$. Although $\mathbf{F}_1^{\mathbf{U}}(t)$ and $\delta\mathbf{F}^{\mathbf{U}}(t)$ have the same mean, they have different variances; the variance of the latter is smaller at short times but it eventually becomes larger. Since $\mathbf{F}_0(t)$ is close to $\mathbf{F}_1^{\mathbf{U}}(t)$ at short times, subtracting it reduces the variance. However, since it eventually becomes independent of $\mathbf{F}_1^{\mathbf{U}}(t)$, subtracting it rather increases the variance. Hence, $\delta\mathbf{F}^{\mathbf{U}}(t)$ is a better estimate for the drag force at short times, whereas $\mathbf{F}_1^{\mathbf{U}}(t)$ is better for large t. In Fig. 4.5(A), the ratios of $\left\langle \mathbf{F}_1^{\mathbf{U}}(t) \right\rangle$ and $\left\langle \delta\mathbf{F}^{\mathbf{U}}(t) \right\rangle$ to $\mathbf{U}$ are compared with the time integral of $K_0(t)$.

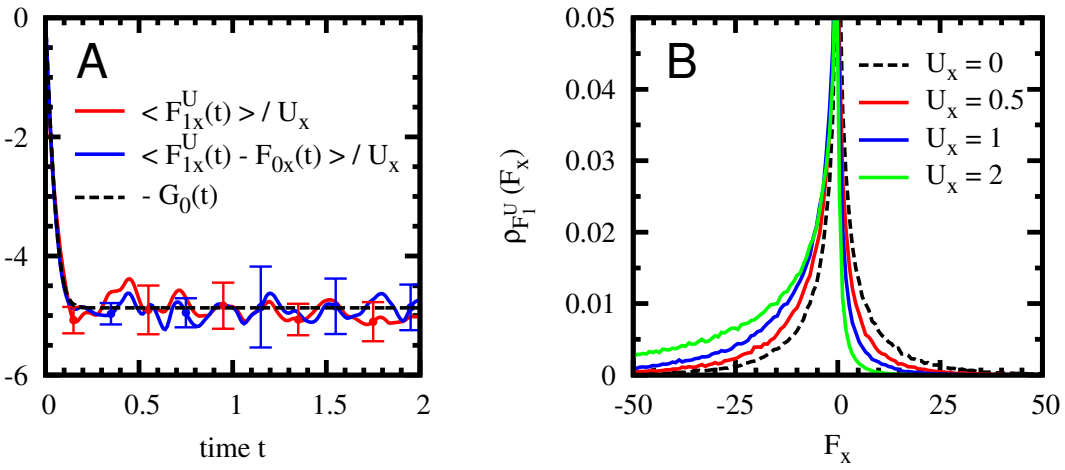

Figure 4.5: Pulling experiment. (A) From the ratio of the average force $\left\langle \mathbf{F}_1^{\mathbf{U}}(t) \right\rangle$ to the pulling velocity $\mathbf{U}$, the time integral of the limit memory function, denoted by $G_0(t)$, and the friction coefficient γ can be estimated. $\left\langle \mathbf{F}_1^{\mathbf{U}}(t) \right\rangle$ can be replaced by $\left\langle \mathbf{F}_1^{\mathbf{U}}(t) - \mathbf{F}_0(t) \right\rangle$. The simulation results for $\mathbf{U} = (0.2, 0)$ are shown with the error bars corresponding to ± 2 standard deviations. (B) The skewness in the stationary distribution of the force $\mathbf{F}_1^{\mathbf{U}}$ against the direction of $\mathbf{U}$ explains the drag force on the pulled Brownian particle. For $\mathbf{U} = (U_x, 0)$, the marginal density for the x-component of $\mathbf{F}_1^{\mathbf{U}}$ is plotted. The statistical errors are very small and error bars are omitted for clear presentation. For larger U_x, the distribution becomes more negatively skewed and the magnitude of the mean force becomes larger.

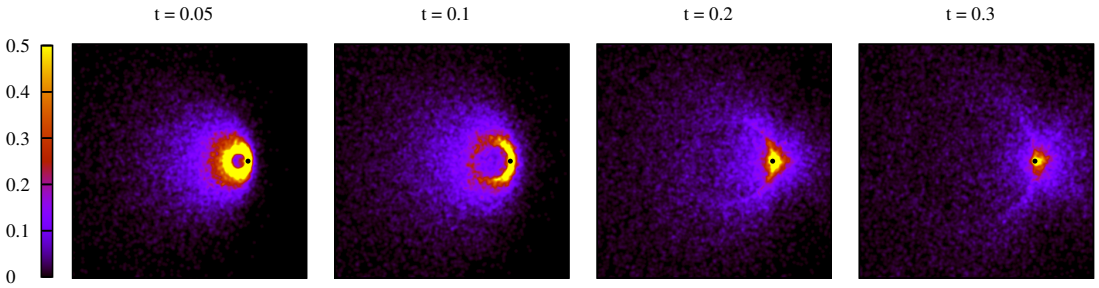

Figure 4.6: Force difference between the frozen and the constant-velocity dynamics in the pulling experiment. Besides the skewness, its distributions at short times exhibit some interesting structures. For $\mathbf{U} = (0.1, 0)$, its densities $\rho_{\delta\mathbf{F}(t)}(F_x, F_y)$ at different times t are plotted. In each plot, the x and y components of a point correspond to F_x and F_y and the color at the point shows the density value $\rho_{\delta\mathbf{F}(t)}$ according to the color box on the left. The region where the density value is greater than 0.5 is colored in yellow. At $t = 0.05$, the density has a local minimum, which is surrounded by the yellow ring. As t becomes larger, although the surrounding ring becomes less distinct, the ring shape is maintained with its diameter increasing. In addition, while the density spreads as t increases, the region in front of the ring shape gains weight.

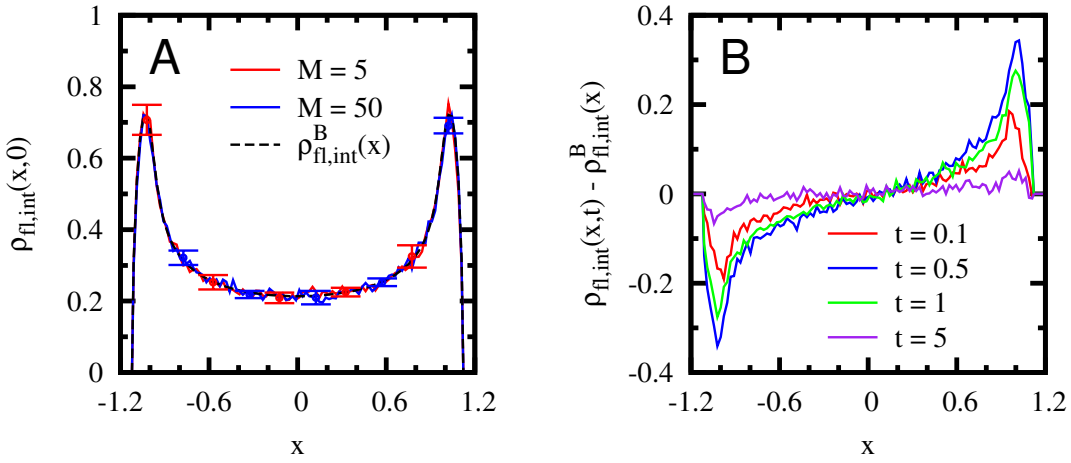

Figure 4.7: Development and decline of the skewness in the fluid environment for the full dynamics. In order to clearly see the skewness in the density of the bath particles located inside the interaction range, its marginal density $\rho_{\mathrm{fl,int}}(x,t)$ along the direction of $\mathbf{V}(0)$ at time t is presented. (A) Initially, the fluid environment is isotropic and $\rho_{\mathrm{fl,int}}(x,0)$ coincides with the theoretical prediction $\rho^{\mathrm{B}}_{\mathrm{fl,int}}(x)$ obtained from the Boltzmann distribution law. (B) The skewness in the marginal density increases as t increases at short times and then decreases and eventually disappears. The results for $M = 5$ are shown. While the simulation results in panel (A) are plotted with the error bars corresponding to ± 2 standard deviations, error bars are omitted in panel (B) for clear presentation.

Now we investigate the distribution of $\mathbf{F}_1(t)$, the mean of which becomes the drag force at time t. The distribution is initially isotropic and, at short times, it becomes more skewed against the direction of $\mathbf{U}$ as t increase. Eventually, it becomes stationary, which gives a stationary value of $\langle \mathbf{F}_1(t) \rangle$. In Fig. 4.5(B), the stationary distribution of the x-component of $\mathbf{F}_1$ is plotted and its dependence on U_x is shown. For short times, the asymmetry developing in the system, which is introduced by pulling, is clearly observed from the distribution of $\delta\mathbf{F}^{\mathbf{U}}(t)$ and shown in Fig. 4.6. We also note that for small $\mathbf{U}$ and small t, the distribution of $\mathbf{A}_1(t)$ can be estimated from this distribution.

4.3.4 Surrounding bath distribution in the full dynamics

Since the instantaneous force on the Brownian particle is determined by the arrangement of the bath particles inside the interaction range, the drag force is closely related to the skewness of the surrounding bath distribution. In order to observe time-transient change in the surrounding bath distribution, we consider the marginal density $\rho_{\mathrm{fl,int}}(x,t)$ of the bath particles inside the interaction range along the direction of $\mathbf{V}(0)$. In other words, for the position $\mathbf{r}$ inside the interaction range of the Brownian particle located at $\mathbf{X}$, x is defined as $(\mathbf{r}-\mathbf{X})\cdot\mathbf{V}(0)/|\mathbf{V}(0)|$. We note that $\rho_{\mathrm{fl,int}}(x,t)$ is a ρ-averaged quantity. For the equilibrium bath density $\rho^{\mathrm{B}}_{\mathrm{fl}}(\mathbf{r})$, the corresponding marginal density is denoted as $\rho^{\mathrm{B}}_{\mathrm{fl,int}}(x)$. In Fig. 4.7(A), the initial marginal densities for two values of M are plotted and compared with $\rho^{\mathrm{B}}_{\mathrm{fl,int}}(x)$. The observed agreement reveals the validity of the assumptions made on the equilibrium distribution ρ.

In Fig. 4.7(B), the skewness developed at different times is observed through $\rho_{\mathrm{fl,int}}(x,t)-\rho^{\mathrm{B}}_{\mathrm{fl,int}}(x)$. The marginal distribution becomes more positively skewed at short times and achieves the maximal skewness. Then, it becomes less skewed and eventually retrieves its initial symmetry. The deviation $\rho_{\mathrm{fl,int}}(x,t)-\rho^{\mathrm{B}}_{\mathrm{fl,int}}(x)$ is observed to be proportional to $M^{-1/2}$. The time $\tau_{\max}$ for the maximal skewness is independent of M and the decay rate of the skewness after $\tau_{\max}$ decreases as M increases.

We note that $\rho_{\mathrm{fl,int}}(x,t)$ is closely related with $\langle\mathbf{V}(0)\cdot\mathbf{F}(t)\rangle$ and that our observations for $\rho_{\mathrm{fl,int}}(x,t)$ are consistent with the time behavior of $\langle\mathbf{V}(0)\cdot\mathbf{F}(t)\rangle$. At short time, it grows negatively as $-\frac{d}{\beta M}\int_0^t K_0(s)ds$ and then it decays asymptotically as $-\frac{d\gamma}{\beta M}\exp(-\frac{\gamma}{M}t)$. The long-time decay of skewness in the surrounding bath distribution can be understood as follows. If we consider a very large number of realizations

of the system with given $\mathbf{V}(0)$, the bath arrangement in each realization tends to be skewed against $\mathbf{V}(0)$ around time $\tau_{\max}$. Similarly, at large time t, the bath arrangement is maximally skewed against $\mathbf{V}(t-\tau_{\max})$. Since the correlation between $\mathbf{V}(t-\tau_{\max})$ and $\mathbf{V}(0)$ decreases exponentially as $\exp(-\frac{\gamma}{M}(t-\tau_{\max}))$, the skewness in the bath arrangement at time t against $\mathbf{V}(0)$ becomes less distinct as t increases.

4.4 Discussion

Based on our theoretical and simulation results, we conclude that the friction force originates from the deviation of the system trajectory due to the movement of a Brownian particle. The trajectories of the surrounding bath particles become perturbed compared to the frozen dynamics and, correspondingly, the deviation of the force on the Brownian particle is observed for each initial configuration of the system. We interpret the force in the frozen dynamics as the thermal noise and the average force deviation over the initial configurations with given initial condition of the Brownian particle as the friction force. Our interpretation explains the physical intuition that the friction force is proportional to the velocity of the Brownian particle. In addition, the microscopic expression for the noise intensity $\Delta = \frac{2}{d}\int_0^\infty \langle \mathbf{F}_0(0)\cdot\mathbf{F}_0(t)\rangle\, dt$, which is obtained by combining Eq. (4.2.21) and the fluctuation-dissipation relation $2\gamma = \beta\Delta$ of Eq. (4.1.2), reveals that the thermal noise becomes the frozen dynamics force in the Brownian limit.

As shown in Eqs. (4.2.26) and (4.2.27), our interpretation is consistent with the memory function approach in the Brownian limit. However, the microscopic interpretations of Eq. (4.1.1) are different, which are explained as follows. Since the fluctuation-dissipation relation, which should be provided with the microscopic

interpretation of Eq. (4.1.1), is expressed by the ensemble average, the microscopic definition of the friction force and the thermal noise for each configuration of the system does not need to be unique. We emphasize that compared with the memory function approach, our approach gives a very clear picture of Brownian motion in the near-Brownian-limit regime. In addition, our approach allows all the quantities introduced in the theory to be evaluated by MD simulations.

Heuristic explanation of the Langevin description in the near-Brownian-limit regime follows through the time scale separation of the microscopic time scale $\tau_{\rm m}$ and the larger Brownian time scale $\tau_{\rm Br}$. While $\tau_{\rm m}$ is chosen as the time that $K_0(t)$ shrinks to zero (i.e., $K_0(t) = 0$ for $t > \tau_{\rm m}$), $\tau_{\rm Br}$ is given as $\frac{M}{\gamma}$ from the exponential decay of the velocity autocorrelation function. If we can assume a time scale τ_* such that $\tau_{\rm m} \ll \tau_* \ll \tau_{\rm Br}$, for each time interval $n\tau_* < t < (n+1)\tau_*$, $\mathbf{V}(t)$ is almost constant, i.e., $\mathbf{V}(t) \approx \mathbf{V}(n\tau_*)$. Hence, after time $\tau_{\rm m}$, the drag force becomes stationary, i.e., for $n\tau_* + \tau_{\rm m} < t < (n+1)\tau_*$, $\mathbf{F}_{\rm fr}(t) = -\gamma \mathbf{V}(n\tau_*)$. By neglecting time-transient behavior of duration $\tau_{\rm m}$, we have $\mathbf{F}_{\rm fr}(t) = -\gamma \mathbf{V}(t)$ on the time scale τ_*. At the same time, since $\mathbf{F}_{\rm th}$ is approximated by $\mathbf{F}_0$ and the correlation length of $\mathbf{F}_0$ is $\tau_{\rm m}$ by the fluctuation-dissipation relation, the autocorrelation function of $\mathbf{F}_{\rm th}$ is approximated by a δ function on the time scale τ_* (i.e., $\mathbf{F}_{\rm th}$ becomes white noise). As explained from Eqs. (4.2.28) and (4.2.29), the independence of $\mathbf{F}_{\rm fr}$ and $\mathbf{F}_{\rm th}$ follows. Since we can achieve the time scale separation by increasing M, the Langevin equation is valid in the Brownian limit. It is also expected that a larger value of M is needed if $K_0(t)$ exhibits an oscillating tail and does not decay fast (i.e., $\tau_{\rm m}$ is large). We note that there is another reason for the failure of the Langevin description for small M. In this case, since the inertia of the fluid cannot be neglected, $K(t)$ has a long tail which extends beyond the microscopic time scale $\tau_{\rm m}$ estimated from $K_0(t)$.

Finally, we note that our approach can be used to investigate interesting results of

the single-particle Brownian motion. We have demonstrated that previously known results for the microscopic theory of Brownian motion are derived, including the formula for γ, the linear response expression for $\mathbf{F}_0$ and $\mathbf{F}_1$, the independence of $\mathbf{F}_{\rm fr}$ and $\mathbf{F}_{\rm th}$ and the fluctuation-dissipation relation in the Brownian limit. We have also explained that, for linear regression $\mathbf{F}^+ = c\mathbf{F} + \xi$ with ξ the error term, the coefficient c is observed to be $1-\mathrm{O}(M^{-1})$. Furthermore, we have obtained the higher-order corrections of the time correlation functions $\langle \mathbf{V}(0)\cdot\mathbf{F}(t)\rangle$ and $\langle \mathbf{F}(0)\cdot\mathbf{F}(t)\rangle$, the forces $\mathbf{F}_{\rm fr}^{\rm Mori}$ and $\mathbf{F}_{\rm th}^{\rm Mori}$, and the memory function $K(t)$. We have also observed the dependence of $\langle \mathbf{F}^+(t)\rangle_\Theta$ on $\mathbf{V}(0)$. Since the leading-order terms cancel in the quantity, the higher-order results are employed to derive the leading term of the quantity. Depending on the magnitude of $\mathbf{V}(0)$, $\langle \mathbf{F}^+(t)\rangle_\Theta$ is parallel or antiparallel to $\mathbf{V}(0)$.

Chapter Five

Rayleigh Gas Model:

Effects of Confinement

5.1 Introduction

The generalized Langevin equation (GLE) approach [168], which is also known as the memory function method, provides an effective tool to analyze the phenomena of Brownian motion and anomalous diffusion. The approach has a solid theoretical background. The equation has been derived from a microscopic equilibrium system [107, 140] and from an incompressible fluid described by the fluctuating hydrodynamics [79] and shown to hold for a broad class of stochastic processes [148]. Reduction to the Langevin equation has been demonstrated on microscopic scales [89] and on hydrodynamic scales [79]. Generalization to nonequilibrium systems has also been considered [95]. In addition, the GLE is versatilely applicable to interpret experimental data over a broad range of time scales. Theoretical predictions on Brownian motion at short time scales have been experimentally confirmed by single-particle tracking techniques in the framework of the GLE [121]. A model based on the GLE and the fractional Gaussian noise has been used to explain subdiffusion dynamics in the conformational fluctuation of a protein molecule [105] and a phenomenological model, which combines the Basset force and the generalized Stokes force, has been proposed for the hydrodynamic and subdiffusive motion of a tracer in a viscoelastic medium [69].

There are two types of the GLE approach. In the first approach, diffusion and velocity relaxation of a tracer particle are investigated through the *deterministic* GLE, which is formally derived by the projection operator technique [107, 140]. Two essential quantities are the memory function and the autocorrelation function of the fluctuating force. They are related by the fluctuation-dissipation theorem [107, 140], and several methods have been proposed to determine these functions from trajectory realizations [22, 101, 136, 164]. The temporal behavior of the velocity autocorrela-

tion function and the mean square displacement function is explained by the memory function [102, 164, 194]. In addition, whether the diffusion is normal or anomalous is determined by the tail behavior of the memory function [100, 139]; only if the time integral of the memory function converges to a positive value, the diffusion is normal. On the other hand, the second approach employs the *stochastic* GLE, where the fluctuating force in the deterministic GLE is replaced by an independent random noise process. Considering that the relationship between the fluctuating force and the velocity is complicated in the deterministic GLE, the stochastic GLE is more easily investigated analytically and numerically and used in stochastic modeling. For a Gaussian random process (such as the Gaussian colored noise or the fractional Gaussian noise) and a certain analytic form of the memory function (such as exponential and power-law decaying functions), plenty of analytic results are available [33, 104, 155, 168, 186, 190]. Also, one can use standard numerical techniques to generate sample trajectories of the stochastic GLE [9, 168].

If the mass of a tracer particle is much larger than that of a fluid particle, the time scale of the movement of the former is correspondingly larger than that of the latter. Due to large time scale separation, the motion of the Brownian particle is approximately described by a Markovian process (i.e., the Langevin equation) [172]. Complete time scale separation would occur in the Brownian limit, where the Brownian particle has an infinite mass. Microscopically, this corresponds to the *frozen* dynamics, where the Brownian particle is fixed and the fluid particles move under the presence of the Brownian particle. The force autocorrelation function of this dynamics provides information not only for the macroscopic Markovian description through the adiabatic approximation but also for the microscopic description of systems in the near-Brownian-limit regime. The friction coefficient in the Langevin equation is calculated from the time integral of the frozen dynamics force autocorrelation func-

tion. As the mass M of the Brownian particle increases, the autocorrelation function of the fluctuating force converges to the frozen-dynamics force autocorrelation function and, by the fluctuation-dissipation theorem, the Brownian limit of the memory function, which we will call the *limit memory function*, is also obtained by the frozen dynamics [51]. An asymptotic expression for the velocity autocorrelation function with respect to M is available in terms of the limit memory function [97].

In this chapter, we investigate Brownian motion in a confined Rayleigh gas through the deterministic GLE. The Rayleigh gas is a simplified model consisting of a heavy Brownian particle and a surrounding *ideal* gas, where elastic collisions of the Brownian particle with gas particles are usually assumed. Owing to the noninteracting bath assumption, hydrodynamic effects of the surrounding fluid become suppressed whereas the effects of direct interaction between the Brownian particle and gas particles become dominant. The unconfined Rayleigh gas has been extensively studied by analytic means. It has been proved that the motion of the Brownian particle converges to the Ornstein–Uhlenbeck process in the Brownian limit [39, 175]. The friction coefficient [44, 70, 96, 138] and the velocity autocorrelation function [88, 128] have been obtained by various techniques. The convergence proofs have also been given for the systems generalized in the following ways: the Brownian particle has a convex shape and rotates [40]; the space is confined by a wall [19]; there are several Brownian particles and the elastic collisional dynamics is replaced by dynamics under a continuous interaction potential [108]. In a confined Rayleigh gas, a gas particle can perform a series of collisions alternately with the Brownian particle and the boundary wall. As a result, the interaction between the Brownian particle and the ideal gas becomes complicated and a long-time tail in the memory function is expected to emerge. Although a tail is also present in the memory function in the unconfined case, it decays exponentially and its magnitude becomes negligible when

the mass of the Brownian particle is sufficiently large [88]. Hence, by investigating the long-time tail in the memory function of the confined case, we discuss the effects of confinement in the Rayleigh gas. More specifically, we observe the power-law tail and investigate its dependence on system parameters such as the dimensionality of the space and the size of confinement. In addition, we investigate the effects of the stochastic thermal wall satisfying Maxwell boundary condition [178, 180]. However, we note that the confinement effects observed in our model are different in nature from those on Brownian motion in a liquid, where hydrodynamic interactions play an important role [21, 91, 189].

We use both an analytical approach and molecular dynamics (MD) simulation approach in a complementary way, which have been employed to investigate the memory function of the unconfined Rayleigh gas with a continuous interaction potential function [96]. From the analytical approach, we obtain an expression for the limit memory function by using an analytic expression of the frozen dynamics force autocorrelation function. In the frozen dynamics of the Rayleigh gas model, the dynamics of each gas particle becomes decoupled from those of the other gas particles and, thus, each relevant physical quantity is written as an ensemble average of a functional of the single-gas-particle trajectory. On the other hand, from the MD simulation approach, we investigate the system with a finite-mass Brownian particle and/or the stochastic thermal walls. However, in general, analyzing the tail of a time correlation function by means of MD simulations is not so straightforward due to the difficulty in accurately estimating the time correlation function over a large time interval. In this case, analytic results for the limiting situation are very helpful for guiding the MD simulation approach. In turn, we also confirm the analytic results by the MD simulation results.

In order to make full use of analytic features, we consider a cube of fixed ori-

entation as the Brownian particle rather than a spherical shape. We shall see that by assuming all collisions are elastic, the diffusions along the directions other than the transverse direction[1] to the channel become identical to the unconfined case and decoupled from the one along the transverse direction in the Brownian limit. Since the generalization to a higher-dimensional space is straightforward, we consider a hypercube in d-dimensional space with $d \geq 2$. A similar setting of the system (a hypercube in a half space confined by a single wall) has been considered in the mathematical proof for the convergence of the diffusion process [19]. A sufficient condition for the convergence has been given in terms of the velocity distribution of gas particles. For the three-dimensional equilibrium ideal gas, which satisfies the condition, the diffusion process in the Brownian limit becomes the Ornstein–Uhlenbeck-type process with a position-dependent friction coefficient. However, it has been pointed out that the condition does not hold in the two-dimensional equilibrium case, which suggests the possibility of failure in converging to normal diffusion. We shall see that the tail of the memory kernel decays like t^{-1} in the two-dimensional case with the elastic walls, which implies anomalous diffusion.

The rest of the chapter is organized as follows. In Section 5.2, we explain the system. In Section 5.3, we present analytic results. In Section 5.4, we show MD simulation results. In Section 5.5, we provide the derivation of two analytic results: the GLE and the frozen dynamics force autocorrelation function. In Section 5.6, we present a summary and discussion.

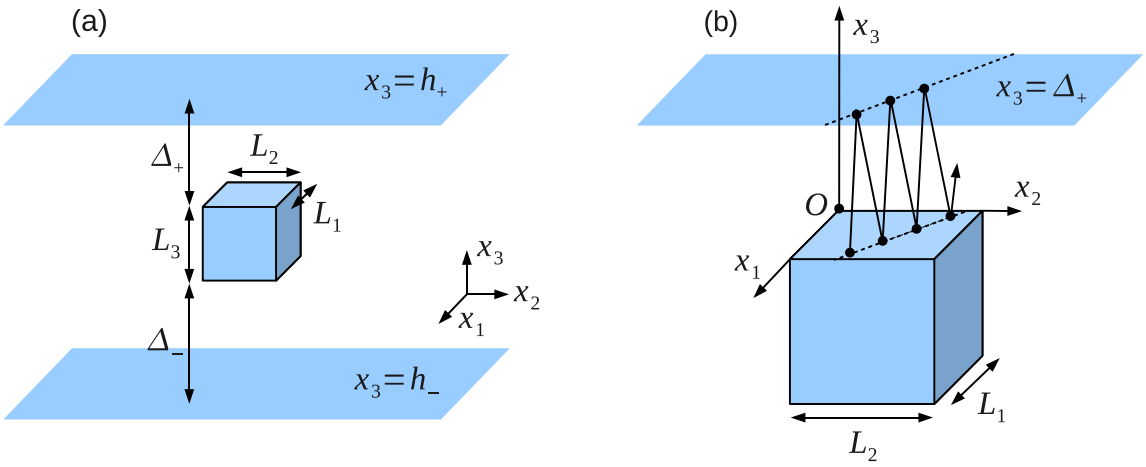

Figure 5.1: In panel (a), the geometry of the system is depicted for the three-dimensional case. For the definitions of the symbols, see the text. In panel (b), a trajectory of a gas particle colliding alternatively with the (purely elastic) upper wall and the upper face of the fixed cube is depicted.

5.2 System

We consider the d-dimensional space with $d \geq 2$ and denote the coordinates of a point as $(x_1, x_2, \cdots, x_d)$. Two parallel walls normal to the x_d-axis are located at $x_d = h_\pm$. In the space between the two walls, a hypercube with sides L_1, L_2, $\cdots$, L_d is placed. We fix the orientation of the cube so that the edges with length L_i $(i = 1, 2, \cdots, d)$ are parallel to the x_i-axes, respectively. Then, two faces of the cube are parallel to the walls. Depending on their x_d-coordinates, we call the two walls as the upper and lower walls and the two faces of the hypercube as the upper and lower faces. We also call the direction parallel to the x_d-axis as the transverse direction (to the channel). The remaining space between the walls is filled with an *ideal* gas. We denote the mass of a gas particle as m and the number density of the gas as a, respectively. For the geometry of the walls and the hypercube for $d = 3$, see Fig. 5.1 (a).

[1]The definition of the transverse and longitudinal directions used in this chapter may be opposite to what has been employed in some literature.

We first explain the dynamics of the system with a *finite-mass* hypercube and *elastic* walls. For the frozen dynamics and the stochastic thermal walls, see below. We denote the mass of the hypercube as M and assume that it collides with a gas particle elastically. When a gas particle with velocity $(v_1, v_2, \cdots, v_d)$ collides with the hypercube with velocity $(V_1, V_2, \cdots, V_d)$ through one of the faces normal to the x_i-axis, the ith velocity components of the gas particle and the hypercube become

$$v_i \to v_i - \frac{2M}{m+M}(v_i - V_i), \quad V_i \to V_i + \frac{2m}{m+M}(v_i - V_i), \tag{5.2.1}$$

respectively, and the other components do not change. When a gas particle collides with one of the elastic walls, its velocity $(v_1, v_2, \cdots, v_d)$ becomes $(v_1, v_2, \cdots, -v_d)$. We assume that gas particles do not interact among themselves.

In addition, we introduce a harmonic potential to the hypercube along the transverse direction. By denoting the force constant as k, the hypercube located at $(X_1, X_2, \cdots, X_d)$ experiences the linear restoring force $(0, 0, \cdots, -kX_d)$. In order to avoid the direct interaction of the hypercube with the walls, we assume that k is sufficiently large so that there is almost no chance for it to reach the walls. We note that in the Brownian limit considered in Ref. [19] (i.e., $m \to 0$ while the mass and the size of the cube are kept fixed and the number density and the velocity distribution of the ideal gas are appropriately scaled), it has been proved that the cube never reaches the wall. We also note that a similar experimental setting (i.e., a particle under a harmonic potential, which is suspended in a liquid confined by a wall) has been employed to investigate confined colloidal diffusion at hydrodynamic scales by the optical trap technique [21, 91, 189].

We assume that the system is in equilibrium and obeys the Boltzmann distribution. We denote the inverse temperature of the system by $\beta = (k_{\mathrm{B}}T)^{-1}$. We call

this dynamics (i.e., with the finite-mass hypercube under the harmonic potential) *full dynamics*.

Frozen dynamics In this dynamics, the hypercube is assumed to have an infinite mass so that it is held fixed at given position regardless of elastic collisions with gas particles. If a gas particle with velocity $(v_1, v_2, \cdots, v_d)$ collides with a face normal to the x_i-axis, the ith component becomes $-v_i$ and the other components do not change. We denote the distances between the upper wall and the upper face and between the lower wall and the lower face as Δ_+ and Δ_-, see Fig. 5.1 (a). We note that, in the frozen dynamics, neither M nor k is defined and the separation distances $\Delta_\pm$ are given as parameters.

Thermal walls We employ a stochastic thermal wall model satisfying the Maxwell boundary condition [178, 180]. We first explain the thermalizing procedure of the gas-particle velocity at the walls. If a gas particle collides with one of the walls, the particle is instantly released from the wall with a randomly sampled velocity $(v_1, v_2, \cdots, v_d)$ from the following distributions

$$\psi_\parallel(v_i) = \sqrt{\frac{\beta m}{2\pi}} e^{-\frac{1}{2}\beta m v_i^2}, \quad i = 1, 2, \cdots, d-1, \tag{5.2.2a}$$

$$\psi_\perp(v_d) = \beta m |v_d| e^{-\frac{1}{2}\beta m v_d^2}, \tag{5.2.2b}$$

where $\psi_\perp(v_d)$ is defined for $v_d > 0$ at the lower wall and for $v_d < 0$ at the upper wall. Then, we define the accommodation factor $0 \leq \phi \leq 1$, which is the probability that gas particles are thermalized when colliding with the walls. We call the cases $\phi = 0$ and $\phi = 1$, respectively, purely elastic and fully thermalizing walls.

5.3 Analytic results

Throughout this section, we only consider the purely elastic walls so that every collision occurring in the system is elastic and the dynamics is deterministic. We present analytic results as follows. We first consider the full dynamics and present the form of the GLE for the finite-mass hypercube in Section 5.3.1. Then, we investigate its Brownian limit. We provide an analytic expression of the frozen dynamics force autocorrelation function and investigate its power-law decaying tail in Section 5.3.2. We obtain the limit memory function in Section 5.3.3. We discuss the Langevin description and obtain its position-dependent friction coefficients in Section 5.3.4. We present the derivation of the GLE and the frozen dynamics force autocorrelation function in Section 5.5.

5.3.1 GLE

By using the Mori projection method [140, 168], we show in Section 5.5.1 that the position $\mathbf{X} = (X_1, X_2, \cdots, X_d)$ and velocity $\mathbf{V} = (V_1, V_2, \cdots, V_d)$ of the hypercube having mass M satisfy the following GLE:

$$\dot{X}_i(t) = V_i(t), \tag{5.3.1a}$$

$$M\dot{V}_i(t) = -\int_0^t K_i(t-s)V_i(s)ds + F_i^+(t), \quad i = 1, 2, \cdots, d-1, \tag{5.3.1b}$$

$$\dot{X}_d(t) = V_d(t), \tag{5.3.1c}$$

$$M\dot{V}_d(t) = -kX_d(t) - \int_0^t K_d(t-s)V_d(s)ds + F_d^+(t), \tag{5.3.1d}$$

where the memory function $K_i(t)$ and the fluctuating force $F_i^+(t)$ satisfy the fluctuation-dissipation relation

$$K_i(t) = \beta \left\langle F_i^+(0) F_i^+(t) \right\rangle, \quad i = 1, 2, \cdots, d, \tag{5.3.2a}$$

$$\left\langle F_i^+(0) F_j^+(t) \right\rangle = 0, \quad \text{for } i \neq j. \tag{5.3.2b}$$

In addition, the fluctuating force is uncorrelated with $X_d(0)$ and $\mathbf{V}(0)$:

$$\left\langle X_d(0) F_i^+(t) \right\rangle = 0, \quad i = 1, 2, \cdots, d, \tag{5.3.3a}$$

$$\left\langle V_i(0) F_j^+(t) \right\rangle = 0, \quad i, j = 1, 2, \cdots, d. \tag{5.3.3b}$$

We note that since $\mathbf{V}(t)$ changes discontinuously whenever it collides with gas particles, its time derivative $\dot{\mathbf{V}}(t) = \frac{1}{M}\mathbf{F}(t)$ is understood as a formal derivative containing a series of Dirac delta functions and so is the fluctuating force. We also note that Eq. (5.3.1) is exact and equivalent to the original time evolution equation although, in general, it cannot be used to generate sample trajectories because the fluctuating force is very complicatedly related with $\mathbf{X}$ and $\mathbf{V}$.

In order to derive the GLE, we make the assumption that the harmonic potential is so stiff that the direct interaction between the hypercube and the walls is negligible. In Section 5.5.1.1, we show that in this case the following equilibrium distribution of the hypercube along the transverse direction can be assumed:

$$\rho(X_d) = \sqrt{\frac{\beta k}{2\pi}} e^{-\frac{1}{2}\beta k X_d^2}. \tag{5.3.4}$$

Since this distribution becomes exactly valid in the case that the hypercube is subject to a harmonic potential but suspended in an unbounded ideal gas, Eq. (5.3.1) is exact in the latter case.

5.3.2 Frozen dynamics force autocorrelation function

Denoting the force exerted on the fixed hypercube by the ideal gas as $\mathbf{F}_0 = (F_{0,1}, F_{0,2}, \cdots, F_{0,d})$, we derive the following analytic expression for the frozen dynamics force autocorrelation in Section 5.5.2:

$$\langle F_{0,i}(0)F_{0,i}(t)\rangle = \frac{8a}{\beta}\sqrt{\frac{2m}{\pi\beta}}\left(\prod_{\substack{j=1\\ j\neq i}}^{d} L_j\right)\delta(t), \quad i = 1, 2, \cdots, d-1, \tag{5.3.5a}$$

$$\langle F_{0,d}(0)F_{0,d}(t)\rangle = \frac{8a}{\beta}\sqrt{\frac{2m}{\pi\beta}}\left(\prod_{j=1}^{d-1} L_j\right)\delta(t) + I_2^+(t) + I_2^-(t). \tag{5.3.5b}$$

Here, $I_2^{\pm}(t) = I_2(t;\Delta_{\pm})$, where

$$I_2(t;\Delta) = A(t;\Delta)\prod_{i=1}^{d-1} B(t;L_i), \tag{5.3.6a}$$

$$A(t;\Delta) = 4am^2\sum_{n=1}^{\infty}\frac{(2n\Delta)^4}{t^5}\varphi\left(\frac{2n\Delta}{t}\right), \tag{5.3.6b}$$

$$B(t;L) = L\,\mathrm{erf}\left(\frac{L}{t}\sqrt{\frac{\beta m}{2}}\right) - t\sqrt{\frac{2}{\pi\beta m}}\left(1 - e^{-\frac{\beta m L^2}{2t^2}}\right), \tag{5.3.6c}$$

with $\varphi(v) = \sqrt{\frac{\beta m}{2\pi}}e^{-\frac{\beta m}{2}v^2}$ and $\mathrm{erf}(x) = \frac{2}{\sqrt{\pi}}\int_0^x e^{-y^2}dy$. The longitudinal-direction force autocorrelation functions $\langle F_{0,i}(0)F_{0,i}(t)\rangle$ $(i = 1, 2, \cdots, d-1)$ contain only a delta function[2]. This indicates that the effects of collisions are instantaneous and uncorrelated as in the unbounded case. On the other hand, the transverse-direction force autocorrelation function $\langle F_{0,d}(0)F_{0,d}(t)\rangle$ contains also slowly decaying parts $I_2^+(t)$ and $I_2^-(t)$, which result from repeated collisions with the upper and lower wall, respectively. As $\Delta \to \infty$, $I_2^{\pm}(t)$ becomes zero and we retrieve the unbounded case.

We make the following observations on the time profile of $I_2(t;\Delta)$. It is zero

[2] we use $\int_0^{\infty}\delta(t)dt = \frac{1}{2}\int_{-\infty}^{\infty}\delta(t)dt = \frac{1}{2}$ rather than $\int_0^{\infty}\delta(t)dt = 1$.

at $t = 0$ and nonnegative for all t. At short times, it has very small values until it exhibits a sharp increase and attains a maximum, and then it monotonically decreases to zero. The short-time behavior of $I_2(t;\Delta)$ is explained by that it takes time for a gas particle to collide again with the hypercube. Hence, the time when the maximum value appears is of the order of $\Delta/\langle|v_d|\rangle$. On the other hand, at large time t, $A(t;\Delta)$ and $B(t;L)$ become

$$A(t;\Delta) \approx \frac{2am^2}{\Delta}\int_0^\infty y^4\varphi(y)dy = \frac{3a}{\beta^2\Delta}, \tag{5.3.7a}$$

$$B(t;L) \approx \frac{L^2}{t}\sqrt{\frac{\beta m}{2\pi}}. \tag{5.3.7b}$$

Hence, we obtain

$$I_2(t;\Delta) \approx \frac{3a}{\beta^2}\left(\frac{\beta m}{2\pi}\right)^{\frac{d-1}{2}}\frac{L_1^2L_2^2\cdots L_{d-1}^2}{t^{d-1}\Delta}, \tag{5.3.8}$$

and observe that the tail decays like $t^{-(d-1)}$. In addition, we observe that at large times the magnitude of the tail is inversely proportional to the separation distance Δ and proportional to the square of the area of the upper or lower face.

In Fig. 5.2, the time profile of $\langle F_{0,d}(0)F_{0,d}(t)\rangle$ is shown for the two-dimensional case. If the hypercube is fixed at the center of the channel (i.e., $\Delta_+ = \Delta_- = \Delta$), $\langle F_{0,d}(0)F_{0,d}(t)\rangle = \frac{2}{\beta}\gamma_d^*\delta(t) + 2I_2(t;\Delta)$ and we observe the shape of $I_2(t;\Delta)$. Otherwise, the tail may have two local maxima as a result of superposing $I_2(t;\Delta_+)$ and $I_2(t;\Delta_-)$.

5.3.3 Limit memory function

As the mass of the Brownian particle increases, the memory function $K_i(t)$ defined in Eq. (5.3.1) converges to the limit memory function $K_i^{\mathrm{BL}}(t)$, where BL stands for the Brownian limit $M \to \infty$. Compared with the free Brownian case in an unbounded

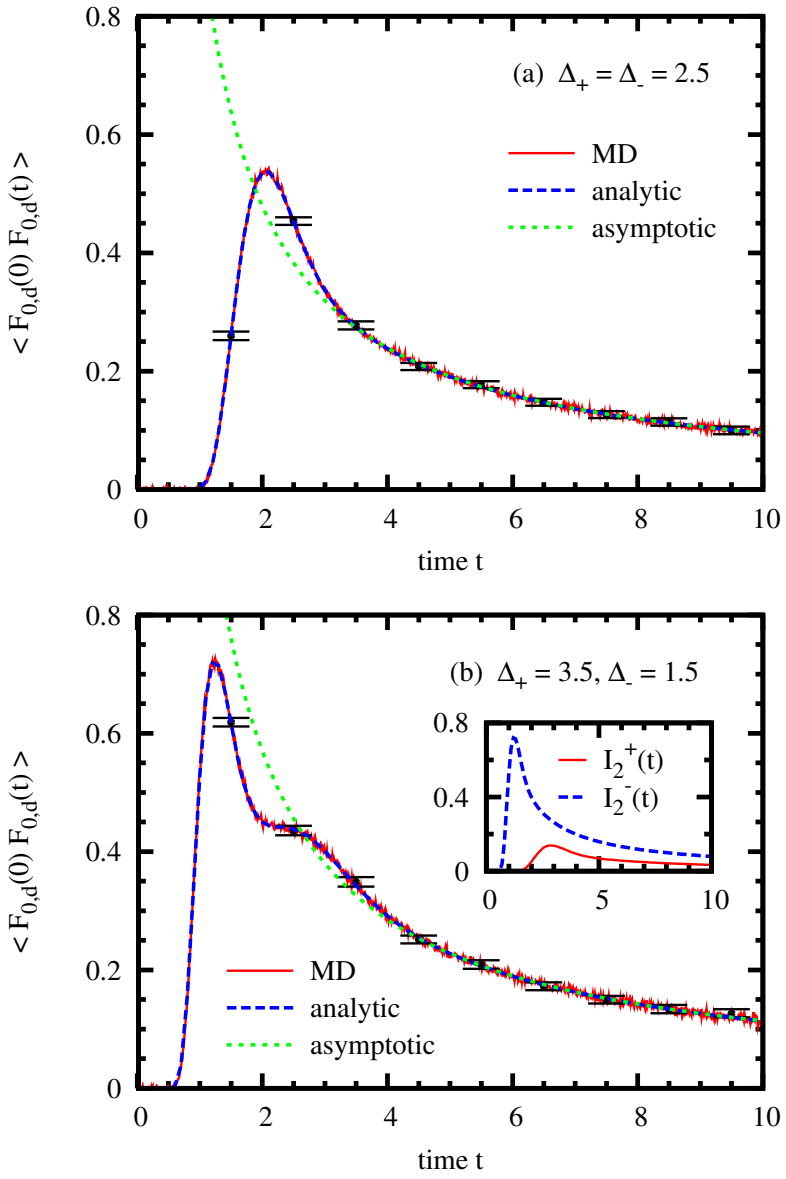

Figure 5.2: The frozen dynamics force autocorrelation function for the transverse direction to the channel in the two-dimensional case. The width of the channel is 6 (i.e., $h_\pm = \pm 3$) and the hypercube has sides $L_1 = L_2 = 1$ and is fixed at $X_d = 0$ (i.e., $\Delta_\pm = 2.5$) in panel (a) and at $X_d = -1$ (i.e., $\Delta_+ = 3.5$ and $\Delta_- = 1.5$). The other parameters are given as $m = a = \beta = 1$. The analytic result (depicted by the dashed line), see Eq. (5.3.5b), is compared with the frozen dynamics MD simulation result (depicted by the solid line). The error bars correspond to statistical errors with two standard deviations. The long-time asymptotic result, see Eq. (5.3.8), is also plotted by the dotted line. In the inset of panel (b), the time profiles of $I_2^\pm(t) = I_2(t; \Delta_\pm)$, see Eq. (5.3.6), are plotted.

space, where a simple relation $K_i^{\mathrm{BL}}(t) = \beta \langle F_{0,i}(0) F_{0,i}(t) \rangle$ holds, the frozen dynamics force autocorrelation function depends on the position of the hypercube (through the separation distance $\Delta_\pm$) and the limit memory function $K_i^{\mathrm{BL}}(t)$ is expected to be expressed as the average of $\langle F_{0,i}(0) F_{0,i}(t) \rangle$ over the equilibrium distribution of the hypercube. By assuming

$$K_i^{\mathrm{BL}}(t) = \beta \int \rho(X_d) \langle F_{0,i}(0) F_{0,i}(t) \rangle \, dX_d \tag{5.3.9}$$

and using Eq. (5.3.5), we obtain the limit memory function as follows:

$$K_i^{\mathrm{BL}}(t) = 2\gamma_i^* \delta(t), \quad i = 1, 2, \cdots, d-1, \tag{5.3.10a}$$

$$K_d^{\mathrm{BL}}(t) = 2\gamma_d^* \delta(t) + \tilde{K}_d^{\mathrm{BL}}(t), \tag{5.3.10b}$$

where

$$\gamma_i^* = 4a\sqrt{\frac{2m}{\pi\beta}} \prod_{\substack{j=1 \\ j \neq i}}^{d} L_j, \quad i = 1, 2, \cdots, d, \tag{5.3.11}$$

$$\tilde{K}_d^{\mathrm{BL}}(t) = \beta \int \rho(X_d) \left[I_2(t; \Delta_+) + I_2(t; \Delta_-) \right] dX_d. \tag{5.3.12}$$

We note that the separation distances $\Delta_\pm$ are functions of X_d defined as $\Delta_+ = h_+ - X_d - \frac{1}{2}L_d$ and $\Delta_- = X_d - \frac{1}{2}L_d - h_-$, see Fig. 5.1 (a). In addition, by letting $\Delta \to \infty$, we see that γ_i^* is the friction coefficient of the unbounded case. Rather than analytically investigating the convergence of $K_i(t)$ to $K_i^{\mathrm{BL}}(t)$ in the Brownian limit or the validity of Eq. (5.3.9), numerical validation by using MD simulations is performed, see Fig. 5.7.

5.3.4 Langevin description

Based on the adiabatic approximation due to time scale separation, the following Langevin equation is proposed in the Brownian limit:

$$\dot{X}_i(t) = V_i(t), \tag{5.3.13a}$$

$$M\dot{V}_i(t) = -\gamma_i^* V_i(t) + \Gamma_i(t), \quad i = 1, 2, \cdots, d-1, \tag{5.3.13b}$$

$$\dot{X}_d(t) = V_d(t), \tag{5.3.13c}$$

$$M\dot{V}_d(t) = -kX_d(t) - \gamma_d(X_d)V_i(t) + \Gamma_d(t), \tag{5.3.13d}$$

where γ_i^* and $\gamma_d(X_d)$ are the friction coefficients in the corresponding directions and $\Gamma_i(t)$ $(i = 1, 2, \cdots, d)$ is Gaussian white noise.

For the longitudinal directions $(i = 1, 2, \cdots, d-1)$, γ_i^* is expressed by Eq. (5.3.11) from $\gamma_i^* = \beta \int_0^\infty \langle F_{0,i}(0)F_{0,i}(t)\rangle$ and the noise correlation is correspondingly given as $\langle \Gamma_i(t)\Gamma_j(t')\rangle = \frac{2\gamma_i^*}{\beta}\delta_{ij}\delta(t-t')$. Hence, the Langevin description in these directions is identical to the unbounded case. On the other hand, for the transverse direction, since $\langle F_{0,d}(0)F_{0,d}(t)\rangle$ depends on the position of the hypercube through X_d, $\gamma_d(X_d)$ becomes a position-dependent friction coefficient. For $d = 2$, since the time integral of $\langle F_{0,d}(0)F_{0,d}(t)\rangle$ diverges from Eq. (5.3.8), the Langevin description fails and anomalous diffusion is expected. For $d \geq 3$, we have

$$\gamma_d(X_d) = \gamma_d^* + \delta\gamma(\Delta_+) + \delta\gamma(\Delta_-), \quad \text{where } \delta\gamma(\Delta) = \beta \int_0^\infty I_2(t;\Delta)dt. \tag{5.3.14}$$

We note that due to the presence of the walls, γ_d depends on the separation distances $\Delta_\pm$ and becomes larger than the unconfined one. In case of normal diffusion, $\Gamma_d(t)$ is given as $\sqrt{\frac{2\gamma_d(X_d)}{\beta}}\dot{W}_t$, where W_t is the standard Wiener process independent of $\Gamma_i(t)$.

An asymptotic expression of $\delta\gamma(\Delta)$ for large Δ is obtained as follows. As Δ becomes larger, it takes longer time for a gas particle to recollide with the wall and the time interval where $A(t;\Delta)$ attains considerable values appears later. In this case, we approximate $I_2(t;\Delta)$ in Eq. (5.3.6a) by replacing $B(t;L)$ with its long-time asymptotic expression given in Eq. (5.3.7b). Then, by integrating this with respect to t, we obtain

$$\delta\gamma(\Delta) \approx 64am^2\beta \left(\frac{\beta m}{2\pi}\right)^{d/2} \frac{L_1^2 L_2^2 \cdots L_{d-1}^2}{\Delta^{d-1}} \sum_{n=1}^{\infty} \frac{1}{n^{d-1}} \int_0^\infty y^{d+2} e^{-2\beta m y^2} dy. \tag{5.3.15}$$

From Eq. (5.3.15), we see that for $d = 2$, $\delta\gamma(\Delta)$ diverges and for higher d, it is proportional to $\Delta^{-(d-1)}$. For $d = 3$, Eq. (5.3.15) becomes

$$\delta\gamma(\Delta) \approx \frac{a}{3}\sqrt{\frac{2\pi m}{\beta}} \frac{L_1^2 L_2^2}{\Delta^2}. \tag{5.3.16}$$

In Fig. 5.3, the dependence of $\delta\gamma(\Delta)$ on Δ is plotted for $d = 3$ and compared with Eq. (5.3.16).

Before closing this section, we obtain the friction coefficient $\gamma_{d-\text{sphere}}$ of a d-dimensional hypersphere by using the analytic expression of $\langle F_{0,i}(0)F_{0,i}(t)\rangle$. We note that its δ-weight is proportional to the area of corresponding face and that the contribution of the collisions on an area element is uncorrelated with that on the other area elements. Hence, we can define its density $\overline{\langle \mathbf{F}_0(0)\cdot\mathbf{F}_0(t)\rangle} = \frac{4a}{\beta}\sqrt{\frac{2m}{\pi\beta}}\delta(t)$ per unit area, from which the friction coefficient $\gamma_{d-\text{sphere}}$ for a hypersphere of radius R in the unbounded d-dimensional space is obtained. By denoting the area of the hypersphere as $S_{d-1}(R)$, we have $\langle \mathbf{F}_0(0)\cdot\mathbf{F}_0(t)\rangle = \overline{\langle \mathbf{F}_0(0)\cdot\mathbf{F}_0(t)\rangle} S_{d-1}(R)$. From the relation $\gamma = \frac{\beta}{d}\int_0^\infty \langle \mathbf{F}_0(0)\cdot\mathbf{F}_0(t)\rangle\, dt$ for the isotropic case [89], we obtain

$$\gamma_{d-\text{sphere}} = 2a\frac{\pi^{(d-1)/2}}{\Gamma\left(\frac{d}{2}+1\right)}\sqrt{\frac{2m}{\beta}}R^{d-1}. \tag{5.3.17}$$

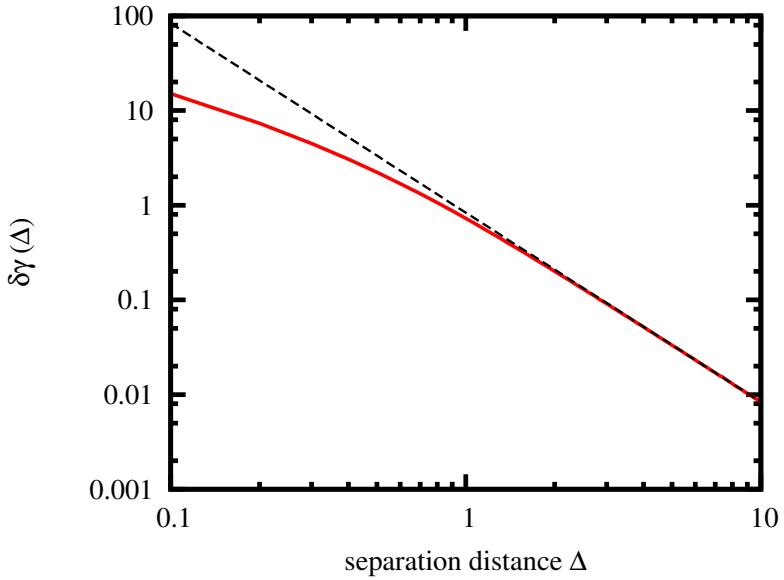

Figure 5.3: Log-log plot of the increment $\delta\gamma(\Delta)$ in the transverse-direction friction coefficient γ_d due to the wall separated by distance Δ, see Eq. (5.3.14), versus Δ. The result is obtained from the three-dimensional case and the other parameters are given as $L_1 = L_2 = 1$, and $m = a = \beta = 1$. The asymptotic expression of $\delta\gamma(\Delta)$ for large Δ, see Eq. (5.3.16), is also plotted by the dotted line.

This general formula coincides with the previous results for $d = 2$ and 3 [44, 70, 96, 128, 138] and even for $d = 1$ [31]. We also note that a similar argument can be applied to the computation of the friction coefficient of a convex body [40].

5.4 MD simulation results

In this section, we present MD simulation results for the frozen and full dynamics of the two- and three-dimensional confined Rayleigh gas. In Section 5.4.1, we explain the MD procedures as well as the simulation parameters. In Section 5.4.2, we confirm the analytic results for the frozen dynamics and investigate the effects of the thermal walls. In Section 5.4.3, we observe the memory function of the finite-mass hypercube under the harmonic potential.

5.4.1 MD procedures

Physical parameters For the two-dimensional system, a square with $L_1 = L_2 = 1$ in a channel of width $H_{\text{channel}} = 6$ (i.e., $h_\pm = \pm 3$) is considered. In order to mimic an infinite channel, the length of the channel is set as $L_{\text{channel}} = 100$ and periodic boundary condition is imposed along the direction of the channel axis. The mass m of a gas particle and the inverse temperature β and number density a of the ideal gas are chosen as $m = \beta = a = 1$. In the frozen dynamics, the hypercube is fixed in the middle of the channel (i.e., $\Delta_\pm = 2.5$) and the accommodation factor ϕ of the thermal walls is varied from $\phi = 0$ (purely elastic) to $\phi = 1$ (fully thermalizing). The hypercube fixed at $X_d = -1$ (i.e., $\Delta_+ = 3.5$ and $\Delta_- = 1.5$) is also simulated with $\phi = 0$. In the full dynamics, the force constant k of the harmonic potential is chosen as $k = 4$, 6, and 8 and the mass M of the square is chosen as $M = 10$, 20, 50, 100, 200, and 500. Only the purely elastic walls are considered. For the frozen dynamics of the three-dimensional system, a cube with $L_1 = L_2 = L_3 = 1$ in a channel with $H_{\text{channel}} = 6$ is considered and periodic boundary condition with $L_{\text{channel}} = 100$ is imposed to the x_1- and x_2-axes. While the same values $m = \beta = 1$ are used, $a = 0.01$ is used to reduce the mean number of the gas particles. The value of ϕ is varied from $\phi = 0$ to $\phi = 1$.

In order to investigate the case of a single-wall system, we additionally simulate the frozen dynamics of the two- and three-dimensional systems with larger values of $H_{\text{channel}} = 12$, 24, and 48 but with $\Delta_+ = 2.5$ fixed and observe $\langle F_+(0)F_+(t)\rangle$. When we increase the volume of the system, we correspondingly decrease the value of a so that the mean number of the gas particles remains the same, which is for computational convenience. Since the frozen dynamics force autocorrelation is linearly proportional to a, we normalize it by a before comparison.

Generating initial configurations For the frozen dynamics, the initial configuration of the ideal gas is sampled from Eq. (5.5.13). In other words, the number of the gas particles is sampled from the Poisson distribution with mean $a(H_{\text{channel}}L_{\text{channel}} - L_1L_2)$ for $d = 2$ and $a(H_{\text{channel}}L_{\text{channel}}^2 - L_1L_2L_3)$ for $d = 3$. Then, the position and velocity of each gas particle are sampled from the uniform distribution and the Maxwell–Boltzmann distribution, respectively. For the full dynamics, the initial position $(X_1, X_2, \cdots, X_d)$ of the hypercube is determined as follows: $X_1 = \cdots = X_{d-1} = 0$ and X_d is sampled from Eq. (5.3.4). Its velocity is sampled from the Maxwell–Boltzmann distribution. Then, the initial configuration of the ideal gas is sampled as in the frozen dynamics case.

Calculating trajectories For the MD simulations of the frozen dynamics, a standard event-driven algorithm for hard-core systems [2, 4] is employed. In other words, we repeat the following procedure: calculate the next collision time from the smallest collision time among all possible collisions; move all particles forward until collision occurs; implement collision dynamics for the colliding gas particle. For the MD simulation with the finite-mass hypercube under the harmonic potential, where an event/time-driven hybrid method should be used in order to properly handle with the collisional dynamics as well as the dynamics under the continuous potential, the collision Verlet algorithm [86] is employed. The basic idea is to approximate the continuous dynamics between the collisions by the Verlet map. In our case (i.e., under the harmonic potential), the collision time between the hypercube and a gas particle under the Verlet map is formally solved for and thus the next collision time is accurately estimated without employing any iterative solver.

Evaluating forces and time correlation functions In frozen dynamics, the force $\mathbf{F}_0(t)$ on the fixed hypercube at time t is calculated from the average force in the time interval $[t, t+\Delta t]$ (i.e., the impulse divided by Δt). Every time step, each component of $\mathbf{F}_0(n\Delta t)$ is calculated and, for the transverse direction, $F_+(n\Delta t)$ and $F_-(n\Delta t)$ are separately calculated. In full dynamics, the total force $\mathbf{F}(t)$ is obtained from the sum of the harmonic force $(0, \cdots, 0, -kX_d(t))$ and the average force due to the collisions in the time interval $[t, t+\Delta t]$. Every time step, $\mathbf{F}(n\Delta t)$ is calculated along with the trajectory $(\mathbf{X}(n\Delta t), \mathbf{V}(n\Delta t))$.

Using a standard technique to estimate time correlation functions [4], the following time correlation functions are calculated: $\langle F_{0,i}(0)F_{0,i}(t)\rangle$ and $\langle F_{\pm}(0)F_{\pm}(t)\rangle$ for the frozen dynamics and the auto/cross-correlation functions among $\mathbf{X}(t)$, $\mathbf{V}(t)$, and $\mathbf{F}(t)$ for the full dynamics. The δ-weights in the force autocorrelation functions are separately estimated as follows. For each collision with the faces normal to the x_i-axis, we calculate the square of the momentum change of the colliding gas particle. From the sum of these values divided by the total simulation time, we estimate the δ-weight in the force autocorrelation function of the x_i-component of the force.

The procedures to calculate the force and the δ-weight in the force autocorrelation function are elaborated by considering the frozen dynamics. For the full dynamics, the procedures are essentially the same. In the frozen dynamics, the force $F_{0,i}(t)$ is expressed as

$$F_{0,i}(t) = -\sum_k \Delta p_{i,k}\delta(t-\tau_k), \tag{5.4.1}$$

where $\Delta p_{i,k}$ and τ_k are, respectively, the momentum change of a colliding gas particle in the x_i-direction and the collision time at kth collision. The force at the time step

$n\Delta t$ is estimated as

$$F_{0,i}^{\mathrm{MD}}(n\Delta t) = \frac{1}{\Delta t}\int_{n\Delta t}^{(n+1)\Delta t} F_{0,i}(t)dt = -\frac{1}{\Delta t}\sum_{\tau_k\in[n\Delta t,(n+1)\Delta t)} \Delta p_{i,k}. \tag{5.4.2}$$

The force autocorrelation function $\langle F_{0,i}(0)F_{0,i}(n\Delta t)\rangle$ is evaluated from $F_{0,i}^{\mathrm{MD}}(t)$ except the point $n = 0$ where the delta function affects the value. The expression for the δ-weight in $\langle F_{0,i}(0)F_{0,i}(t)\rangle$ is obtained from the following time average expression:

$$\begin{aligned}\langle F_{0,i}(0)F_{0,i}(t)\rangle &\overset{\mathcal{T}\to\infty}{=} \frac{1}{\mathcal{T}}\int_0^{\mathcal{T}} F_{0,i}(\tau)F_{0,i}(\tau+t)d\tau \\ &= \frac{1}{\mathcal{T}}\sum_{\tau_k\in[0,\mathcal{T}]}\sum_l \Delta p_{i,k}\Delta p_{i,l}\delta(t+\tau_k-\tau_l).\end{aligned} \tag{5.4.3}$$

Here, the last equality is obtained by substituting Eq. (5.4.1) and integrating the delta function $\delta(\tau - \tau_k)$. Hence, the δ-weight is estimated from $\frac{1}{\mathcal{T}}\sum_{\tau_k\in[0,\mathcal{T}]}\Delta p_{i,k}^2$.

Calculating the memory function Next, we explain how to evaluate the transverse-direction memory function $K_d(t)$. For the other directions, the same procedure with $k = 0$ can be applied. In principle, we need to solve the following Volterra equation for $K_d(t)$:

$$\langle V_d(0)F_d(t)\rangle = -k\langle V_d(0)X_d(t)\rangle - \int_0^t K_d(s)\langle V_d(0)V_d(t-s)\rangle\, ds. \tag{5.4.4}$$

This is obtained by multiplying $V_d(0)$ to Eq. (5.3.1d) and taking ensemble average with Eq. (5.3.3b). One expected difficulty we encounter in the collisional dynamics is that the memory function contains a δ-peak, which should be handled with care separately from the continuous part. In addition, since Eq. (5.4.4) is the first kind Volterra equation, its solution is numerically unstable. To resolve these issues, we

convert Eq. (5.4.4) into its second kind equation by differentiating with respect to t:

$$\langle F_d(0)F_d(t)\rangle = kM\,\langle V_d(0)V_d(t)\rangle + \frac{1}{\beta}K_d(t) + \int_0^t K_d(s)\,\langle V_d(0)F_d(t-s)\rangle\,ds. \quad (5.4.5)$$

Then, we decompose $\langle F_d(0)F_d(t)\rangle$ and $K_d(t)$ into the δ-peaks and continuous parts:

$$\langle F_d(0)F_d(t)\rangle = a_1\delta(t) + a_2(t), \quad K_d(t) = b_1\delta(t) + b_2(t). \quad (5.4.6)$$

By substituting Eq. (5.4.6) into Eq. (5.4.5) and equating the δ-peaks and continuous parts, we obtain

$$b_1 = \beta a_1, \quad (5.4.7)$$

$$\begin{aligned}\frac{1}{\beta}b_2(t) + \int_0^t b_2(s)\,\langle V_d(0)F_d(t-s)\rangle\,ds \\ = a_2(t) - kM\,\langle V_d(0)V_d(t)\rangle - \frac{1}{2}b_1\,\langle V_d(0)F_d(t)\rangle\,.\end{aligned} \quad (5.4.8)$$

The numerical procedure to calculate the δ-peak and continuous part of $K_d(t)$ is summarized as follows. By using the δ-weight a_1 of $\langle F_{0,d}(0)F_{0,d}(t)\rangle$, which is estimated from MD simulation as described above, b_1 is determined by Eq. (5.4.7). Then, the continuous part $b_2(t)$ of $K_d(t)$ is obtained from numerically solving Eq. (5.4.8). The convolution integral is discretized by the trapezoidal rule and the values of $b_2(n\Delta t)$ is successively obtained for $n = 1, 2, \cdots$ [123, 164].

Numerical parameters Each trajectory is calculated up to time $T_{\rm sim} = 10^3$ with $\Delta t = 0.01$. The time correlation functions are calculated up to time $T_{\rm corr}$ from each trajectory and their ensemble averages are obtained from $N_{\rm sample}$ samples. Correspondingly, the memory function is calculated up to time $T_{\rm corr}$. The values of $T_{\rm corr}$ and $N_{\rm sample}$ are chosen as follows: for the two-dimensional frozen dynamics, $T_{\rm corr} = 20$, $N_{\rm sample} = 2^{20} \approx 10^6$; for the three-dimensional frozen dynamics,

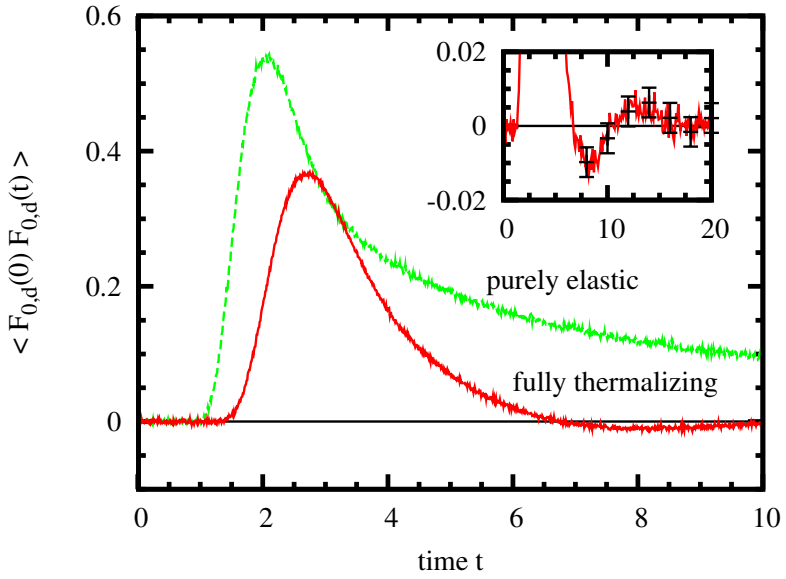

Figure 5.4: For the two-dimensional systems with two values of the accommodation factor $\phi = 0$ (purely repulsive) and $\phi = 1$ (fully thermalizing), the time profiles of the frozen dynamics force autocorrelation function $\langle F_{0,d}(0)F_{0,d}(t)\rangle$ for the transverse direction are plotted by the dashed and solid lines, respectively. The separation distances are $\Delta_+ = \Delta_- = 2.5$. In the inset, negative values in the tail of the fully thermalizing case are shown with the error bars corresponding to two standard deviations.

$T_{\rm corr} = 10$, $N_{\rm sample} = 2^{20} \approx 10^6$; for the two-dimensional full dynamics, $T_{\rm corr} = 100$, $N_{\rm sample} = 2^{18} \approx 2.6 \times 10^5$ or $T_{\rm corr} = 250$, $N_{\rm sample} = 2^{17} \approx 1.3 \times 10^5$ (only used in the computations for Fig. 5.10).

5.4.2 Frozen dynamics results

We first observe MD simulation results with purely elastic walls, by which we can numerically confirm our analytic results presented in Section 5.3.2. For the two-dimensional system with the parameters given in Section 5.4.1, the estimated values of the δ-weights in $\langle F_{0,i}(0)F_{0,i}(t)\rangle$ $(i = 1, 2)$ coincide with the theoretical value. The ratio of the statistical errors to the theoretical value is estimated as 1×10^{-4}. The MD result for the tail part of $\langle F_{0,d}(0)F_{0,d}(t)\rangle$ also agrees very well with the analytic

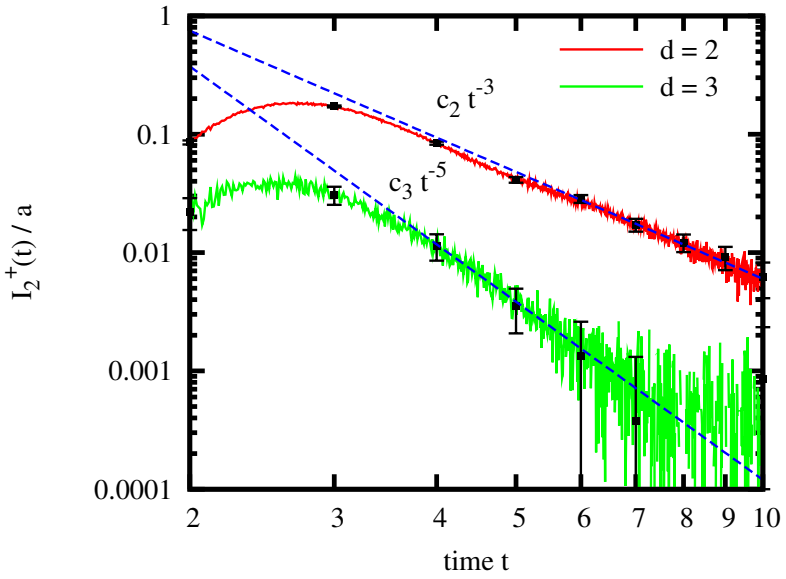

Figure 5.5: For the two- and three-dimensional systems with the fully thermalizing walls, where the hypercube is located near the upper wall ($\Delta_+ = 2.5$) but far from the lower wall ($\Delta_- = 44.5$), the long-time decays of the autocorrelation function of F_+ is observed through the log-log plot of the normalized $I_2^+(t)$ versus t. Error bars correspond to the statistical errors with two standard deviations. For comparison, the decays of t^{-3} and t^{-5} are also plotted.

result, see Fig. 5.2. The statistical error at the maximum of the tail is estimated as 7×10^{-3} of the theoretical value. Similarly, for the three-dimensional system, excellent agreement of the MD results with the analytic results is observed. The ratios of the statistical errors to the theoretical values are estimated as 5×10^{-4} for the δ-weights and 0.06 for the maximum value of the tail, respectively.

Now we observe the effects of the thermal walls. While the δ-weight of $\langle F_{0,d}(0)F_{0,d}(t)\rangle$ does not depend on the accommodation factor ϕ, the tail part has the following dependence on ϕ. As the stochastic character of the walls increases (i.e., ϕ increases), the tail appears at a later time and decays faster. In addition, its maximum has a smaller value and appears at a later time. In Fig. 5.4, the time profiles of the tail for the two extreme cases $\phi = 0$ and $\phi = 1$ are compared for $d = 2$. The tail behavior with faster decay and smaller maximum can be explained by that

the repeated collision pattern is destroyed and randomized when the colliding particle is thermalized by the wall. The time delay in the appearance of the tail can be understood as follows. The time when the tail appears is related with the time for a gas particle to recollide with the hypercube. Specifically, the time when the tail is about to appear and increase is related with the recollisions of gas particles with large velocities in the transverse direction. If these particles are thermalized, their new velocities tend to be smaller and thus it takes more time for them to recollide with the wall.

One more interesting observation is that under the thermal walls, the tail exhibits negative values as shown in the inset of Fig. 5.4. We note that this is possible only when F_+ and F_- are correlated. Actually, under the thermal walls, there is a nonzero probability that a gas particle collides sequentially with the upper face, the upper wall, the lower wall, and the lower face, which contributes to the correlation of F_+ and F_-. Hence, the superposition of the wall effects separately calculated from F_+ and F_-, see Eq. (5.3.5b), is no more valid.

We also investigate the long-time tail decay behavior under the thermal wall and compare it with the purely elastic wall case, i.e., $t^{-(d-1)}$. As described above, the long-time decay also becomes faster as ϕ increases. By sufficiently increasing the separation distance Δ_- from the lower wall, we mimic the system with a single wall and investigate the long-time decay of $I_2^+(t)$ or $\langle F_+(0)F_+(t)\rangle - \langle F_+\rangle^2$. As shown in Fig. 5.5, under the fully thermalizing wall, the tail is observed to decay like t^{-3} for $d = 2$ and t^{-5} for $d = 3$. Under the stochastic walls, the tail is also observed in the longitudinal-direction force autocorrelation function. However, the magnitude is much smaller than the transverse direction, and the decaying exponent cannot be estimated due to relatively large statistical errors.

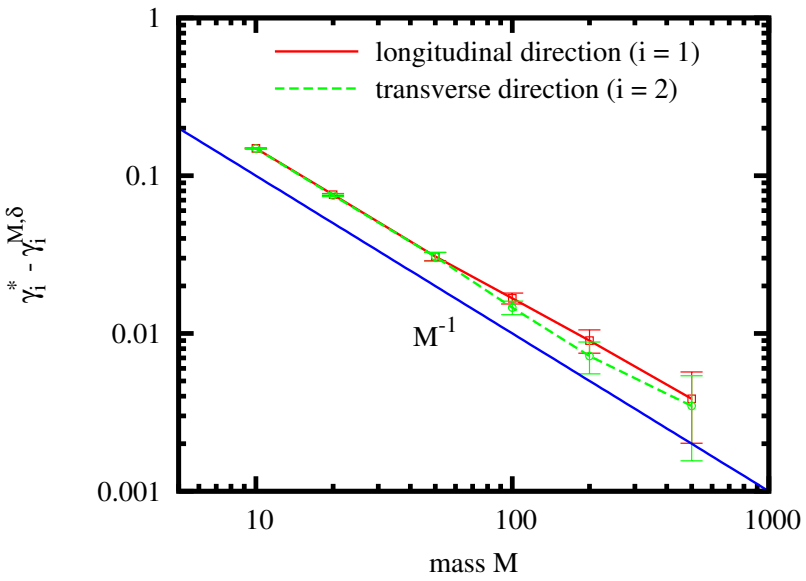

Figure 5.6: For various values of the mass M of the hypercube in the two-dimensional system, the δ-weights $\gamma_i^{M,\delta}$ in the memory functions $K_i^M(t)$ are estimated and their deviations from the Brownian-limit values γ_i^* in the unbounded case are plotted versus M in the log-log plot with the error bars corresponding to two standard deviations. The force constant of the harmonic potential is $k = 4$. For comparison, M^{-1} is also plotted.

5.4.3 Full dynamics results

From the two-dimensional full-dynamics simulations, we mainly observe the memory function $K_i^M(t)$ in the x_i-direction, where the superscript M indicates the mass of the hypercube. As we increase M, we compare this function with the corresponding limit memory function $K_i^{\rm BL}(t)$ to confirm the analytic expression of $K_i^{\rm BL}(t)$, see Eq. (5.3.10), and investigate the convergence behaviors of $K_i^M(t)$ to $K_i^{\rm BL}(t)$. We decompose $K_i^M(t)$ as the sum of the δ-peak and tail parts: $K_i^M(t) = 2\gamma_i^{M,\delta}\delta(t) + \tilde{K}_i^M(t)$. We added the superscript δ in the δ-weight to emphasize that it is obtained from the δ-peak rather than the time integral of $K_i^M(t)$. We first observe the δ-peak in the memory function and then the tail part.

For both longitudinal and transverse directions to the channel (i.e., $i = 1, 2$), we

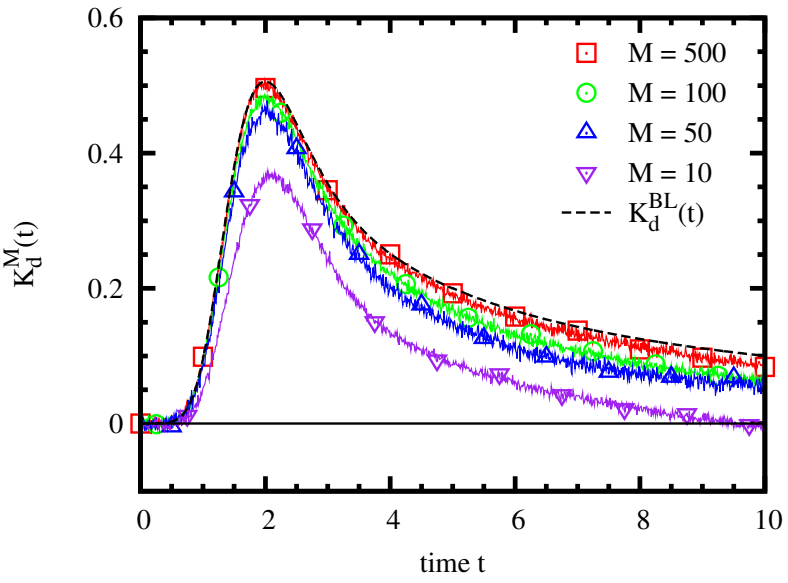

Figure 5.7: The time profiles of the transverse-direction memory function $K_d^M(t)$ are plotted for various values of M. The force constant of the harmonic potential is $k = 4$. For comparison, the limit memory function $K_d^{\mathrm{BL}}(t)$ is plotted by the dashed line.

observe that $\gamma_i^{M,\delta}$ has a smaller value than γ_i^* and converges to γ_i^* as M increases. We also observe that $\gamma_1^{M,\delta}/L_2$ and $\gamma_2^{M,\delta}/L_1$ have the (statistically) same value for a wide range of values of M. Although this would be quite expected in the free unbounded case, this implies, in our case, that the δ-peak depends neither on the confined geometry nor on the external potential as long as the surrounding ideal gas stays in the identical equilibrium state. In Fig. 5.6, the deviation $\gamma_i^{M,\delta} - \gamma_i^*$ is plotted versus M, where a clear linear dependence on M^{-1} is shown. Hence, we observe

$$\gamma_i^{M,\delta} = \gamma_i^* - \mathrm{O}(M^{-1}), \quad i = 1, 2, \cdots, d. \tag{5.4.9}$$

Now we observe the convergence of the tail part $\tilde{K}_d^M(t)$. In Fig. 5.7, the time profiles of $\tilde{K}_d^M(t)$ are plotted for various values of M. For sufficiently large values of M, the tail has a similar shape to the limit memory function; after achieving the maximum, the tail monotonically decreases. From these results, we confirm the

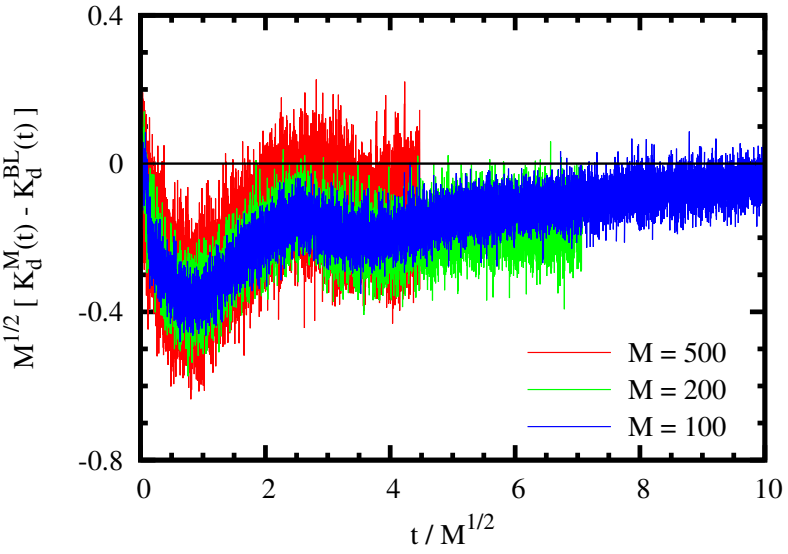

Figure 5.8: The deviation of the memory function $K_d^M(t)$ from the limit memory function $K_d^{\rm BL}(t)$ is plotted versus t. For three values of the mass M of the hypercube, the magnitude of the deviations and time are scaled with respect to $\sqrt{M}$, see Eq. (5.4.10). Since the time profiles of $K_d^M(t)$ are calculated up to time 100 in all cases, the time domains of the scaled curves become shorter as M increases. The force constant of the harmonic potential is $k = 4$.

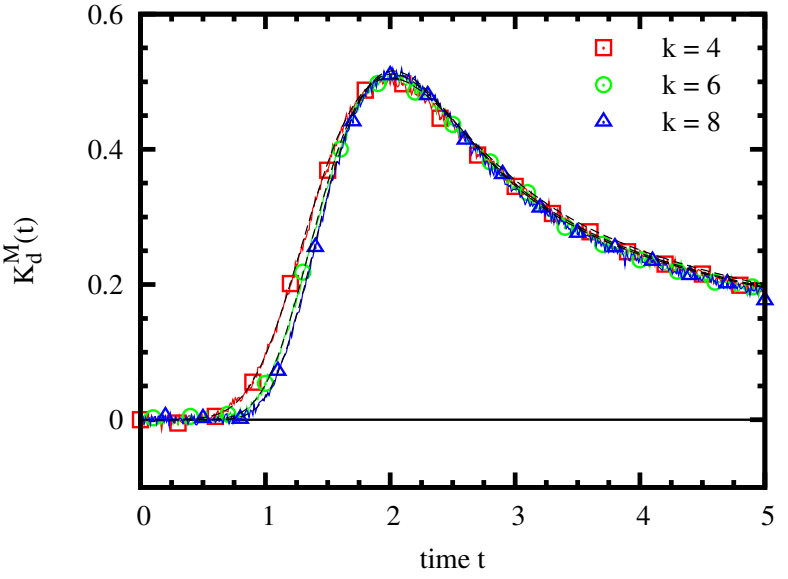

Figure 5.9: The time profiles of the transverse-direction memory function $K_d^M(t)$ are plotted for three values of the force constant k. The mass of the hypercube is $M = 500$. For comparison, corresponding time profiles of the limit memory function $K_d^{\rm BL}(t)$ are plotted by the dashed lines.

convergence of $\tilde{K}_d^M(t)$ to $\tilde{K}_d^{\mathrm{BL}}(t)$; as M increases, the magnitude of the tail increases and it becomes closer to $\tilde{K}_d^{\mathrm{BL}}(t)$. Then, we investigate the scaling behavior of the deviation $\tilde{K}_d^M(t) - \tilde{K}_d^{\mathrm{BL}}(t)$ with respect to the mass M. In Fig. 5.8, the following form of scaling behavior is tested

$$\tilde{K}_d^M(t) \approx \tilde{K}_d^{\mathrm{BL}}(t) + \frac{1}{\sqrt{M}} g\left(\frac{t}{\sqrt{M}}\right). \tag{5.4.10}$$

From the coincidence of the scaled curves, Eq. (5.4.10) is confirmed and the shape of the function $g(t)$ is obtained.

For the other values of the force constant k, we similarly observe the convergence. In Fig. 5.9, the time profiles of $\tilde{K}_d^M(t)$ with the largest value of $M = 500$ are compared with those of the corresponding $\tilde{K}_d^{\mathrm{BL}}(t)$ for various values of k. For each value of k, two time profiles show clear agreement, which confirms again Eq. (5.3.10). As k increases, the tail appears later. This is because the hypercube tends to stay in the middle of the channel under a stiffer harmonic potential and thus it takes more time for a gas particle to recollide with either the upper or lower face. For the chosen values of k, the decaying parts of the tail are quite similar.

We finally report that a slow oscillation is observed after the main peak of the tail for small values of M. We first check whether it is a numerically spurious one. We note that insufficient sample averaging of the time correlation functions may cause a spurious oscillatory tail as follows. When we determine the value of $K_d^M(n\Delta t)$ from Eq. (5.4.8), we use estimated values of the δ-weight and estimated time correlation functions up to time $n\Delta t$, which contain statistical errors. As a result, the solution also accumulates errors. In this case, the error in the solution satisfies a similar Volterra equation [123] and thus it is proportional to the statistical errors in the input values. We observe that the use of insufficient sample average

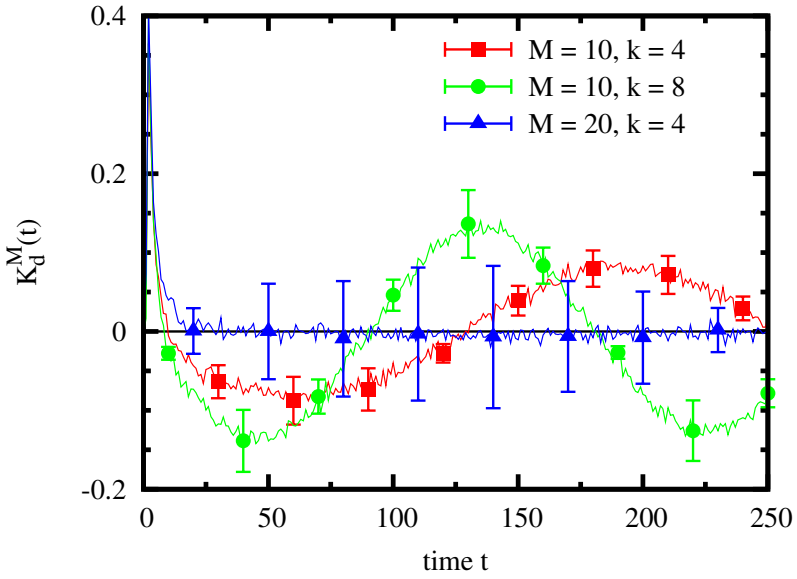

Figure 5.10: The time profiles of $K_d^M(t)$ are plotted up to time 250 for three sets of values (M, k): (10,4) (squares), (10,8) (circles), and (20,4) (triangles). Error bars correspond to the statistical errors with two standard deviations.

causes a spurious oscillatory tail, the magnitude and phase of which may be very different among independent realizations. This unfavorable effects of course can be reduced by increasing the size of sample average, which, however, seriously increases computational cost. By increasing the sample size, we rule out the possibility that numerically originated spurious oscillation dominates the long-time tail. In Fig. 5.10, the slow oscillations in $K_d^M(t)$ are shown for small values of M. We observe that the period is inversely proportional to $\sqrt{k}$ and the magnitude is proportional to $\sqrt{k}$. In addition, we observe that as M increases, the magnitude decreases and the period increases. Due to the computational limitations, however, quantitative analysis is not systematically performed.

5.5 Derivation

5.5.1 GLE

In order to derive Eqs. (5.3.1)–(5.3.3), we use the Mori projection method [140, 168]. Since the Mori projection operator is defined in terms of equilibrium average, we discuss the equilibrium distribution of the hypercube and the ensemble averages of relevant quantities in Section 5.5.1.1. We present the standard form of the GLE obtained from the Mori projection method in Section 5.5.1.2. Then, we show how this equation is reduced to Eq. (5.3.1) in our specific case in Section 5.5.1.3.

5.5.1.1 Equilibrium distribution and average

We assume the system is in equilibrium and follows the Boltzmann distribution. The equilibrium distribution of the hypercube is expressed as

$$\rho_{\mathrm{eq}}(\mathbf{X}, \mathbf{V}) = \rho_1(X_1, X_2, \cdots, X_{d-1})\rho_2(X_d)\rho_{\mathbf{V}}(\mathbf{V}) \tag{5.5.1}$$

and ρ_1 and $\rho_{\mathbf{V}}$ follow the uniform and Maxwell–Boltzmann distribution, respectively. The approximation of $\rho_2(X_d)$ by $\rho(X_d)$ defined in Eq. (5.3.4) for large k is explained as follows. Suppose that a repulsive interaction potential U between the hypercube and the walls is imposed and it depends on the separation distance from a wall with short cutoff distance ϵ. Then, $\rho_2(X_d)$ is expressed as

$$\rho_2(X_d) \propto e^{-\beta\left[\frac{1}{2}kX_d^2 + U(h_+ - X_d - \frac{1}{2}L_d) + U(X_d - \frac{1}{2}L_d - h_-)\right]} \tag{5.5.2}$$

for $X_d \in \left(h_- + \frac{1}{2}L_d, h_+ - \frac{1}{2}L_d\right)$. If k is sufficiently large that the probability of the hypercube being in the interaction range of U is negligible, $\rho_2(X_d)$ is approximated by $\rho(X_d)$. Hence, the validity depends on the distances $|h_\pm \mp \epsilon|$ as well as k and β. Actually, the assumption becomes exactly valid as $h_\pm \to \pm\infty$, which corresponds to the case that the hypercube is subject to the harmonic potential but suspended in an *unbounded* ideal gas.

From Eq. (5.5.1) with $\rho_2(X_d)$ replaced by $\rho(X_d)$, we obtain the following equilibrium averages, which are used in Section 5.5.1.3:

$$\begin{aligned} \left\langle V_i^2 \right\rangle &= (\beta M)^{-1}, \quad \langle V_i F_i \rangle = 0, \quad \text{for } i = 1, 2, \cdots, d, \\ \left\langle X_d^2 \right\rangle &= (\beta k)^{-1}, \quad \langle X_d V_d \rangle = 0, \quad \langle X_d F_d \rangle = -\beta^{-1}, \end{aligned} \tag{5.5.3}$$

where $\mathbf{F} = (F_1, F_2, \cdots, F_d) \equiv M\dot{\mathbf{V}}$. The other ensemble averages containing two quantities from different directions (e.g., $\langle X_d V_1 \rangle$) are all zero.

Ensemble averages containing the force need some discussion. In a collisional dynamics, $\langle V_i(0) F_i(t) \rangle$ has a jump discontinuity at $t = 0$, which can be seen from that its time derivative $-\frac{1}{M} \langle F_i(0) F_i(t) \rangle$ has a delta function due to elastic collisions. Hence, $\langle V_i F_i \rangle$ is actually undefined. This is also explained by that the velocity of the hypercube discontinuously changes whenever a collision occurs and thus $\langle V_i(0) F_i(0+) \rangle$ and $\langle V_i(0) F_i(0-) \rangle$ are different. On the other hand, in a system under a continuous interaction potential, $\langle V_i(0) F_i(t) \rangle$ is continuous $t = 0$ and $\langle V_i F_i \rangle = 0$ from $\langle V_i(0) F_i(-t) \rangle = -\langle V_i(0) F_i(t) \rangle$. By considering that our system is obtained as a limit where a continuous repulsive potential becomes an infinite potential barrier, we *formally* define $\langle V_i F_i \rangle = 0$. The average $\langle X_d F_d \rangle$ is obtained from that the conditional expectation of F_d given X_d is $-kX_d$ and thus $\langle X_d F_d \rangle = -k \langle X_d^2 \rangle$.

5.5.1.2 Mori projection

For a phase variable $\mathbf{A} = (A_1, A_2, \cdots, A_n)^T$ defined on a Hamiltonian system, the Mori projection operators are defined as

$$\mathcal{P}(\bullet) = \langle \bullet \, \mathbf{A}^* \rangle \langle \mathbf{A}\mathbf{A}^* \rangle^{-1} \mathbf{A}, \quad \mathcal{Q} = \mathcal{I} - \mathcal{P}, \tag{5.5.4}$$

where subscripts ^{T} and * denote the transpose and the conjugate transpose, respectively, and $\mathcal{I}$ is the identity operator. The time evolution equation of $\mathbf{A}$, $\dot{\mathbf{A}}(t) = i\mathcal{L}\mathbf{A}(t)$, where $i\mathcal{L}$ is the Liouville operator of the system, is cast into the following GLE:

$$\frac{d}{dt}\mathbf{A}(t) = i\mathbf{\Omega}\mathbf{A}(t) - \int_0^t \mathbf{K}(t-s)\mathbf{A}(s)ds + \mathbf{B}(t), \tag{5.5.5}$$

where the frequency matrix $i\mathbf{\Omega}$, the fluctuating force vector $\mathbf{B}(t)$, and the memory function matrix $\mathbf{K}(t)$ are defined as

$$i\mathbf{\Omega} = \langle (i\mathcal{L}\mathbf{A})\mathbf{A}^* \rangle \langle \mathbf{A}\mathbf{A}^* \rangle^{-1}, \tag{5.5.6a}$$

$$\mathbf{B}(t) = e^{\mathcal{Q}i\mathcal{L}t}\mathcal{Q}i\mathcal{L}\mathbf{A}(0), \tag{5.5.6b}$$

$$\mathbf{K}(t) = \langle \mathbf{B}(t)\mathbf{B}^*(0) \rangle \langle \mathbf{A}\mathbf{A}^* \rangle^{-1}. \tag{5.5.6c}$$

Since $\mathcal{P}\mathbf{B}(t) = 0$, the following condition holds:

$$\langle \mathbf{B}(t)\mathbf{A}^*(0) \rangle = 0, \tag{5.5.7}$$

which implies every pair of a component of $\mathbf{A}(0)$ and that of $\mathbf{B}(t)$ is uncorrelated.

5.5.1.3 Derivation of Eqs. (5.3.1)–(5.3.3)

We apply the results in Section 5.5.1.2 to phase variable $\mathbf{A} = (X_d, V_1, V_2, \cdots, V_d)^T$. A technical difficulty of including X_i $(i = 1, 2, \cdots, d-1)$ is that $\langle X_i^2 \rangle$ is not clearly defined. Since Eq. (5.3.1b) for $\dot{V}_i(t)$ $(i = 1, 2, \cdots, d-1)$ does not contain $X_i(t)$, Eq. (5.3.1a) for $\dot{X}_i(t)$ can be included after obtaining Eqs. (5.3.1b)–(5.3.1d).

The frequency matrix $i\mathbf{\Omega}$ is calculated from Eq. (5.5.6a). By substituting Eq. (5.5.3) into $\langle (i\mathcal{L}\mathbf{A})\mathbf{A}^* \rangle$ and $\langle \mathbf{A}\mathbf{A}^* \rangle$, $i\mathbf{\Omega}$ becomes a matrix containing two nonzero elements $(i\mathbf{\Omega})_{1,d} = 1$ and $(i\mathbf{\Omega})_{d,1} = -\frac{k}{M}$. Hence, we obtain

$$i\mathbf{\Omega}\mathbf{A}(t) = \left(V_d, 0, 0, \cdots, -\frac{k}{M} X_d \right). \tag{5.5.8}$$

Many components of $\mathbf{K}(t)$ and the first component of $\mathbf{B}(t)$ become zero in our case, as seen in Eq. (5.3.1). Although the resulting equation is consistent with physical intuition, showing this without relying on it is not straightforward. It is because $\mathbf{K}(t)$ is defined through the fluctuation-dissipation relation, Eq. (5.5.6c), in terms of the orthogonal dynamics $\mathbf{B}(t)$. We first consider the simplest case $d = 2$ and show which components of $\mathbf{K}(t)$ and $\mathbf{B}(t)$ are nonzero. Then, we discuss the general case and derive Eqs. (5.3.1)–(5.3.3).

For $d = 2$, the GLE is written as

$$\begin{bmatrix} \dot{X}_2 \\ \dot{V}_1 \\ \dot{V}_2 \end{bmatrix}_t = \begin{bmatrix} V_2 \\ 0 \\ -\frac{k}{M} X_2 \end{bmatrix}_t + \int_0^t ds \begin{bmatrix} K_{11} & K_{12} & K_{13} \\ K_{21} & K_{22} & K_{23} \\ K_{31} & K_{32} & K_{33} \end{bmatrix}_s \begin{bmatrix} X_2 \\ V_1 \\ V_2 \end{bmatrix}_{t-s} + \begin{bmatrix} B_1 \\ B_2 \\ B_3 \end{bmatrix}_t, \tag{5.5.9}$$

where the subscripts in the matrix and vectors indicate the time that their compo-

nents are evaluated. Since $\dot{X}_2 = V_2$, the first component of vector equation (5.5.9) becomes

$$\int_0^t K_{11}(s)X_2(t-s)ds + \int_0^t K_{12}(s)V_1(t-s)ds + \int_0^t K_{13}(s)V_2(t-s)ds + B_1(t) = 0. \tag{5.5.10}$$

By multiplying $X_2(0)$, $V_1(0)$, and $V_2(0)$ and taking average, we have

$$\int_0^t K_{11}(s)\left\langle X_2(0)X_2(t-s)\right\rangle ds + \int_0^t K_{13}(s)\left\langle X_2(0)V_2(t-s)\right\rangle ds = 0, \tag{5.5.11a}$$

$$\int_0^t K_{12}(s)\left\langle V_1(0)V_1(t-s)\right\rangle ds = 0, \tag{5.5.11b}$$

$$\int_0^t K_{11}(s)\left\langle V_2(0)X_2(t-s)\right\rangle ds + \int_0^t K_{13}(s)\left\langle V_2(0)V_2(t-s)\right\rangle ds = 0. \tag{5.5.11c}$$

Here, we have used Eq. (5.5.7). Differentiating Eq. (5.5.11a) with respect to t and adding Eq. (5.5.11c), we obtain $\langle X_2^2\rangle K_{11}(t) = 0$ and thus $K_{11}(t) = K_{13}(t) = 0$. From Eq. (5.5.11b), we have $K_{12}(t) = 0$. Hence, we have $B_1(t) = 0$ and the first component of the vector equation becomes $\dot{X}_2 = V_2$, as expected. For the other components, the same procedure is applicable to show that $K_{21}(t) = K_{23}(t) = K_{31}(t) = K_{32}(t) = 0$. Therefore, only $K_{22}(t)$ and $K_{33}(t)$ are nonzero components. In addition, from Eq. (5.5.6c), we have $K_{22}(t) = \beta M\langle B_2(0)B_2(t)\rangle$, $K_{33}(t) = \beta M\langle B_3(0)B_3(t)\rangle$, $\langle B_2(0)B_3(t)\rangle = \langle B_3(0)B_2(t)\rangle = 0$. From Eq. (5.5.7), we also have $\langle X_2(0)B_i(t)\rangle = \langle V_1(0)B_i(t)\rangle = \langle V_2(0)B_i(t)\rangle = 0$ for $i = 2, 3$.

For the d-dimensional case, we can similarly show (i) $K_{ii}(t)$ and $B_i(t)$ ($i = 2, 3, \cdots, d+1$) are nonzero; (ii) $K_{ii}(t) = \beta M\langle B_i(0)B_i(t)\rangle$; (iii) $\langle B_i(0)B_j(t)\rangle = 0$ for $i \neq j$; (iv) $\langle X_d(0)B_i(t)\rangle = 0$ ($i = 2, 3, \cdots, d+1$); and (v) $\langle V_i(0)B_j(t)\rangle = 0$ ($i = 1, 2, \cdots, d$ and $j = 2, 3, \cdots, d+1$). Eq. (5.3.1) is obtained by defining $K_i(t)$ and $F_i^+(t)$ ($i = 1, 2, \cdots, d$) in Eq. (5.3.1) as $MK_{i+1,i+1}(t)$ and $MB_{i+1}(t)$, respectively. Then, Eqs. (5.3.2) and (5.3.3) are obtained from (ii)–(v).

5.5.2 Frozen dynamics force autocorrelation function

In this section, we derive the analytic expression for $\langle F_{0,i}(0)F_{0,i}(t)\rangle$ $(i = 1, 2, \cdots, d)$ given in Eq. (5.3.5). For the frozen dynamics with the purely elastic walls and the fixed hypercube of the upright orientation, we make the following observations, which our derivation is based on:

(i) if a gas particle collides with a face, it never collides with the other faces;

(ii) repeated collisions with the hypercube are possible only when a gas particle collides with the upper or lower face;

(iii) $F_{0,i}(t)$ is attributed to the collisions with the faces normal to the x_i-axis.

For the schematic of the repeated collisions in the case of $d = 3$, see Fig. 5.1 (b).

From observations (i) and (iii) and $\langle F_{0,i}\rangle = 0$ $(i = 1, 2, \cdots, d)$ by symmetry, all cross-correlations $\langle F_{0,i}(0)F_{0,j}(t)\rangle$ $(i \neq j)$ become zero. From observation (ii), $\langle F_{0,i}(0)F_{0,i}(t)\rangle$ $(i = 1, 2, \cdots, d-1)$ contains only a δ-peak. We also note that the form of the δ-weight is the same as that of $\langle F_{0,d}(0)F_{0,d}(t)\rangle$. In fact, by taking the separation distances $\Delta_\pm$ to infinity, we have $I_2^\pm(t) \to 0$ and retrieve the unconfined case. Hence, in what follows, we only derive Eq. (5.3.5b). To this end, we decompose the force $F_{0,d} = F_+ + F_-$, where F_+ and F_- are the forces on the upper and lower faces, respectively. By using that F_+ and F_- are uncorrelated, we have

$$\langle F_{0,d}(0)F_{0,d}(t)\rangle = \langle F_+(0)F_+(t)\rangle + \langle F_-(0)F_-(t)\rangle + 2\langle F_+\rangle\langle F_-\rangle\,. \tag{5.5.12}$$

In Section 5.5.2.1, we explain in detail the geometry and initial configuration of the system in the frozen dynamics. In Section 5.5.2.2, we express $\langle F_+ \rangle$ and $\langle F_+(0)F_+(t)\rangle$ as ensemble averages of functionals of the single-gas-particle trajectory. In Section 5.5.2.3, we analyze the single-gas-particle trajectories contributing to the ensemble averages. In Section 5.5.2.4, we obtain analytic expressions for $\langle F_\pm \rangle$ and $\langle F_\pm(0)F_\pm(t)\rangle$ and, thus, Eq. (5.3.5b).

5.5.2.1 Geometry and initial configuration

Since translating the system does not affect the frozen dynamics, we assume that the upper wall is located at $x_d = \Delta_+$ and the upper face of the fixed hypercube is on the plane $x_d = 0$. Furthermore, we assume that the domain of the upper face on the plane is denoted as $(0, L_1) \times (0, L_2) \times \cdots \times (0, L_{d-1})$. For the case $d = 3$, see Fig. 5.1 (b).

We assume that the system is initially at equilibrium and the initial configuration of the system is described by the Poisson field as follows. By denoting the position and velocity of a gas particle as $\mathbf{x} = (x_1, x_2, \cdots, x_d)$ and $\mathbf{v} = (v_1, v_2, \cdots, v_d)$, respectively, the probability that a gas particle is found in the volume element $d\mathbf{x}d\mathbf{v}$ is given as

$$\lambda(d\mathbf{x}, d\mathbf{v}) = a \left(\prod_{i=1}^{d} \varphi(v_i) dx_i dv_i \right) \mathbb{I}_{\text{geom}}(\mathbf{x}), \tag{5.5.13}$$

where $\varphi(v) = \sqrt{\frac{\beta m}{2\pi}} e^{-\frac{\beta m}{2} v^2}$ and $\mathbb{I}_{\text{geom}}(\mathbf{x})$ is 1 if $\mathbf{x}$ is in the geometrically accessible region (i.e., outside the hypercube and between the walls) and otherwise 0. In other words, the gas particles are distributed uniformly outside the hypercube with the number density a and their velocities following the Maxwell–Boltzmann distribution.

5.5.2.2 Reduction to single-gas-particle properties

Since the dynamics of each gas particle is decoupled from those of the other gas particles in the frozen dynamics, we express $\langle F_+ \rangle$ and $\langle F_+(0)F_+(t)\rangle$ in terms of a single particle quantity. By denoting the x_d-component of the force exerted on the upper face by the gas particle with initial condition $(\mathbf{x}, \mathbf{v})$ as $f_+(t; \mathbf{x}, \mathbf{v})$, these quantities are expressed as

$$\langle F_+ \rangle = \int f_+(0; \mathbf{x}, \mathbf{v})\lambda(d\mathbf{x}, d\mathbf{v}), \tag{5.5.14}$$

$$\langle F_+(0)F_+(t)\rangle = \int f_+(0; \mathbf{x}, \mathbf{v})f_+(t; \mathbf{x}, \mathbf{v})\lambda(d\mathbf{x}, d\mathbf{v}) + \langle F_+ \rangle^2 . \tag{5.5.15}$$

These expressions are obtained as follows. By denoting the initial configuration of the ideal gas as $\left\{\mathbf{x}^{(\alpha)}, \mathbf{v}^{(\alpha)}\right\}_{\alpha=1}^{\infty}$, we define the corresponding measure $\mu(d\mathbf{x}, d\mathbf{v}) = \sum_{\alpha=1}^{\infty} \delta(\mathbf{x} - \mathbf{x}^{(\alpha)})\delta(\mathbf{v} - \mathbf{v}^{(\alpha)})d\mathbf{x}d\mathbf{v}$. Since the initial configuration is given as the Poisson field with mean $\lambda(d\mathbf{x}, d\mathbf{v})$, we have $\langle \mu(d\mathbf{x}, d\mathbf{v})\rangle = \lambda(d\mathbf{x}, d\mathbf{v})$. Hence, from $F_+(t) = \int f_+(t; \mathbf{x}, \mathbf{v})\mu(d\mathbf{x}, d\mathbf{v})$, we obtain Eq. (5.5.14). We obtain Eq. (5.5.15) by using the decomposition $\mu(d\mathbf{x}, d\mathbf{v}) = \lambda(d\mathbf{x}, d\mathbf{v})+\tilde{\mu}(d\mathbf{x}, d\mathbf{v})$ and applying the following Itô isometry for $\tilde{\mu}(d\mathbf{x}, d\mathbf{v})$

$$\left\langle \int f_+(0)\tilde{\mu}(d\mathbf{x}, d\mathbf{v}) \int f_+(t)\tilde{\mu}(d\mathbf{x}, d\mathbf{v}) \right\rangle = \int f_+(0)f_+(t)\lambda(d\mathbf{x}, d\mathbf{v}). \tag{5.5.16}$$

As in Eq. (5.5.16), we suppress the dependence on $(\mathbf{x}, \mathbf{v})$ unless needed.

5.5.2.3 Meaningful trajectories

In Eqs. (5.5.14) and (5.5.15), we note that we only need to consider gas particles colliding with the upper face instantaneously (i.e., at $t = 0$). However, in order to

properly handle with the δ-character in $f_+(0)$, we consider all gas particles colliding first with the upper face. By introducing the indicator function $\mathbb{I}(A)$, which is 1 if the condition A is valid and otherwise 0, these particles are characterized by the following function:

$$\mathbb{I}_0(\mathbf{x},\mathbf{v}) = \mathbb{I}\left(0 < x_d < \Delta_+, v_d < 0\right) \prod_{i=1}^{d-1} \mathbb{I}\left(0 < x_i - \frac{x_d}{v_d} v_i < L_i\right). \tag{5.5.17}$$

For the gas particle satisfying $\mathbb{I}_0 = 1$, the collision time is given as $\tau_0 = -x_d/v_d$ and $f_+(t)$ is expressed as

$$f_+(t) = 2mv_d \left[\mathbb{I}_0 \delta(t-\tau_0) + \sum_{n=1}^{\infty} \mathbb{I}_n \delta(t-\tau_n)\right], \tag{5.5.18}$$

where $\mathbb{I}_n$ indicates whether the $(n+1)$th collision with the upper face occurs and τ_n is the corresponding collision time.

5.5.2.4 $\langle F_\pm \rangle$ and $\langle F_\pm(0) F_\pm(t) \rangle$

Calculating $\langle F_+ \rangle$ is straightforward. We first integrate $f_+(0) = -2mv_d^2 \mathbb{I}_0 \delta(x_d)$ with respect to x_d and obtain $\int f_+(0) dx_d = -2mv_d^2 \bar{\mathbb{I}}_0$, where

$$\bar{\mathbb{I}}_0 = \mathbb{I}(v_d < 0) \prod_{i=1}^{d-1} \mathbb{I}(0 < x_i < L_i). \tag{5.5.19}$$

We note that integrating $\delta(x_d)$ led us to take the limit $x_d \to 0$ for the remaining terms and the overbar notation was introduced for this limit. By further integrating with respect to $(x_1, x_2, \cdots, x_{d-1})$ and $\mathbf{v}$, we obtain

$$\langle F_+ \rangle = -2m(aL_1 L_2 \cdots L_{d-1}) \int_{-\infty}^{0} v_d^2 \varphi(v_d) dv_d = -\frac{a}{\beta} L_1 L_2 \cdots L_{d-1}. \tag{5.5.20}$$

We note that $\langle F_+ \rangle$ does not depend on the separation distance Δ_+.

Now we obtain an analytic expression for $\langle F_+(0)F_+(t)\rangle$. As we did for $f_+(0)$ above, we first integrate $f_+(0)f_+(t)$ with respect to x_d and obtain

$$\int f_+(0)f_+(t)dx_d = -4m^2v_d^3\left[\bar{\mathbb{I}}_0\delta(t) + \sum_{n=1}^{\infty}\bar{\mathbb{I}}_n\delta(t-\bar{\tau}_n)\right], \tag{5.5.21}$$

where

$$\bar{\mathbb{I}}_n = \bar{\mathbb{I}}_0\prod_{i=1}^{d-1}\mathbb{I}\left(0 < x_i - \frac{2n\Delta_+v_i}{v_d} < L_i\right), \quad \bar{\tau}_n = -\frac{2n\Delta_+}{v_d}. \tag{5.5.22}$$

We note that $\bar{\mathbb{I}}_n$ checks whether the gas particle collides with the upper face of the hypercube instantaneously at $t = 0$ and then has further n successive collisions. From Eq. (5.5.21), the integration of $f_+(0)f_+(t)$ with respect to $\lambda(d\mathbf{x}, d\mathbf{v})$ is decomposed into two parts as follows:

$$\int f_+(0)f_+(t)\lambda(d\mathbf{x}, d\mathbf{v}) = I_1\delta(t) + I_2^+(t). \tag{5.5.23}$$

We note that the δ-peak is attributed to the instantaneous collision whereas the tail part $I_2^+(t)$ is due to the repeated collisions. We obtain the intensity of the δ-peak as follows:

$$I_1 = -4m^2(aL_1L_2\cdots L_{d-1})\int_{-\infty}^{0} v_d^3\varphi(v_d)dv_d = \frac{4a}{\beta}\sqrt{\frac{2m}{\pi\beta}}L_1L_2\cdots L_{d-1}. \tag{5.5.24}$$

Calculating the tail part is more involved since the domain of integration with respect to $(x_1, x_2, \cdots, x_{d-1})$ and $(v_1, v_2, \cdots, v_{d-1})$ is restricted by $\bar{\mathbb{I}}_n = 1$. $I_2^+(t)$ is

expressed as

$$I_2^+(t) = -4am^2 \sum_{n=1}^{\infty} \int_{-\infty}^{0} dv_d \, \delta\left(t + \frac{2n\Delta_+}{v_d}\right) v_d^3 \varphi(v_d) \prod_{i=1}^{d-1} J_{i,n}(v_d, t), \tag{5.5.25}$$

where

$$J_{i,n}(v_d, t) = \int_0^{L_i} dx_i \int_{\frac{v_d x_i}{2n\Delta_+}}^{-\frac{v_d(L_i - x_i)}{2n\Delta_+}} dv_i \varphi(v_i). \tag{5.5.26}$$

By using $\delta\left(t + \frac{2n\Delta_+}{v_d}\right) = \frac{2n\Delta_+}{t^2}\delta\left(v_d + \frac{2n\Delta_+}{t}\right)$, we perform the integration with respect to v_d and finally obtain $I_2^+(t) = I_2(t; \Delta_+)$.

For the force F_-, we follow the same procedure to obtain $\langle F_- \rangle = -\langle F_+ \rangle$ and similar expressions to Eqs. (5.5.15) and (5.5.23) with all plus subscripts replaced with minus ones and $I_2^-(t) = I_2(t; \Delta_-)$. By substituting them into Eq. (5.5.12), we finally obtain Eq. (5.3.5b).

5.6 Summary and discussion

We have systematically investigated Brownian motion of the d-dimensional hypercube in the slit-pore through the analytical and computational analysis of its memory function. The hypercube interacts with the surrounding ideal gas particles via elastic collisions. To avoid direct interaction with the walls, the hypercube is also subject to a stiff harmonic potential along the transverse direction to the channel.

In the analytic approach, for the case where the hypercube has a finite mass and every collision in the system is elastic, we have obtained the GLE [Eqs. (5.3.1)–(5.3.3)] from the Mori projection method. Then, we have obtained the limit memory function [Eq. (5.3.10)] from the analytic expression of the frozen dynamics force auto-

correlation function [Eq. (5.3.5)] through the adiabatic approximation [Eq. (5.3.9)]. From the emergence of the power-law decaying ($t^{-(d-1)}$) tail in the transverse direction [Eq. (5.3.8)], we have observed the anomalous diffusion for $d = 2$ and the increase in the position-dependent friction coefficient for $d = 3$ [Eqs. (5.3.14) and (5.3.16)].

In the MD simulation approach, we have numerically verified our analytic results by observing the convergence of the finite-mass memory function to the limit memory function. We have also observed its converging behaviors [Eqs. (5.4.9)–(5.4.10)]. In addition, the effects of stochastic thermal walls have been investigated. We have observed that the superposition of wall effects is no more valid and that the long-time decay of the transverse-direction memory function due to a single wall becomes faster (t^{-3} for $d = 2$ and t^{-5} for $d = 3$).

We have used these two approaches in a complementary way. Elastic collisions introduce a series of delta functions in the force on the hypercube. Hence, handling the force properly with care is required in the analytic approach. Moreover, results obtained by using delta functions cannot be rigorously justified. Our analytic results possessing the following issues have been numerically verified by MD simulations: application of the Mori GLE to collisional dynamics, formal definition of $\langle V_i F_i \rangle = 0$, approximation of $\rho(X_d)$, adiabatic approximation [Eq. (5.3.9)], convergence of the memory function. In addition, by MD simulations, we have observed the system with the finite-mass hypercube and/or thermal walls, which is not easily investigated by the analytic approach. On the other hand, we have developed the numerical procedure to calculate the δ-weight and continuous part of the memory function from MD trajectories and verified it with the analytic results.

The deviation of the finite-mass memory function from its limit memory function

is related with how inaccurate the adiabatic approximation is for a given value of mass M. We have observed that the scaling behavior of the deviation with respect to M is different from the free unbounded case [89, 97]. In the free unbounded case, the leading term in the deviation is attributed to nonzero velocity of the Brownian particle, which we believe is also true in our case. Compared with the free unbounded case, where the linear dependence on the velocity disappears by the isotropy of the system, we expect that this linear dependence does not disappear in our case, which may be related with the $\sqrt{M}$-dependence of the tail deviation (note that the velocity is $\mathrm{O}(M^{-1/2})$ from the equipartition theorem). Another possible origin of the deviation is the coupling with the harmonic force. For small values of M, we have clearly observed that the memory function contains a slow oscillation and its magnitude and period depend on the force constant k as well as the mass M. We expect that for larger value of M this oscillatory tail is still present although it is computationally difficult to clearly characterize it due to its small magnitude and its large period.

Finally, we discuss the fixed upright orientation of the hypercube. As demonstrated in this chapter, it allows enormous analytic tractability for the analysis of the frozen dynamics. The trajectories of gas particles become simple and the effects of the two purely elastic walls can be separately considered and superimposed. Using these properties, we have obtained the analytic expressions and expected anomalous diffusion in the two-dimensional case. As mentioned in Section 5.1, our results explain why the convergence to normal diffusion has not been proved for the two-dimensional case in Ref. [19]. However, we think that the t^{-1} decay behavior may be *singular* in the sense that under any tilted orientations faster decay is expected. It is because the repeated collisions with the same patterns are no more possible under these orientations. In addition, the regular collision patterns are also easily

destroyed by the thermal walls, which causes faster decay. Regarding the effects of geometric shape, we are currently investigating the Brownian motion of a disk and a sphere in a slit pore with thermal walls and the effects of confinement with thermal walls and we will present our results in the future publication.

Part B

Uncertainty Quantification

Chapter Six

Statistical Errors: Evaluation of the Diffusion Coefficient

6.1 Introduction

The estimation of transport coefficients is one of the most notable applications of the molecular dynamics (MD) simulation technique [4, 73, 59, 157, 52]. They can be calculated through nonequilibrium MD simulation methods [52], which are direct and intuitive but require to generate nonequilibrium steady states. Statistical mechanics provide two types of relations by which the transport coefficients can be computed from equilibrium MD simulations [4, 73, 59, 157]. In the Green–Kubo relations [71, 106], the transport coefficients are expressed as the time integrals of corresponding time autocorrelation functions. On the other hand, in the Einstein–Kubo–Helfand relations [80, 187, 188], they are expressed as the long-time slopes of the mean-squared differences of corresponding Helfand moments. For example, the diffusion coefficient D of a tracer particle can be estimated from the slope of the mean-squared displacement (MSD) at large time:

$$D = \lim_{t\to\infty} \frac{\left\langle [x(t) - x(0)]^2 \right\rangle}{2t} = \frac{1}{2} \lim_{t\to\infty} \frac{d}{dt} \left\langle [x(t) - x(0)]^2 \right\rangle , \tag{6.1.1}$$

where x is one component of the particle's position vector and the brackets denote the ensemble average over the equilibrium distribution of the system. Alternatively, D can be estimated from the time integral of the velocity autocorrelation function (VACF):

$$D = \int_0^\infty \langle v(0)v(t)\rangle \, dt, \tag{6.1.2}$$

where v is one component of the particle's velocity vector. In an isotropic case, one may use $\langle [\mathbf{x}(t) - \mathbf{x}(0)]^2 \rangle$ and $\langle \mathbf{v}(0) \cdot \mathbf{v}(t) \rangle$, where $\mathbf{x}$ and $\mathbf{v}$ are the d-dimensional position and velocity vectors of the particle. Then, in Eqs. (6.1.1) and (6.1.2), they are normalized by the dimensionality d.

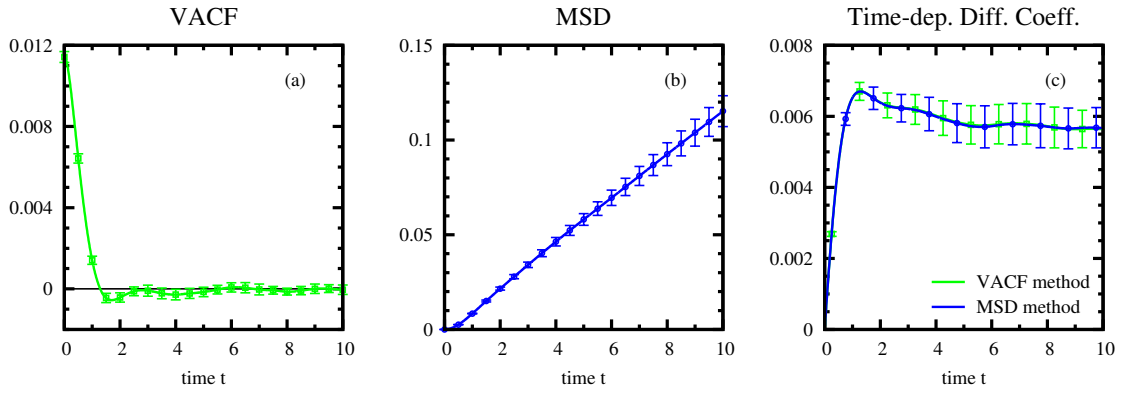

Figure 6.1: Typical MD simulation results for the evaluation of the diffusion coefficient of a tracer particle in a fluid by the VACF and MSD methods. The diffusion coefficient is calculated either from the time integral of the VACF or from the long-time slope of the MSD, see Eq. (6.1.3). For detailed description of the system, see Section 6.4.1. The standard errors are estimated from 16 independent MD runs and the error bars denote two standard deviations.

6.1.1 Computational considerations

When transport coefficients are computed from an equilibrium MD simulation, various types of errors may be involved. One possible source of errors is inaccuracy of the MD simulation model [58], which is due to approximate interaction potential function [5], finite system size [195, 81], large time step size, and insufficiently equilibrated initial configuration, to name but a few. Another source of errors comes from evaluation methods for transport coefficients: truncation of the time integral in the Green–Kubo relations or evaluation of the slope at a finite time in the Einstein–Kubo–Helfand relations. These two types of errors are reproducible and called *systematic errors*. On the other hand, the estimated values of transport coefficients are subject to random fluctuations as the estimated time correlation functions or mean-squared differences are. Since the latter quantities are defined in terms of equilibrium averages of the system and the equilibrium MD simulation technique is based on sampling method, finite sampling inevitably introduces *statistical errors*. The uncertainty due to the statistical error can be quantified in terms of the standard

error (i.e., the standard deviation of the statistical error). It has been known that when the length of a sample trajectory, $\mathcal{T}$, or the number of independent sample trajectories, $\mathcal{N}$, increases, the standard error of an averaged quantity decreases like $\mathcal{T}^{-1/2}$ or $\mathcal{N}^{-1/2}$ [4, 59, 147, 197]. It is noted that, in order to computationally investigate systematic errors, the level of statistical errors should be suppressed. Hence, quantifying statistical errors is crucial for the accurate estimation of transport coefficients. In this chapter, we mainly investigate statistical errors by theoretical and computational means. We demonstrate our approach by analyzing the VACF and MSD methods for the diffusion coefficient D of a tracer particle in a fluid.

In order to introduce the motivating questions for this chapter, we first consider typical MD simulation procedures of evaluating D. As shown in Fig. 6.1, after the MSD or the VACF is evaluated from an MD simulation, the time-dependent diffusion coefficient $D(t)$ is calculated by

$$D(t) \equiv \frac{1}{2}\frac{d}{dt}\left\langle [x(t) - x(0)]^2 \right\rangle = \int_0^t \langle v(0)v(t')\rangle \, dt', \tag{6.1.3}$$

and D is estimated from the long-time plateau value of $D(t)$. In order to estimate the standard errors of the MD simulation results, a number of independent MD runs are performed. Then, a natural question would be which method is better. Fig. 6.1 shows that the VACF and MSD methods seem to produce the same mean values with the same level of the statistical errors. The coincidence is not accidental but is typically observed in various molecular systems. We shall theoretically confirm the equivalence of the two methods by addressing the following two questions.

- How are the statistical errors in the original MD data (i.e., the VACF or the MSD) propagated into the time-integrated or time-differentiated data (i.e., $D(t)$)?

It is important to note that, in principle, even if we know the standard errors (i.e., error bars) of the VACF or the MSD, we cannot calculate the standard errors (i.e., error bars) of $D(t)$. This is because the statistical errors, $\varepsilon(t_1)$ and $\varepsilon(t_2)$, at different times in the original data are correlated with each other and thus we need to know the *error correlation function* $\langle \varepsilon(t_1)\varepsilon(t_2) \rangle$. We shall derive relations between the standard errors of $D(t)$ and the error correlation functions of the VACF and the MSD. Hence, from the latter functions, we can calculate the standard errors of $D(t)$ as well as the VACF and the MSD.

- Can we calculate the error correlation functions of the VACF and the MSD from the VACF under some reasonable assumptions?

If this is the case, once the VACF is calculated in order to estimate $D(t)$, the standard errors of both quantities can be readily estimated without an additional MD ensemble run. For various averaging procedures such as time-averaging and ensemble-averaging, we shall derive expressions for the error correlation functions of the VACF and the MSD. Combining these expressions with the aforementioned relations, we shall obtain expressions for the standard errors of $D(t)$.

6.1.2 Theoretical considerations

Theoretical analysis on the statistical errors in MD simulation data dates back to early days of MD simulations. Zwanzig and Ailawadi [197] have investigated the statistical errors occurring in the evaluation of time correlation function $\langle A(0)A(t) \rangle$ for a general property A. For time-averaging procedure over a long time interval of length $\mathcal{T}$, they have obtained an expression for the error correlation function of

$\langle A(0)A(t)\rangle$ in terms of $\langle A(0)A(t)\rangle$. As expected, the error correlation function has been shown to be inversely proportional to $\mathcal{T}$. In the derivation, they have introduced the Gaussian process approximation (GPA) of the underlying process $A(t)$. Since all high-order statistics can be expressed in terms of the second-order statistics under the GPA, they have expressed the four-time correlation function $\langle A(0)A(t_1)A(t_2)A(t_3)\rangle$ in terms of $\langle A(0)A(t)\rangle$. Frenkel [57] has applied their results to two types of correlation functions for a system consisting of N identical particles. For a correlation function of a single-particle property (e.g., the VACF), he has shown that averaging over particles also introduces the $N^{-1/2}$-scaling behavior in the standard errors. However, for an N-particle property (e.g., the total dipole moment), he has concluded that such a scaling behavior is not expected. Recently, Jones and Mandadapu [93] have employed the error analysis of Zwanzig and Ailawadi [197] and Frenkel [57] and investigated the statistical errors present in the time integral of a time correlation function. They have obtained an upper bound for the variance of the statistical error and employed it for the development of an adaptive Green–Kubo methodology to calculate transport coefficients. To the best of our knowledge, despite extensive use of the MSD method, systematic error analysis of the method has not been available. Through our theoretical approach, we present a complete systematic analysis of the statistical errors occurring in the VACF and MSD methods. By assuming the GPA and following Zwanzig and Ailawadi [197] and Frenkel [57], we obtain *explicit* expressions for the standard errors of the time-dependent diffusion coefficient $D(t)$ as well as the VACF and the MSD. Besides the time-averaging procedure over a single sample trajectory, we analyze various averaging procedures, including averaging over independent sample trajectories and averaging over identical particles.

6.1.3 Comparison

In our computational approach, we confirm our theoretical results as follows. We first *verify* them by simulating the Langevin equation, where the GPA is exactly valid. Then, we *validate* them by performing MD simulations for the self-diffusion in a Lennard-Jones (LJ) fluid and the tracer diffusion of a large and massive colloidal particle in the fluid. In other words, for these molecular systems, we computationally investigate the validity of the GPA and the agreement of our theory with the simulation results. These systems have been extensively investigated and the diffusion coefficient has been reported for various fluid states and various tracer-particle parameters. For recent MD simulation studies on the self-diffusion of pure LJ fluids, we refer the reader to Refs. [134, 20]. For the tracer diffusion in LJ fluids, we refer to Refs. [144, 162, 163, 146]. We note that, despite extensive MD studies on these systems, systematic estimation of the standard errors in estimated transport coefficients has not been performed.

In order to accurately estimate the level of the statistical errors, we perform large-sized MD ensemble runs. With the help of parallel computing techniques, independent sample trajectories are concurrently simulated, MD simulations results are collected, and the mean values and standard errors are computed. We do not use the block averaging technique [54], which has been used for estimating the standard error of a simple (i.e., time-independent) equilibrium average [4, 59, 157]. However, we shall discuss a relevant concept, which is similar to the statistical inefficiency in correlated data [61]. The latter indicates the time difference of two time points in a time series which can be considered to be effectively uncorrelated.

The rest of the chapter is organized as follows. In Section 6.2, we present our theoretical results, including the statistical error estimates for the VACF, the MSD, and

the time-dependent diffusion coefficient as well as relations for the uncertainty propagation in simulations under time integration and differentiation. In Section 6.3, we verify our theoretical results by using the Langevin equation model. In Section 6.4, we perform two kinds of MD simulations and validate the GPA and our theoretical estimates. Finally, we conclude the chapter by providing a brief summary and discussion in Section 6.5.

6.2 Theoretical error estimates

In this section, we obtain theoretical estimates for the level of the statistical errors present in the VACF, the MSD, and the time-dependent diffusion coefficient $D(t)$. After setting up notations and defining the VACF, the MSD, and the time-dependent diffusion coefficient $D(t)$ in Section 6.2.1, we consider three types of averaging procedures and formulate our problem by defining estimators representing the VACF and MSD methods in Section 6.2.2. In Section 6.2.3, we derive relations between the error statistics of the time-differentiated/integrated data and the original data. After discussing the assumptions of our theoretical approach in Section 6.2.4, we derive explicit expressions for the error estimates of the VACF, the MSD, and $D(t)$ in Section 6.2.5.

6.2.1 VACF, MSD, and time-dependent diffusion coefficient $D(t)$

For a tracer particle undergoing free Brownian motion, we denote a component of the position vector as x and the corresponding component of the velocity vector as

v. Then, we have

$$\dot{x}(t) = v(t), \quad x(t) - x(0) = \int_0^t v(t')dt', \tag{6.2.1}$$

and the MSD and VACF of the particle are denoted as $\langle [x(t) - x(0)]^2 \rangle$ and $\langle v(0)v(t) \rangle$, respectively, where the ensemble average over the equilibrium distribution of the system is denoted by the brackets $\langle\ \rangle$. Later, we also use Var [ ] and Cov [,] to denote the variance and covariance over the equilibrium distribution.

The time-dependent diffusion coefficient $D(t)$ is defined through either the MSD or the VACF, see Eq. (6.1.3). Equality of the two expressions in Eq. (6.1.3) can be readily shown as follows. By the invariance of an equilibrium average under the shift of time origin, we have $\langle [x(t) - x(0)]^2 \rangle = \langle [x(0) - x(-t)]^2 \rangle$. Then, after differentiating both sides with respect to t and applying the time shift invariance again, we obtain

$$\langle [x(t) - x(0)]\, v(t) \rangle = \langle [x(t) - x(0)]\, v(0) \rangle\,. \tag{6.2.2}$$

By noting that putting the differential and integral operators inside the brackets on both sides of Eq. (6.1.3) leads to those of Eq. (6.2.2), we show the equality in Eq. (6.1.3).

6.2.2 Formulation

Here, we formulate our problem by introducing estimators that correspond to averaging and time-differentiating/integrating procedures performed in MD simulations. In Table 6.1, we summarize the estimators to be defined in this subsection. In Fig. 6.2, we present schematic diagrams for three types of averaging procedures to be considered in this subsection.

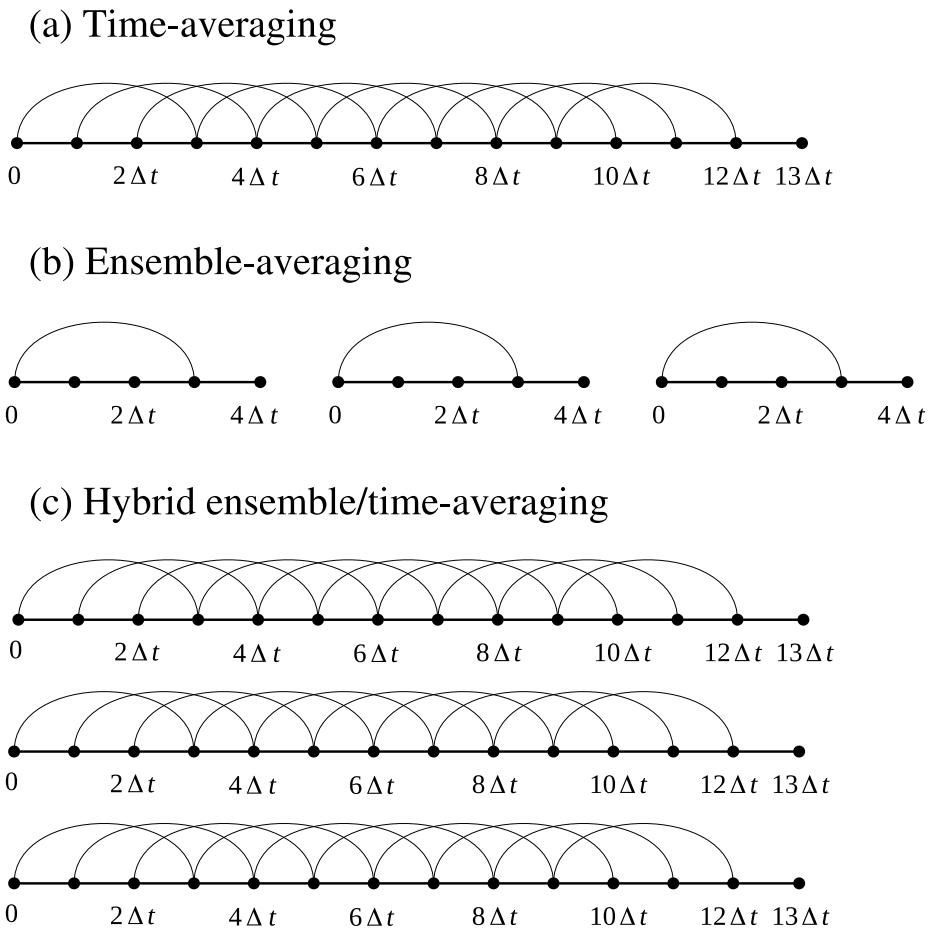

Figure 6.2: Schematic diagrams for three types of averaging procedures in VACF/MSD evaluation. The straight lines represent MD sample trajectories and the points on them indicate discrete times $i\Delta t$ ($i = 0, 1, 2, \cdots$). We depict the case that VACF/MSD for $t = n\Delta t$ (with $n = 3$) is calculated. The pairs of two time points connected by curly lines are used to calculate averages. In (a) and (c), the value of $\mathcal{T}$ is chosen as $10\Delta t$. In (b) and (c), a total of $\mathcal{N}$ (with $\mathcal{N} = 3$) line segments represent independent MD trajectories. The sample trajectories needed for the calculation of VACF/MSD up to time $n_{\max}\Delta t$ (with $n_{\max} = 4$) are drawn.

	Estimator for	Defined in Eq.
$\hat{y}(t)$	VACF at time t	(6.2.4a), (6.2.6a), (6.2.7a)
$\hat{z}(t)$	Time integral of VACF up to time t	(6.2.8)
$\hat{D}^{\mathrm{VACF}}(t)$	Time-dep. diff. coeff. from VACF method	(6.2.10a)
$\hat{b}(t)$	MSD at time t	(6.2.4b), (6.2.6b), (6.2.7b)
$\hat{a}(t_1, t_2)$	Average slope of MSD over time interval $[t_1, t_2]$	(6.2.9)
$\hat{D}^{\mathrm{MSD}}(t)$	Time-dep. diff. coeff. from MSD method	(6.2.10b)

Table 6.1: Summary of the estimators to be analyzed in this chapter. Their physical meanings and equation numbers for definition are listed. Note that each estimator is defined for three types of averaging procedures, which are specified by subscript, (e.g., $\hat{y}_{\mathrm{time}}(t)$, $\hat{y}_{\mathrm{ens}}(t)$, and $\hat{y}_{\mathrm{hybrid}}(t)$).

Time-averaging In an MD simulation, the VACF and the MSD are usually estimated through time-averaging as follows:

$$\langle v(0)v(n\Delta t)\rangle \approx \frac{1}{N}\sum_{i=0}^{N-1} v(i\Delta t)v((i+n)\Delta t), \tag{6.2.3a}$$

$$\left\langle [x(n\Delta t) - x(0)]^2 \right\rangle \approx \frac{1}{N}\sum_{i=0}^{N-1} \left[x((i+n)\Delta t) - x(i\Delta t)\right]^2, \tag{6.2.3b}$$

where $0 \le n \le n_{\max}$ and N is the number of sample pairs used for time-averaging. We note that N is usually much larger than $n_{\max}$ and the sample trajectory needs to be calculated up to $(N + n_{\max} - 1)\Delta t = \mathrm{O}(N\Delta t)$, see Fig. 6.2(a). In order to analyze these time-averaging procedures, we define the following estimators $\hat{y}_{\mathrm{time}}(t)$ and $\hat{b}_{\mathrm{time}}(t)$, respectively, for the VACF and the MSD:

$$\hat{y}_{\mathrm{time}}(t) = \frac{1}{\mathcal{T}}\int_0^{\mathcal{T}} v(t')v(t'+t)dt', \tag{6.2.4a}$$

$$\hat{b}_{\mathrm{time}}(t) = \frac{1}{\mathcal{T}}\int_0^{\mathcal{T}} \left[x(t'+t) - x(t')\right]^2 dt'. \tag{6.2.4b}$$

We note that, by taking $\Delta t \to 0$ in Eq. (6.2.3) with $\mathcal{T} = N\Delta t$ fixed, we retrieve Eq. (6.2.4). In practice, slightly different definitions may be used: for a sample

trajectory of length $\mathcal{T}$, $\frac{1}{\mathcal{T}-t}\int_0^{\mathcal{T}-t} v(t')v(t'+t)dt'$ and $\frac{1}{\mathcal{T}-t}\int_0^{\mathcal{T}-t}\left[x(t'+t)-x(t')\right]^2 dt'$. However, under the usual assumption $t \ll \mathcal{T}$, these definitions produce identical asymptotic results for large $\mathcal{T}$.

Ensemble-averaging By generating a total of N_{sample} independent equilibrated samples and simulating them up to time $n_{\max}\Delta t$, the VACF and the MSD can be estimated through ensemble-averaging as follows:

$$\langle v(0)v(n\Delta t)\rangle \approx \frac{1}{N_{\text{sample}}}\sum_{k=1}^{N_{\text{sample}}} v^{(k)}(0)v^{(k)}(n\Delta t), \tag{6.2.5a}$$

$$\left\langle \left[x(n\Delta t)-x(0)\right]^2\right\rangle \approx \frac{1}{N_{\text{sample}}}\sum_{k=1}^{N_{\text{sample}}}\left[x^{(k)}(n\Delta t)-x^{(k)}(0)\right]^2, \tag{6.2.5b}$$

where the subscript $^{(k)}$ indicates that the labeled quantities belong to the kth sample, see Fig. 6.2(b). We analyze these ensemble averages by defining the following estimators $\hat{y}_{\text{ens}}(t)$ and $\hat{b}_{\text{ens}}(t)$:

$$\hat{y}_{\text{ens}}(t) = \frac{1}{\mathcal{N}}\sum_{k=1}^{\mathcal{N}} v^{(k)}(0)v^{(k)}(t), \tag{6.2.6a}$$

$$\hat{b}_{\text{ens}}(t) = \frac{1}{\mathcal{N}}\sum_{k=1}^{\mathcal{N}}\left[x^{(k)}(t)-x^{(k)}(0)\right]^2. \tag{6.2.6b}$$

We have replaced N_{sample} with a general finite-sampling parameter $\mathcal{N}$ in order to also consider averaging over identical particles later. But, in this section, we assume that the processes $\{x^{(k)}(t), v^{(k)}(t)\}_{k=1}^{\mathcal{N}}$ are independent of one another.

Hybrid ensemble/time-averaging From an ensemble of sample trajectories, the VACF and the MSD can be estimated through the *ensemble averages of the time averages*, see Fig. 6.2(c). We call them the hybrid ensemble/time-averages. In this

case, estimators for the VACF and the MSD are defined as follows:

$$\hat{y}_{\text{hybrid}}(t) = \frac{1}{\mathcal{N}\mathcal{T}} \sum_{k=1}^{\mathcal{N}} \int_0^{\mathcal{T}} v^{(k)}(t') v^{(k)}(t'+t) dt', \tag{6.2.7a}$$

$$\hat{b}_{\text{hybrid}}(t) = \frac{1}{\mathcal{N}\mathcal{T}} \sum_{k=1}^{\mathcal{N}} \int_0^{\mathcal{T}} \left[x^{(k)}(t'+t) - x^{(k)}(t') \right]^2 dt'. \tag{6.2.7b}$$

Estimators for time-integrated/differentiated MD data Now we define estimators for the time-dependent diffusion coefficient $D(t)$ by considering two types of operations on the VACF and MSD estimators. For estimators $\hat{y}_{\text{ens}}(t)$, $\hat{y}_{\text{time}}(t)$, and $\hat{y}_{\text{hybrid}}(t)$ for the VACF, we define their time integral estimators $\hat{z}_{\text{ens}}(t)$, $\hat{z}_{\text{time}}(t)$, and $\hat{z}_{\text{hybrid}}(t)$ as follows:

$$\hat{z}_\bullet(t) = \int_0^t \hat{y}_\bullet(t') dt', \tag{6.2.8}$$

where the bullets indicate that for any type of averaging procedure, including the three averages defined above, its time integral is correspondingly defined. Similarly, for the estimators $\hat{b}_\bullet(t)$ for the MSD, we define their average slope estimators over the interval $[t_1, t_2]$ as follows:

$$\hat{a}_\bullet(t_1, t_2) = \frac{\hat{b}_\bullet(t_2) - \hat{b}_\bullet(t_1)}{t_2 - t_1}. \tag{6.2.9}$$

Then, following Eq. (6.1.3), we define estimators for $D(t)$ from the VACF and MSD methods as follows:

$$\hat{D}_\bullet^{\text{VACF}}(t) = \hat{z}_\bullet(t), \tag{6.2.10a}$$

$$\hat{D}_\bullet^{\text{MSD}}(t) = \frac{1}{2} \lim_{\Delta t \to 0} \hat{a}_\bullet(t, t + \Delta t). \tag{6.2.10b}$$

Unbiasedness of estimators Before closing this subsection, we show that all estimators are unbiased. Since $\langle v(t')v(t'+t)\rangle$ and $\left\langle v^{(k)}(t')v^{(k)}(t'+t)\right\rangle$ are equal to $\langle v(0)v(t)\rangle$, we obtain $\langle \hat{y}_\bullet(t)\rangle = \langle v(0)v(t')\rangle$ after taking average in Eqs. (6.2.4a), (6.2.6a), and (6.2.7a). Similarly, for the MSD estimators defined Eqs. (6.2.4b), (6.2.6b), and (6.2.7b), we obtain $\langle \hat{b}_\bullet(t)\rangle = \langle [x(t)-x(0)]^2\rangle$. Hence, all estimators for $D(t)$ are also unbiased:

$$\begin{aligned}&\langle \hat{D}^{\mathrm{VACF}}_{\mathrm{time}}(t)\rangle = \langle \hat{D}^{\mathrm{VACF}}_{\mathrm{ens}}(t)\rangle = \langle \hat{D}^{\mathrm{VACF}}_{\mathrm{hybrid}}(t)\rangle \\ &= \langle \hat{D}^{\mathrm{MSD}}_{\mathrm{time}}(t)\rangle = \langle \hat{D}^{\mathrm{MSD}}_{\mathrm{ens}}(t)\rangle = \langle \hat{D}^{\mathrm{MSD}}_{\mathrm{hybrid}}(t)\rangle = D(t).\end{aligned} \tag{6.2.11}$$

6.2.3 Relations for time integration and linear regression of MD data

In Section 6.2.2, we have defined $\hat{z}_\bullet$ and $\hat{a}_\bullet$ in terms of $\hat{y}_\bullet$ and $\hat{b}_\bullet$, respectively. Hence, the statistical errors present in the former estimators are attributed to those in the latter estimators. Here, we investigate how the standard errors of $\hat{z}_\bullet$ and $\hat{a}_\bullet$ are expressed in terms of the error correlation functions of $\hat{y}_\bullet$ and $\hat{b}_\bullet$, respectively. Since the resulting relations do not depend on which type of averaging procedure is employed, we drop the subscripts on the estimators in this subsection. In addition, we consider a linear regression estimator $\hat{A}$, which generalizes the estimator $\hat{a}$.

Relation for time integration For estimators $\hat{y}(t)$ and $\hat{z}(t)$ satisfying

$$\hat{z}(t) = \int_0^t \hat{y}(t')dt', \tag{6.2.12}$$

their statistical errors, defined as $\varepsilon_{\hat{y}}(t) = \hat{y}(t) - \langle\hat{y}(t)\rangle$ and $\varepsilon_{\hat{z}}(t) = \hat{z}(t) - \langle\hat{z}(t)\rangle$, satisfy the following relation:

$$\left\langle \varepsilon_{\hat{z}}^2(t) \right\rangle = \int_0^t dt' \int_0^t dt'' \left\langle \varepsilon_{\hat{y}}(t')\varepsilon_{\hat{y}}(t'') \right\rangle . \tag{6.2.13}$$

Eq. (6.2.13) is obtained as follows. From the interchangeability of time integral operator with the ensemble average $\langle\ \rangle$, $\langle\varepsilon_{\hat{z}}^2\rangle = \langle\hat{z}^2(t)\rangle - \langle\hat{z}(t)\rangle^2$ is equal to $\int_0^t dt' \int_0^t dt''\ \mathrm{Cov}\left[\hat{y}(t'), \hat{y}(t'')\right]$. Then, Eq. (6.2.13) follows from $\mathrm{Cov}\left[y(t'), y(t'')\right] = \langle\varepsilon_{\hat{y}}(t')\varepsilon_{\hat{y}}(t'')\rangle$.

Relation for average slope For estimators $\hat{b}(t)$ and $\hat{a}(t)$ satisfying

$$\hat{a}(t_1, t_2) = \frac{\hat{b}(t_2) - \hat{b}(t_1)}{t_2 - t_1}, \tag{6.2.14}$$

their statistical errors, defined as $\varepsilon_{\hat{b}}(t) = \hat{b}(t) - \left\langle\hat{b}(t)\right\rangle$ and $\varepsilon_{\hat{a}}(t_1, t_2) = \hat{a}(t_1, t_2) - \left\langle\hat{a}(t_1, t_2)\right\rangle$, satisfy the following relation:

$$\left\langle \varepsilon_{\hat{a}}^2(t_1, t_2) \right\rangle = \frac{\left\langle \left[\varepsilon_{\hat{b}}(t_2) - \varepsilon_{\hat{b}}(t_1)\right]^2 \right\rangle}{(t_2 - t_1)^2}. \tag{6.2.15}$$

Eq. (6.2.15) is obtained as follows. After substitution of Eq. (6.2.14) and subsequent simple algebra, $\langle\varepsilon_{\hat{a}}^2(t_1, t_2)\rangle = \langle\hat{a}^2(t_1, t_2)\rangle - \langle\hat{a}(t_1, t_2)\rangle^2$ becomes $(t_2 - t_1)^{-2}\{\mathrm{Var}[\hat{b}(t_1)] - 2\mathrm{Cov}[\hat{b}(t_1), \hat{b}(t_2)] + \mathrm{Var}[\hat{b}(t_2)]\}$. Then, by using $\mathrm{Var}[\hat{b}(t_i)] = \langle\varepsilon_{\hat{b}}^2(t_i)\rangle$ $(i = 1, 2)$ and $\mathrm{Cov}[\hat{b}(t_1), \hat{b}(t_2)] = \langle\varepsilon_{\hat{b}}(t_1)\varepsilon_{\hat{b}}(t_2)\rangle$, Eq. (6.2.15) is obtained.

Relation for linear regression The above result for the average slope can be generalized to the simple linear regression of an m-point data set $\{t_i, \hat{b}(t_i)\}_{i=1}^m$. For

the least squares estimator for the slope written as

$$\hat{A}(t_1, t_2, \cdots, t_m) = \frac{\sum_{i=1}^{m} \sum_{j=i+1}^{m} \left[\hat{b}(t_j) - \hat{b}(t_i)\right] (t_j - t_i)}{\sum_{i=1}^{m} \sum_{j=i+1}^{m} (t_j - t_i)^2}, \tag{6.2.16}$$

the variance of its statistical error $\langle \varepsilon^2_{\hat{A}}(t_1, t_2, \cdots, t_m) \rangle = \mathrm{Var}[\hat{A}(t_1, t_2, \cdots, t_m)]$ is expressed as

$$\frac{\sum_{i=1}^{m} \sum_{j=i+1}^{m} \sum_{k=1}^{m} \sum_{l=k+1}^{m} \langle [\varepsilon_{\hat{b}}(t_j) - \varepsilon_{\hat{b}}(t_i)] [\varepsilon_{\hat{b}}(t_l) - \varepsilon_{\hat{b}}(t_k)] \rangle (t_j - t_i)(t_l - t_k)}{\left[\sum_{i=1}^{m} \sum_{j=i+1}^{m} (t_j - t_i)^2\right]^2}. \tag{6.2.17}$$

We note that for $m = 2$, Eq. (6.2.17) reduces to Eq. (6.2.15). Eq. (6.2.17) is obtained as follows. By using $\mathrm{Var}[\sum_i X_i] = \sum_{i,j} \mathrm{Cov}[X_i, X_j]$, the variance of $\hat{A}$ is expressed as a weighted sum of $\mathrm{Cov}[\hat{b}(t_j) - \hat{b}(t_i), \hat{b}(t_l) - \hat{b}(t_k)]$. Then, after replacing the latter by $\langle [\varepsilon_{\hat{b}}(t_j) - \varepsilon_{\hat{b}}(t_i)] [\varepsilon_{\hat{b}}(t_l) - \varepsilon_{\hat{b}}(t_k)] \rangle$, Eq. (6.2.17) is obtained.

Discussion Before closing this subsection, we discuss the resulting relations, Eqs. (6.2.13), (6.2.15), and (6.2.17). Most importantly, these relations demonstrate that the level of statistical errors in the processed data is determined by the error correlation function of the original data, i.e., $\langle \varepsilon_{\hat{y}}(t') \varepsilon_{\hat{y}}(t'') \rangle$ or $\langle \varepsilon_{\hat{b}}(t') \varepsilon_{\hat{b}}(t'') \rangle$. Since the statistical errors in the original data at different times are correlated, the levels of their standard deviations, i.e., $\langle \varepsilon^2_{\hat{y}}(t) \rangle$ or $\langle \varepsilon^2_{\hat{b}}(t) \rangle$, provide insufficient information. As mentioned in the Introduction, this implies that even if the error bars are available in the VACF or MSD data obtained from MD simulations, we cannot, in principle, estimate the error bars in the estimated values of $D(t)$ unless we estimate the error correlation function from MD simulations, which requires huge computational overhead. We shall see that this issue can be circumvented by introducing the GPA.

For the *instantaneous* slope of $\hat{b}$ at time t, $\lim_{\Delta t \to 0} \hat{a}(t, t+\Delta t)$ is considered. By applying L'Hôpital's rule twice to Eq. (6.2.15), we obtain the following equation for the level of the statistical error in the instantaneous slope:

$$\lim_{\Delta t \to 0} \langle \varepsilon_{\hat{a}}^2(t, t+\Delta t) \rangle = \lim_{\Delta t \to 0} \frac{d^2}{d\Delta t^2} \left[\frac{1}{2} \langle \varepsilon_{\hat{b}}^2(t+\Delta t) \rangle - \langle \varepsilon_{\hat{b}}(t) \varepsilon_{\hat{b}}(t+\Delta t) \rangle \right]. \tag{6.2.18}$$

We use this later to calculate the standard errors of $\hat{D}^{\mathrm{MSD}}(t)$.

6.2.4 Assumptions

Before presenting our theoretical error estimates in Section 6.2.5, we summarize the assumptions to be introduced.

Assumptions on the dynamics The most important assumption is the GPA of the underlying process stating that the velocity process $v(t)$ is a Gaussian process. This assumption implies that, for any finite set of time points $\{t_i\}$, the joint distribution of $\{v(t_i)\}$ follows a multivariate normal distribution [94]. As shown in Ref. [197], we shall see that the error correlation function $\langle \varepsilon_{\hat{y}}(t') \varepsilon_{\hat{y}}(t'') \rangle$ contains a four-time correlation function of v. Under the GPA, we decompose the latter into the sum of the products of two-time correlation functions:

$$\begin{aligned} \langle v(0)v(t_1)v(t_2)v(t_3) \rangle = & \langle v(0)v(t_1) \rangle \langle v(0)v(t_3 - t_2) \rangle \\ & + \langle v(0)v(t_2) \rangle \langle v(0)v(t_3 - t_1) \rangle \\ & + \langle v(0)v(t_3) \rangle \langle v(0)v(t_3 - t_2) \rangle . \end{aligned} \tag{6.2.19}$$

Hence, under the GPA, we can express relevant quantities in terms of the VACF. In addition, we note that, from Eq. (6.2.1), the GPA of $v(t)$ implies that the process

$x(t)-x(0)$ is also a Gaussian process. We shall use this property to express the error correlation function $\langle \varepsilon_{\hat{b}}(t')\varepsilon_{\hat{b}}(t'')\rangle$.

It is important to note that the GPA is not always exactly valid even if the marginal distribution of $v(t_i)$ is Gaussian at each time t_i. Hence, the GPA needs to be validated for each case. One plausible explanation for the GPA in particle diffusion phenomena is given by the generalized Langevin equation [168], which is a formally exact equation for the dynamics of a tracer particle:

$$m\dot{v}(t) = -\int_0^t K(t-t')v(t')dt' + f^+(t), \tag{6.2.20}$$

where $f^+(t)$ is the fluctuating force and $K(t)$ is the memory function. In the case of a large tracer particle suspended in a dense fluid, where the distribution of the fluctuating force becomes Gaussian [164], the linearity of Eq. (6.2.20) implies that $v(t)$ also becomes a Gaussian process. The limiting case of this argument is the Langevin equation, where the fluctuating force becomes Gaussian white noise and the memory function becomes a delta function.

Although analyzing the force on the tracer particle seems useful for investigating the validity of the GPA, it is also important to note that our theoretical framework does not rely on any assumption on the form of the force. For the dynamics of the system, we only assume the relation between x and v, see Eq. (6.2.1), and the GPA of v. Hence, our theoretical approach is applicable not only to MD systems where the force is fully deterministic but also to mesoscopic simulation methods such as the Langevin dynamics [168] and the dissipative particle dynamics [72], where stochastic forces are introduced. However, our approach may not be applicable to the Brownian dynamics [168], where Eq. (6.2.1) does not hold.

Assumptions on averaging procedures For time-averaging, we assume that the VACF eventually decays to zero and the length $\mathcal{T}$ of the time-averaging interval is much longer than the characteristic decay time scale of the VACF. We need these assumptions to obtain the $\mathcal{T}^{-1}$-dependence of the error correlation functions. We use the following approximation, which becomes asymptotically valid for large $\mathcal{T}$:

$$\frac{1}{\mathcal{T}^2}\int_0^{\mathcal{T}} dt' \int_0^{\mathcal{T}} dt''\, h(t'-t'') \approx \frac{1}{\mathcal{T}}\int_{-\infty}^{\infty} h(\alpha)d\alpha, \tag{6.2.21}$$

where $h(t)$ is an integrable function decaying sufficiently fast. This approximation has been heuristically introduced in Refs. [59, 197, 57]. In 6.6.1, we provide the error term of the approximation and a condition for the decay rate of $h(t)$.

For ensemble-averaging, we assume that $\{x^{(k)}(t), v^{(k)}(t)\}_{k=1}^{\mathcal{N}}$ are independent of one another and each of them has the same statistical properties as $\{x(0), v(0)\}$. In other words, they are *independent replicas*. Since we are interested only in average values, we actually need a weaker condition: uncorrelatedness rather independence. When we take particle-average in an MD simulation of a system consisting of identical particles, we shall investigate the uncorrelatedness assumption.

Finally, we assume that Δt is sufficiently small that any systematic error due to discretization is negligible. For the errors due to insufficient equilibration and early truncation of the time integral of the VACF, we refer the reader to Ref. [93].

6.2.5 Main theoretical results

Here, we present theoretical estimates for the standard errors of the VACF, the MSD, and $D(t)$, which are obtained from the error correlation functions of the VACF and

the MSD. Since the error correlation functions depend on the type of averaging procedure, we calculate them and present the resulting theoretical estimates for each type of averaging procedure. From these results, we show that the standard errors of $\hat{D}_{\bullet}^{\mathrm{VACF}}(t)$ and $\hat{D}_{\bullet}^{\mathrm{MSD}}(t)$ are identical. We start with the ensemble-averaging case, which is the simplest, in Section 6.2.5.1 and the time-averaging and hybrid ensemble/time-averaging cases follow in Section 6.2.5.2 and Section 6.2.5.3, respectively. In Section 6.2.5.4, we compare our theoretical results with previous results.

6.2.5.1 Ensemble-averaging case

In 6.6.2, we derive the following expression for the error correlation function of $\hat{y}_{\mathrm{ens}}$:

$$\langle \varepsilon_{\hat{y}_{\mathrm{ens}}}(t')\varepsilon_{\hat{y}_{\mathrm{ens}}}(t'')\rangle = \frac{1}{\mathcal{N}}\left[\langle v^2\rangle \langle v(0)v(t''-t')\rangle + \langle v(0)v(t')\rangle \langle v(0)v(t'')\rangle\right]. \tag{6.2.22}$$

Hence, the mean-squared errors in $\hat{y}_{\mathrm{ens}}$ and $\hat{z}_{\mathrm{ens}}$ are written as

$$\langle \varepsilon^2_{\hat{y}_{\mathrm{ens}}}(t)\rangle = \frac{1}{\mathcal{N}}\left[\langle v^2\rangle^2 + \langle v(0)v(t)\rangle^2\right], \tag{6.2.23}$$

$$\langle \varepsilon^2_{\hat{z}_{\mathrm{ens}}}(t)\rangle = \frac{1}{\mathcal{N}}\int_0^t dt'\int_0^t dt''\left[\langle v^2\rangle\langle v(0)v(t''-t')\rangle + \langle v(0)v(t')\rangle \langle v(0)v(t'')\rangle\right]. \tag{6.2.24}$$

Here, we have used Eq. (6.2.13) to obtain Eq. (6.2.24).

We also derive the error correlation function of $\hat{b}_{\mathrm{ens}}$ in 6.6.2:

$$\left\langle \varepsilon_{\hat{b}_{\mathrm{ens}}}(t')\varepsilon_{\hat{b}_{\mathrm{ens}}}(t'')\right\rangle = \frac{2}{\mathcal{N}}\left\langle [x(t')-x(0)]\,[x(t'')-x(0)]\right\rangle^2. \tag{6.2.25}$$

Hence, the mean-squared error in $\hat{b}_{\mathrm{ens}}$ is expressed as

$$\langle \varepsilon^2_{\hat{b}_{\mathrm{ens}}}(t)\rangle = \frac{2}{\mathcal{N}}\left\langle [x(t)-x(0)]^2\right\rangle^2. \tag{6.2.26}$$

As discussed in Section 6.2.3, the mean-squared error in the instantaneous slope of $\hat{b}_{\text{ens}}$ is calculated from Eq. (6.2.18). By substituting Eq. (6.2.25) to Eq. (6.2.18) and simplifying the result using Eqs. (6.2.1) and (6.2.2), we obtain

$$\lim_{\Delta t\to 0}\langle \varepsilon^2_{\hat{a}_{\text{ens}}}(t,t+\Delta t)\rangle = \frac{4}{\mathcal{N}}\left[\langle v^2\rangle\langle [x(t)-x(0)]^2\rangle + \langle [x(t)-x(0)]v(0)\rangle^2\right]. \quad (6.2.27)$$

In order to compare the standard errors of $\hat{D}^{\text{VACF}}_{\text{ens}}(t)$ and $\hat{D}^{\text{MSD}}_{\text{ens}}(t)$, we compare Eqs. (6.2.24) and (6.2.27). By using the relations $\int_0^t dt' \int_0^t dt'' \, \langle v(t')v(t'')\rangle = \langle [x(t)-x(0)]^2\rangle$ and $\int_0^t \langle v(0)v(t')\rangle \, dt' = \langle v(0)[x(t)-x(0)]\rangle$, we show that the variance in Eq. (6.2.24) is one fourth of that in Eq. (6.2.27). Hence, from Eq. (6.2.10), we conclude that the two methods produce the same level of statistical errors for $D(t)$:

$$\text{Var}\left[\hat{D}^{\text{VACF}}_{\text{ens}}(t)\right] = \text{Var}\left[\hat{D}^{\text{MSD}}_{\text{ens}}(t)\right]. \quad (6.2.28)$$

6.2.5.2 Time-averaging case

As mentioned in Section 6.2.4, all expressions presented here become asymptotically valid for large $\mathcal{T}$. In 6.6.3, the error correlation function of $\hat{y}_{\text{time}}$ is derived as follows:

$$\begin{aligned}\langle \varepsilon_{\hat{y}_{\text{time}}}(t')\varepsilon_{\hat{y}_{\text{time}}}(t'')\rangle = \frac{1}{\mathcal{T}}\int_{-\infty}^{\infty} d\alpha \, [&\langle v(0)v(\alpha)\rangle\langle v(0)v(\alpha+t''-t')\rangle \\ &+\langle v(0)v(\alpha-t')\rangle\langle v(0)v(\alpha+t'')\rangle].\end{aligned} \quad (6.2.29)$$

Hence, the mean-squared errors in $\hat{y}_{\text{time}}$ and $\hat{z}_{\text{time}}$ are written as

$$\langle \varepsilon^2_{\hat{y}_{\text{time}}}(t)\rangle = \frac{1}{\mathcal{T}}\int_{-\infty}^{\infty} d\alpha \left[\langle v(0)v(\alpha)\rangle^2 + \langle v(0)v(\alpha-t)\rangle \langle v(0)v(\alpha+t)\rangle\right], \tag{6.2.30}$$

$$\begin{aligned}\langle \varepsilon^2_{\hat{z}_{\text{time}}}(t)\rangle = \frac{1}{\mathcal{T}}\int_{-\infty}^{\infty} d\alpha \int_0^t dt' \int_0^t dt''\Big[&\langle v(0)v(\alpha)\rangle \langle v(0)v(\alpha+t''-t')\rangle \\ &+ \langle v(0)v(\alpha+t')\rangle \langle v(0)v(\alpha-t'')\rangle \Big].\end{aligned} \tag{6.2.31}$$

Here, we have used Eq. (6.2.13) to obtain Eq. (6.2.31).

For the MSD estimator $\hat{b}_{\text{time}}$, we similarly derive the error correlation function in 6.6.3:

$$\langle \varepsilon_{\hat{b}_{\text{time}}}(t')\varepsilon_{\hat{b}_{\text{time}}}(t'')\rangle = \frac{2}{\mathcal{T}}\int_{-\infty}^{\infty} d\alpha \, \langle [x(t')-x(0)][x(\alpha+t'')-x(\alpha)]\rangle^2. \tag{6.2.32}$$

Hence, the mean-squared error of the estimator is given as

$$\langle \varepsilon^2_{\hat{b}_{\text{time}}}(t)\rangle = \frac{2}{\mathcal{T}}\int_{-\infty}^{\infty} d\alpha \, \langle [x(t)-x(0)]\,[x(\alpha+t)-x(\alpha)]\rangle^2 . \tag{6.2.33}$$

From Eq. (6.2.15), the variance of the instantaneous slope estimator is obtained. After lengthy algebra, we obtain the following expression showing that the variance is four times that of the time integral estimator $\hat{z}_{\text{time}}$:

$$\begin{aligned}&\lim_{\Delta t\to 0} \text{Var}\left[\hat{a}_{\text{time}}(t,t+\Delta t)\right] = 4\text{Var}\left[\hat{z}_{\text{time}}(t)\right] \\ &= \frac{4}{\mathcal{T}}\int_{-\infty}^{\infty} d\alpha \Big[\langle v(0)v(\alpha)\rangle\langle [x(t)-x(0)][x(\alpha+t)-x(\alpha)]\rangle \\ &\qquad + \langle v(0)[x(\alpha)-x(\alpha-t)]\rangle\langle v(0)[x(\alpha+t)-x(\alpha)]\rangle\Big].\end{aligned} \tag{6.2.34}$$

Hence, from Eq. (6.2.10), we show that the two estimators for $D(t)$ produce the same

level of statistical errors:

$$\mathrm{Var}\left[\hat{D}^{\mathrm{VACF}}_{\mathrm{time}}(t)\right] = \mathrm{Var}\left[\hat{D}^{\mathrm{MSD}}_{\mathrm{time}}(t)\right]. \tag{6.2.35}$$

6.2.5.3 Hybrid ensemble/time-averaging case

In this case, all results are essentially the same as the time-averaging case, see Eqs. (6.2.29)–(6.2.34), except that $\mathcal{N}^{-1}$-dependence appears. Hence, the equivalence of the two methods is established also in this case. The variances of the two estimators for $D(t)$ are expressed in terms of the VACF, $f(t) = \langle v(0)v(t)\rangle$, as follows:

$$\begin{aligned}
&\mathrm{Var}\left[\hat{D}^{\mathrm{VACF}}_{\mathrm{hybrid}}(t)\right] = \mathrm{Var}\left[\hat{D}^{\mathrm{MSD}}_{\mathrm{hybrid}}(t)\right] \\
&= \frac{1}{\mathcal{N}\mathcal{T}}\int_{-\infty}^{\infty} d\alpha \left[f(\alpha)\int_0^t dt' \int_{\alpha}^{\alpha+t} dt'' f(t'-t'') + \int_{\alpha}^{\alpha+t} f(t')dt' \int_{\alpha-t}^{\alpha} f(t')dt'\right].
\end{aligned} \tag{6.2.36}$$

6.2.5.4 Comparison with previous results

We compare our results for the time-averaging case with previous results by Zwanzig and Ailawadi [197], by Frenkel [57], and by Jones and Mandadapu [93]. Only Zwanzig and Ailawadi have considered the error correlation function of $\hat{y}_{\mathrm{time}}$ rather than directly calculating the mean-squared error $\langle \varepsilon^2_{\hat{y}_{\mathrm{time}}}(t)\rangle$. However, they have estimated the error correlation function very roughly as a constant: $\langle \varepsilon_{\hat{y}_{\mathrm{time}}}(t')\varepsilon_{\hat{y}_{\mathrm{time}}}(t'')\rangle \approx \frac{2}{\mathcal{T}}\int_{-\infty}^{\infty}\langle v(0)v(t)\rangle^2 dt$. Frenkel and also Jones and Mandadapu have shown that

$$\langle \varepsilon^2_{\hat{y}_{\mathrm{time}}}(t)\rangle = \frac{a(t)}{\mathcal{T}}\int_{-\infty}^{\infty}\langle v(0)v(\alpha)\rangle^2 d\alpha, \tag{6.2.37}$$

where $a(0) = 2$ and $\lim_{t\to\infty} a(t) = 1$. By using Eq. (6.2.29), we can easily show Eq. (6.2.37).

We can also re-derive the following result obtained by Jones and Mandadapu:

$$\lim_{t\to 0} \frac{d}{dt}\langle \varepsilon^2_{\hat{z}_{\text{time}}}(t)\rangle = 0, \quad \lim_{t\to\infty} \frac{d}{dt}\langle \varepsilon^2_{\hat{z}_{\text{time}}}(t)\rangle = \frac{4D^2}{\mathcal{T}}. \tag{6.2.38}$$

By differentiating Eq. (6.2.31) with respect to t, we have

$$\begin{aligned} \frac{d}{dt}\langle \varepsilon^2_{\hat{z}_{\text{time}}}(t)\rangle &= \frac{2}{\mathcal{T}} \int_{-\infty}^{\infty} d\alpha \int_0^t dt' \, [f(\alpha) f(\alpha + t - t') + f(\alpha) f(\alpha + t + t')] \\ &= \frac{2}{\mathcal{T}} \int_{-\infty}^{\infty} d\alpha \int_0^{2t} dt' \, f(\alpha) f(\alpha + t'), \end{aligned} \tag{6.2.39}$$

where $f(t) = \langle v(0)v(t)\rangle$. Hence, the first result in Eq. (6.2.38) is easily obtained and the second one is obtained from

$$\lim_{t\to\infty} \frac{d}{dt}\langle \varepsilon^2_{\hat{z}_{\text{time}}}(t)\rangle = \frac{4}{\mathcal{T}} \left(\int_0^{\infty} f(t')dt' \right)^2. \tag{6.2.40}$$

In addition, from Eq. (6.2.39), we can also obtain the second derivative of the mean-squared error of $\hat{z}_{\text{time}}$ as follows:

$$\frac{d^2}{dt^2}\langle \varepsilon^2_{\hat{z}_{\text{time}}}(t)\rangle = \frac{4}{\mathcal{T}} \int_{-\infty}^{\infty} f(\alpha) f(\alpha + 2t) d\alpha. \tag{6.2.41}$$

6.3 Verification: Langevin equation

In this section, we investigate the statistical errors occurring in simulation of the following Langevin equation:

$$m\dot{v}(t) = -\gamma v(t) + \xi(t), \tag{6.3.1}$$

where m and γ are the mass and friction coefficient of the particle, respectively, and $\xi(t)$ is Gaussian white noise satisfying $\langle \xi(t')\xi(t'')\rangle = 2k_{\mathrm{B}}T\gamma\delta(t'-t'')$ with the temperature of the system T.

This system has the following features that enable us to verify our theoretical estimates given in Section 6.2. First, the velocity process $v(t)$ is a Gaussian process. Second, this system allows full analytic tractability. The VACF, MSD, and time-dependent diffusion coefficient are given as

$$\langle v(0)v(t)\rangle = \frac{k_{\mathrm{B}}T}{m} e^{-\frac{\gamma}{m}|t|}, \tag{6.3.2}$$

$$\langle [x(t)-x(0)]^2\rangle = \frac{2k_{\mathrm{B}}T}{\gamma}|t| - \frac{2mk_BT}{\gamma^2}\left(1-e^{-\frac{\gamma}{m}|t|}\right), \tag{6.3.3}$$

$$D(t) = \frac{k_{\mathrm{B}}T}{\gamma}\left(1-e^{-\frac{\gamma}{m}t}\right), \quad \text{for } t \geq 0, \tag{6.3.4}$$

respectively. In Section 6.3.1, we obtain closed-form expressions for the theoretical error estimates. In Section 6.3.2, we present simulation results and compare numerical error estimates with the theoretical ones. Since the GPA is exactly valid, they are expected to match, from which we verify our theoretical results.

6.3.1 Closed-form expressions for the error estimates

Ensemble-averaging case Substituting Eq. (6.3.2) into Eq. (6.2.22), we obtain the error correlation function and the mean-squared error of $\hat{y}_{\rm ens}$:

$$\langle \varepsilon_{\hat{y}_{\rm ens}}(t')\varepsilon_{\hat{y}_{\rm ens}}(t'')\rangle = \frac{1}{\mathcal{N}}\left(\frac{k_{\rm B}T}{m}\right)^2\left(e^{-\frac{\gamma}{m}|t'-t''|}+e^{-\frac{\gamma}{m}(t'+t'')}\right), \tag{6.3.5}$$

$$\langle \varepsilon^2_{\hat{y}_{\rm ens}}(t)\rangle = \frac{1}{\mathcal{N}}\left(\frac{k_{\rm B}T}{m}\right)^2\left(1+e^{-\frac{2\gamma t}{m}}\right). \tag{6.3.6}$$

Similarly, by using Eq. (6.3.2), we obtain the following expression for the error correlation function of $\hat{b}_{\rm ens}$ from Eq. (6.2.25): for $0 \le t_1 \le t_2$,

$$\langle \varepsilon_{\hat{b}_{\rm ens}}(t_1)\varepsilon_{\hat{b}_{\rm ens}}(t_2)\rangle = \frac{2}{\mathcal{N}}\left(\frac{k_{\rm B}T}{\gamma}\right)^2\left[2t_1-\frac{m}{\gamma}\left(1-e^{-\frac{\gamma t_1}{m}}-e^{-\frac{\gamma t_2}{m}}+e^{-\frac{\gamma(t_2-t_1)}{m}}\right)\right]^2. \tag{6.3.7}$$

Here, we have used $\langle[x(t_1)-x(0)][x(t_2)-x(0)]\rangle = \int_0^{t_1}dt'\int_0^{t_2}dt''\langle v(0)v(t''-t')\rangle$. Then, the mean-squared error of the estimator is written as

$$\langle \varepsilon^2_{\hat{b}_{\rm ens}}(t)\rangle = \frac{2}{\mathcal{N}}\left(\frac{k_{\rm B}T}{\gamma}\right)^2\left[2t-\frac{2m}{\gamma}\left(1-e^{-\frac{\gamma t}{m}}\right)\right]^2. \tag{6.3.8}$$

The variances of the two estimators for $D(t)$ are calculated from the error correlation functions. For $\hat{D}^{\rm VACF}_{\rm ens}(t)$, Eq. (6.3.5) is substituted into Eq. (6.2.13). Similarly, for $\hat{D}^{\rm MSD}_{\rm ens}(t)$, Eq. (6.3.7) is substituted into Eq. (6.2.15). Finally, we obtain

$$\mathrm{Var}\left[\hat{D}^{\rm VACF}_{\rm ens}(t)\right] = \mathrm{Var}\left[\hat{D}^{\rm MSD}_{\rm ens}(t)\right] = \frac{1}{\mathcal{N}}\left(\frac{k_{\rm B}T}{\gamma}\right)^2\left[\frac{2\gamma t}{m}-1+e^{-\frac{2\gamma t}{m}}\right]. \tag{6.3.9}$$

Time-averaging case By substituting Eq. (6.3.2) into Eq. (6.2.29), we obtain the following error correlation function of $\hat{y}_{\text{time}}$: for $0 \le t_1 \le t_2$,

$$\begin{aligned}&\langle \varepsilon_{\hat{y}_{\text{time}}}(t_1)\varepsilon_{\hat{y}_{\text{time}}}(t_2)\rangle \\ &= \frac{1}{\mathcal{T}}\left(\frac{k_{\text{B}}T}{m}\right)^2 e^{-\frac{\gamma(t_1+t_2)}{m}}\left[\frac{m}{\gamma}\left(1+e^{\frac{2\gamma t_1}{m}}\right)+t_1\left(1-e^{\frac{2\gamma t_1}{m}}\right)+t_2\left(1+e^{\frac{2\gamma t_1}{m}}\right)\right],\end{aligned} \tag{6.3.10}$$

Hence, the mean-squared error of $\hat{y}_{\text{time}}$ is written as

$$\langle \varepsilon^2_{\hat{y}_{\text{time}}}(t)\rangle = \frac{1}{\mathcal{T}}\left(\frac{k_{\text{B}}T}{m}\right)^2\left[\frac{m}{\gamma}\left(1+e^{-\frac{2\gamma t}{m}}\right)+2te^{-\frac{2\gamma t}{m}}\right]. \tag{6.3.11}$$

By using Eq. (6.3.2), the error correlation function of $\hat{b}_{\text{time}}$ is calculated from Eq. (6.2.32). The function $\langle [x(t_1)-x(0)][x(\alpha+t_2)-x(\alpha)]\rangle$ in Eq. (6.2.32) is calculated from $\int_0^{t_1} dt' \int_\alpha^{\alpha+t_2} dt'' \langle v(0)v(t''-t')\rangle$. Since the explicit expression of $\langle \varepsilon_{\hat{b}_{\text{time}}}(t')\varepsilon_{\hat{b}_{\text{time}}}(t'')\rangle$ is complicated, we only present the mean-squared error of $\hat{b}_{\text{time}}$:

$$\begin{aligned}\langle \varepsilon^2_{\hat{b}_{\text{time}}}(t)\rangle = \frac{1}{\mathcal{T}}\cdot\frac{4(k_{\text{B}}T)^2}{3\gamma^5}\Big[&15m^3\left(3-4e^{-\frac{\gamma t}{m}}+e^{-\frac{2\gamma t}{m}}\right) \\ &-6m^2\gamma t\left(4+2e^{-\frac{\gamma t}{m}}-e^{-\frac{2\gamma t}{m}}\right)+4\gamma^3t^3\Big].\end{aligned} \tag{6.3.12}$$

As in the ensemble-averaging case, the variances of the two estimators for $D(t)$ are obtained from the error correlation functions as follows:

$$\begin{aligned}&\text{Var}\left[\hat{D}^{\text{VACF}}_{\text{time}}(t)\right] = \text{Var}\left[\hat{D}^{\text{MSD}}_{\text{time}}(t)\right] \\ &= \frac{1}{\mathcal{T}}\left(\frac{k_{\text{B}}T}{\gamma}\right)^2\left[\left(4+2e^{-\frac{2\gamma t}{m}}\right)t-\frac{3m}{\gamma}\left(1-e^{-\frac{2\gamma t}{m}}\right)\right].\end{aligned} \tag{6.3.13}$$

6.3.2 Simulation results and discussion

By numerically generating sample trajectories of the Langevin equation (6.3.1), we calculate the VACF, the MSD, and time-dependent diffusion coefficient $D(t)$ through

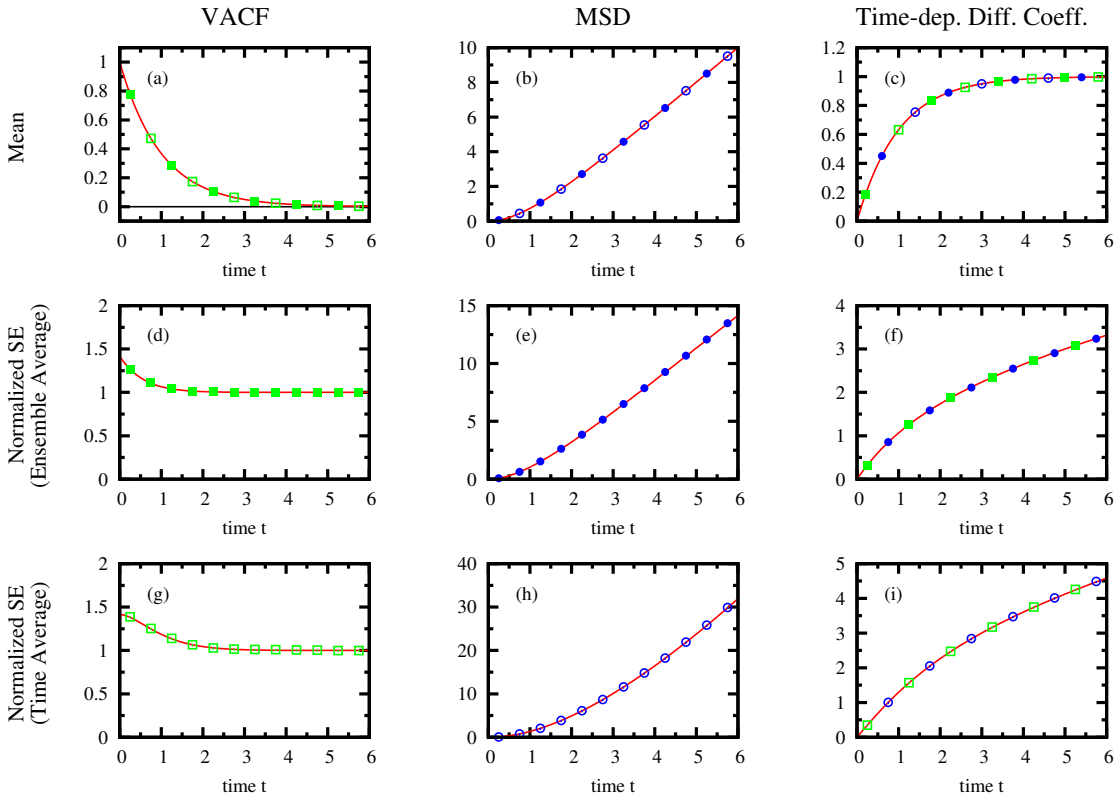

Figure 6.3: Numerical simulation results of the Langevin equation (6.3.1) with $m = \gamma = k_{\rm B}T = 1$. The VACF, MSD, and time-dependent coefficient $D(t)$ and their standard errors are calculated through either ensemble-averaging with $\mathcal{N} = 1000$ or time-averaging with $\mathcal{T} = 1000$ by generating a total of $N_{\rm r} = 32768$ realizations. The time profiles of the three quantities are shown in the plots in the top row. The normalized standard errors (SE) are presented in the middle row for ensemble-averaging and in the bottom row for time-averaging. The standard errors are normalized by $\sqrt{\mathcal{N}}$ for the ensemble-averaging case, whereas they are normalized by $\sqrt{\mathcal{T}}$ for the time-averaging case, see Eq. (6.3.15). Hence, the standard errors of the mean values in the top row are estimated from the normalized standard errors $\bar{\sigma}$ as $\bar{\sigma}/\sqrt{N_{\rm r}\mathcal{N}}$ in the ensemble-averaging case and $\bar{\sigma}/\sqrt{N_{\rm r}\mathcal{T}}$. The red lines depict analytic results, whereas four different symbols depict simulation results: filled green squares (VACF method, ensemble-averaging), empty green squares (VACF method, time-averaging), filled blue circles (MSD method, ensemble-averaging), and empty blue circles (MSD method, time-averaging).

ensemble-averaging and time-averaging, and estimate the standard errors in the VACF, the MSD, and $D(t)$. The system parameters are chosen as $m = \gamma = k_{\mathrm{B}}T = 1$. Sample trajectories are generated by the Euler scheme [99] with $\Delta t_{\mathrm{LE}} = 0.001$. The initial condition of v is sampled from the equilibrium distribution of v,

$$\rho_{\mathrm{eq}}(v) = \sqrt{\frac{m}{2\pi k_{\mathrm{B}}T}} \exp\left(-\frac{mv^2}{2k_{\mathrm{B}}T}\right), \tag{6.3.14}$$

by a standard Gaussian random number generator. The VACF, MSD, and $D(t)$ are calculated up to time $T_{\max} = 10$ with $\Delta t = 10\Delta t_{\mathrm{LE}} = 0.01$. The finite sampling size parameters are chosen as $\mathcal{N} = 1000$ and $\mathcal{T} = 1000$ for ensemble averaging and time averaging, respectively. In order to estimate the standard errors of the estimators $\hat{y}_\bullet$, $\hat{D}_\bullet^{\mathrm{VACF}}$, $\hat{b}_\bullet$, and $\hat{D}_\bullet^{\mathrm{MSD}}$, a total of $N_{\mathrm{r}} = 32768$ realizations for each estimator are obtained. In other words, a total of $\mathcal{N}N_{\mathrm{r}}$ trajectories of length $T_{\max}$ are calculated for ensemble-averaging, whereas a total of N_{r} trajectories of length $\mathcal{T}$ are calculated for time-averaging. For each quantity, the mean-squared error $\langle \varepsilon^2(t) \rangle$ is estimated from N_{r} realizations and the *normalized* standard error $\bar{\sigma}$ is calculated as follows:

$$\bar{\sigma}_{\mathrm{ens}} = \sqrt{\mathcal{N}\langle \varepsilon_{\mathrm{ens}}^2(t) \rangle}, \quad \bar{\sigma}_{\mathrm{time}} = \sqrt{\mathcal{T}\langle \varepsilon_{\mathrm{time}}^2(t) \rangle}. \tag{6.3.15}$$

Then, the normalized standard error is expected to have little dependence on the sampling size parameters $\mathcal{N}$ and $\mathcal{T}$ and the mean value obtained from averaging over N_{r} realizations has standard error $\bar{\sigma}_{\mathrm{ens}}/\sqrt{N_{\mathrm{r}}\mathcal{N}}$ in the ensemble-averaging case and $\bar{\sigma}_{\mathrm{time}}/\sqrt{N_{\mathrm{r}}\mathcal{T}}$ in the time-averaging case. Simulation results are compared with theoretical results in Fig. 6.3. The agreement is excellent, so we verify our results in this case.

We make several observations on the time profile of the standard errors of the estimators. As expected from Eq. (6.2.37), the initial value of the standard error

of $\hat{y}_{\text{time}}$ eventually decreases by factor of $\frac{1}{\sqrt{2}}$. Although the same ratio of the long-time value to the initial value is observed for $\hat{y}_{\text{ens}}$, the time profile at short times is different from the former case and the transition is faster than the former case. This is because the time average uses correlated sample points and the statistical errors at different times are more correlated. By comparing Eqs. (6.2.22) and (6.2.29), we see that the same expression is obtained as the coefficient of $\mathcal{N}^{-1}$ dependence in Eq. (6.2.22) if $\alpha = 0$ is substituted into the integrand in Eq. (6.2.29). This implies that the integration with respect to α in the time-averaging case *blurs* the temporal dependence in the error correlation function. In the MSD calculation, the standard error asymptotically increases like t in the ensemble-averaging case and $t^{3/2}$ in the time-averaging case. For the evaluation of $D(t)$, even after $D(t)$ attains a plateau, the standard deviations of the estimators increase asymptotically as $\sqrt{t}$ in both averaging cases.

Based on these observations, we discuss the long-time behavior of the relative errors. Since the VACF decays rapidly as $t \to \infty$ but its standard error decreases only by factor $\frac{1}{\sqrt{2}}$, the relative error increases rapidly. Hence, in order to guarantee statistical reliability of the long-time tail of the VACF, one needs to severely increase the values of sampling size parameters such as $\mathcal{N}$ and $\mathcal{T}$. For the MSD, the long-time behaviors of the relative errors are very different depending on the type of averaging procedure. Since the MSD asymptotically becomes proportional to t, the relative error becomes constant in the ensemble-averaging case, but it asymptotically increases like $\sqrt{t}$ in the time-averaging case. Since the standard errors of $D(t)$ asymptotically increase like $\sqrt{t}$ in both cases, the relative errors also increase like $\sqrt{t}$.

Before closing this section, we consider a time scale τ^* such that a sample point after time τ^* can be regarded as an uncorrelated sample point. Then, we may consider a time average over a trajectory of length $\mathcal{T}$ as an ensemble average over

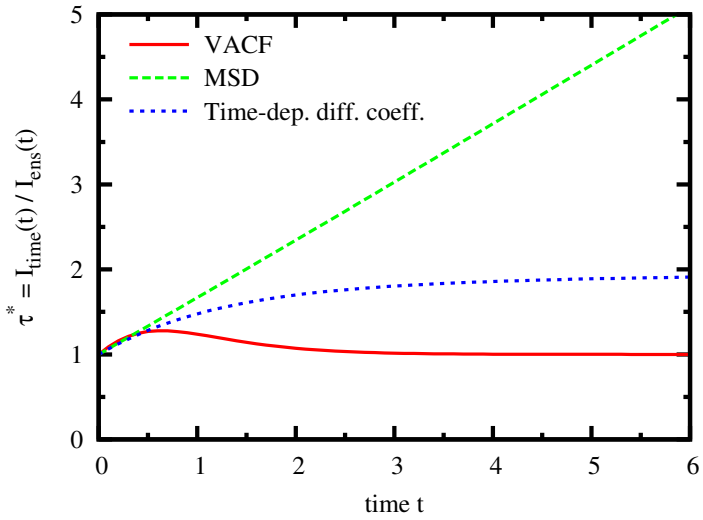

Figure 6.4: For the VACF, MSD, and time-dependent diffusion coefficient, the ratio of $I_{\text{time}}(t)$ to $I_{\text{ens}}(t)$ is plotted. For the definition of $I_{\text{time}}(t)$ and $I_{\text{ens}}(t)$, see the text. The ratio can be considered as a time scale τ^* such that two points in a sample trajectory are effectively uncorrelated if their time difference is greater than τ^*.

a total of $\mathcal{N}^* = \mathcal{T}/\tau^*$ uncorrelated samples. By denoting the coefficients of $\mathcal{N}^{-1}$- and $\mathcal{T}^{-1}$-dependence for the ensemble and time averaging, respectively, as $I_{\text{ens}}(t)$ and $I_{\text{time}}(t)$ (see, e.g., Eqs. (6.2.23) and (6.2.30)), we equate $\frac{1}{\mathcal{T}} I_{\text{time}}(t)$ with $\frac{1}{\mathcal{N}^*} I_{\text{ens}}(t)$, which yields

$$\tau^* = \frac{I_{\text{time}}(t)}{I_{\text{ens}}(t)}. \tag{6.3.16}$$

For the VACF, the MSD, and $D(t)$, the time profiles of τ^* calculated from Eq. (6.3.16) are shown in Figure 6.4. For the VACF and $D(t)$, τ^* maintains consistent values over the time interval, meaning that τ^* is well-defined for these quantities. On the other hand, τ^* increases linearly for the MSD, so τ^* is not well-defined in this case. From the closed-form expressions for the error estimates, we obtain the long-time limits of the ratio $I_{\text{time}}(t)/I_{\text{ens}}(t)$ for the three quantities:

$$\frac{I^{\text{VACF}}_{\text{time}}(t)}{I^{\text{VACF}}_{\text{ens}}(t)} \to \frac{m}{\gamma}, \quad \frac{I^{\text{MSD}}_{\text{time}}(t)}{I^{\text{MSD}}_{\text{ens}}(t)} \to \infty, \quad \frac{I^{D}_{\text{time}}(t)}{I^{D}_{\text{ens}}(t)} \to \frac{2m}{\gamma}. \tag{6.3.17}$$

We note that the time scale for the exponential decay of the VACF (see Eq. (6.3.2))

is m/γ. Hence, Eq. (6.3.17) shows that the time scale τ^* for uncorrelated sample points depends on the quantity to be averaged and may not always be well-defined.

6.4 Validation: MD simulation

In this section, we investigate the error statistics involved in the estimation of the diffusion coefficient for two kinds of MD systems: a pure LJ fluid and a colloidal particle suspended in a LJ fluid. We observe the self-diffusion of a fluid particle in the former case and the tracer diffusion of a colloidal particle in the latter case. We call the two systems as the pure LJ fluid system vs. the colloidal system or the self-diffusion case vs. the tracer diffusion case. Based on the discussion given in Section 6.2.4, see Eq. (6.2.20), the GPA is expected to be better satisfied in the tracer diffusion of a larger and heavier colloidal particle. We investigate the validity of the GPA in the MD systems by calculating the covariance function $\mathrm{Cov}[v(0)v(t_1), v(0)v(t_2)]$ and comparing both sides of the following relation, which holds under the GPA:

$$\mathrm{Cov}[v(0)v(t_1), v(0)v(t_2)] \overset{\text{GPA}}{=} \langle v^2\rangle\langle v(0)v(t_1-t_2)\rangle + \langle v(0)v(t_1)\rangle\langle v(0)v(t_2)\rangle. \quad (6.4.1)$$

Then, we assess the agreement of our theoretical predictions with the actual standard errors estimated from MD simulations and relate the level of agreement with the level of validity of the GPA. In addition, for the pure LJ fluid system, we consider averaging over identical particles and investigate the scaling behavior of the standard errors on the number of averaged particles. For accurate estimation, all calculations are carried out with a large-sized MD ensemble of 32768 independent sample trajectories.

6.4.1 Simulation details

We report all simulation quantities in the LJ reduced units. In other words, we choose the mass of a fluid particle m_{fl}, the diameter of a fluid particle σ_{fl}, and the energy parameter of the LJ potential ϵ_{fl} as the units of mass, length, and energy, respectively.

System parameters The pure LJ fluid system is defined as follows. The number density and temperature of the system are chosen as $\rho_{\mathrm{fl}} = 0.8442$ and $T = 0.722$, which is close to the triple point of the fluid. This state has been frequently used as a reference state after investigated in Ref. [118]. The number of fluid particles is set $N_{\mathrm{fl}} = 2048$, so the side of the cubic simulation box L_{box} is 13.44. Periodic boundary conditions are imposed for all directions. A sufficiently long cutoff radius $r_{\mathrm{cut}} = 5$ is used.

For the colloidal system, a colloidal particle of mass $M_{\mathrm{tracer}} = 60$ is placed in the LJ fluid system described above. The interaction potential between a colloidal particle and a fluid particle is given as the Week–Chandler–Andersen potential with $\sigma_{\mathrm{fl-tracer}} = 2.5$ and $\epsilon_{\mathrm{fl-tracer}} = 1$. In other words, the interaction potential is a shifted LJ potential with cutoff $2^{1/6}\sigma_{\mathrm{fl-tracer}}$, which contains only a repulsive contribution. From the values of σ_{fl} and $\sigma_{\mathrm{fl-tracer}}$, we can infer that the radius of the colloidal particle is $R_{\mathrm{tracer}} = 2$.

MD simulation procedures The same simulation procedures are performed for the pure LJ fluid system and the colloidal system. A total of $N_{\mathrm{r}} = 32768$ sample trajectories are calculated by the velocity Verlet algorithm with time step size $\Delta t =$

0.0025. The initial configurations for the samples in equilibrium are prepared as follows. After the position and velocity of each particle are randomly sampled from the uniform distribution and the Maxwell-Boltzmann distribution, respectively, a total of 20 velocity scaling procedures are performed after every run of $10^4\Delta t = 25$. So, the whole equilibration procedure is performed through the period of $2\times 10^5\Delta t = 500$.

The evaluation procedures of the VACF and the MSD are performed as follows. They are calculated up to time 10 through the ensemble-averaging and time-averaging procedures. In the ensemble-averaging case, the normalized standard error (see Eq. (6.3.15)) is calculated for $\mathcal{N} = 1$ with $N_\mathrm{r} = 32768$ realizations. This is because the generation of equilibrium samples through long equilibration is expensive. In the time-averaging case, the normalized standard error is calculated for $\mathcal{T} = 500$ with the same number of realizations.

For the calculation of the covariance function $\mathrm{Cov}[v(0)v(t_1), v(0)v(t_2)]$, the correlation function $\langle v(0)v(t_1)v(0)v(t_2)\rangle$ $(t_1, t_2 \in [0, t_\mathrm{max}])$ is additionally calculated in an ensemble-averaging manner as follows:

$$\frac{1}{mN_\mathrm{r}}\sum_{k=1}^{N_\mathrm{r}}\sum_{i=0}^{m-1} v^{(k)}(it_\mathrm{max})v^{(k)}(it_\mathrm{max}+t_1)v^{(k)}(it_\mathrm{max})v^{(k)}(it_\mathrm{max}+t_2). \tag{6.4.2}$$

For both systems, it is roughly calculated with $m = 1$ and $t_\mathrm{max} = 10$ and. Then, it is more accurately calculated with $m = 64$ and $t_\mathrm{max} = 1$ for the pure LJ fluid and $t_\mathrm{max} = 4$ for the colloidal system.

For averaging over identical particles in the pure LJ fluid, the number of averaged particles n varies from 1 to 2048. Since the calculation of the VACF and the MSD for each fluid particle requires large memory and computational time in the time-

averaging case, we reduce the computation size by simulating a smaller number of sample trajectories, $N_{\mathrm{r}} = 512$.

Mean-squared velocity $\langle v^2 \rangle$ In order to confirm that the equilibration is well performed and the temperature is well maintained during production runs, the mean-squared velocity $\langle v^2 \rangle$ is monitored. For the pure LJ fluid system, we obtain $\langle v^2 \rangle = 0.7218$ with standard error 9.7×10^{-5} from time-averaging, which is consistent with the equipartition theorem $\langle v^2 \rangle = k_{\mathrm{B}}T/m_{\mathrm{fl}}$ with the target temperature $T = 0.722$. For the colloidal particle system, we obtain $\langle v^2_{\mathrm{tracer}} \rangle = 1.1684 \times 10^{-2}$ with standard error 3.7×10^{-6} from time-averaging. In this case, we need to compare this value with the value estimated from the following expression for $NVE\mathbf{PG}$ ensemble [184]:

$$\left\langle v^2_{\mathrm{tracer}} \right\rangle = \frac{k_{\mathrm{B}}T}{M_{\mathrm{tracer}}} \frac{N_{\mathrm{fl}} m_{\mathrm{fl}}}{M_{\mathrm{tracer}} + N_{\mathrm{fl}} m_{\mathrm{fl}}}. \tag{6.4.3}$$

In other words, for a finite multi-component system, if a microcanonical-ensemble (i.e., NVE) MD simulation is performed under periodic boundary conditions, the equipartition theorem $\langle v^2_{\mathrm{tracer}} \rangle = k_{\mathrm{B}}T/M_{\mathrm{tracer}}$ does not exactly hold. This is attributed to constraints on $\mathbf{P}$ (total linear momentum) and $\mathbf{G}$ (generator of infinitesimal Galilean boosts), which are additionally imposed on the system. Since the values of the mean-squared velocity predicted by Eq. (6.4.3) and the equipartition theorem are 1.1691×10^{-2} and 1.2033×10^{-2}, respectively, the simulation result accurately confirms Eq. (6.4.3).

6.4.2 Simulation results

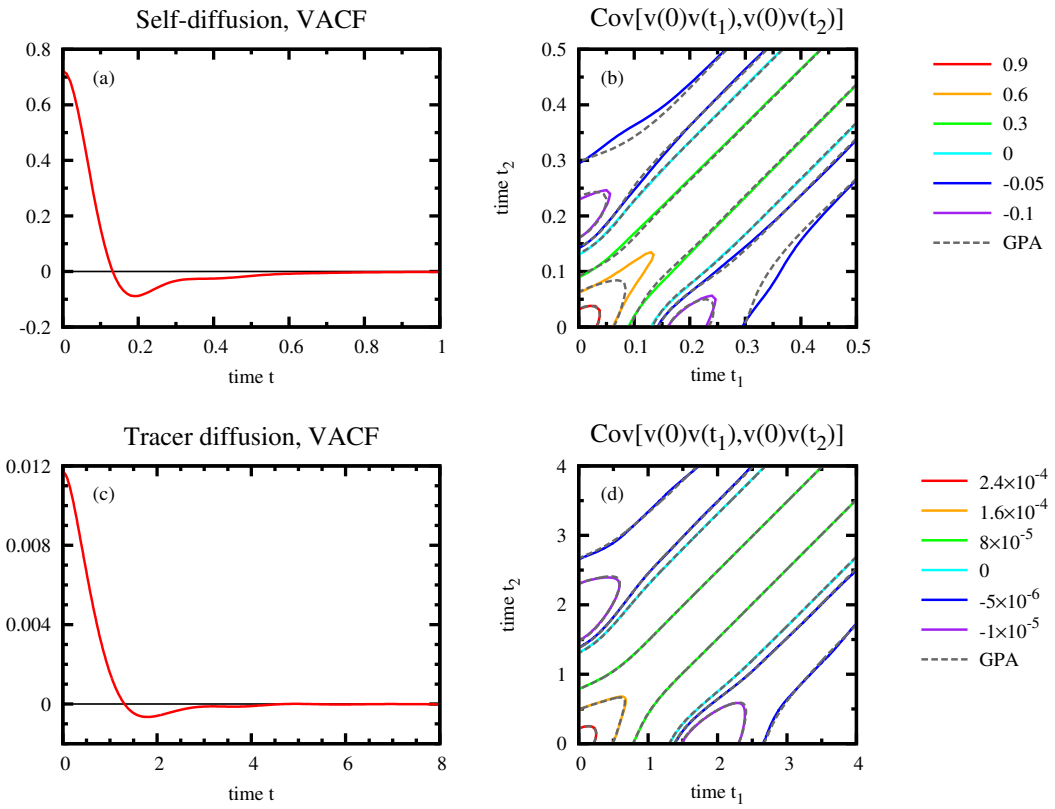

Figure 6.5: For the self-diffusion of the pure LJ fluid and the tracer diffusion of the colloidal system, the time profiles of the VACF and the contour plots of covariance function $\mathrm{Cov}[v(0)v(t_1), v(0)v(t_2)]$ are presented. In the contour plots, the GPA predictions from Eq. (6.4.1) are also plotted by the dashed lines.

Validity of GPA As mentioned above, the validity of the GPA is investigated by the covariance function $\mathrm{Cov}[v(0)v(t_1), v(0)v(t_2)]$. For each system, the MD result calculated from the direct calculation of $\langle v(0)v(t_1)v(0)v(t_2)\rangle$ is compared with the GPA result calculated through Eq. (6.4.1) by using the VACF. Figure 6.5 shows the time profile of the VACF and the comparison of the MD and GPA results for the covariance function. Although the VACF of the tracer particle decays more slowly due to its large mass than the VACF of a fluid particle, the time profiles of the two VACFs have similar shapes containing a negative tail. While the agreement of the MD and GPA results for the covariance function is overall good in the self-diffusion case, the agreement is excellent in the tracer diffusion case. This observation is consistent with the physical explanation of the GPA based on the generalized Langevin equation given in Section 6.2.4, see Eq. (6.2.20). We also note that the tracer diffusion case, where the GPA holds very accurately, is different from the Langevin model system, see Eq. (6.3.1), since its VACF has a negative tail.

Time profiles of VACF, MSD, and $D(t)$ Before analyzing the error statistics, we observe the time profiles of the VACF, the MSD, and $D(t)$, which are shown in the top row of Fig. 6.6 for the self-diffusion case and Fig. 6.7 for the tracer diffusion case. As mentioned above, the time scale for the decay of the VACF is larger in the tracer diffusion case due to large mass of the tracer particle. This time scale can be also found in the asymptotic linear increase of the MSD and the long-time saturation of $D(t)$. However, except different magnitudes of the time scales, the overall shapes of the three quantities are more or less similar for the two cases. Hence, we may not predict the level of validity of the GPA by investigating the VACF or the MSD.

Since the time profiles of the VACF, the MSD and $D(t)$ presented in Fig. 6.6 and Fig. 6.7 are obtained from the time-averaging, their statistical errors are estimated as

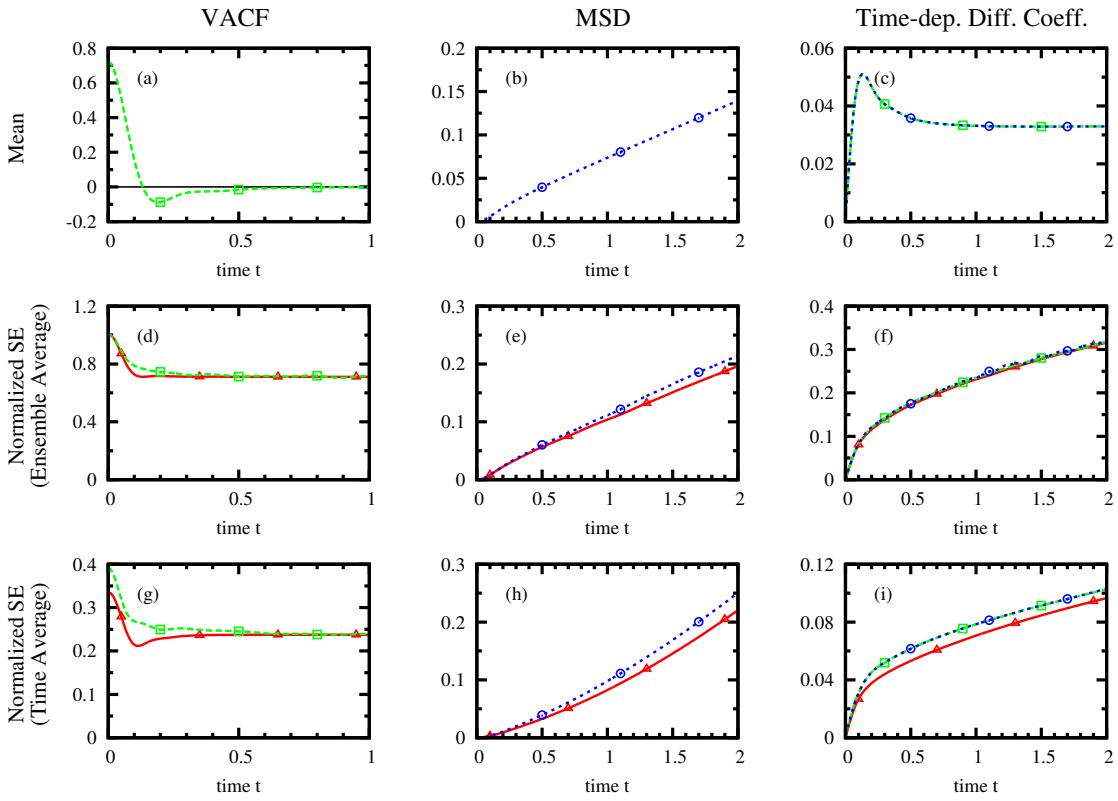

Figure 6.6: For the pure LJ fluid system, the time profiles of the VACF, the MSD, and the time-dependent diffusion coefficient and their normalized standard errors (SE) are presented. The MD simulation data obtained from the time-averaging procedure with $\mathcal{T} = 500$ and $N_r = 32768$ realizations are plotted in the top row and their normalized standard errors $\bar{\sigma}$ (see Eq. (6.3.15)) are plotted in the middle row. The standard errors of the three quantities plotted in the top row are estimated by $\bar{\sigma}/\sqrt{N_r \mathcal{T}}$. In the bottom row, the normalized standard errors estimated from the ensemble-averaging procedure with $\mathcal{N} = 1$ and the same number of realizations are plotted. The red lines with the triangles indicates the GPA prediction estimated from the VACF and the MSD through our theoretical error estimates derived in Section 6.2.5. The green lines with the squares and the blue lines with the circles indicate the MD simulation results obtained by the VACF and MSD methods, respectively.

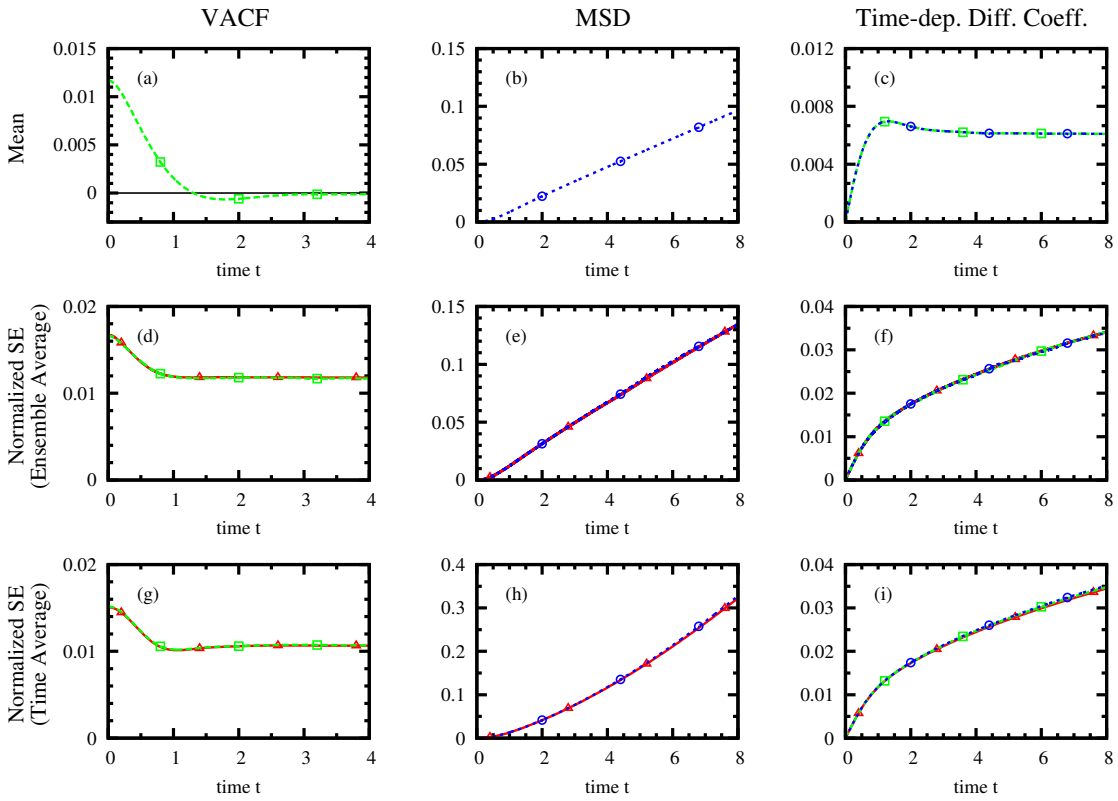

Figure 6.7: For the colloidal system, the time profiles of the VACF, the MSD, and the time-dependent diffusion coefficient and their normalized standard errors (SE) are presented. Since the plots are presented in the same manner as in Fig. 6.6, see the caption of Fig. 6.6.

$\bar{\sigma}/\sqrt{N_{\rm r}\mathcal{T}}$ from the normalized standard errors $\bar{\sigma}$. From the plateau values of $D(t)$, the diffusion coefficients are estimated from time interval $[9, 10]$ as $3.303\times10^{-2}\pm5.3\times10^{-5}$ in the self-diffusion and $6.083\times10^{-3}\pm9.6\times10^{-6}$ in the tracer diffusion case. The value of the self-diffusion coefficient is consistent with the value 3.2619×10^{-2} obtained by using 1372 fluid particles in Ref. [134].

Validity of theoretical error estimates In Fig. 6.6 and Fig. 6.7, the standard errors estimated from the MD ensemble runs are compared with our theoretical error estimates derived in Section 6.2.5. While the agreement is overall good in the self-diffusion case, the agreement is perfect in the tracer-diffusion case. This is consistent with the observation for the level of validity of the GPA in the two systems. Considering that even rough error estimates are useful in practice, our theoretical error estimates provide fairly accurate information for the level of the statistical errors even if the GPA does not hold exactly.

Scaling behavior of standard errors for particle-averaging Finally, we consider averaging over identical particles and investigate the scaling behavior of the statistical errors for the number of averaged particle n. If n is much smaller than the total number N of identical particles in the system, then we expect that the velocity processes of the averaged particles are almost uncorrelated and thus the statistical errors decrease by factor of $n^{-1/2}$. However, if n is comparable to N, then we may not neglect the correlation among the velocity processes and the scaling behavior $n^{-1/2}$ may fail to hold. In 6.6.4, under the GPA of the velocity processes, we show that this scaling behavior still holds for the $NVE\mathbf{PG}$ ensemble of a pure fluid system. We test this prediction for the pure LJ fluid system. For various values of n from 1 to $N_{\rm fl} = 2048$, we calculate the normalized standard errors by additionally multiplying

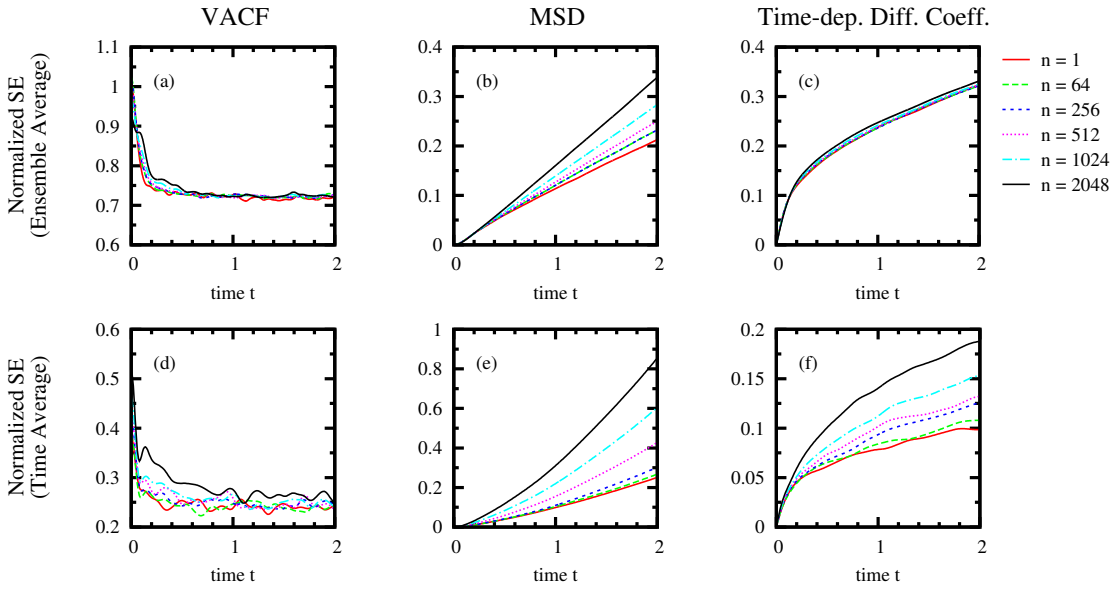

Figure 6.8: For the pure LJ fluid system, the normalized standard errors (SE) estimated from the ensemble-particle and time-particle averaging procedures are plotted. Due to additional averaging over identical particles, the standard errors are also normalized by $\sqrt{n}$, where n is the number of averaged particles. The accordance of the curves indicates the scaling behavior of the statistical error as $n^{-1/2}$. Due to expensive computation, a smaller number of realizations $N_{\mathrm{r}} = 512$ is used.

the factor $\sqrt{n}$. As shown in Fig. 6.8, the scaling behavior of the standard errors is well maintained up to $n = 256$ for all quantities. However, beyond this value of n, the scaling behavior fails in some cases. In the ensemble-averaging case, it is well maintained for the VACF and $D(t)$. Even for the MSD, it is still valid for short times. In the time-averaging case, it is roughly valid for the VACF and only valid at short times for $D(t)$. We guess that the failure of the prediction given in 6.6.4 is due to the failure of the GPA for the velocity processes, which is even stronger than the GPA for a single velocity process.

6.5 Summary and discussion

For the evaluation of the diffusion coefficient D from MD simulations, we have investigated the uncertainty due to finite sampling (i.e., statistical errors). We have analyzed two standard methods, which use the time integral of the VACF and the long-time slope of the MSD. By using theoretical and computational approaches, we have presented a complete systematic analysis on the standard errors of all quantities involved in both methods. We have concluded that the VACF and MSD methods are equivalent in the sense that they provide the same mean values with the same standard errors. The equivalence of the VACF and MSD methods can be understood as follows: although the quality of the MSD data is much better than that of the VACF data, the former becomes worse through time differentiation and the latter becomes better through time integration.

In our theoretical approach, we have derived explicit expressions for the standard errors of the VACF, the MSD, and the time-dependent diffusion coefficient $D(t)$, see Section 6.2.5. It is the error correlation functions of the VACF and the MSD that play a crucial role. Compared with the standard errors of the VACF and the MSD, they contain additional information on the error statistics between different times. We have derived relations (6.2.13) and (6.2.15), which have enabled us to calculate the standard errors of $D(t)$ from the error correlation functions. However, since the direct calculation of the error correlation functions from MD simulations is impractical due to huge computational overhead, we have introduced the GPA of the velocity process. By using the property that all higher-order statistics of a Gaussian process can be expressed in terms of the second-order statistics, we have expressed all theoretical error estimates in terms of the VACF. For example, see Eq. (6.2.36) for the mean-squared error of $D(t)$ estimated from hybrid ensemble/time-averaging. Since

the error correlation functions depend on the type of averaging procedure, we have defined estimators representing several averaging procedures and calculated their error correlation functions. We have considered time-averaging, ensemble-averaging, hybrid ensemble/time-averaging as well as averaging over identical particles.

In our computational approach, we have investigated the validity of our theoretical results. Most importantly, since the accuracy of our theoretical error estimates largely relies on the validity of the GPA, we have investigated the latter for two kinds of molecular systems: the pure LJ fluid system and the colloidal system. In both cases, we have observed that the GPA holds very well. As expected from the physical explanation of the GPA based on the generalized Langevin equation, see Eq. (6.2.20), we have also observed that the GPA holds almost perfectly for the tracer diffusion of a large and heavy colloidal particle. Then, by comparing the standard errors estimated from MD simulations with our theoretical error estimates, we have confirmed the validity of our theoretical results. In order to accurately estimate the standard errors in a direct way from MD simulations, we have performed large-sized MD ensemble runs of size $N_{\mathrm{r}} = 32678$.

The practical implications of the present work are as follows. First of all, once the VACF is roughly estimated, the order of magnitude for the standard errors of all relevant quantities can be readily estimated from our theoretical estimates. This is useful especially when MD simulation is so expensive that the standard errors cannot be directly estimated from a large-sized ensemble run. Second, for a pure fluid system, averaging over *all* identical particles is favorable for ensemble averaging but not so practical for time averaging. While the all-particle-averaging is not so expensive for the ensemble-averaging procedure, it requires huge memory and computational time for the time-averaging. Furthermore, it has been observed that the $n^{-1/2}$ scaling behavior of the standard errors on the number of averaged particle

n quickly fails when n increases in the time-averaging case.

Our theoretical approach has the following advantageous features. First, it is applicable to particle-based methods such as the Langevin dynamics and the dissipative particle dynamics. As discussed in Section 6.2.4, it basically requires only the condition $\dot{x}(t) = v(t)$ and the GPA of v. Second, it can be generalized to the evaluation of other transport coefficients such as the shear viscosity and the thermal diffusivity, which are computable from the Green–Kubo relations or the Einstein–Kubo–Helfand relations. The most important issue may be the validity of the GPA for the underlying process.

6.6 Appendix

6.6.1 Asymptotic approximation for large $\mathcal{T}$

For an arbitrary integrable function $h(t)$, the following relation holds:

$$\frac{1}{\mathcal{T}^2}\int_0^{\mathcal{T}} dt' \int_0^{\mathcal{T}} dt''\, h(t'-t'') = \frac{1}{\mathcal{T}}\int_{-\infty}^{\infty} h(\alpha)d\alpha + \varepsilon \tag{6.6.1}$$

where

$$\varepsilon = -\frac{1}{\mathcal{T}^2}\int_0^{\mathcal{T}} dt \int_t^{\infty} d\alpha\, [h(\alpha) + h(-\alpha)]\,. \tag{6.6.2}$$

We obtain Eq. (6.6.1) as follows. By introducing a new variable $\alpha = t' - t''$ to the inner integral of the left-hand side of Eq. (6.6.1), we have $\frac{1}{\mathcal{T}^2}\int_0^{\mathcal{T}} dt' \int_{t'-\mathcal{T}}^{t'} d\alpha\ h(\alpha)$. By approximating the latter by $\frac{1}{\mathcal{T}^2}\int_0^{\mathcal{T}} dt' \int_{-\infty}^{\infty} d\alpha\ h(\alpha)$ (i.e., by extending the integration range of its inner integral), we obtain the first term in the right-hand side of Eq. (6.6.1). The error of the approximation becomes the term ε defined in Eq. (6.6.2).

If $h(t)$ becomes zero rapidly as $t \to \pm\infty$, ε becomes negligible in Eq. (6.6.1) as $\mathcal{T} \to \infty$. More precisely, if $I_\varepsilon = -\int_0^\infty dt \int_t^\infty d\alpha \, [h(\alpha) + h(-\alpha)]$ is finite, then we have $\mathcal{T}^2\varepsilon \to I_\varepsilon$ as $\mathcal{T} \to \infty$ and, thus, $\mathcal{T}\varepsilon \to 0$. Hence, for large $\mathcal{T}$, we can neglect the ε term in the right-hand side of Eq. (6.6.1), which is equal to $\frac{1}{\mathcal{T}}\left(\int_{-\infty}^{\infty} h(\alpha)d\alpha + \mathcal{T}\varepsilon\right)$. Two simple examples of $h(t)$ having finite I_ε are as follows: (1) If there is a time scale τ such that $h(t) = 0$ for $|t| > \tau$, then $I_\varepsilon = -\int_0^\tau dt \int_t^\tau d\alpha \, [h(\alpha) + h(-\alpha)]$; (2) If $h(t)$ decays exponentially, i.e., $h(t) = Ae^{-|t|/\tau}$, then $I_\varepsilon = -2A\tau^2$.

6.6.2 Derivation of Eqs. (6.2.22) and (6.2.25)

In the ensemble-averaging case, the following relations for covariance are used:

$$\mathrm{Cov}[X, Y] = \langle (X - \langle X \rangle)(Y - \langle Y \rangle) \rangle, \tag{6.6.3}$$

$$\mathrm{Cov}\big[\textstyle\sum_i X_i, \sum_j Y_j\big] = \sum_{i,j} \mathrm{Cov}[X_i, Y_j], \tag{6.6.4}$$

$$\mathrm{Cov}[X, Y] = 0, \quad \text{if } X \text{ and } Y \text{ are uncorrelated.} \tag{6.6.5}$$

Eq. (6.2.22) is obtained as follows:

$$\begin{aligned} &\langle \varepsilon_{\hat{y}_{\mathrm{ens}}}(t')\varepsilon_{\hat{y}_{\mathrm{ens}}}(t'') \rangle = \mathrm{Cov}[\hat{y}_{\mathrm{ens}}(t'), \hat{y}_{\mathrm{ens}}(t'')] \\ &= \tfrac{1}{N^2} \textstyle\sum_{k,l} \mathrm{Cov}[v^{(k)}(0)v^{(k)}(t'), v^{(l)}(0)v^{(l)}(t'')] \\ &= \tfrac{1}{N} \mathrm{Cov}[v(0)v(t'), v(0)v(t'')]. \end{aligned} \tag{6.6.6}$$

Here, the first and second equalities are obtained from Eqs. (6.6.3) and (6.6.4), respectively. Since the covariance terms with $k \neq l$ become zero from Eq. (6.6.5), the last expression is obtained. By applying the GPA (i.e., Eq. (6.2.19)) to the latter, Eq. (6.2.22) is obtained.

Similarly, Eq. (6.2.25) is obtained as follows:

$$\begin{aligned}
&\langle \varepsilon_{\hat{b}_{\mathrm{ens}}}(t')\varepsilon_{\hat{b}_{\mathrm{ens}}}(t'')\rangle = \mathrm{Cov}[\hat{b}_{\mathrm{ens}}(t'), \hat{b}_{\mathrm{ens}}(t'')] \\
&= \tfrac{1}{\mathcal{N}^2}\textstyle\sum_{k,l}\mathrm{Cov}\big[\left(x^{(k)}(t') - x^{(k)}(0)\right)^2, \left(x^{(l)}(t'') - x^{(l)}(0)\right)^2\big] \\
&= \tfrac{1}{\mathcal{N}}\mathrm{Cov}\big[\left(x(t') - x(0)\right)^2, \left(x(t'') - x(0)\right)^2\big].
\end{aligned} \tag{6.6.7}$$

Here, the first, second, and third equalities are obtained from Eqs. (6.6.3), (6.6.4), (6.6.5), respectively. Eq. (6.2.25) is obtained by applying the GPA of x to the last expression.

6.6.3 Derivation of Eqs. (6.2.29) and (6.2.32)

In the time-averaging case, Eq. (6.6.3) and the following relation for covariance are used:

$$\mathrm{Cov}\big[\textstyle\int_0^t X(t')dt', \int_0^t Y(t'')dt''\big] = \int_0^t dt' \int_0^t dt'' \,\mathrm{Cov}[X(t'), Y(t'')]. \tag{6.6.8}$$

Eq. (6.2.29) is obtained as follows:

$$\begin{aligned}
&\langle \varepsilon_{\hat{y}_{\mathrm{time}}}(t_1)\varepsilon_{\hat{y}_{\mathrm{time}}}(t_2)\rangle = \mathrm{Cov}[\hat{y}_{\mathrm{time}}(t_1), \hat{y}_{\mathrm{time}}(t_2)] \\
&= \tfrac{1}{\mathcal{T}^2}\textstyle\int_0^{\mathcal{T}} dt' \int_0^{\mathcal{T}} dt'' \,\mathrm{Cov}[v(t')v(t'+t_1), v(t'')v(t''+t_2)] \\
&= \tfrac{1}{\mathcal{T}^2}\textstyle\int_0^{\mathcal{T}} dt' \int_0^{\mathcal{T}} dt'' \,\big[\langle v(0)v(t''-t')\rangle\langle v(0)v(t''-t'+t_2-t_1)\rangle \\
&\quad + \langle v(0)(t''-t'-t_1)\rangle\langle v(0)v(t''-t'+t_2)\big].
\end{aligned} \tag{6.6.9}$$

Here, the first and second equalities are obtained from Eqs. (6.6.3) and (6.6.8), respectively. By applying the GPA (i.e., Eq. (6.2.19)) to the covariance term, the last expression is obtained. Eq. (6.2.29) is obtained from the asymptotic approximation (6.6.1) for large $\mathcal{T}$.

Similarly, Eq. (6.2.32) is obtained as follows:

$$\begin{aligned}
&\langle \varepsilon_{\hat{b}_{\text{time}}}(t_1)\varepsilon_{\hat{b}_{\text{time}}}(t_2)\rangle = \text{Cov}[\hat{b}_{\text{time}}(t_1), \hat{b}_{\text{time}}(t_2)] \\
&= \tfrac{1}{\mathcal{T}^2}\int_0^{\mathcal{T}} dt' \int_0^{\mathcal{T}} dt'' \,\text{Cov}\left[\left(x(t'+t_1)-x(t')\right)^2, \left(x(t''+t_2)-x(t'')\right)^2 \right] \\
&= \tfrac{2}{\mathcal{T}^2}\int_0^{\mathcal{T}} dt' \int_0^{\mathcal{T}} dt'' \left\langle \left[x(t'+t_1)-x(t')\right]\left[x(t''+t_2)-x(t'')\right]\right\rangle^2 \\
&= \tfrac{2}{\mathcal{T}^2}\int_0^{\mathcal{T}} dt' \int_0^{\mathcal{T}} dt'' \left\langle \left[x(t_1)-x(0)\right]\left[x(t''-t'+t_2)-x(t''-t')\right]\right\rangle^2 .
\end{aligned} \tag{6.6.10}$$

Here, the first and second equalities are obtained from Eqs. (6.6.3) and (6.6.8), respectively. The third equality is obtained by applying the GPA of x to the covariance term and the fourth one is obtained from the invariance of shifting time origin. Eq. (6.2.32) is finally obtained from the asymptotic approximation (6.6.1) for large $\mathcal{T}$.

6.6.4 Scaling behavior of standard errors for particle-averaging in a pure liquid

For a pure fluid system consisting of N identical fluid particles, we first investigate a scaling behavior of the standard errors for a particle-averaging estimator for the VACF and then discuss a general scaling behavior for an estimator including particle-averaging. The particle-averaging estimator for the VACF is defined as follows:

$$\hat{w}(t) = \frac{1}{n}\sum_{i=1}^{n} v_i(0)v_i(t) \tag{6.6.11}$$

where n is the number of identical particles to be included for averaging and v_i is the velocity of the ith particle. Then, we have $\langle \hat{w}(t)\rangle = \langle v(0)v(t)\rangle$ and

$$\text{Var}[\hat{w}(t)] = \frac{1}{n^2}\sum_{i=1}^{n}\sum_{j=1}^{n} \text{Cov}[v_i(0)v_i(t), v_j(0)v_j(t)]. \tag{6.6.12}$$

Under the GPA of the processes $\{v_i(t)\}_{i=1}^N$, we have

$$\begin{aligned}\mathrm{Var}[\hat{w}(t)] = &\frac{1}{n}\left\{\langle v^2\rangle^2 + \langle v(0)v(t)\rangle^2\right\} \\ &+ \frac{1}{n^2}\sum_{i=1}^{n}\sum_{j\neq i}\left\{\langle v_i v_j\rangle^2 + \langle v_i(0)v_j(t)\rangle\langle v_j(0)v_i(t)\rangle\right\}.\end{aligned} \tag{6.6.13}$$

Hence, if the processes $\{v_i(t)\}_{i=1}^n$ are uncorrelated, then we obtain the same result as the ensemble-averaging case, see Eq. (6.2.23). However, in the NVE**PG** ensemble, we have $\sum_{j=1}^N v_j(t) = 0$. By multiplying $v_i(0)$ and taking average, we obtain

$$\langle v_i(0)v_j(t)\rangle = -\frac{1}{N-1}\langle v(0)v(t)\rangle, \quad \text{for } i \neq j. \tag{6.6.14}$$

By substituting Eq. (6.6.14) into Eq. (6.6.13), we obtain

$$\mathrm{Var}[\hat{w}(t)] = \frac{1}{n}\left[1 + \frac{n-1}{(N-1)^2}\right]\left\{\langle v^2\rangle^2 + \langle v(0)v(t)\rangle^2\right\}. \tag{6.6.15}$$

The scaling factor behaves almost like $\frac{1}{n}$ for $1 \leq n \leq N$; even in the case $n = N$, the scaling factor becomes $\frac{1}{N-1}$.

We note that the same argument is applicable to the error correlation function of $\hat{w}$, and hybrid estimators including particle-averaging for the VACF. Hence, almost-like $\frac{1}{\sqrt{n}}$ scaling behavior of the standard errors is expected for the VACF method. Similarly, it is applicable to the MSD method. However, we note that the GPA of the processes $\{v_i(t)\}_{i=1}^N$ is even stronger than that of a single process $v(t)$.

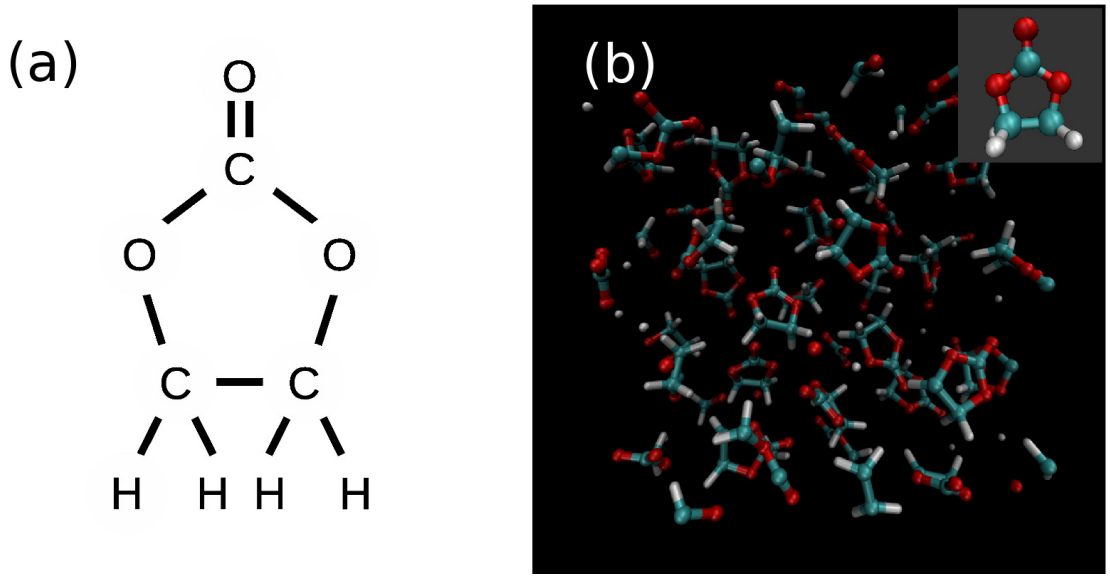

Figure 6.9: (a) Structural formula of ethylene carbonate. (b) Snapshot of the MD simulation for ethylene carbonate liquid.

6.7 Addendum: Validation case-study—MD simulation of ethylene carbonate liquid

In order to investigate the validity of our theoretical error estimates for realistic MD simulations, an ethylene carbonate (EC) liquid system is considered. EC is a polar aprotic organic solvent, see Fig. 6.9 (a), which has played an important role in the lithium battery development; currently, most lithium batteries employ EC mixed with one or more linear carbonates as a solvent [193]. By using a highly transferable, quantum-chemistry-based force field, which is called the atomistic polarizable potential for liquids, electrolytes, & polymers (APPLE&P) [14], we perform MD simulations for the EC liquid system. In Section 6.7.1, we describe MD simulation details. In Section 6.7.2, we present and analyze MD simulation results.

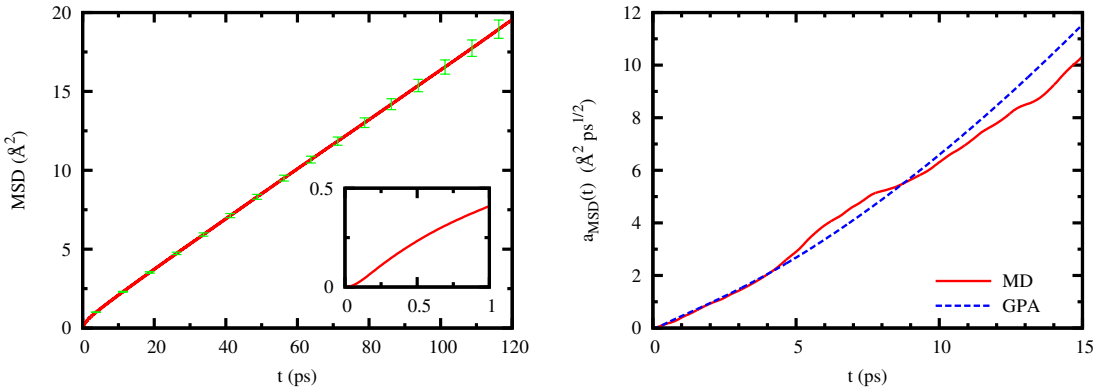

Figure 6.10: In the left panel, the time profile of the MSD of an EC molecule is plotted with the error bars. The MSD results averaged over 512 molecules are used and the error bars correspond two standard deviations. In the right panel, the time profiles of the normalized standard error $a_{\mathrm{MSD}}(t)$ are plotted. The red solid line indicates the MD result which is estimated from the MSD values calculated from a single molecule. The blue dashed line depicts the values predicted by our theoretical error estimate based on the GPA.

6.7.1 MD simulation details

A constant-temperature and constant-volume (NVT ensemble) MD simulation is performed for a three-dimensional, periodic cubic simulation cell consisting of 512 EC molecules, see Fig. 6.9 (b). The simulation box size is 38.61 Å, which corresponds to density 1.321 g/cm^3. The temperature is set to 313.15 K. The MD simulation is run for 2.4 ns and the configuration of the system is saved every 3 fs. The system trajectory is divided into 16 segments of length 150 ps. From each segment, the MSD is calculated for a single molecule (i.e., without particle average) and for 512 molecules (i.e., with particle average), and the time-dependent diffusion coefficient $D(t)$ and the VACF are calculated by numerical differentiation of the MSD. The standard errors present in these quantities are estimated from 16 segments.

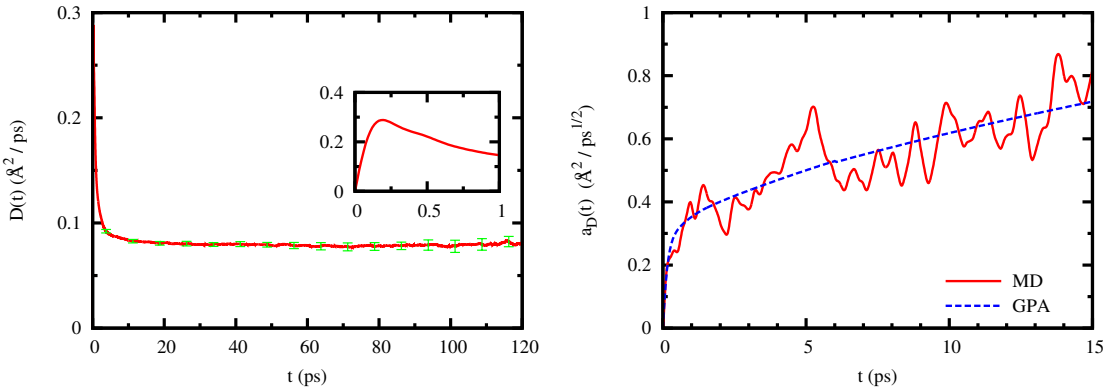

Figure 6.11: Time profiles of the time-dependent diffusion coefficient $D(t)$ of an EC molecule (in the left panel) and its normalized standard error $a_D(t)$ (in the right panel). Since the plots are presented in the same manner as in Fig. 6.10, see the caption of Fig. 6.10.

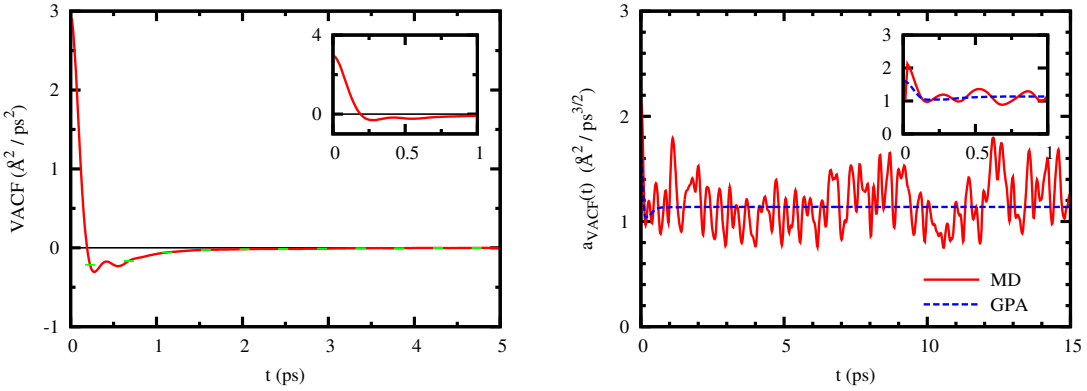

Figure 6.12: Time profiles of the VACF of an EC molecule (in the left panel) and its normalized standard error $a_{\mathrm{VACF}}(t)$ (in the right panel). Since the plots are presented in the same manner as in Fig. 6.10, see the caption of Fig. 6.10.

6.7.2 Results

The time profiles of the MSD, $D(t)$, and VACF are given in the left panels of Figs. 6.10, 6.11, and 6.12, respectively. The plateau in the time profile of $D(t)$ is observed and the diffusion coefficient is estimated as $D = 7.9 \times 10^{-6}$ cm^2/s with standard error 3×10^{-7} cm^2/s, which is consistent with an experimental value for the diffusion coefficient of EC pure solvent, $D = 7.641 \times 10^{-6}$ cm^2/s [23].

In order to investigate the validity of our theoretical error estimates, for the three quantities, we calculate their normalized standard errors $a(t)$ defined through the relation

$$\sqrt{\langle \varepsilon^2(t) \rangle} = \frac{a(t)}{\sqrt{\mathcal{N}\mathcal{T}}}. \tag{6.7.1}$$

Here, $\sqrt{\langle \varepsilon^2(t) \rangle}$ is the standard error of a quantity calculated from a single molecule and the values of $\mathcal{N}$ and $\mathcal{T}$ are 16 and 150 ps, respectively. On the other hand, the analytic expressions for $a(t)$ are obtained from Eqs. (6.2.33), (6.2.31) and (6.2.30), and their values are calculated by using the VACF result obtained from MD simulation. As shown in the right panels of Figs. 6.10, 6.11, and 6.12, our theoretical error estimates accurately predict the standard errors in the MD simulation results for the three quantities. Hence, for a polar organic solvent system, the GPA is shown to be valid.

Finally, we investigate the reduction of the standard error due to particle-averaging. If n molecules are used for average and their motions are uncorrelated, the right-hand side of Eq. (6.7.1) becomes $a(t)/\sqrt{n\mathcal{N}\mathcal{T}}$. However, since the motions of the molecules are correlated in general, n is replaced by the effective particle number n^*, where $1 \leq n^* \leq n$. From the standard errors $\sqrt{\langle \varepsilon^2(t) \rangle_n}$ (from n-particle

average) and $\sqrt{\langle \varepsilon^2(t) \rangle}$ (without particle-averaging), n^* is estimated as

$$n^* = \left(\frac{\sqrt{\langle \varepsilon^2(t) \rangle_1}}{\sqrt{\langle \varepsilon^2(t) \rangle_n}} \right)^2 . \tag{6.7.2}$$

For $n = 512$, the values of n^* are calculated for the three quantities. Although the relative errors are significant due to relatively small number of samples $\mathcal{N} = 16$, the values of n^* are estimated as $n^* \approx 50$ for the MSD around $t = 4$ and $n^* \approx 100$ for $D(t)$ around $t = 2$. Because of fast decay of the VACF, n^* cannot be estimated. However, $n^* \approx n$ is expected at large times. It is also observed that n^* increases as time increases. This is due to the fact that the correlation of motions of two molecules becomes weak at large times due to diffusion.

Chapter Seven

Finite-System-Size Effects: Evaluation of the Diffusion Coefficient

7.1 Introduction

Due to severe limitation on the number of particles that can be calculated by the molecular dynamics (MD) simulation technique, the usual MD system size is much smaller than the macroscopic continuum scale. To make a system more like an infinite system, periodic boundary conditions (PBCs) are usually employed by repeating the MD simulation box without introducing any physical boundary. However, material properties which are calculated under the PBCs may be still different from the true ones that would be obtained from the infinite system.

Finite-system-size effects are unphysical behaviors observed in a finite system. For a system under the PBCs, they are due to the spurious interaction of the system with its PBC images. As the system size increases, the deviations between MD results and the true values are expected to decrease, which can be described by asymptotic expressions in terms of the system size. A finite-system-size correction refers to the estimation of the true value for a physical quantity from an MD value by using such an asymptotic expression. Finite-system-size corrections are important for periodic systems under long-range interactions such as electrostatic or hydrodynamic interactions, which are usually analyzed by the Ewald summation method [53, 115].

In this chapter, we investigate finite-system-size effects on the MD evaluation of the diffusion coefficient D. They have been extensively investigated by using the following finite-system-size correction with respect to the system size L [38]:

$$D_\infty = D_L + \frac{2.837 k_\mathrm{B} T}{6\pi\eta L}, \tag{7.1.1}$$

where η is the shear viscosity of the solvent and D_L and D_∞ are the diffusion coefficient of a solute particle in the finite and infinite systems, respectively. For the

literature review on this correction and MD case studies, see Section 7.2.2. However, we note that the correction is obtained from the hydrodynamic theory, the validity of which should be verified in each case. Rather than relying on the hydrodynamic description (based on the Markovian and continuum assumptions), we investigate the finite-system-size effects on D by investigating the velocity autocorrelation function $C(t)$.

As deduced from the relation between D and $C(t)$,

$$D = \int_0^\infty C(t)dt, \tag{7.1.2}$$

finite-system-size effects on D can be analyzed by the corresponding finite-system-size effects on the VACF. In fact, even since the early days of MD simulation, the following observations have been made [1, 3]; due to its algebraic decay, $t^{-3/2}$, for the three-dimensional case, the long-time tail of the VACF significantly contributes to the time integral value of the VACF (i.e., D), but the tail behavior is very sensitive to the finite system size. For the literature review on the algebraic decay of the long-time tail of the VACF, see Section 7.2.1. Finite-system-size effects on the long-time tail of the VACF have been discussed by using the time scale $\tau_s = L/c_s$ of the sound wave crossing a simulation box (c_s = speed of sound, L = simulation box size) [58]. It is advised that the values of the VACF after this time scale may not be very reliable because of the fast decay resulting from the spurious correlation of the acoustic mode. However, although this type of qualitative discussion has been given frequently in the literature [58], quantitative and systematic analysis on the finite-system-size effects on the VACF has been very limited. This is largely due to computational limitation. While the magnitude of the long-time tail is much smaller than the initial value of the VACF, the level of statistical errors present in the former is comparable to that in the latter [197]. Hence, relative errors in the long-time tail are very large, which

render the clear observation of the tail challenging; in a sufficiently large system, large sampling is required so that the statistical errors be suppressed. In addition, except for theoretical predictions of the mode-coupling theory [48], very little has been theoretically known about asymptotic behaviors of the VACF with respect to the system size.

By using both computational and theoretical approaches, we investigate the finite-system-size effects on the VACF and discuss implications to the evaluation of the diffusion coefficient. By performing large-sized-ensemble MD runs, we calculate the long-time tail of the VACF so accurately that finite-size-effects are clearly observed. We also calculate the memory function of the VACF and find its asymptotic expression for the system size, from which we deduce the corresponding asymptotic expressions of the VACF and the diffusion coefficient.

The rest of this chapter is organized as follows. In Section 7.2, we provide literature reviews on the long-time tail of the VACF and the finite-system-size correction of the diffusion coefficient. In Section 7.3, we present MD simulation results for two states of the Week–Chandler–Andersen (WCA) fluid. In Section 7.4, we provide our memory function approach analysis. In Section 7.5, we conclude this chapter with summary and discussion.

7.2 Literature review

7.2.1 Long-time tail of the VACF

The algebraic decay of the VACF has been first reported computationally by Alder and Wainwright from MD simulations of the hard-sphere system [3]. Subsequently, it was explained theoretically using kinetic theory by Dorfman and Cohen [35, 36, 37] and using the hydrodynamic mode-coupling theory by Ernst, Hauge, and van Leeuwen [46, 47]. For a binary mixture, the algebraic decay has been also theoretically explained by Pomeau [153]. For a review, see Ref. [154]; see also a critique regarding the rigor of theoretical and computational approaches on this subject [55]. As demonstrated by Alder and Wainwright [3], the physical origin of the long-time tail is the formation of a vortex ring, which is related to the ring-collision events in the kinetic theory [26, 27]. The algebraic decay of the VACF has turned out to be universal, and similar power-law decay patterns have been observed in various time correlation functions [45].

From both the kinetic theory and the mode-coupling theory, the following expression has been obtained for the VACF at large time t [35, 46]:

$$C(t) = \frac{1}{3}\langle \mathbf{v}(0)\cdot\mathbf{v}(t)\rangle = \frac{2k_{\mathrm{B}}T}{3\rho_{\mathrm{m}}}\left[4\pi(\nu+D)t\right]^{-3/2}, \tag{7.2.1}$$

where ρ_{m} is the mass density of the fluid and $\nu = \eta/\rho_{\mathrm{m}}$ is the kinematic viscosity of the fluid. For a heuristic but insightful derivation of Eq. (7.2.1), see Refs. [7, 34, 85]. This derivation not only demonstrates that Eq. (7.2.1) results from a coupling between particle diffusion and shear modes in the fluid, but also suggests that this form may be applicable to a general case (i.e., for a broad range of fluid densities

or for the VACF of a colloidal particle in a fluid). By using a finite-system version of the mode-coupling theory, Wood and Erpenbeck have obtained a corresponding expression for the VACF $C_L(t)$ of a finite system with box size L [48].

The validity of Eq. (7.2.1) has also been investigated in the literature. Wood and Erpenbeck have extensively investigated the hard-disk and hard-sphere systems and addressed issues on the finite-system-size effects [48, 49, 50]. Levesque and Ashurst have investigated a continuous potential case by considering the WCA fluid [117]. Subsequently, McDonough, Russo, and Snook [132] and Dib, Ould-Kaddour, and Levesque [34] have extended this investigation by considering the Lennard-Jones (LJ) fluid and investigating a broader range of fluid densities. McDonough, Russo, and Snook [132], Schmidt and Skinner [162], and Ould-Kaddour and Levesque [146] have investigated the mass and size effects of a colloidal particle in a binary mixture system.

7.2.2 Finite-system-size correction of D

By noting that the finite-system-size effects on the diffusion coefficient are due to the long-range hydrodynamic interaction, Dünweg and Kremer [38] and Yeh and Hummer [195] have obtained the finite-system-size correction, Eq. (7.1.1). Although many case studies have followed after their work, Hasimoto had earlier obtained a similar result with the next-order correction by considering the viscous flow past lattices of spheres [78]:

$$D_\infty = D_L + \frac{k_\mathrm{B}T}{6\pi\eta L}\left(2.837 - \frac{4\pi R^2}{3L^2}\right), \tag{7.2.2}$$

where R is the radius of a spherical solute. For the hard-sphere system, Fushiki [63] has proposed the following correction:

$$D_\infty = D_L + \frac{2.902 k_\mathrm{B} T}{6\pi\eta L} \frac{\nu}{\nu + D_\mathrm{E}}, \tag{7.2.3}$$

where D_E is the Enskog estimate of the diffusion coefficient. Compared with Eq. (7.1.1), the slightly different constant 2.902 is due to the approximation of the unit cell with the Wigner–Seitz sphere [191]. More importantly, following a similar argument for the long-time behavior of the VACF made by Alder and Wainwright [3], the correction factor $\nu/(\nu + D_\mathrm{E})$ is included to account for the intermolecular diffusion, particularly at low densities. Botan, Marry, Rotenberg have derived a finite-system-size correction formula for anisotropic systems [18].

The validity of Eq. (7.1.1) has been investigated for various systems. The system size dependence has been investigated for homogeneous systems under the hard-core interaction or the WCA potential [63, 82, 81] and for binary systems [169, 146]. It has been also investigated for water molecules [65, 159, 179], cations in electrolyte solutions [170], ionic liquids [64], and star polymers [166].

7.3 MD simulation results

We perform two sets of MD simulations for the WCA fluid for two states corresponding to $\rho = 0.2$, $T = 2.07$ and $\rho = 0.85$, $T = 1$ (in the usual reduced units for the LJ/WCA system with $m = \sigma = \epsilon = 1$), which we call the lower and higher density cases, respectively. The lower density case has been simulated in Ref. [34], whereas the higher one in Ref. [20]. Compared with these previous MD studies, we perform

large-sized-ensemble MD runs (with 32768 samples) for various system sizes (up to 65536 particles) so that the finite-system-size effects be clearly observed without the interference of statistical errors.

In Section 7.3.1, we describe the MD simulation details. In Section 7.3.2, we present the MD simulation results for the VACF and the time-dependent diffusion coefficient $D(t)$ and analyze the finite-system-size effects.

7.3.1 MD simulation details

In order to investigate the finite-system-size effects, the number of fluid particles in a system is increased from $N_{\rm fl} = 32$ to 65536. The simulation box size L is accordingly increased by $L = \sqrt[3]{\frac{N_{\rm fl}}{\rho}}$. As mentioned above, fluid particles interact under the WCA potential and PBCs are imposed in all directions.

A total of $N_{\rm sample} = 32768$ equilibrium samples are generated as follows. Initial configurations are randomly generated. For equilibration, a prerun of length $T_{\rm equil} = 2500$ is performed with velocity scaling every $T_{\rm scaling} = 250$. For the time integration of the MD simulation, the velocity Verlet scheme is used with time-step size $\Delta t_{\rm MD} = 0.0025$.

The VACF and its time integral are calculated during the main run of length $T_{\rm sim} = 1000$ by using time-averaging. Except for $N_{\rm fl} = 32$, particle-averaging with 64 particles is also used. Then, the quantities are obtained from the ensemble average of $N_{\rm sample}$ samples. The magnitudes of the standard errors of the VACF at time zero and large times are evaluated as 6.4×10^{-5} and 3.8×10^{-5}, respectively, for the lower density case with $N_{\rm fl} = 65536$. Considering that the ratio of the standard error to

the mean value at time zero is 3×10^{-5}, our MD simulation results have a much higher level of precision than usual MD studies.

In order to calculate the values of the time-dependent diffusion coefficient $D(t)$ at very large times (> 100), the MSD is also calculated. For the calculation of the memory function $K(t)$ of the VACF $C(t)$, which satisfies the Volterra equation

$$m\dot{C}(t) = -\int_0^t K(t-t')C(t')dt', \tag{7.3.1}$$

the procedure described in Ref. [164] is employed.

7.3.2 Results

In order to observe behaviors of the VACFs in the infinite-system case, $C_\infty(t)$, we first observe the time profiles of the VACFs of the largest systems, which are shown in Fig. 7.1. In the lower density case, after an initial exponential decay, the long-time tail appears. On the other hand, in the higher density case, after a rapid decay, the VACF has negative values in the intermediate time region, and then the long-time tail appears. The rapid decay and the negative values in the higher density case are explained by the cage effect due to neighboring particles. For both cases, the long-time tails have positive values and decay like $t^{-3/2}$. In the lower density case, the long-time tail appears in a larger time with smaller magnitudes than in the higher density case.

To confirm that these tails are the ones which would be observed in the infinite systems and to observe finite-system-size effects on $C_L(t)$, we compare the time profiles of $C_L(t)$ for various values of the system size L. As shown in Fig. 7.2, the

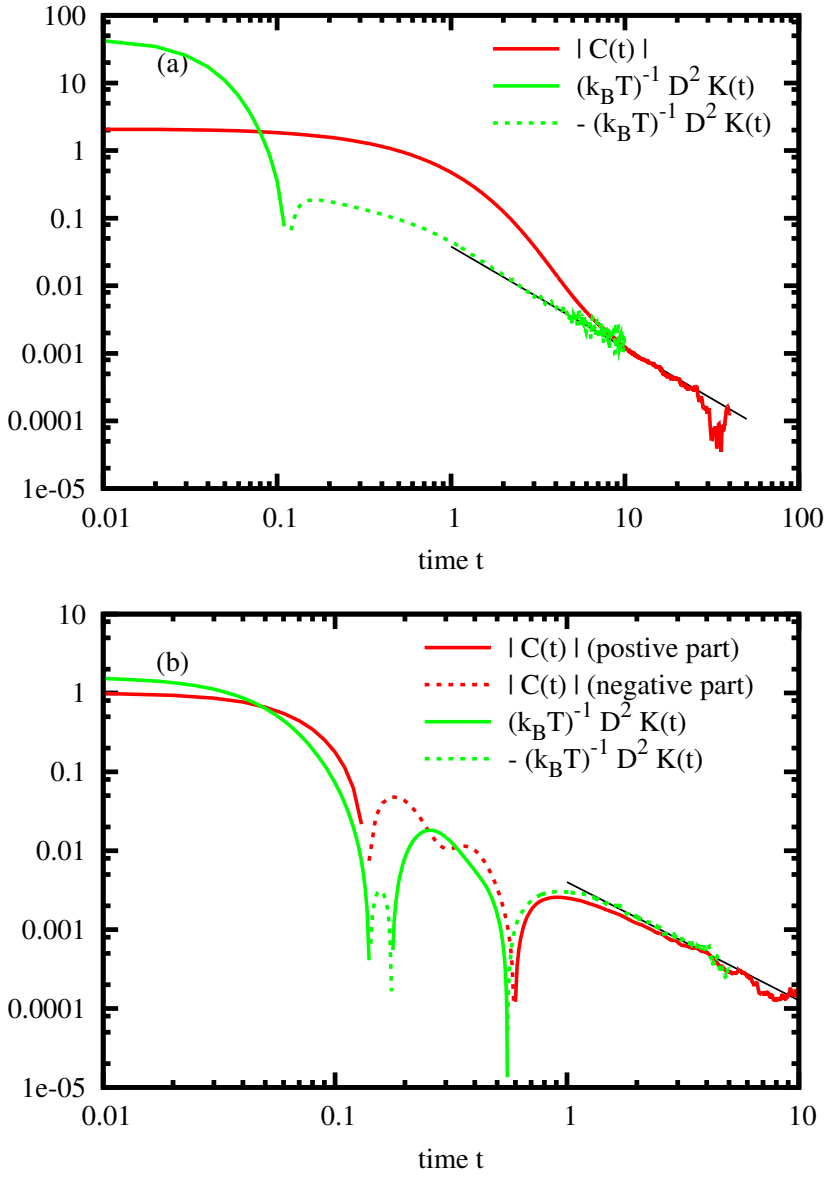

Figure 7.1: Log-log plots of the VACFs $C(t)$ and the memory functions $K(t)$. In panels (a) and (b), results for the lower and higher density cases with $N_{\rm fl} = 65536$ are plotted, respectively. The red lines depict the values of $|C(t)|$, whereas the green lines correspond to $|(k_{\rm B}T)^{-1}D^2K(t)|$, see Eq. (7.4.1). For positive and negative values, the solid and dotted lines are used, respectively. The black lines correspond to $\alpha t^{-3/2}$, where α is obtained by fitting the function to $C(t)$.

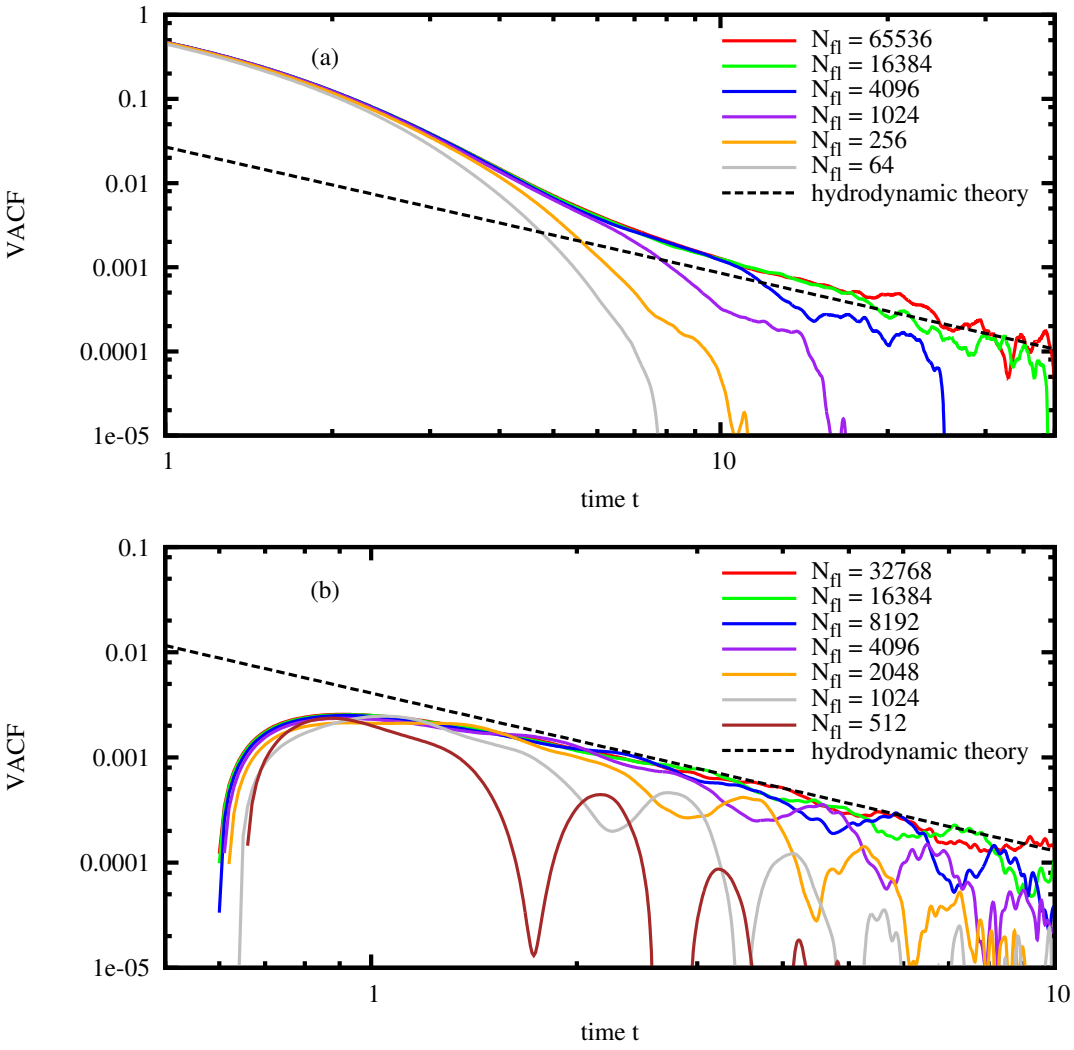

Figure 7.2: Log-log plots of the VACFs for various system sizes. Results for the lower and higher density cases are plotted in panels (a) and (b), respectively. The dotted lines depict the values predicted by the hydrodynamic theory, Eq. (7.2.1).

time profile of the VACF of a smaller system deviates from that of the largest system and the time scale for the onset of the deviation is proportional to the system size L. In the lower density case, it is observed that the time scale is accurately predicted by $\tau_{\rm s} = L/c_{\rm s}$ with $c_{\rm s} = 2.682$ [34]. After $C_L(t)$ deviates from the algebraic decay pattern of $C_\infty(t)$, its decay becomes faster as predicted in Ref. [48]. By using the values of D, which are obtained from a procedure to be described below, and the values of ν from Refs. [20, 34], the theoretical values of the prefactor $\alpha_{\rm theory}$ for the algebraic decay are estimated from Eq. (7.2.1). By using the MD results of the largest systems, corresponding values of $\alpha_{\rm MD}$ are estimated from linear fitting. For the lower density case, we obtain $\alpha_{\rm theory} = 0.0269$ (from $D = 1.50$ and $\nu = 1.71$) and $\alpha_{\rm MD} = 0.035$, and the theory underestimates the value of α by about 25%. For the higher density case, we obtain $\alpha_{\rm theory} = 0.00409$ (from $D = 0.0685$ and $\nu = 2.58$) and $\alpha_{\rm MD} = 0.0037$, and the theory overestimates the value of α by about 10%. We note that the estimated values of $\alpha_{\rm theory}$ may contain significant errors due to the uncertainty in the values of ν, which are obtained from the literature [20, 34]. For the accurate comparison of $\alpha_{\rm theory}$ and $\alpha_{\rm MD}$, an accurate estimation of ν is required.

Using the VACF data, we investigate the scaling behaviors of the finite-system deviation $\Delta C_L(t) = C_L(t) - C_\infty(t)$ of the VACF (not shown). For the infinite-system VACF $C_\infty(t)$, the VACFs of the largest systems are used. As expected, the magnitude of $\Delta C_L(t)$ decreases as L increases. However, it is difficult to find any clear scaling behavior for the magnitude. Also, an attempt to fit $\Delta C_L(t)$ into the form of $L^{-a} f(t/L^b)$ or the sum of a few terms with this form was not successful. It will be shown in Section 7.4.1 that the finite-system deviation $\Delta K_L(t) = K_L(t) - K_\infty(t)$ of the memory function has some scaling behaviors with respect to the system size L and can be fitted into the sum of three terms of the form $L^{-a} f(t/L^b)$. By using this asymptotic expansion, we will derive a corresponding expression for $\Delta C_L(t)$ in

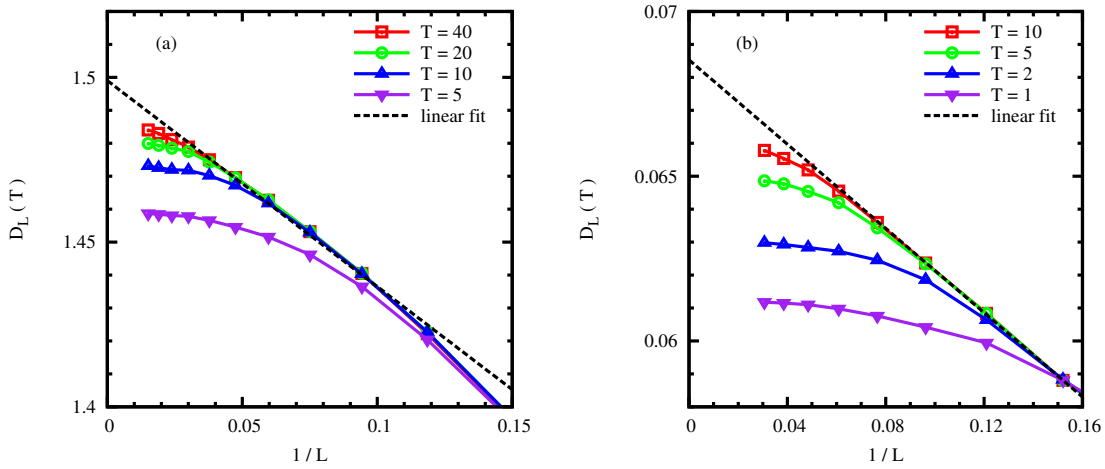

Figure 7.3: Plots of the time-dependent diffusion coefficients $D_L(T)$ versus $1/L$ for various values of T. Results for the lower and higher density cases are plotted in panels (a) and (b), respectively. The dotted lines depict the linear fits obtained from the results for $T = 200$ (lower density case) and $T = 100$ (higher density case).

Section 7.4.2.

Now we investigate the finite-system-size effects on the diffusion coefficient D. Although $D_L = \int_0^\infty C_L(t)dt$ should be estimated from the time integral of $C_L(t)$ over the entire time interval, in practice it is estimated by the time-dependent diffusion coefficient

$$D_L(T) = \int_0^T C(t)dt, \tag{7.3.2}$$

which is estimated at a certain time T. As shown in Fig. 7.3, for a fixed value of T, the value of $D_L(T)$ converges to a certain value as L increases. However, the limit value, which is not the true value D, depends on the value of T, and it increases as T increases. This behavior can be explained by the fast decay of $C_L(t)$ due to the finite system size. If the fast decay of $C(t)$ occurs before time T, its values at times larger than T become negligible and $D_L(T) \approx D_L$. For a sufficiently large system, where the fast decay occurs much later than time T, $D_L(T)$ is different from D_L since $\int_T^\infty C_L(t)dt$ is not negligible. Hence, if we do not increase T as L increases, we cannot observe the $1/L$-dependence of D_L, which is predicted by Eq. (7.1.1), from

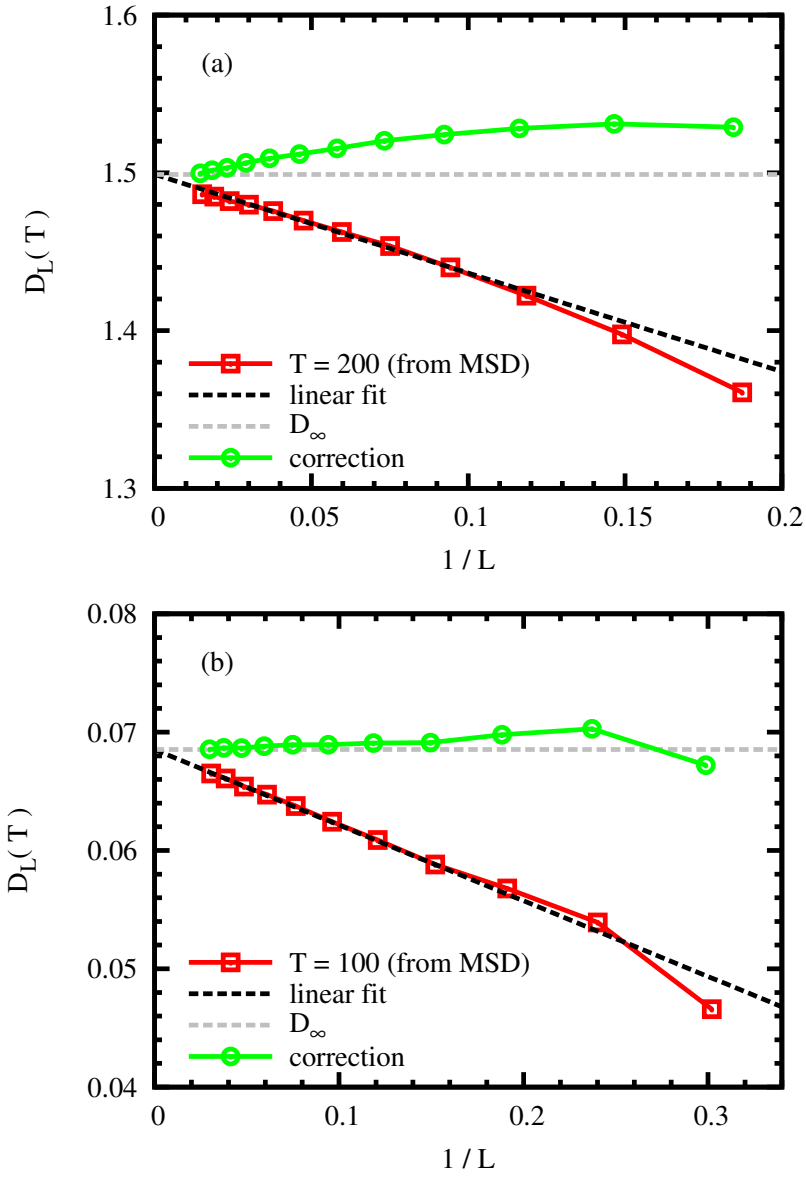

Figure 7.4: The $1/L$ dependence of the finite-system diffusion coefficient D_L and the finite-system-size correction. Results for the lower and higher density cases are shown in panels (a) and (b), respectively. The values of D_L are estimated from $D_L(T)$ for $T = 200$ (lower density case) and $T = 100$ (higher density case), and plotted by the red solid lines. The linear fits are also plotted by the black dotted lines. The hydrodynamic corrections obtained from Eq. (7.1.1) are plotted by the green solid lines.

the values of $D_L(T)$. In other words, in order to estimate the value of D from $D_L(T^*)$ by using

$$D = \lim_{L\to\infty} D_L(T^*), \tag{7.3.3}$$

the truncation time T^* of the time integral should be increased as L increases. From the time scale τ_s, it is expected that T^* should be linearly proportional to L. As shown in Fig. 7.4, for each case, the value of D is estimated from $D_L(T)$ with a very large value of T. As reported above, the diffusion coefficients are estimated as $D = 1.50$ for the lower density case and $D = 0.0685$ for the higher density case. Our value of D for the higher density case is larger than the value 0.062 reported in Ref. [20], where the D_L values were reported for $N_{\rm fl} = 256$ to 8192 and they converged to 0.062 for $N_{\rm fl} \geq 2048$. Although the exact value of the truncation time T for $D_L(T)$ was not reported in Ref. [20], based on our discussion for the convergence of each curve in Fig. 7.3, we suspect that the value of T was not sufficiently large. We note that similar flaws in Refs. [41, 42, 171] have been discussed by Erpenbeck and Wood in Ref. [50].

Finally, we examine the validity of the finite-system-size correction given in Eq. (7.1.1). As shown in Fig. 7.4, the correction is more accurate in the higher density case. For the lower density case, the slope of the $1/L$-dependence is estimated as -0.625 and the slope in the correction is 0.910 (error = 45%). For the higher density case, the slope is estimated as -0.0638 and the slope in the correction is 0.0687 (error = 8%). By introducing the scaling factor $\nu/(\nu + D_{\rm E})$ [63], see Eq. (7.2.3), the correction becomes more accurate for the lower density case. This is because the diffusion of a tracer particle is not considered in the correction, Eq. (7.1.1). In the lower density case, where D is comparable to ν, the scaling factor improves the quality of the correction, whereas in the higher density case, where $D \ll \nu$, the improvement is not significant.

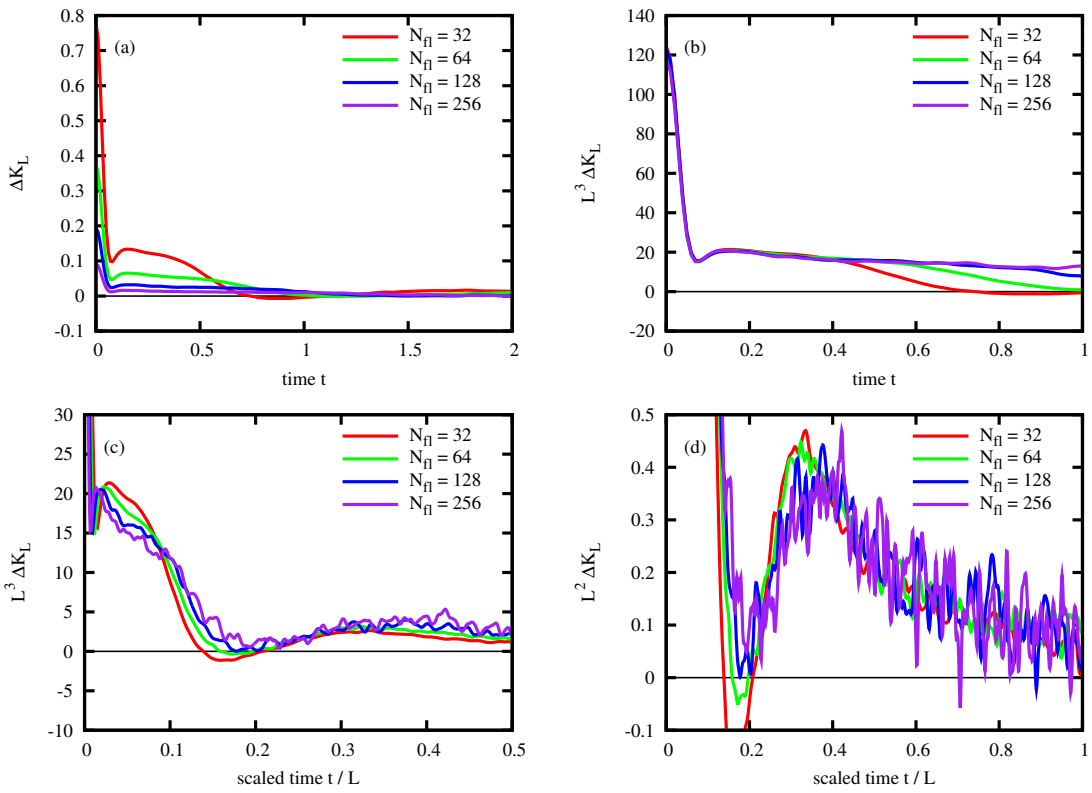

Figure 7.5: Scaling behaviors of the finite-system deviation $\Delta K_L(t)$ of the memory function. For the lower density case, the time profiles of $\Delta K_L(t)$ are plotted under the following scalings. Panel (a): ΔK_L versus t; panel (b): $L^3\Delta K_L$ versus t; panel (c): $L^3\Delta K_L$ versus t/L; panel (d): $L^2\Delta K_L$ versus t/L. The system size L is equal to $\sqrt[3]{N_{\mathrm{fl}}/\rho}$.

7.4 Memory function approach

In Section 7.4.1, we propose an asymptotic expression for the finite-system deviation $\Delta K_L(t) = K_L(t) - K_\infty(t)$ from the MD results. In Section 7.4.2, by using this expression, we derive corresponding asymptotic expressions for $C_L(t)$ and D_L.

7.4.1 Asymptotic scaling behaviors of $\Delta K_L(t)$

We first investigate behaviors of the infinite-system memory function $K_\infty(t)$ by observing $K_L(t)$ of the largest systems. As shown in Fig. 7.1, in the lower density case the value of the memory function changes its sign once, whereas in the higher density case three times. In each case, a long-time tail is observed. Its value is negative and it decays algebraically like $t^{-3/2}$ as the VACF. In fact, this has been predicted by Corngold [28, 29]; for large t,

$$C(t) = -\frac{D^2}{k_{\rm B}T}K(t). \tag{7.4.1}$$

In Fig. 7.1, we computationally confirm this long-time relation between $C_\infty(t)$ and $K_\infty(t)$. We also observe that, for the lower density case, there is a large time scale separation between $C(t)$ and $K(t)$ and the algebraic decay of $K(t)$ occurs earlier.

Now we observe the scaling behaviors of $\Delta K_L(t)$. As shown in Fig. 7.5 (b), the short-time region is well fitted into the form $L^{-3}A_1(t)$. However, the second peak in the intermediate-time region is better fitted when the scaled time t/L is used, see Fig. 7.5 (c). As shown in Fig. 7.5 (d), for large times, $\Delta K_L(t)$ is well fitted into the form $L^{-2}A_3(t/L)$. From these observations, we propose the following asymptotic expression for $\Delta K_L(t)$:

$$\Delta K_L(t) = K_L(t) - K_\infty(t) = \frac{1}{L^3}A_1(t) + \frac{1}{L^3}A_2\left(\frac{t}{L}\right) + \frac{1}{L^2}A_3\left(\frac{t}{L}\right). \tag{7.4.2}$$

We note that although the validity of Eq. (7.4.2) largely depends on the reliability of our computational results, it is clearly observed that there are at least two contributions with time scales t and t/L. The contribution with time scale t is dominant

at small times. By considering the relation

$$K(0) = \frac{\langle \mathbf{F} \cdot \mathbf{F} \rangle}{3k_{\mathrm{B}}T} \tag{7.4.3}$$

and the fact that the mean-squared force on the particle can be calculated by the radial distribution, this contribution can be explained by the finite-system-size effects on the distribution of surrounding fluid particles, which is expected to have a $1/N_{\mathrm{fl}}$-dependence (i.e., a $1/L^3$-dependence). On the other hand, the contribution with time scale t/L can be explained by the finite-system-size effects on the momentum diffusion.

7.4.2 Asymptotic expressions for $C_L(t)$ and D_L

For the asymptotic expression for $K_L(t) = K_\infty(t) + \Delta K_L(t)$, Eq. (7.4.2), we first derive a corresponding asymptotic expression for $C_L(t)$ by using the Laplace transform technique. A similar procedure has been used in Ref. [97].

By denoting the Laplace transform of a function $f(t)$ by $\tilde{f}(s) = \int_0^\infty e^{-ts} f(t) dt$, the Laplace transform of the Volterra equation, Eq. (7.3.1) becomes

$$m\left(s\tilde{C}(s) - C(0)\right) = -\tilde{K}(s)\tilde{C}(s). \tag{7.4.4}$$

Hence, by using $C(0) = k_{\mathrm{B}}T/m$, we have

$$\tilde{C}_L(s) = \frac{k_{\mathrm{B}}T}{ms + \tilde{K}_L(s)}, \tag{7.4.5}$$

$$\tilde{C}_\infty(s) = \frac{k_{\mathrm{B}}T}{ms + \tilde{K}_\infty(s)}. \tag{7.4.6}$$

By substituting $\tilde{K}_L(s) = \tilde{K}_\infty(s) + \Delta\tilde{K}_L(s)$ into Eq. (7.4.5), we have

$$\tilde{C}(s) = \frac{k_\mathrm{B}T}{ms + \tilde{K}_\infty(s)} \frac{1}{1 + \frac{\Delta\tilde{K}_L(s)}{ms+\tilde{K}_\infty(s)}}. \tag{7.4.7}$$

By using Eq. (7.4.6) and assuming that $\Delta\tilde{K}_L(s)$ is sufficiently small, we have

$$\tilde{C}_L(s) = \tilde{C}_\infty(s) \sum_{k=0}^{\infty} \left(-\frac{\Delta\tilde{K}_L(s)}{ms + \tilde{K}_\infty(s)} \right)^k. \tag{7.4.8}$$

By using Eq. (7.4.6) again, we obtain

$$\tilde{C}_L(s) = \tilde{C}_\infty(s) + \tilde{C}_\infty(s) \sum_{k=1}^{\infty} \left(-\frac{1}{k_\mathrm{B}T} \Delta\tilde{K}_L(s)\tilde{C}_\infty(s) \right)^k. \tag{7.4.9}$$

Note that in Eq. (7.4.9) we have expressed $\tilde{C}_L(s)$ in terms of $\tilde{C}_\infty(s)$ and $\Delta\tilde{K}_L(s)$. Hence, we finally obtain

$$C_L(t) = C_\infty(t) + C_\infty(t) * \sum_{k=1}^{\infty} \left(-\frac{1}{k_\mathrm{B}T} \Delta K_L(t) * C_\infty(t) \right)^{*k}, \tag{7.4.10}$$

where $*$ and $(\ )^{*k}$ denote convolution and k-fold convolution, respectively. By assuming $\Delta K_L(t) \approx \frac{1}{L^2} A_3\left(\frac{t}{L}\right)$ from Eq. (7.4.2), we obtain the lowest-order correction

$$C_L(t) \approx C_\infty(t) - \frac{1}{k_\mathrm{B}T} A_3\left(\frac{t}{L}\right) * C_\infty(t) * C_\infty(t) \cdot \frac{1}{L^2}. \tag{7.4.11}$$

Now we obtain an asymptotic expression for D_L from Eq. (7.4.9). From $D_L = \tilde{C}_L(0)$ and $D_\infty = \tilde{C}_\infty(0)$, we have

$$D_L = D_\infty + D_\infty \sum_{k=1}^{\infty} \left(-\frac{\Delta\tilde{K}_L(0) D_\infty}{k_\mathrm{B}T} \right)^k. \tag{7.4.12}$$

By introducing $a_i = \int_0^\infty A_i(t)dt$ $(i = 1, 2, 3)$, we have

$$\Delta\tilde{K}_L(0) = \int_0^\infty \Delta K_L(t)dt = \frac{a_1}{L^3} + \frac{a_2}{L^2} + \frac{a_3}{L}, \tag{7.4.13}$$

and thus

$$D_L = D_\infty \left[1 + \sum_{k=1}^{\infty} \left(-\frac{D_\infty}{k_\mathrm{B}T}\right)^k \left(\frac{a_1}{L^3} + \frac{a_2}{L^2} + \frac{a_3}{L}\right)^k\right]. \tag{7.4.14}$$

Hence, we obtain the lowest-order correction of D_L:

$$D_L \approx D_\infty \left(1 - \frac{D_\infty a_3}{k_\mathrm{B}T} \cdot \frac{1}{L}\right). \tag{7.4.15}$$

By introducing the Stokes–Einstein relation $D_\infty = k_\mathrm{B}T/(6\pi\eta R)$ into Eq. (7.4.15), we obtain the following form, which is similar to Eq. (7.1.1),

$$D_L \approx D_\infty \left(1 - \frac{a_3}{6\pi\eta R} \cdot \frac{1}{L}\right). \tag{7.4.16}$$

7.5 Summary and discussion

In this chapter, we have investigated the finite-system-size effects on the VACF $C(t)$ and the diffusion coefficient D. By performing large-sized-ensemble MD runs for two states of the WCA fluid, we have presented the time profiles of the VACF for various system sizes, where the statistical errors were substantially suppressed. From these results, the algebraic decay pattern as well as the fast decay pattern due to the finite system size have been clearly observed. By investigating the dependence of the time-dependent diffusion coefficient $D_L(T)$ on both the system size L and the evaluation time T, we have shown that in order to observe the $1/L$-dependence of

D_L, the value of T should be increased as L increases. This has been explained by the fast decay of the VACF due to the finite system size.

By investigating the scaling behaviors of $K_L(t)$ with respect to L, we have obtained the asymptotic expressions of $C_L(t)$ and D_L. From the computational results of $K_L(t)$, we have proposed its asymptotic expression given in Eq. (7.4.2). We have shown that there are two time scales in $\Delta K_L(t)$. The contribution with time scale t/L have been explained as the finite-system-size effects on the momentum diffusion, whereas the contribution with time scale t have been explained as the finite-system-size effects on the surrounding fluid distribution. Then, we have obtained the corresponding expressions for $C_L(t)$ and D_L, see Eqs. (7.4.11) and (7.4.15), by using the Laplace transform technique.

The theoretical predictions for the prefactor of the algebraic decay in the long-time tail of the VACF and the slope of the $1/L$-dependence of D_L have been observed to be more accurate for the higher density case. This is consistent with the fact that these theoretical predictions are obtained from the hydrodynamic theory. For the lower density case, where the diffusion coefficient D is comparable to the kinematic viscosity ν, it has been observed that the scaling factor $\nu/(\nu + D_{\mathrm{E}})$ improves the quality of the correction.

We note that the finite-system-size correction for D_L, Eq. (7.1.1), does not use any information about a tracer particle and uses only the viscosity of the solvent. Although this simple form may be practical and useful, it may pose a subtle issue when it is applied to a multi-component system. It will be interesting to compare Eq. (7.1.1) with our asymptotic expression, Eq. (7.4.15), which has been obtained from the memory function approach.

Chapter Eight

Future work

8.1 Memory function approach for molecular systems

GLEs for multiple particles

Compared with the generalized Langevin equation (GLE) formulation for a single particle, GLEs for multiple particles have not been rigorously formulated very well. For example, although the following form of GLEs has been, in practice, employed

$$M_i\dot{\mathbf{V}}_i(t) = -\sum_{j\neq i}\nabla U_{ij}^{\mathrm{eff}}(|\mathbf{X}_i(t)-\mathbf{X}_j(t)|) - \int_0^t \mathbf{K}_i(t-t')\mathbf{V}_i(t')dt' + \mathbf{F}_i^+(t), \quad (8.1.1)$$

it is not derived from the Mori–Zwanzig formalism. In fact, the effective force part has been borrowed from Zwanzig's approach, where the conditional expectation is used as the projection operator, whereas the form of the time convolution and the fluctuating force has been suggested by Mori's approach, where the linear (or vector) projection is used [66]. In addition, a valid form of the fluctuation-dissipation relation is required to be used [192]. The assumption on the form of the effective potential (i.e., the sum of pairwise interaction potentials) also needs to be investigated. Hence, investigation of Eq. (8.1.1) from a rigorous theoretical view point is needed. In other words, it is necessary to understand how, or under which conditions, a general form of GLEs [83] is reduced to Eq. (8.1.1). On the other hand, from a practical view point, it is necessary to develop an efficient method to estimate U^{eff}, $\mathbf{K}_i$, and $\langle\mathbf{F}_i(0)\mathbf{F}_j(t)\rangle$ from MD simulations.

The GLEs for multiple particles can be used to provide an improved model for mesoscopic multiscale methods such as the dissipative particle dynamics (DPD). To this end, it is favorable to include state dependence (e.g., on the inter-particle

distance) in the memory term and the fluctuating force. For the development of a DPD model from MD simulation under the Markovian assumption, see Ref. [122]. By developing a DPD model with state-dependent memory, one can simulate a system where complicated molecular interactions are important. Both the construction of the model from MD simulation and the implementation of the model should be efficient.

Brownian motion in electrolyte solutions

Although Brownian motion usually occurs in electrolyte solutions, corresponding microscopic models and relevant microscopic theories have been limited. This is because the description of a microscopic system containing all four types of species—colloidal particles, solvent particles, cations, and anions–is challenging. Hence, one needs to rely on computational results from MD simulation. By comparing the memory function of a colloidal in an electrolyte solution with that in a neutral solvent, essential effects of charged species can be investigated. This can be used to understand limitations of the primitive model and to develop an improved model. In addition, Brownian motion in electrolyte solutions can be used as a test problem for multiple-particle GLEs.

Anomalous diffusion phenomena in confined systems

It has been reported that the confinement of a system may induce an anomalous diffusion behavior [6, 10, 92]. However, in many cases, it takes long time for this behavior to be clearly observed from the mean-squared displacement or the velocity autocorrelation function, which may prevent one from observing the phenomenon

directly from simulation. Since the algebraic decay exponent of the memory function is identical to that of the velocity autocorrelation function [28, 29], the anomalous diffusion behavior can be investigated by the memory function. In the case that the onset of the algebraic decay in the memory function is earlier than that in the velocity autocorrelation function (for example, when the particle has large mass), investigation through the memory function is more effective.

8.2 Uncertainty quantification for MD simulation

Accurate assessment of the validity of the hydrodynamic description

The investigation of the validity of the hydrodynamic description at the molecular level has up to the present time been only qualitative and in many cases inconclusive (even for the Stokes–Einstein relation). This is partially because, while the investigation mainly relies on MD simulation results, these results are not usually sufficiently accurate and precise. By performing large-sized-ensemble MD runs and subsequently applying a valid finite-system-size correction procedure, one can examine the validity of hydrodynamic relations and expressions in a quantitative manner.

UQ analysis for MD simulation of battery electrolytes

Our theoretical and computational uncertainty quantification (UQ) framework is applicable to more practical MD simulations. For example, the analysis of the pure EC solvent system can be extended to lithium-salt-doped EC systems such

as EC:DMC/$LiPF_6$ (DMC = dimethyl carbonate) [16, 17], which have direct applications to lithium battery development. Due to the formation of Li^+–EC complexes in such systems, the validity of the GPA becomes highly questionable. Hence, these systems may serve as a nontrivial case that should be investigated in order to establish the general validity of the GPA and of our theoretical statistical-error estimates.

One of the unphysical features of the finite-system-size correction, Eq. (7.1.1) is that it does not use any information about a tracer particle (e.g., the size of the particle). For multi-component systems, this leads to the same corrections to the values of the diffusion coefficients of all species even if the diffusion coefficients are very different. This problem can be effectively investigated by the AN-$LiCF_3CO_2$ and AN-LiFSI electrolyte systems (AN = acetonitrile, FSI^- = bis(fluorosulfonyl)imide) [15, 74]. The former is a strongly aggregated case (where the salt is not dissociated into ions), whereas the latter is a largely dispersed case (where the salt is dissociated into cations and anions). By comparing these two cases, it can be found how the finite-system-size correction can be improved for multi-component systems. It will be also interesting to observe how the correlation due to aggregation influences the finite-system-size errors.

Bibliography

[1] Alder, B., Gass, D., Wainwright, T.: Studies in molecular dynamics. VIII. The transport coefficients for a hard-sphere fluid. J. Chem. Phys **53**, 3813–3826 (1970)

[2] Alder, B., Wainwright, T.: Studies in molecular dynamics. I. General method. J. Chem. Phys. **31**, 459 (1959)

[3] Alder, B., Wainwright, T.: Decay of the velocity autocorrelation function. Phys. Rev. A **1**, 18–21 (1970)

[4] Allen, M., Tildesley, D.: Computer Simulation of Liquids. Clarendon Press, Oxford (1987)

[5] Angelikopoulos, P., Papadimitriou, C., Koumoutsakos, P.: Bayesian uncertainty quantification and propagation in molecular dynamics simulations: A high performance computing framework. J. Chem. Phys. **137**, 144,103 (2012)

[6] Ball, C., MacWilliam, N., Percus, J., Bowles, R.: Normal and anomalous diffusion in highly confined hard disk fluid mixtures. J. Chem. Phys. **130**, 054,504 (2009)

[7] van Beijeren, H.: Transport properties of stochastic Lorentz models. Rev. Mod. Phys. **1982**, 195–234 (1982)

[8] Bell, J., Garcia, A., Williams, S.: Numerical methods for the stochastic Landau–Lifshitz Navier–Stokes equations. Phys. Rev. E **76**, 016,708 (2007)

[9] Berkowitz, M., Morgan, J., McCammon, J.: Generalized Langevin dynamics simulations with arbitrary time-dependent memory kernels. J. Chem. Phys. **78**, 3256–3261 (1983)

[10] Bleibel, J., Domíngues, A., Günther, F., Harting, J., Oettel, M.: Hydrodynamic interactions induce anomalous diffusion under partial confinement. Soft Matter **10**, 2945–2948 (2014)

[11] Blum, J., Bruns, S., Rademacher, D., Voss, A., Willenberg, B.: Measurement of the translational and rotational Brownian motion of individual particles in a rarefied gas. Phys. Rev. Lett. **97**, 230,601 (2006)

[12] Bologna, M.: Asymptotic solution for first and second order linear Volterra integro-differential equations with convolution kernels. J. Phys. A: Math. Theor. **43**, 375,203 (2010)

[13] Boon, J., Yip, S.: Molecular Hydrodynamics. Dover Publications (1991)

[14] Borodin, O.: Polarizable force field development and molecular dynamics simulations of ionic liquids. J. Phys. Chem. B **113**, 11,463–11,478 (2009)

[15] Borodin, O., Han, S.D., Daubert, J., Seo, D., Yun, S.H., Henderson, W.: Electrolyte solvation and ionic association. J. Electrochem. Soc. **162**, A501–A510 (2015)

[16] Borodin, O., Smith, G.: LiTFSI structure and transport in ethylene carbonate from molecular dynamics simulations. J. Phys. Chem. B **110**, 4971–4977 (2006)

[17] Borodin, O., Smith, G.: Quantum chemistry and molecular dynamics simulation study of dimethyl carbonate: ethylene carbonate electrolytes doped with $LiPF_6$. J. Phys. Chem. B **113**, 1763–1776 (2009)

[18] Botan, A., Marry, V., Rotenberg, B.: Diffusion in bulk liquids: Finite-size effects in anisotropic systems. Mol. Phys. (2015 (published online)). DOI 10.1080/00268976.2015.1021730

[19] Calderoni, P., Dürr, D., Kusuoka, S.: A mechanical model of Brownian motion in half-space. Rev. Math. Phys **55**, 649–693 (1989)

[20] Cappelezzo, M., Capellari, C., Pezzin, S., Coelho, L.: Stokes–Einstein relation for pure simple fluids. J. Chem. Phys. **126**, 224,516 (2007)

[21] Carbajal-Tinoco, M., Lopez-Fernandez, R., Arauz-Lara, J.: Asymmetry in colloidal diffusion near a rigid wall. Phys. Rev. Lett. **99**, 138,303 (2007)

[22] Carof, A., Vuilleumier, R., Rotenberg, B.: Two algorithms to compute projected correlation functions in molecular dynamics simulations. J. Chem. Phys. **140**, 124,103 (2014)

[23] Castriota, M., Cazzanelli, E., Nicotera, I., Coppola, L., Oliviero, C., Ranieri, G.: Temperature dependence of lithium ion solvation in ethylene carbonate–$LiClO_4$ solutions. J. Chem. Phys. **118**, 5537–5541 (2003)

[24] Cencini, M., Palatella, L., Pigolotti, S., Vulpiani, A.: Macroscopic equations for the adiabatic piston. Phys. Rev. E **76**, 051,103 (2007)

[25] Cohen, A., Moerner, W.: Suppressing Brownian motion of individual biomolecules in solution. Proc. Natl. Acad. Sci. USA **103**, 4362–4365 (2006)

[26] Cohen, E.: Fifty years of kinetic theory. Physica A **194**, 229–257 (1993)

[27] Cohen, E.: Kinetic theory: Understanding nature through collisions. Am. J. Phys. **61**, 524–533 (1993)

[28] Corngold, N.: Behavior of autocorrelation functions. Phys. Rev. A **6**, 1570–1573 (1972)

[29] Corngold, N., Duderstadt, J.: Perturbative theory of self-diffusion in classical many-particle system. I. Velocity autocorrelation function. Phys. Rev. A **2**, 836–843 (1970)

[30] Cukier, R., Deutch, J.: Microscopic theory of Brownian motion: The multiple-time-scale point of view. Phys. Rev. **177**, 240–244 (1969)

[31] Dekker, H.: Long-time tail in velocity correlations in a one-dimensional Rayleigh gas. Phys. Lett. **88A**, 21–25 (1982)

[32] Delgado, V., Breton, J., Girardet, C.: Generalized Langevin equation approach for the rotational relaxation of a molecule trapped in a 3D crystal. I. Theoretical considerations. J. Chem. Phys. **87**, 4802–4808 (1987)

[33] Despósito, M., Viñales, A.: Subdiffusive behavior in a trapping potential: Mean square displacement and velocity autocorrelation function. Phys. Rev. E **80**, 021,111 (2009)

[34] Dib, R., Ould-Kaddour, F., Levesque, D.: Long-time behavior of the velocity autocorrelation function at low densities and near the critical point of simple fluids. Phys. Rev. E **74**, 011,202 (2006)

[35] Dorfman, J., Cohen, E.: Velocity correlation functions in two and three dimensions. Phys. Rev. Lett. **25**, 1257–1260 (1970)

[36] Dorfman, J., Cohen, E.: Velocity-correlation functions in two and three dimensions: Low density. Phys. Rev. A **6**, 776–790 (1972)

[37] Dorfman, J., Cohen, E.: Velocity-correlation function in two and three dimensions. II. Higher density. Phys. Rev. A **12**, 292–316 (1975)

[38] Dünweg, B., Kremer, K.: Molecular dynamics simulation of a polymer chain in solution. J. Chem. Phys. **99**, 6983–6997 (1993)

[39] Dürr, D., Goldstein, S., Lebowitz, J.: A mechanical model of Brownian motion. Commun. Math. Phys. **78**, 507–530 (1981)

[40] Dürr, D., Goldstein, S., Lebowitz, J.: A mechanical model for the Brownian motion of a convex body. Zeitschrift für Wahrscheinlichkeitstheorie und Verwandte Gebiete **62**, 427–448 (1983)

[41] Easteal, A., Woolf, L., Jolly, D.: Self-diffusion in a dense hard-sphere fluid: A molecular dynamics simulation. Physica **121A**, 286–292 (1983)

[42] Easteal, A., Woolf, L., Jolly, D.: On the number dependence of hard-spheres diffusion of coefficients from molecular dynamics simulations. Physica **127A**, 344–346 (1984)

[43] Einstein, A.: Über die von der molekularkinetischen Theorie der Wärme geforderte Bewegung von in ruhenden Flüssigkeiten suspendierten Teilchen. Annalen der Physik **322**(8), 549–560 (1905)

[44] Epstein, P.: On the resistance experienced by spheres in their motion through gases. Phys. Rev. **23**, 710–733 (1924)

[45] Ernst, M.: Universal power law tails of time correlation functions. Phys. Rev. E **71**, 030,101(R) (2005)

[46] Ernst, M., Hauge, E., van Leeuwen, J.: Asymptotic time behavior of correlation functions. Phys. Rev. Lett. **25**, 1254–1256 (1970)

[47] Ernst, M., Hauge, E., van Leeuwen, J.: Asymptotic time behavior of correlation functions. I. Kinetic terms. Phys. Rev. A **4**, 2055–2065 (1971)

[48] Erpenbeck, J., Wood, W.: Molecular-dynamics calculations of the velocity-autocorrelation function. Methods, hard-disk results. Phys. Rev. A **26**, 1648–1675 (1982)

[49] Erpenbeck, J., Wood, W.: Molecular-dynamics calculation of the velocity autocorrelation function: Hard-sphere results. Phys. Rev. A **32**, 412–422 (1985)

[50] Erpenbeck, J., Wood, W.: Self-diffusion coefficient for the hard-sphere fluid. Phys. Rev. A **43**, 4254–4261 (1991)

[51] Español, P., Zúñiga, I.: Force autocorrelation function in Brownian motion theory. J. Chem. Phys. **98**, 574–580 (1993)

[52] Evans, D., Morriss, G.: Statistical Mechanics of Nonequilibrium Liquids, 2 edn. Cambridge University Press, Cambridge (2008)

[53] Ewald, P.: Die Berechnung optischer und elektrostatischer Gitterpotentiale. Ann. Phys. **369**, 253–287 (1921)

[54] Flyvbjerg, H., Petersen, H.: Error estimates on averages of correlated data. J. Chem. Phys. **91**, 461–466 (1989)

[55] Fox, R.: Long-time tails and diffusion. Phys. RevȦ **27**, 3216–3233 (1983)

[56] Franosch, T., Grimm, M., Belushkin, M., Mor, F., Foffi, G., Forró, L., Jenny, S.: Resonances arising from hydrodynamic memory in Brownian motion. Nature **478**, 85–88 (2011)

[57] Frenkel, D.: Intermolecular spectroscopy and computer simulations. In: Proceedings of the international school of physics "Enrico Fermi", vol. 75, pp. 156–201. Elsevier (1980)

[58] Frenkel, D.: Simulations: The dark side. In: Proceedings of the international school of physics "Enrico Fermi", vol. 184, pp. 195–227. Elsevier (2013). Also published in Eur. Phys. J. Plus 128 (2013) 10.

[59] Frenkel, D., Smit, B.: Understanding Molecular Simulation: From Algorithms to Applications, 2 edn. Academic Press, San Diego (2002)

[60] Frey, E., Kroy, K.: Brownian motion: A paradigm of soft matter and biological physics. Ann. Phys. (Leipzig) **14**, 20–50 (2005)

[61] Friedberg, R., Cameron, J.: Test of the Monte Carlo method: Fast simulation of a small Ising lattice. J. Chem. Phys. **52**, 6049–6058 (1970)

[62] Fruleux, A., Kawai, R., Sekimoto, K.: Momentum transfer in nonequilibrium steady state. Phys. Rev. Lett. **108**, 160,601 (2012)

[63] Fushiki, M.: System size dependence of the diffusion coefficient in a simple liquid. Phys. Rev. E **68**, 021,203 (2003)

[64] Gabl, S., Schröder, C., Steinhauser, O.: Computational studies of ionic liquids: Size does matter and time too. J. Chem. Phys. **137**, 094,501 (2012)

[65] Gereben, O., Pusztai, L.: System size and trajectory length dependence of the static structure factor and the diffusion coefficient as calculated from molecular dynamics simulations: The case of SPC/E water. J. Mol. Liq. **161**, 36–40 (2011)

[66] Givon, D., Kupferman, R., Hald, O.: Existence proof for orthogonal dynamics and the Mori–Zwanzig formalism. Israel J. Math. **145**, 221–241 (2005)

[67] Goodyear, G., Larsen, R., Stratt, R.: Molecular origin of friction in liquids. Phys. Rev. Lett. **76**, 243–246 (1996)

[68] Grabert, H.: Projection Operator Techniques in Nonequilibrium Statistical Mechanics. Springer-Verlag, New York (1982)

[69] Grebenkov, D., Vahabi, M., Bertseva, E., Forró, L., Jeney, S.: Hydrodynamic and subdiffusive motion of tracers in a viscoelastic medium. Phys. Rev. E **88**, 040,701(R) (2013)

[70] Green, M.: Brownian motion in a gas of noninteracting molecules. J. Chem. Phys. **19**, 1036–1046 (1951)

[71] Green, M.: Markoff random processes and the statistical mechanics of time-dependent phenomena. II. Irreversible processes in fluids. J. Chem. Phys. **22**, 398–413 (1954)

[72] Groot, R., Warren, P.: Dissipative particle dynamics: Bridging the gap between atomistic and mesoscopic simulation. J. Chem. Phys. **107**, 4423–4435 (1997)

[73] Haile, J.: Molecular Dynamics Simulation: Elementary Methods. Wiley-Interscience, New York (1997)

[74] Han, S.D., Borodin, O., Seo, D., Zhou, Z.B., Hendersen, W.: Electrolyte solvation and ionic association V. Acetonitrile-lithium bis(fluorosulfonyl)imide (LiFSI) mixtures. J. Electrochem. Soc. **161**, A2042–A2053 (2014)

[75] Hänggi, P.: 100 years of Brownian motion: Historical items and surveys. http://www.physik.uni-augsburg.de/theo1/hanggi/History/BM-History.html

[76] Hänggi, P., Łuzka, J., Talkner, P. (eds.): Focus Issue: Brownian Motion and Diffusion in the 21 Century. New J. Phys. **7** (2005)

[77] Hänggi, P., Marchesoni, F. (eds.): Focus Issue: 100 Years of Brownian Motion. Chaos **15** (2005)

[78] Hasimoto, H.: On the periodic fundamental solutions of the Stokes equations and their application to viscous flow past a cubic array of spheres. J. Fluid Mech. **5**, 317 (1959)

[79] Hauge, E., Martin-Löf, A.: Fluctuating hydrodynamics and Brownian motion. J. Stat. Phys. **7**, 259–281 (1973)

[80] Helfand, E.: Transport coefficients from dissipation in a canonical ensemble. Phys. Rev. **119**, 1–9 (1960)

[81] Heyes, D.: System size dependence of the transport coefficients and Stokes–Einstein relationship of hard sphere and Week–Chandler–Andersen fluids. J. Phys.: Condens. Matter **19**, 376,106 (2007)

[82] Heyes, D., Cass, M., Powles, J., Evans, W.: Self-diffusion coefficient of the hard-sphere fluid: System size dependence and empirical correlations. J. Phys. Chem. B **111**, 1455–1464 (2007)

[83] Hijón, C., Español, P., Vanden-Eijnden, E., Delgado-Buscalioni, R.: Mori–Zwanzig formalism as a practical computational tool. Faraday Discuss. **144**, 301–322 (2010)

[84] Hinch, E.: Application of the Langevin equation to fluid suspensions. J. Fluid Mech. **72**, 499–511 (1975)

[85] den Hollander, F.: Long time tails in physics and mathematics. In: G. Grimmett (ed.) Probability and Phase Transition, pp. 123–137. Kluwer Academic Publisher (1994)

[86] Houndonougbo, Y., Laird, B., Leimkuhler, B.: A molecular dynamics algorithm for mixed hard-core/continuous potentials. Mol. Phys. **98**, 309–316 (2000)

[87] Huang, R., Chavez, I., Taute, K., Lukić, B., Jeney, S., Raizen, M., Florin, E.L.: Direct observation of the full transition from ballistic to diffusive Brownian motion in a liquid. Nature Phys. **7**, 576–580 (2011)

[88] Hynes, J.: Nonlinear fluctuations in master equation system. I. Velocity correlation function for the Rayleigh model. J. Chem. Phys. **62**, 2972–2981 (1975)

[89] Hynes, J., Kapral, R., Weinberg, M.: Microscopic theory of Brownian motion: Mori friction kernel and Langevin-equation derivation. Physica A **80**, 105–127 (1975)

[90] Jannasch, A., Mahamdeh, M., Schäffler, E.: Inertial effects of a small Brownian particle cause a colored power spectral density of thermal noise. Phys. Rev. Lett. **107**, 228,301 (2011)

[91] Jeney, S., Lukić, B., Kraus, J., Franosch, T., Forró, L.: Anisotropic memory effects in confined colloidal diffusion. Phys. Rev. Lett. **100**, 240,604 (2008)

[92] Jeon, J.H., Leijnse, N., Oddershede, L., Metzler, R.: Anomalous diffusion and power-law relaxation of the time averaged mean squared displacement in worm-like micellar solutions. New J. Phys. **15**, 045,011 (2013)

[93] Jones, R., Mandadapu, K.: Adaptive Green–Kubo estimates of transport coefficients from molecular dynamics based on robust error analysis. J. Chem. Phys. **136**, 154,102 (2012)

[94] van Kampen, N.: Stochastic Processes in Physics and Chemistry. Elsevier North-Holland, New York (1981)

[95] Kawai, S., Komatsuzaki, T.: Derivation of the generalized Langevin equation in nonstationary environments. J. Chem. Phys. **134**, 114,523 (2011)

[96] Kim, C., Karniadakis, G.: Microscopic theory of Brownian motion revisited: The Rayleigh model. Phys. Rev. E **87**, 032,129 (2013)

[97] Kim, C., Karniadakis, G.: Time correlation functions of Brownian motion and evaluation of friction coefficient in the near-Brownian-limit regime. Multiscale Model. Simul. **12**, 225–248 (2014)

[98] Kirkwood, J.: The statistical mechanical theory of transport processes. J. Chem. Phys. **14**, 180–201 (1946)

[99] Kloeden, P., Platen, E.: Numerical Solution of Stochastic Differential Equations. Springer-Verlag, Berlin (1992)

[100] Kneller, G.: Generalized Kubo relations and conditions for anomalous diffusion: Physical insights from a mathematical theorem. J. Chem. Phys. **134**, 224,106 (2011)

[101] Kneller, G., Hinsen, K.: Computing memory functions from molecular dynamics simulations. J. Chem. Phys. **115**, 11,097–11,105 (2001)

[102] Kneller, G., Hinsen, K., Sutmann, G.: Mass and size effects on the memory function of tracer particles. J. Chem. Phys. **118**, 5283–5286 (2003)

[103] Kneller, G., Sutmann, G.: Scaling of the memory function and Brownian motion. J. Chem. Phys. **120**, 1667–1669 (2004)

[104] Kou, S.: Stochastic modeling in nanoscale biophysics: Subdiffusion within proteins. Ann. Appl. Stat. **2**, 501–535 (2008)

[105] Kou, S., Xie, X.: Generalized Langevin equation with fractional Gaussian noise: Subdiffusion within a single protein molecule. Phys. Rev. Lett. **93**, 180,603 (2004)

[106] Kubo, R.: Statistical-mechanical theory of irreversible processes. I. General theory and simple applications to magnetic and conduction problems. J. Phys. Soc. Jpn. **12**, 570–586 (1957)

[107] Kubo, R.: The fluctuation-dissipation theorem. Rep. Prog. Phys. **29**, 255–284 (1966)

[108] Kusuoka, S., Liang, S.: A classical mechanical model of Brownian motion with plural particles. Rev. Math. Phys. **22**, 733–838 (2010)

[109] Landau, L., Lifschitz, E.: Fluid Mechanics. Pergamon Press (1959)

[110] Langevin, P.: Sur la théorie du mouvement brownien. C. R. Acad. Sci. (Paris) **146**, 530–533 (1908)

[111] Leal, L.: Advanced Transport Phenomena: Fluid Mechanics and Convective Transport Processes. Cambridge University Press (2010)

[112] Lebowitz, J., Résibois, P.: Microscopic theory of Brownian motion in an oscillating field; Connection with macroscopic theory. Phys. Rev. **139**, A1101–A1111 (1965)

[113] Lebowitz, J., Rubin, E.: Dynamical study of Brownian motion. Phys. Rev. **131**, 2381–2396 (1963)

[114] Lee, S., Kapral, R.: Friction and diffusion of a Brownian particle in a mesoscopic solvent. J. Chem. Phys. **121**, 11,163–11,169 (2004)

[115] de Leeuw, S., Perram, J., Smith, E.: Simulation of electrostatic systems in periodic boundary conditions. I. Lattice sums and dielectric constants. Proc. R. Soc. London Ser. A **373**, 27–56 (1980)

[116] Lemons, D., Gythiel, A.: Paul Langevin's 1908 paper "On the theory of Brownian motion" ["Sur la théorie du mouvement brownien," C. R. Acad. Sci. (Paris) 146, 530–533 (1908)]. Am. J. Phys. **65**, 1079–1081 (1997)

[117] Levesque, D., Ashurst, W.: Long-time behavior of the velocity autocorrelation function for a fluid of soft repulsive particles. Phys. Rev. Lett. **33**, 277–280 (1974)

[118] Levesque, D., Verlet, L., Kürkijarvi, J.: Computer "experiments" on classical fluids. IV. Transport properties and time-correlation functions of the Lennard-Jones liquid near its triple point. Phys. Rev. A **7**, 1690–1700 (1973)

[119] Li, G., Tam, L.K., Tang, J.: Amplified effect of Brownian motion in bacterial near-surface swimming. Proc. Natl. Acad. Sci. USA **105**, 18,355–18,359 (2008)

[120] Li, T., Kheifets, S., Medellin, D., Raizen, M.: Measurement of the instantaneous velocity of a Brownian particle. Science **328**, 1673–1675 (2010)

[121] Li, T., Raizen, M.: Brownian motion at short time scales. Ann. Phys. (Berlin) **525**, 281–295 (2013)

[122] Li, Z., Bian, X., Caswell, B., Karniadakis, G.: Construction of dissipative particle dynamics models for complex fluids *via* the Mori–Zwanzig formulation. Soft Matter **10**, 8659–8672 (2014)

[123] Linz, P.: Analytical and Numerical Methods for Volterra Equations. Society for Industrial and Applied Mathematics (1987)

[124] Lisý, V., Tóthová, J., Glod, L.: On the correlation properties of thermal noise in fluids. Int. J. Thermophys. **34**, 629–641 (2013)

[125] Locsei, J.: Persistence of direction increases the drift velocity of run and tumble chemotaxis. J. Math. Biol. **55**, 41–60 (2007)

[126] Lukić, B., Jeney, S., Tischer, C., Kulik, A., Ferró, L.: Direct observation of nondiffusive motion of a Brownian particle. Phys. Rev. Lett. **95**, 160,601 (2005)

[127] Mansour, M., Garcia, A., Baras, F.: Hydrodynamic description of the adiabatic piston. Phys. Rev. E **73**, 016,121 (2006)

[128] Mazo, R.: Momentum-correlation function in a Rayleigh gas. J. Chem. Phys. **35**, 831–835 (1961)

[129] Mazo, R.: On the theory of Brownian motion. VIII. A Brownian particle in a dilute gas with inelastic collisions. J. Stat. Phys. **12**, 427–436 (1975)

[130] Mazo, R.: Brownian Motion: Fluctuation, Dynamics, and Applications. Clarendon, Oxford (2002)

[131] Mazur, P., Oppenheim, I.: Molecular theory of Brownian motion. Physica **50**, 241–258 (1970)

[132] McDonough, A., Russo, S., Snook, I.: Long-time behavior of the velocity autocorrelation function for moderately dense, soft-repulsive, and Lennard-Jones fluids. Phys. Rev. E **63**, 026,109 (2001)

[133] McPhie, M., Davis, P., Snook, I., Ennis, J., Evans, D.: Generalized Langevin equation for nonequilibrium systems. Physica A **299**, 412–426 (2001)

[134] Meier, K., Laesecke, A., Kabelac, S.: Transport coefficients of the Lennard-Jones model fluid. II Self-diffusion. J. Chem. Phys. **121**, 9526–9535 (2004)

[135] Michaels, I., Oppenheim, I.: Long-time tails and Brownian motion. Physica A **81**, 221–240 (1975)

[136] Min, W., Luo, G., Cherayil, B.J., Kou, S., Xie, X.: Observation of a power-law memory kernel for fluctuations within a single protein molecule. Phys. Rev. Lett. **94**, 198,302 (2005)

[137] Monaghan, J.: Smoothed particle hydrodynamics. Rep. Prog. Phys. **68**, 1703–1759 (2005)

[138] Montgomery, D.: Brownian motion from Boltzmann's equation. Phys. Fluids **14**, 2088–2090 (1971)

[139] Morgado, R., Oliveira, F.: Relation between anomalous and normal diffusion in systems with memory. Phys. Rev. Lett. **89**, 100,601 (2002)

[140] Mori, H.: Transport, collective motion, and Brownian motion. Prog. Theor. Phys. **33**, 423–455 (1965)

[141] Munakata, T., Ogawa, H.: Dynamical aspects of an adiabatic piston. Phys. Rev. E **64**, 036,119 (2001)

[142] Nelson, E.: Dynamical Theories of Brownian Motion, 2 edn. Princeton University Press (2001)

[143] Nowakowski, B.: Solution of the Fokker–Planck equation for reactive Rayleigh gas. Phys. Rev. E **53**, 2964–2967 (1996)

[144] Ould-Kaddour, F., Levesque, D.: Molecular-dynamics investigation of tracer diffusion in a simple fluid: Test of the Stokes–Einstein law. Phys. Rev. E **63**, 011,205 (2000)

[145] Ould-Kaddour, F., Levesque, D.: Determination of the friction coefficient of a Brownian particle by molecular-dynamics simulation. J. Chem. Phys. **118**, 7888–7891 (2003)

[146] Ould-Kaddour, F., Levesque, D.: Diffusion of nanoparticles in dense fluids. J. Chem. Phys. **127**, 154,514 (2007)

[147] Papoulis, A.: Probability, Random Variables, and Stochastic Processes. McGraw-Hill, New York (1965)

[148] Pechukas, P.: Generalized Langevin equation of Mori and Kubo. Phys. Rev. **164**, 174–175 (1967)

[149] Petravic, J.: Equilibrium calculation of the friction coefficient for a massive particle moving in finite liquid volume. J. Chem. Phys. **129**, 114,502 (2008)

[150] Petravic, J.: Force autocorrelation function in linear response theory and the origin of friction. J. Chem. Phys. **129**, 094,503 (2008)

[151] Plyukhin, A., Schofield, J.: Langevin equation for the Rayleigh model with finite-range interactions. Phys. Rev. E **68**, 041,107 (2003)

[152] Plyukhin, A., Schofield, J.: Langevin equation for the extended Rayleigh model with an asymmetric bath. Phys. Rev. E **69**, 021,112 (2004)

[153] Pomeau, Y.: Asymptotic behavior of the Green–Kubo integrands in binary mixtures. J. Chem. Phys. **57**, 2800–2810 (1972)

[154] Pomeau, Y., Résibois, P.: Time dependent correlation functions and mode-mode coupling theories. Phys. Rep. **19**, 63–139 (1975)

[155] Porrà, J., Wang, K.G., Masoliver, J.: Generalized Langevin equations: Anomalous diffusion and probability distributions. Phys. Rev. E **53**, 5872–5881 (1996)

[156] Press, W., Teukolsky, S., Vetterling, W., Flannery, B.: Numerical Recipes: The Art of Scientific Computing, 3 edn. Cambridge University Press (2007)

[157] Rapaport, D.: The Art of Molecular Dynamics Simulation, 2 edn. Cambridge University Press, New York (2004)

[158] Résibois, P., Davis, H.: Transport equation of a Brownian particle in an external field. Physica **30**, 1077–1091 (1964)

[159] Rozmanov, D., Kusalik, P.: Transport coefficients of the TIP4P-2005 water model. J. Chem. Phys. **136**, 044,507 (2012)

[160] Russel, W.: Brownian motion of small particles suspended in liquids. Ann. Rev. Fluid Mech. **13**, 425–455 (1981)

[161] Schlick, T.: Molecular Modeling and Simulation: An Interdisciplinary Guide, 2 edn. Springer-Verlag, New York (2010)

[162] Schmidt, J., Skinner, J.: Hydrodynamic boundary conditions, the Stokes–Einstein law, and long-time tails in the Brownian limit. J. Chem. Phys. **119**, 8062–8068 (2003)

[163] Schmidt, J., Skinner, J.: Brownian motion of a rough sphere and the Stokes–Einstein law. J. Phys. Chem. B **108**, 6767–6771 (2004)

[164] Shin, H., Kim, C., Talkner, P., Lee, E.: Brownian motion from molecular dynamics. Chem. Phys. **375**, 316–326 (2010)

[165] Sickert, M., Rondelez, F., Stone, H.A.: Single-particle Brownian dynamics for characterizing the rheology of fluid Langmuir monolayers. Europhys. Lett. **90**, 126,104 (2007)

[166] Singh, S., Huang, C.C., Westphal, E., Gompper, G., Winkler, R.: Hydrodynamic correlations and diffusion coefficient of star polymers in solution. J. chem. Phys. **141**, 084,901 (2014)

[167] von Smoluchowski, M.: Zur kinetischen Theorie der Brownschen Molekularbewegung und der Suspensionen. Annalen der Physik **326**(14), 756–780 (1906)

[168] Snook, I.: The Langevin and Generalized Langevin Approach to the Dynamics of Atomic, Polymeric and Colloidal Systems. Elsevier, New York (2007)

[169] Sokolovskii, R., Thachuk, M., Patey, G.: Tracer diffusion in hard sphere fluids from molecular to hydrodynamic regimes. J. Chem. Phys. **125**, 204,502 (2006)

[170] Spångberg, D., Hermansson, K.: Effective three-body potentials for $Li^+(aq)$ and $Mg^{2+}(aq)$. J. Chem. Phys. **119**, 7263–7281 (2003)

[171] Speedy, R.: Diffusion in the hard sphere fluid. Mol. Phys. **62**, 509–515 (1987)

[172] Spohn, H.: Kinetic equations from Hamiltonian dynamics: Markovian limits. Rev. Mod. Phys. **53**, 569–615 (1980)

[173] Stella, L., Lorentz, C., Kantorovich, L.: Generalized Langevin equation: An efficient approach to nonequilibrium molecular dynamics of open systems. Phys. Rev. B **89**, 134,303 (2014)

[174] Sutmann, G., Steffen, B.: Correction of finite size effects in molecular dynamics applied to the friction coefficient of a Brownian particle. Comput. Phys. Commun. **147**, 374–377 (2002)

[175] Szász, D., Tóth, B.: A dynamical theory of Brownian motion for the Rayleigh gas. J. Stat. Phys. **47**, 681–693 (1987)

[176] Szász, D., Tóth, B.: Towards a unified dynamical theory of the Brownian particle in an ideal gas. Commun. Math. Phys. **111**, 41–62 (1987)

[177] Takano, M., Terada, T., Sasai, M.: Unidirectional Brownian motion observed in an *in silico* single molecule experiment of an actomyosin motor. Proc. Natl. Acad. Sci. USA **107**, 7769–7774 (2010)

[178] Taniguchi, S., Iwasaki, A., Sugiyama, M.: Relationship between Maxwell boundary condition and two kinds of stochastic thermal wall. J. Phys. Soc. Jpn. **77**, 124,004 (2008)

[179] Tazi, S., Botan, A., Salanne, M., Marry, V., Turq, P., Rotenberg, B.: Diffusion coefficient and shear viscosity of rigid water models. J. Phys.: Condens. Matter **24**, 284,117 (2012)

[180] Tehver, R., Toigo, F., Koplik, J., Banavar, J.R.: Thermal walls in computer simulations. Phys. Rev. E **57**, R17 (1998)

[181] Tischer, C., Altmann, S., Fišinger, S., Heinrich, J., Stelzer, E., Florin, E.L.: Three-dimensional thermal noise imaging. Appl. Phys. Lett. **79**, 3878–3880 (2001)

[182] Tucker, S., Tuckerman, M., Berne, B.: Comparison of rate theories for generalized Langevin dynamics. J. Chem. Phys. **95**, 5809–5826 (1991)

[183] Tuckerman, M., Berne, B.: Vibrational relaxation in simple fluids: Comparison of theory and simulation. J. Chem. Phys. **98**, 7301–7318 (1993)

[184] Uline, M., Siderius, D., Corti, D.: On the generalized equipartition theorem in molecular dynamics ensembles and the microcanonical thermodynamics of small systems. J. Chem. Phys. **128**, 124,301 (2008)

[185] Uranagase, M., Munakata, T.: Piston dynamics from a microscopic ensemble. Phys. Rev. E **75**, 011,110 (2007)

[186] Viñales, A., Despósito, M.: Anomalous diffusion: Exact solution of the generalized Langevin equation for harmonically bounded particle. Phys. Rev. E **73**, 016,111 (2006)

[187] Viscardy, S., Servantie, J., Gaspard, P.: Transport and Helfand moments in the Lennard-Jones fluid. I. Shear viscosity. J. Chem. Phys. **126**, 184,512 (2007)

[188] Viscardy, S., Servantie, J., Gaspard, P.: Transport and Helfand moments in the Lennard-Jones fluid. II. Thermal conductivity. J. Chem. Phys. **126**, 184,513 (2007)

[189] Wang, G., Prabhakar, R., Sevick, E.: Hydrodynamic mobility of an optically trapped colloidal particle near fluid-fluid interfaces. Phys. Rev. Lett. **103**, 248,303 (2009)

[190] Wang, K., Tokuyama, M.: Nonequilibrium statistical description of anomalous diffusion. Physica A **265**, 341–351 (1999)

[191] Wigner, H., Seitz, F.: On the constitution of metallic sodium. Phys. Rev. **43**, 804–810 (1933)

[192] Xiang, T.X., Liu, F., Grant, D.: Generalized Langevin equations for molecular dynamics in solution. J. Chem. Phys. **94**, 4463–4471 (1991)

[193] Xu, K.: Nonaqueous liquid electrolytes for lithium-based rechargeable batteries. Chem. Rev. **104**, 4303–4417 (2004)

[194] Yamgaguchi, T., Kimura, Y., Hirota, N.: Molecular dynamics simulation of solute diffusion in Lennard-Jonnes fluids. Mol. Phys. **94**, 527–537 (1998)

[195] Yeh, I.C., Hummer, G.: System-size dependence of diffusion coefficients and viscosities from molecular dynamics simulations with periodic boundary conditions. J. Phys. Chem. B **108**, 15,873–15,879 (2004)

[196] Zwanzig, R.: Elementary derivation of time-correlation formulas for transport coefficients. J. Chem. Phys. **40**, 2527–2533 (1964)

[197] Zwanzig, R., Ailawadi, N.: Statistical error due to finite time averaging in computer experiments. Phys. Rev. **182**, 280–283 (1969)

[198] Zwanzig, R., Bixon, M.: Compressibility effects in the hydrodynamic theory of Brownian motion. J. Fluid Mech. **69**, 21–25 (1975)